Title
Ion permeation in TMEM16A and TMEM16F

Author
Nguyen, Dung Manh

Publication Date
2021

Peer reviewed|Thesis/dissertation

Ion permeation in TMEM16A and TMEM16F

By

DUNG MANH NGUYEN
DISSERTATION

Submitted in partial satisfaction of the requirements for the degree of

DOCTOR OF PHILOSOPHY

in

Pharmacology and Toxicology

in the

OFFICE OF GRADUATE STUDIES

of the

UNIVERSITY OF CALIFORNIA

DAVIS

Approved:

_____

Tsung-Yu Chen, Chair

_____

Robert H. Fairclough

_____

Jon T. Sack

Committee in Charge

2021

Abstract

TMEM16A and TMEM16F belong to the transmembrane protein 16 family. TMEM16A functions as a Ca^{2+}-activated Cl^- channel, whereas TMEM16F functions as a phospholipid scramblase that also conducts ionic current. The anion-selective TMEM16A has a linear current-voltage relationship, whereas the non-selective TMEM16F has an outwardly rectified current-voltage relationship. I used electrophysiological and biomolecular techniques to study the molecular basis of ion permeation in TMEM16A and TMEM16F. Manipulating the charge of the pore-lining K584 in TMEM16A alters the channel's current-voltage relationship, demonstrating an electrostatic effect. The current-voltage relationship of TMEM16A becomes more outwardly rectified as the charge of this residue becomes more negatively charged. Mutating the analogous residue in TMEM16F, Q599, also alters the current-voltage relationship of TMEM16F. However, there is no correlation between the charge of this residue and the current-voltage relationship of TMEM16F. Interestingly, aromatic mutants of Q559 exhibit a more linear current-voltage relationship and is more resistant to current rundown than the wild-type protein. Since the current rundown in TMEM16A and TMEM16F has been attributed to the depletion of phosphatidylinositol 4,5-bisphosphate from the cell membrane, and the ion permeation (or the phospholipids transport) pathway of TMEM16 proteins is partially exposed to membrane phospholipids, I speculated that mutating Q559 in TMEM16F influences ion

permeation by altering the conformation of phospholipids nearby. Therefore, there is a possibility that divalent cations binding to phospholipids near the intracellular vestibule of TMEM16A and TMEM16F may affect ion permeation in these proteins. Indeed, mM concentration of divalent cations potentiate TMEM16A current and reduce TMEM16F selectivity for Na^+ over Cl^-. Tens of mM concentrations of monovalent cations also affect the interaction between phospholipids and divalent cations. Lowering the concentration of NaCl enhances the potentiation of TMEM16A by divalent cations and enhances the ability of divalent cations to alter the ion selectivity of TMEM16F. The sensitivity of ion selectivity to ionic conditions explains the controversial relative ion permeability of TMEM16F reported in the literature. Also, sequestering negatively charged phospholipids with poly-L-lysine alters the interaction between divalent cations and these two proteins, consistent with the idea that divalent cations can interact with membrane phospholipids.

Acknowledgment

I would like to thank my mentor, Dr. Tsung-Yu Chen, for his support and mentorship. Without your mentorship, I would be banging my head against a wall pursuing projects that end nowhere.

Special thanks to Dr. Jon Sack for sparking my interest in ion channels. Without attending your PTX 201 lecture and doing a rotation in your lab, I would not have ended up studying ion channels.

I would also like to thank Dr. Robert H. Fairclough for helping me with all my manuscripts and being my dissertation advisor.

Special thanks to Dr. Mona Monfared for changing my view on teaching. You have shown me that teaching is fun and a crucial way to improve my scientific knowledge.

To Wei-Ping Yu and Hwoi Chan Kwon, whether my experiments fail or succeed, it was fun working with you guys. Thank you.

To Phan and Kala, thank you for all your support over the years.

Finally, thank you to my mother, who has made so many sacrifices to get me to where I am today.

Table of Contents

Chapter 1: Overview of TMEM16 proteins

1.1 General physiology of TMEM16 proteins

The transmembrane protein 16 (TMEM16) family consists of membrane proteins functioning as calcium-activated chloride channels (CaCC) or phospholipid scramblases. The first member of this gene family, TMEM16A, was functionally identified from a search for the gene that encodes the classical CaCC reported in the 1980s [1-3]. Despite the ubiquitous expression of CaCCs in many tissues, including ductal epithelial cells, the identity of the gene encoding the classical CaCC was unknown for decades. Although Sun et al. identified bestrophin 1 as a CaCC in 2002 [4], bestrophin 1 differs from the classical CaCC in its biophysical properties, such as the current rectification and the activation kinetic [5]. In 2008, three groups of researchers independently identified TMEM16A and demonstrated that TMEM16A's functional behavior is very similar to that of the classical CaCC [6-8]. Later, a different line of study searching for the defective gene responsible for a blood coagulation disease, Scott syndrome, led to the identification of TMEM16F [9]. Interestingly, the underlying mechanism of the blood coagulation problem in Scott syndrome is not due to TMEM16F's abnormal ionic conduction but rather due to the abnormal phospholipid scramblase function of TMEM16F [9]. Currently, molecular cloning work has identified ten mammalian TMEM16 proteins (TMEM16A-K, with no TMEM16I).

Among these members, two are CaCC (TMEM16A and TMEM16B), while most other members, such as TMEM16F, function as phospholipid scramblases. Non-mammalian TMEM16 family members, including nhTMEM16 (*Nectria haematococca*, fungi) [10], afTMEM16 (*Aspergillus fumigatus*, fungi) [11], IST2 (*Saccharomyces cerevisiae*, fungi) [12, 13], and DdTMEM16 (*Dictyostelium discoideum*, amoeba) [14], have also been identified.

TMEM16A, a classical CaCC, is known for its well-documented role in transepithelial fluid transport in exocrine ducts. Therefore, TMEM16A is thought to be very relevant to various pulmonary diseases such as cystic fibrosis, chronic obstructive pulmonary disease, and asthma. Transepithelial fluid transport maintains the airway surface's proper hydration, and many ion channels and transporters are known to be involved in this vital process. In the airway epithelial cells, TMEM16A and cystic fibrosis transmembrane conductance regulator (CFTR) are expressed on the epithelial cells' apical membrane, but TMEM16A appears to have a lower expression level than CFTR and may thus contribute less to the overall fluid secretion [15-18]. However, Benedetto et al. (2017) showed that the function and expression of CFTR are dependent on TMEM16A [15]. They also showed that the activity of TMEM16A is related to abnormal mucus secretion [19], a common symptom of various respiratory diseases. Besides airway epithelial cells, TMEM16A is also expressed in the airway smooth muscle (ASM) [20]. In ASM, the activation of G-protein coupled receptors (GPCR) increases

intracellular Ca^{2+} concentration to a level that is necessary for smooth muscle contraction. The initial increase in intracellular Ca^{2+} concentration by GPCR activation can activate TMEM16A. Generally, smooth muscle cells have a resting potential ranging from −60 mV to −40 mV [21-24] and a Cl^- reversal potential ranging from −33 mV to −6 mV (previously measured in guinea pig, dog, rat, and rabbit) [25]. Therefore, the activation of TMEM16A will lead to an efflux of Cl^- as dictated by the electrochemical driving force. The subsequent membrane depolarization activates voltage-dependent calcium channels, leading further increase in intracellular Ca^{2+}. Therefore, TMEM16A activation can contribute to the GPCR-dependent depolarization that triggers smooth muscle contraction. Thus, TMEM16A inhibition may be a viable strategy for alleviating bronchial hyperreactivity. For example, niflumic acid, a non-selective CaCC inhibitor, can attenuate the serotonin-induced tracheal smooth muscle contraction in rat [26]. TMEM16A also plays a role in the cell volume regulation process [27]. Hypotonic conditions activate various cationic channels, such as TRPM7 and bradykinin B2 receptor [28-30]. The subsequent increase in the intracellular Ca^{2+} concentration activates TMEM16A, which aids in the regulatory volume decrease (RVD) [30]. Since various cation channels and transporters are involved in RVD, many questions regarding TMEM16A's contribution to RVD remain unanswered. Also, a wide variety of tumors have elevated expression

of TMEM16A [31], although the exact role of TMEM16A in cancer biology is still far from clear.

In 1991, Linda Buck and Richard Axel cloned and characterized several olfactory receptors [32]. Within the same year, Steven Kleene and Robert Gesteland discovered the CaCC current in frog olfactory cilia [33]. In 2005, the TMEM16B gene was detected in olfactory sensory neurons [34]. However, it was not until Schroeder et al. identified TMEM16B as a CaCC in 2008 [7] that TMEM16B is thought to be critical for the olfactory sensation. For olfactory signal transduction, the binding of odorants to odorant receptors in the olfactory cilia activates G-proteins, increasing the adenyl cyclase activity to make cyclic AMP (cAMP). The increase of intracellular cAMP opens olfactory cyclic nucleotide-gated channels, causing an influx of Na^+ and Ca^{2+} and depolarizes olfactory neurons [35-37]. Subsequently, the increase of intracellular Ca^{2+} concentration opens Ca^{2+}-activated Cl^- channels [33, 38]. Since the intracellular Cl^- concentration is high [39-41], TMEM16B activation causes an efflux of Cl^- which depolarizes the olfactory sensory neurons and greatly enhances olfactory neurons' sensitivity to odorant stimulation [35, 42, 43]. Besides olfactory signaling functions, TMEM16B was shown to be important for motor coordination and learning in mice [44-46]. TMEM16B seems to modulate action potential and neuronal excitability of lateral septum neurons in the brain [47]. This effect on the neuronal action potential in the central nervous system may be related to

the observation that TMEM16B's activity appears to correlate with anxiety in mice [48].

Another functional group in the mammalian TMEM16 family consists of transmembrane proteins functioning as phospholipid scramblases. In 2010, Suzuki et al. reported that a defect in TMEM16F, which facilitates the bidirectional phospholipid transport between the inner and outer leaflets of the platelet's cell membranes, may be the culprit behind abnormal blood coagulation in Scott syndrome [9]. It is now known that TMEM16F also exhibits ion channel activity, but the physiological role of TMEM16F's ionic current remains poorly understood [49]. In contrast, TMEM16F is best known for regulating membrane phospholipids. The inner and outer leaflets of eukaryotic cell membranes have different phospholipid compositions, with the negatively charged phospholipids, such as phosphatidylserine (PS) or L-α-phosphatidylinositol-4,5-bisphosphate (PIP2), primarily present in the inner leaflet [50]. Flippases and floppases establish such a membrane phospholipid asymmetry by using ATP to facilitate unidirectional phospholipid transport, whereas phospholipid scramblases, such as TMEM16F and Xk-Related Protein 8 (Xkr8) dissipate this asymmetry [9, 51, 52]. The asymmetry of membrane phospholipids plays a vital role in many physiological processes such as apoptosis (programmed cell death) and thrombosis (blood clotting) [53]. During apoptosis, for example, caspase-dependent activation of Xkr8 triggers the PS exposure in apoptotic cells,

which facilitates phagocytosis [52]. Other known phospholipid scramblases besides TMEM16F and Xkr8 include PLSCR1, which is associated with apoptosis, and PLSCR3, which is associated with mitophagy [54]. Unlike other phospholipid scramblases, TMEM16F is known for its essential role in blood coagulation. During thrombosis, activation of TMEM16F triggers PS exposure to the extracellular environment and aids in the assembly of blood coagulation factors on the activated platelets' surface [9, 55]. Thus, a nonfunctional TMEM16F disrupts thrombosis, leading to the abnormal blood coagulation in the Scott syndrome [56, 57]. Besides thrombosis, the PS exposure mediated by TMEM16F was linked to trophoblast fusion and placental development [58]. Recently, Wu et al. (2020) reported that TMEM16F plays a role in repairing mice thymocytes’ membrane that was damaged by pore-forming agents [59]. They showed that the activation of TMEM16F results in membrane blebbing and extracellular vesicle shedding, which is likely necessary for the membrane repair process [59]. Also, their results agree with previous reports of TMEM16F-dependent extracellular vesicle and microparticle shedding [57, 60-65].

Compared to TMEM16A, TMEM16B, and TMEM16F, much less is known about other mammalian family members' physiological functions. TMEM16C, TMEM16D, TMEM16G, and TMEM16J were shown to exhibit phospholipid scramblase activity [66]. TMEM16C (linked to late-onset Alzheimer's disease) and TMEM16D (linked to schizophrenia and bipolar disorder) are

found in the spinal cord, brain stem, cerebellum, and eye [67-70]. Also, TMEM16C knock-out rats exhibit enhanced mechanical and thermal sensitivity, and the protein seems to modulate the Slack sodium-activated potassium channel in dorsal root ganglia [71]. Like TMEM16F, TMEM16E has both phospholipid scramblase and ion channel activities [72]. TMEM16E, expressed in muscle and bone tissues, is linked to gnathodiaphyseal dysplasia, a bone disorder [73]. TMEM16G, expressed only in the prostate, has been associated with aggressive prostate cancer [74, 75]. TMEM16H functions as an endoplasmic reticulum-plasma membrane tethering protein and plays a crucial role in the functioning of calcium release-activated channels [76] associated with various neurodegenerative diseases [77]. Also, the detection of TMEM16H in murine embryonic dorsal root ganglia and neural tube suggests a possible role in vertebrate development [78]. TMEM16J exhibits both phospholipid scramblase and cation-selective channel activity [66, 79]. Murine embryonic esophagus, small intestine, stomach, and pancreas express TMEM16J [78]. While the physiological role of TMEM16J remains poorly understood, stage II and III colorectal cancer tissues from human patients seem to have lower TMEM16J expression than nontumorous tissues [80]. Also, Jun et al. (2009) reported that TMEM16J promotes the proliferation of PANC-1, a human pancreatic cancer cell line [81]. Finally, TMEM16K, localized in the endoplasmic reticulum, is a

phospholipid scramblase that has been associated with spinocerebellar ataxia-10 [82-85].

Studies of non-mammalian TMEM16 proteins have been focused on nhTMEM16, afTMEM16, DdTMEM16, IST2, and a *Drosophila melanogaster* TMEM16 protein, Subdued (CG16718). When reconstituted in liposomes, both nhTMEM16 and afTMEM16 exhibit phospholipid scramblase and non-selective ion channel activity [10, 11, 86]. DdTMEM16 transiently transfected in human embryonic kidney 293 cells (HEK293) also exhibits phospholipid scramblase activity but lack ion channel activity [14]. The physiological roles of these non-mammalian TMEM16 proteins remain poorly understood. *D. melanogaster* Subdued, which exhibits lipid scramblase and ion channel activity, seems to play a role in defense against intestinal bacterial infection and thermal nociception [87-89]. Like TMEM16H, IST2 functions as an endoplasmic reticulum-plasma membrane tethering protein and does not seem to be an ion channel or a phospholipid scramblase [13]. While non-mammalian TMEM16 proteins are not directly relevant to human diseases, the studies of these proteins, especially nhTMEM16 and afTMEM16 [10, 90, 91], have advanced our understanding of the structure of TMEM16 proteins significantly.

1.2 General structure of TMEM16 Proteins

1.2.1 Topology and stoichiometry

The gene sequences of TMEM16 family members were first known from the human genome sequencing project even before the physiological roles of these "**T**rans**mem**brane Proteins of Unknown Functions" were identified. Initial sequence-based topology analysis of TMEM16 proteins suggests that they contain at least eight transmembrane helices (TM) [6, 8, 73, 92-94]. Biochemical experiments such as immunofluorescence labeling of various regions of TMEM16G and analyzing its N-glycosylation sites also suggest that the protein contains eight transmembrane helices [92]. TMEM16 proteins thus were referred to as anoctamin proteins (a combination of "anion" and Latin prefix for eight, "octa") [8]. Hence, TMEM16A-K are also known as ANO1-10. However, Brunner et al. (2014) first noticed that such a membrane topology of eight TM might need to be revised when they report the first high-resolution structure of nhTMEM16 with ten TM [10]. Indeed, all high-resolution structures of TMEM16 proteins published so far show that TMEM16 proteins have ten TM rather than eight TM (**Fig. 1.1**) [10, 82, 90, 95-97]. Since most TMEM16 proteins are not anion channels and all known TMEM16 proteins have ten transmembrane helices, the nomenclature of "anoctamin" has been falling out of favor.

Alternative splicing of TMEM16A precursor mRNA generates various splice variants with different Ca^{2+} affinity and voltage dependence [98].

Splice variants of TMEM16A comprise a combination of four alternative segments labeled ***a***, ***b***, ***c***, and ***d*** (**Fig. 1.1**). Spliced variant ***x*** (***x*** can be any combination of alternative segments ***a***, ***b***, ***c***, and ***d***) of TMEM16A refers to the channel that only contains the alternative segment listed. Splice variants that lack alternative segment ***d*** are similar to variants with this segment, and splice variants that lack the alternative segment ***a*** also lack the other three alternative segments [99]. For this dissertation, we will use the residue numbering of alternatively spliced variant ***a*** of TMEM16A unless stated otherwise.

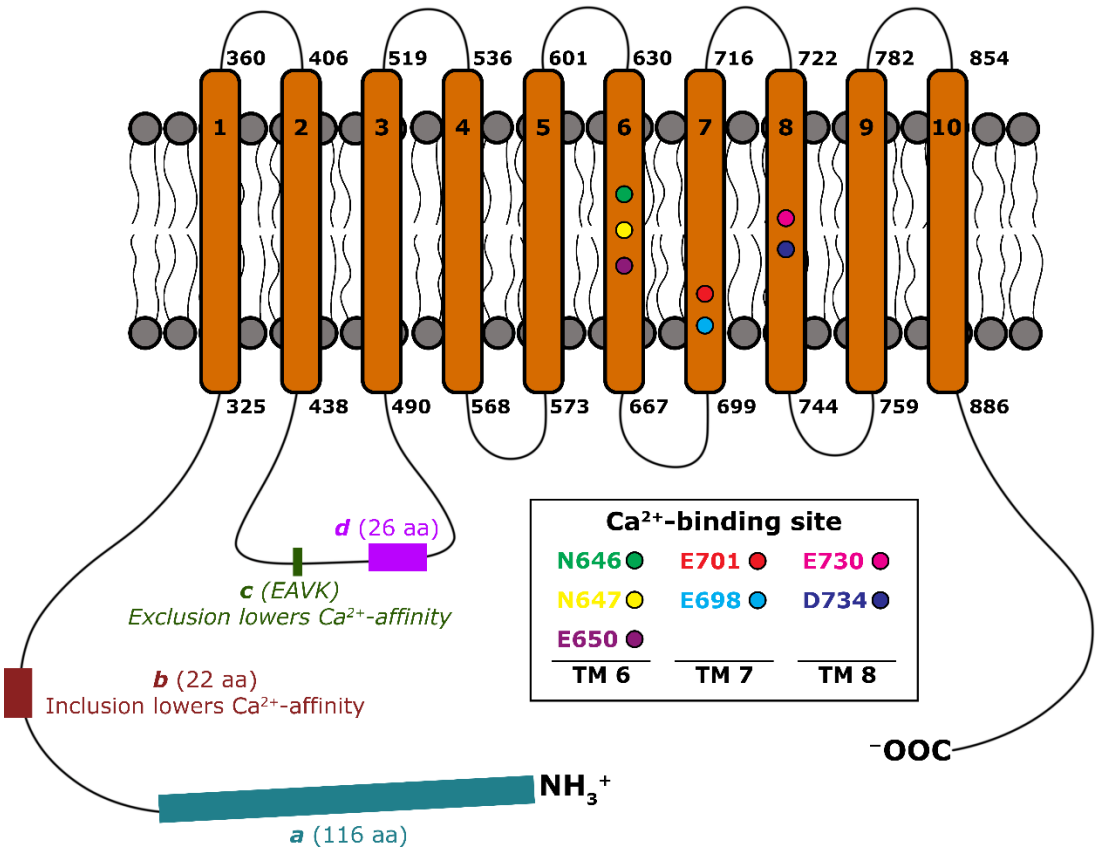

Figure 1.1 The topology of TMEM16 proteins. The ten transmembrane helices are numbered, and the location of TMEM16A alternative segments ***a***-***d*** is shown. The average helix length is ~30 residues. Residues forming the Ca^{2+} binding site of TMEM16A are shown. Approximate sequence numbers of the N-terminal and C-terminal of each transmembrane helices of TMEM16A are shown in black (PDB: 7B5C [100]). The residue number for the Ca^{2+}-binding site is for TMEM16*a* (splice variant ***a*** of TMEM16A). For PDB 7B5C (TMEM16*ac*), N646 (green) is N650, N647 (yellow) is N651, E650 (purple) is E654, E698 (cyan) is E702, E701 (red) is E705, E730 (pink) is E734, D734 (blue) is D738.

Before the availability of high-resolution structures, researchers probed the stoichiometry of TMEM16 proteins using biochemical methods. Fallah et al. (2011) and Sheridan et al. (2011) reported that the denaturation of TMEM16A by sodium dodecyl sulfate shows two protein bands in the polyacrylamide gel [101, 102]. They further showed that the chemical cross-linking of non-denatured TMEM16A yields a prominent polyacrylamide gel band for a dimeric assembly relative to other oligomeric assemblies [101, 102]. These studies suggest that TMEM16A likely adopts a homodimeric structure, which was later confirmed by the publication of high-resolution structures of TMEM16A [97, 103]. Similar to TMEM16A, all available high-resolution structures of TMEM16 proteins show a homodimeric structure [10, 82, 90, 95-97].

1.2.2 High-affinity Ca^{2+}-binding site and ion permeation pathway

High-resolution structures of TMEM16A reveal that residues N646, N647, E650, E698, E701, E730, and D734 appear to surround the bound Ca^{2+} ions (**Fig. 1.1** and **Fig. 1.2**) [97, 103]. The presence of glutamate and aspartate residues in the Ca^{2+}-binding site is not surprising because carboxylate groups are common in various divalent cation chelators. Indeed, many functional studies show that mutating one of these glutamate or aspartate residues can reduce the Ca^{2+} affinity of TMEM16A by 2-3 orders of magnitude [96, 97, 104, 105]. Mutating corresponding residues in TMEM16F, nhTMEM16, an afTMEM16 also reduce their affinity for Ca^{2+} significantly [10,

11, 49]. The alignment of TMEM16 protein sequences suggests that these glutamate or aspartate residues are mostly conserved among various TMEM16 proteins, except for IST2 (**Fig. 1.3**). Also, the high-resolution structure of TMEM16F (**Fig. 1.4**), a phospholipid scramblase, has Ca^{2+}-binding sites similar to that of TMEM16A, an ion channel. Thus, TMEM16 proteins likely share a similar Ca^{2+}-binding motif. Residues located outside of the Ca^{2+} binding site of TMEM16A also influence the Ca^{2+} affinity of the channel. For example, mutating residue Y589 into an alanine increases the Ca^{2+} affinity of the channel by ~2-5 fold, although the effect in altering the calcium affinity is less than the glutamate/aspartate mutations mentioned above [97]. Also, mutating several non-acidic residues in TM 4-7 TMEM16A alters the channel affinity for Ca^{2+} and permeability ratios for iodide (or thiocyanate) over chloride [97]. Nonetheless, it is not clear how these mutations affect the Ca^{2+} affinity of TMEM16A.

Mutating a residue, K584, in TM 5 of TMEM16A into glutamate or glutamine may alter the single-channel conductance [106] and the current-voltage relation of the channel [106, 107]. Similarly, mutating several residues within TM 5-6 of nhTMEM16 and TMEM16F alter these proteins' phospholipid scramblase activity [108-111]. Thus, TM 5 and the surrounding TM (or TM 3-8) likely form the ion permeation or phospholipid transport pathway of TMEM16 proteins. High-resolution structures of TMEM16A and TMEM16 phospholipid scramblases (such as nhTMEM16, afTMEM16, and

TMEM16F) show that they share a similar general structure (see **Fig. 1.2** and **Fig. 1.4** for representative structures of TMEM16 proteins). The ion permeation pathway and the phospholipid transport pathway of TMEM16 proteins has a wide intracellular vestibule, a narrow neck, and a slightly larger extracellular vestibule (**Fig. 1.2** and **Fig. 1.4**, middle panel) [10, 11, 82, 90, 95-97]. Also, the overall structure of TMEM16 proteins (with less than 40% shared identity) share a general homodimeric structure with each monomer containing ten TM and a Ca^{2+} binding site (TM 6-8), consisting of a cluster of acidic residues (**Fig. 1.2** and **Fig. 1.4**, bottom panel) [10, 11, 82, 95-97]. IST2 is the odd member of the TMEM16 family. Unlike other family members, IST2 lacks a cluster of acidic residues that form the Ca^{2+}-binding site in other TMEM16 proteins (**Fig. 1.3**). When incorporated into liposomes, IST2 exhibits no phospholipid scramblase activity [11]. Also, there is no report of IST2 being a Ca^{2+}-activated ion channel either.

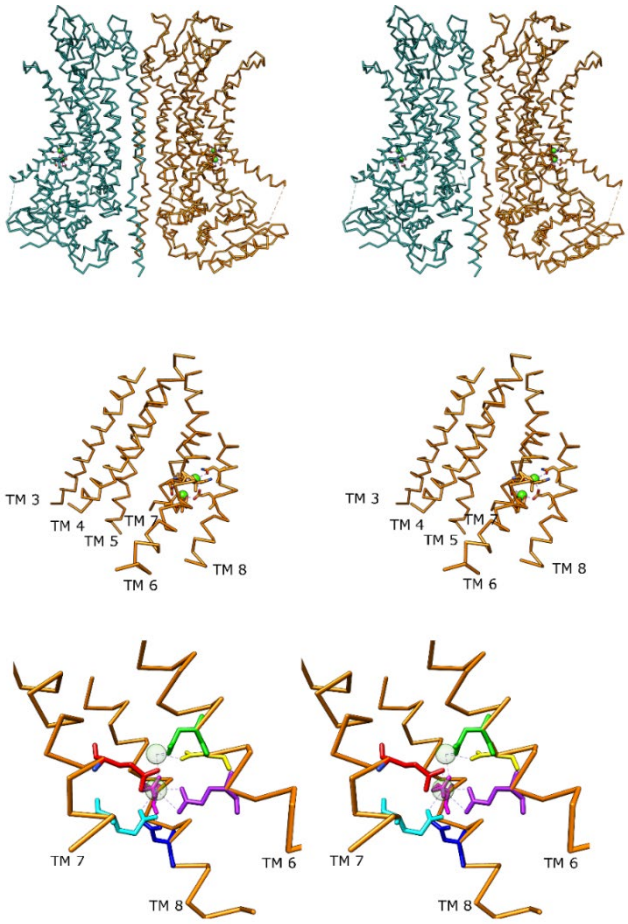

Figure 1.2. (Top) Stereoview (wall-eye) of TMEM16A (PDB: 7B5C [100]). The middle panel shows transmembrane helices 3-8 surrounding the ion permeation pathway of the orange subunit. (Middle) The orange subunit (as shown in the top panel) was rotated 90° clockwise for the middle panel. Green spheres are Ca^{2+} ions. (Bottom) Residues surrounding Ca^{2+} ions (transparent spheres): N646 (green), N647 (yellow), E650 (violet), E698 (cyan), E701 (red), E730 (pink), and D734 (blue). The orange subunit (as shown in the middle panel) was rotated 90° clockwise for the bottom panel. The bottom panel is the zoomed-in view of the Ca^{2+} binding sites.

TMEM16A	648	LF**E**IGIPKMK	657	696	TP**E**YM**E**MIIQ	705	728	II**E**IRL**D**AKK	737
TMEM16B	693	IF**E**IGVPKLK	702	741	TP**E**YM**E**MIIQ	750	773	VI**E**VRL**D**AKK	782
TMEM16C	708	FM**E**LGYPLIQ	717	752	MD**E**YL**E**MVLQ	761	784	II**E**IRL**D**AYK	793
TMEM16D	862	FM**E**LGYPLIQ	871	909	FD**E**YL**E**MILQ	918	941	II**E**IRL**D**AYK	950
TMEM16E	618	IH**E**AFQPLIF	627	661	FY**E**YL**E**TVIQ	670	693	IMGIRV**D**AWK	702
TMEM16F	622	IQ**E**VLLPWVM	631	665	FY**E**YL**E**MIIQ	674	697	IL**E**IRV**D**AWK	706
TMEM16G	599	VQ**E**VLVPKLK	608	642	FH**E**YL**E**MVLQ	651	674	WV**E**IRL**D**ARK	683
TMEM16H	603	LL**D**CGLRLKK	612	740	FQ**D**YQ**E**MFVQ	749	772	LI**E**IRS**D**AFK	781
TMEM16J	482	CV**E**YLCPLLA	491	529	FD**E**FM**E**MMIQ	538	561	LV**E**IRL**D**AIK	570
TMEM16K	459	---HGVRVKR	465	495	FD**D**YL**E**LFLQ	504	527	FT**E**VNS**D**ALK	536
nhTMEM16	450	AT**E**VVVPYIK	459	501	SG**D**YR**E**MVMQ	510	533	WV**E**LRS**D**ALK	542
afTMEM16	443	AL**E**TIVPFVK	452	509	TD**D**LR**E**MCIQ	518	541	WV**E**LRS**D**FFK	550
DdTMEM16	520	--**E**LLGPWIQ	527	559	FQ**E**FNQIIIQ	568	591	IF**E**ERV**D**SYK	600
IST2	621	SP**E**FNSNNEK	630	670	DPSSLSSASS	679	702	AGSAGKKPLA	711
Subdued	734	IL**E**VYLPMFW	743	786	FP**E**YL**E**MVLQ	795	818	IL**E**MRL**D**AKK	827

Figure 1.3. Sequence alignment of TMEM16 proteins Ca^{2+}-binding sites. Sequence alignment was performed with ClustalW2 program [112]. Protein sequences were obtained from the NCBI's reference sequence database (RefSeq) [113]. RefSeq accession number for each protein sequence: TMEM16A, 6BGI_A; TMEM16B, NP_705817.2; TMEM16C, NP_001121575.1; TMEM16D, XP_006513818.1; TMEM16E, NP_808362.2; TMEM16F, 6QP6_A; TMEM16G, NP_996914.1; TMEM16H, NP_001158151.1; TMEM16J, NP_848468.2; TMEM16K, 5OC9_A; nhTMEM16, 6QM9_A; afTMEM16, 6E0H_A; DdTMEM16, XP_647283.1; IST2, QHB06858.1; Subdued, NP_650820.1

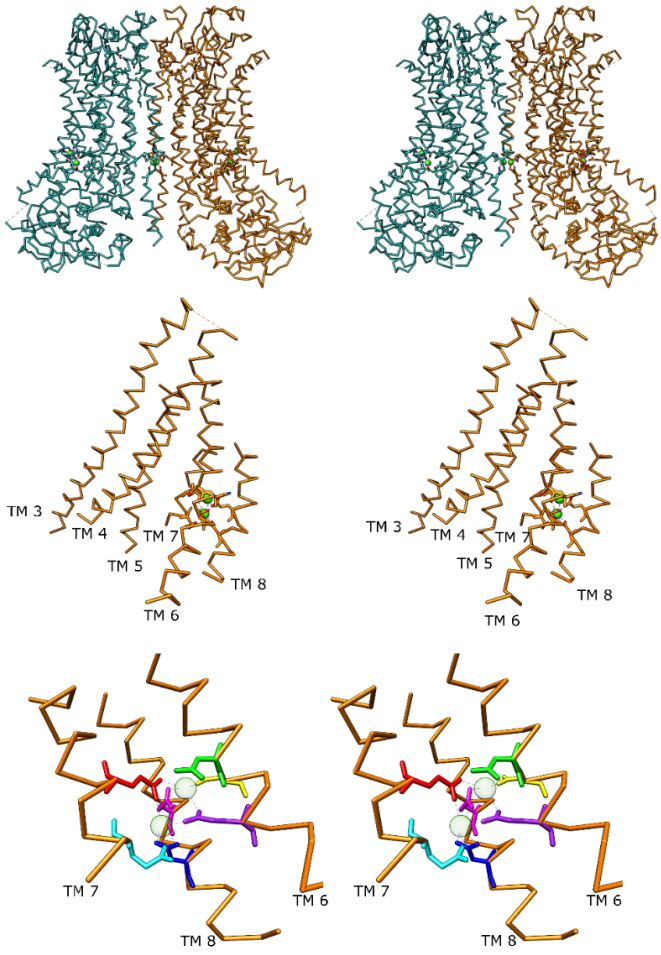

Figure 1.4. (Top) Stereoview (wall-eye) of TMEM16F (PDB: 6QP6 [95]). (Middle) Transmembrane helices 3-8 surrounding the cavity of the orange subunit. The orange subunit (as shown in the top panel) was rotated 90° clockwise. Green spheres are Ca^{2+} ions. (Bottom) Residues surrounding Ca^{2+} ions (transparent spheres): N620 (green), N621 (yellow), E624 (violet), E667 (cyan), E670 (red), E699 (pink), and D703 (blue). The orange subunit (as shown in the middle panel) was rotated 90° clockwise for the bottom panel. The bottom panel is the zoomed-in view of the Ca^{2+} binding sites.

Before the structure of TMEM16A was solved, whether TMEM16A has one or two ion permeation pathways (one ion permeation pathway per subunit) was not known. At one point, a single ion permeation pathway at the dimer interface of TMEM16 molecules was considered [10]. However, Jeng et al. (2016) and Lim et al. (2016) showed that individual TMEM16A subunits could be activated independently [106, 107]. They manipulated the current-voltage relationship of individual TMEM16A subunits and demonstrated that each subunit appears to house its own ion permeation pathway [106, 107]. Thus, their functional results suggest that TMEM16A, like the Cl^- channels in CLC channel/transporter family, is a double-barreled channel. It is currently thought that the two Cl^- permeation pathways (and perhaps the lipid transport pathway in TMEM16 phospholipid scramblases) are located away from the two-fold symmetry axis, as shown in **Fig. 1.2** and **Fig. 1.4**. In addition, they found that mutating residue K584 in TM 5, at the intracellular vestibule of TMEM16A (**Fig. 1.5**) alters the current-voltage (I-V) curve rectification [106, 107]. Thus, this residue likely exerts an electrostatic control on ion permeation in TMEM16A.

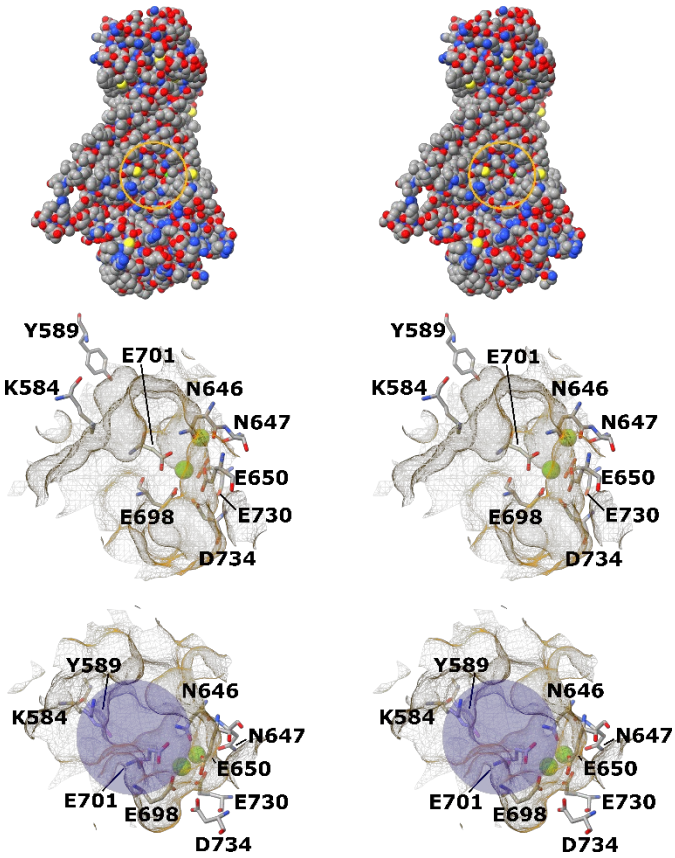

Figure 1.5. (Top) Stereoview (wall-eye) of the spacefill model of TMEM16A (PDB: 7B5C, chain A [100]). The orange circle highlights the intracellular vestibule. (Middle) Stereoview of the highlighted region in the top panel (same orientation but zoomed in). Intracellular vestibule surface is presented as grey/orange mesh. The two green spheres are Ca^{2+} ions. (Bottom) Bottom-up view of the intracellular vestibule. The middle panel is rotated 45° away from the screen around the central axis of the protein that is parallel to the membrane. The approximate location of the ion permeation pathway is highlighted with a transparent blue circle. Note that K584 as discussed in Jeng et al. (2016), is K588 in PDB code 7B5C (shown here). At this resolution (3.7 Å), the extracellular opening is not visible.

1.3 Biophysical properties of TMEM16 Proteins

1.3.1 Ca^{2+} affinity

Although the Ca^{2+}-affinity of TMEM16 proteins significantly varies from each other, the half-maximal effective concentration of Ca^{2+} (EC50) of TMEM16 proteins is roughly in the sub-micromolar to the low micromolar range [6-8, 43, 49, 95, 96, 114, 115]. For TMEM16A and TMEM16B, the EC50 of the channel activation by Ca^{2+} is ~0.5-1 uM without other divalent cations, whereas TMEM16 phospholipid scramblases have higher EC50 values in general. Besides Ca^{2+}, other divalent cations can also activate TMEM16 proteins. For example, Ba^{2+}, Sr^{2+}, Ni^{2+}, and Cd^{2+}, can activate TMEM16A, and Zn^{2+} and Gd^{3+} can activate TMEM16F [105, 115-118]. Similarly, Sr^{2+} can activate nhTMEM16 phospholipid scramblase activity [10], and Mn^{2+}, Sr^{2+}, and Ba^{2+} can activate phospholipid scramblase and ion channel activity of afTMEM16 [11]. Mg^{2+} ions, on the other hand, act as a competitive antagonist for the TMEM16A activation by Ca^{2+}, likely because they can bind to the activation sites but do not induce pore opening [115]. As suggested by high-resolution structures, the single high-affinity Ca^{2+}-binding sites in each subunit of TMEM16A can bind one to two Ca^{2+} ions [10, 82, 90, 95-97]. Consistent with the presence of multiple Ca^{2+} ions, the Ca^{2+} dose-response curves of TMEM16 proteins usually have a Hill coefficient greater than one [8, 43, 49, 95, 114, 115, 119], indicating cooperative Ca^{2+} binding. Besides the high-affinity Ca^{2+}-binding sites (**Fig. 1.3**), there may be

other Ca^{2+} binding sites. For example, the high-resolution structure of TMEM16F (PDB 6QP6) and TMEM16K (PDB 5OC9) show a potential Ca^{2+} binding site formed by TM 2 and 10 [82, 95]. Ca^{2+} ions are seen in this region of those two proteins. However, a more detailed characterization of this Ca^{2+} binding site in TMEM16F and TMEM16K is necessary to determine its relevance to the function of these molecules. Also, TMEM16A exhibits a biphasic dose-response curve, suggesting that high concentrations of Ca^{2+}, beyond saturation level (in mM range), can increase TMEM16A current further [106, 107]. Since this increase in current occurs when the high-affinity Ca^{2+}-binding sites are saturated, Ca^{2+} binding elsewhere is likely responsible for the biphasic dose-response curve.

A recent study suggests that the additional Ca^{2+} binding site formed by TM2 and TM10 in TMEM16A may consist of residues E425, K428, D879, and D884 [120]. For example, two mutations, K428A and D884A, reduce the Ca^{2+} affinity of TMEM16A by ~2-3 fold [120]. Since these residues appear to be conserved in other TMEM16 molecules (**Fig. 1.6**), further investigation into how these residues affect the function of other TMEM16 proteins is warranted.

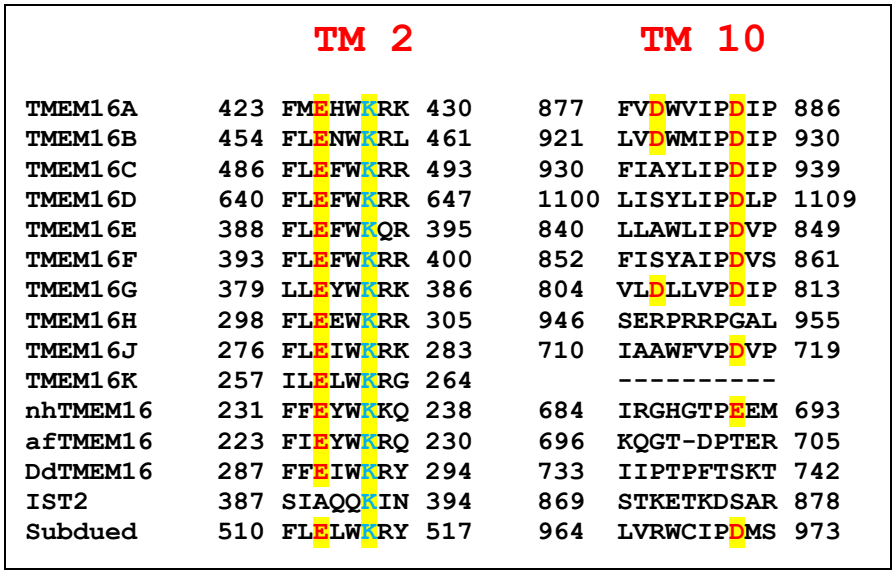

Figure 1.6. Sequence alignment of TMEM16 proteins potential allosteric Ca^{2+}-binding site. Sequence alignment was performed as described in **Fig. 1.3**.

The activation of TMEM16 proteins by Ca^{2+} is voltage-dependent. TMEM16A exhibits a higher affinity for Ca^{2+}, a faster Ca^{2+} binding, and a slower Ca^{2+} dissociation at more depolarized potential [117]. However, splice variants of TMEM16A that lack the alternative segment ***b*** have a higher affinity for Ca^{2+} [99]. Also, Xiao et al. (2011) reported that splice variants of TMEM16A that lack the alternative segment ***c*** (amino acids EAVK) exhibit a more depolarized half-maximal conductance potential ($V_{1/2}$), a lower affinity for Ca^{2+} (EC50 in μM range even at depolarized potentials), and an absence of the voltage dependence of the Ca^{2+} dissociation rate [117]. They suggested that the absence of this alternative segment reduces

the voltage dependence of Ca^{2+}-binding. The fact that the high-affinity Ca^{2+}-binding sites of TMEM16 proteins appear to be within the membrane electric field is consistent with the observation that Ca^{2+} binding affinity to TMEM16 proteins is voltage-dependent. Xiao et al. (2011) also showed that replacing extracellular Cl^- with NO_3^- or SCN^- shifts the $V_{1/2}$ to a more hyperpolarized potential and that TMEM16A can also be activated by membrane depolarization in the absence of Ca^{2+} ions [117, 121]. Interestingly, deleting the alternative segment ***c*** enhances this Ca^{2+}-independent activation [117]. Recently, Segura-Covarrubias et al. (2020) reported that lowering the intracellular pH enhances the activation of TMEM16A by voltage in the absence of Ca^{2+}, and they attributed this pH facilitation of TMEM16A activation to the voltage-dependent protonation of acidic residues in the Ca^{2+} binding sites [122]. Also, they reported that neutralizing acidic residues in the high-affinity Ca^{2+}-binding sites reduces the pH sensitivity of voltage activation of TMEM16A and enhances the voltage activation of TMEM16A at physiological pH [122]. Like TMEM16A, TMEM16B also exhibits a higher affinity for Ca^{2+} at a more depolarized potential [123]. However, TMEM16B cannot be activated by membrane depolarization in the absence of Ca^{2+} [122].

1.3.2 Current-Voltage relationship

TMEM16A and TMEM16B's I-V relationship displays outward rectification at low Ca^{2+} concentration but becomes nearly ohmic when the

channels are activated by saturating Ca^{2+} concentrations [7, 8, 107, 115, 124, 125]. The Ca^{2+}-dependent change in I-V curve rectification could come from multiple reasons. First, the apparent Ca^{2+} binding affinity of TMEM16A and TMEM16B is voltage-dependent. Although the difference between positive voltage and negative voltages is only small (for example, the EC50 values of Ca^{2+} activation of TMEM16A at −40 mV and +40 mV are ~0.4 uM and ~0.5 uM, respectively [115]), the percentage of the current activation in the presence of non-saturating concentrations of Ca^{2+} can still be significant given the very steep dose-response curve with a Hill coefficient value of ~3-4; the dose-response curve of a single TMEM16A subunit also has a Hill coefficient value of ~3-4, suggesting activation of one subunit has a minimal effect on the activation of the other subunit [107]. Secondly, the Ca^{2+} activation sites of TMEM16A and TMEM16B are near the intracellular vestibule of the Cl^- permeation pore. Thus, the bound-Ca^{2+} ions at the binding site may exert an electrostatic force on Cl^- permeation, leading to a Ca^{2+}-dependent shift in current rectification [126]. Finally, intracellular Mg^{2+} competes with Ca^{2+} for the voltage-dependent binding to the binding site [115]. Therefore, with an intracellular solution containing mM concentrations of Mg^{2+}, the TMEM16A and TMEM16B currents always show very significant outward rectification, as shown in many studies using whole-cell recordings [8, 114, 124, 127, 128].

In contrast to TMEM16A and TMEM16B, known TMEM16 phospholipid scramblases that conduct ionic currents show a constant current rectification. The I-V relationship of TMEM16F, TMEM16E, and *D. melanogaster* Subdued display outward rectification even at saturating concentrations of calcium [49, 72, 87, 88]. Most studies on afTMEM16 and nhTMEM16 utilize flux assay to study their ion channel activity, making the I-V relationship of these two proteins unclear. However, one study that utilized whole-cell patch-clamp configuration shows a linear I-V curve for nhTMEM16 at 200 μM Ca^{2+} [109]. Currently, the molecular basis of the outwardly rectified I-V relationship of TMEM16 scramblases remains unknown. Voltage-dependent change in the conformation of TMEM16 scramblases remains unknown.

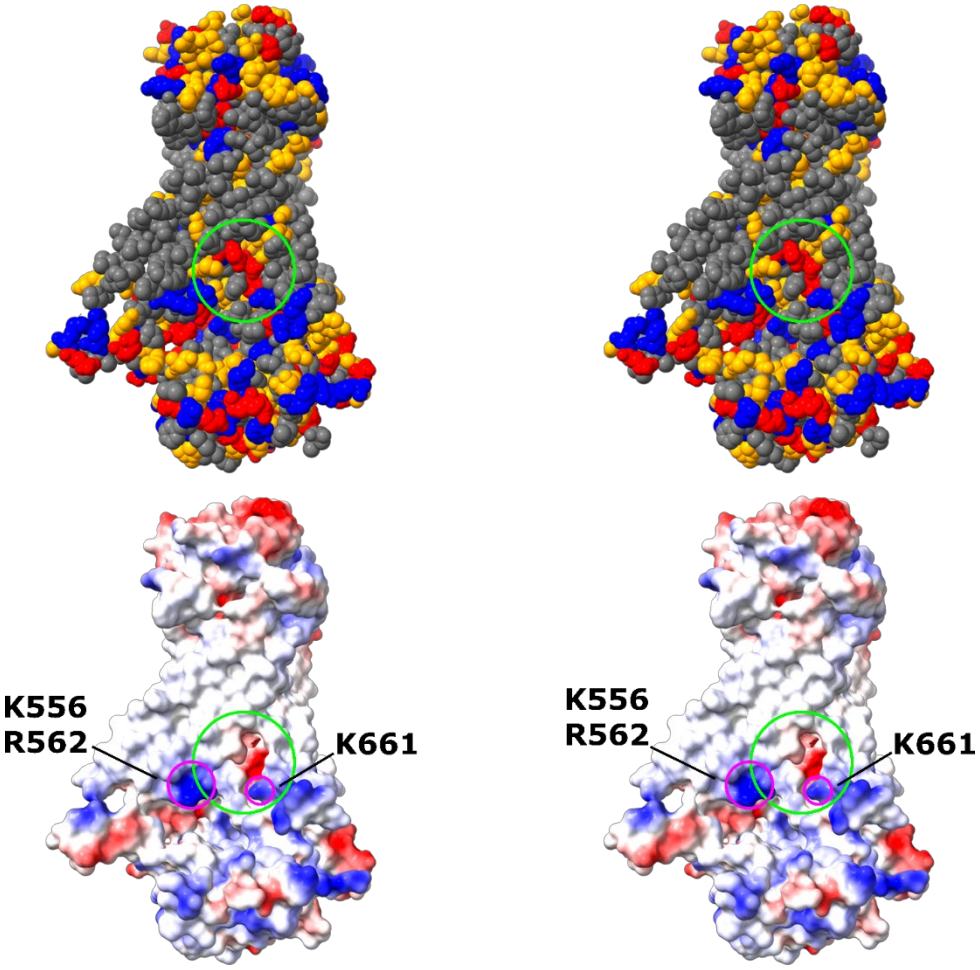

Figure 1.7. (Top) Stereoview (wall-eye) of the spacefill model of a single subunit of TMEM16A. (Bottom) Stereoview of the surface of TMEM16A colored by electrostatic potential using ChimeraX [129]. Red represents negative charges, blue represents positive charges, and white represents neutral residues. Large green circle highlights the approximate location of the intracellular vestibule.

1.3.3 Ion selectivity

CaCCs in the TMEM16 family, TMEM16A and TMEM16B, exhibit a higher selectivity for larger anions over smaller anions ($SCN^- > I^- > Br^- > Cl^-$) [7, 123, 130]. However, they are less permeable to cations with a P_{Na}/P_{Cl} of 0.05 for TMEM16B and 0.03 for TMEM16A [108, 130]. The molecular basis behind TMEM16A and TMEM16B selectivity for anions over cations remains poorly understood. In one study, mutating basic residues within the ion permeation pathway of TMEM16A seems to alter the channel's anion selectivity [131]. As shown in (**Fig. 1.7**), K556, R562, and K661 (TMEM16A***ac***) at the intracellular vestibule entrance may influence the ion-selectivity of TMEM16A. However, TMEM16A***ac*** K556A, R562A, K661A, and wild-type all have a similar selectivity for Cl^- over Na^+ [132]. In another study, TMEM16B K540Q (located in TM 5, corresponding to K584 in TMEM16A) and TMEM16B R573E (located in extracellular loop linking TM 5 and 6) exhibits significantly higher selectivity for Na^+ over Cl^- than wild-type TMEM16B [130]. The ion selectivity of TMEM16 phospholipid scramblases differs from that of TMEM16 CaCCs. Phospholipid scramblases with ion channel activity (TMEM16F, nhTMEM16, afTMEM16, D. *melanogaster* Subdued, and TMEM16E) are rather non-selective compare to TMEM16 CaCCs. There is a lack of consensus regarding the cation versus anion permeability of TMEM16F. Three studies reported that TMEM16F is cation-selective with a P_{Na}/P_{Cl} of 6.8 [49], 2.7 [95], or 1.38 [108]. In contrast,

several studies suggest that TMEM16F is anion-selective with a P_{Na}/P_{Cl} <1 and can be as low as 0.24 [133-136]. Another point of contention regarding the ion permeability of TMEM16F involves a pore mutant, Q559K, that seems to reduce the P_{Na}/P_{Cl} permeability ratio. In one study, this mutant reduces the P_{Na}/P_{Cl} of TMEM16F from 6.8 to 2.2 [49]. However, another study shows that wild-type TMEM16F and TMEM16F Q559K have a similar P_{Na}/P_{Cl} [134]. The varying experimental conditions in these studies may contribute to the lack of consensus. In general, studies that use whole-cell patch-clamp configuration, which involves manipulating extracellular ion concentration, report a lower P_{Na}/P_{Cl}. For inside-out patch-clamp configuration, studies that use non-charged solutes (such as sucrose or mannitol) to adjust intracellular ion concentration tend to report a higher P_{Na}/P_{Cl}. In addition, TMEM16F seems to become more selective for Cl^- over Na^+ as the concentration of Ca^{2+} increases [116]. Thus, the different Ca^{2+} concentrations used among various studies makes a direct comparison of their results difficult also.

Fewer studies examine the ion selectivity of nhTMEM16 and afTMEM16, but they seem to favor cations over anions with a P_K/P_{Cl} of ~1.5 for afTMEM16 and a P_{Na}/P_{Cl} of ~2.3 for nhTMEM16 [11]. Like TMEM16F, the ion selectivity of *D. melanogaster* Subdued is a matter for debate. One study report that *D. melanogaster* Subdued is a CaCC with a P_{Na}/P_{Cl} of 0.16 [87], whereas another study reports that the protein is a phospholipid scramblase/small-conductance Ca^{2+}-activated non-selective ion channel with

a P_{Na}/P_{Cl} of 5.83 [88]. As with TMEM16F, the study that uses whole-cell patch-clamp configuration reports a lower P_{Na}/P_{Cl}. Two studies that examine the ion selectivity of TMEM16E agree. Both studies show that TMEM16E is non-selective [72, 137]. One study reports a P_{Na}/P_{Cl} of ~1.6 for TMEM16E [137].

Despite the varying cation permeability among TMEM16 proteins, they seem to have a similar anion permeability. TMEM16A, TMEM16B and TMEM16F have a similar relative permeability sequence, $SCN^- > I^- > Br^- > Cl^-$ [7, 115, 123, 130, 133, 135]. One study that compares the ion permeability of TMEM16A, TMEM16D, TMEM16F, and TMEM16K also show a similar relative permeability sequence, $I^- > Br^- > Cl^- > HCO_3^-$ [136].

1.3.4 Lipid Selectivity

Data on the lipid selectivity of TMEM16 phospholipid scramblases are limited to nhTMEM16, afTMEM16, and TMEM16K. Both nhTMEM16 and afTMEM16 seem to scramble phosphatidylethanolamine (PE) and phosphatidylserine (PS) equally well [10, 11]. However, TMEM16K scrambles PS roughly three-fold slower than PE and phosphatidylcholine (PC) [82].

1.3.5 Activation mechanism

In 2017, Paulino et al. published structures of Ca^{2+}-free and Ca^{2+}-bound TMEM16A (**Fig. 1.8**) [96]. In the absence of Ca^{2+}, TM 6 curves away from the Ca^{2+}-binding site and toward TM 3-4. The negative electrostatic

environment at the ion permeation pathway's constriction creates a barrier for ion conduction [96]. Experimental data suggest that three hydrophobic residues (I641, I550, and I551) may protrude into the pore and block ion permeation (**Fig. 1.8**, bottom panel) [100]. In the presence of Ca^{2+}, TM 6 bends around the glycine hinge (TMEM16A(***ac***) G644) away from TM 4, away from the intracellular vestibule. Then, TM 6 becomes part of the Ca^{2+} binding pocket in conjunction with TM 7-8. Experimental data support the role of G644 in channel activation. Mutating the glycine hinge to a proline (G644P) locks TMEM16A in a partially open conformation [96]. Besides triggering the movement of TM 6, Ca^{2+} binding also triggers a small movement of TM 3-4. Thus, the activation of TMEM16A involves the movement of TM 3-6.

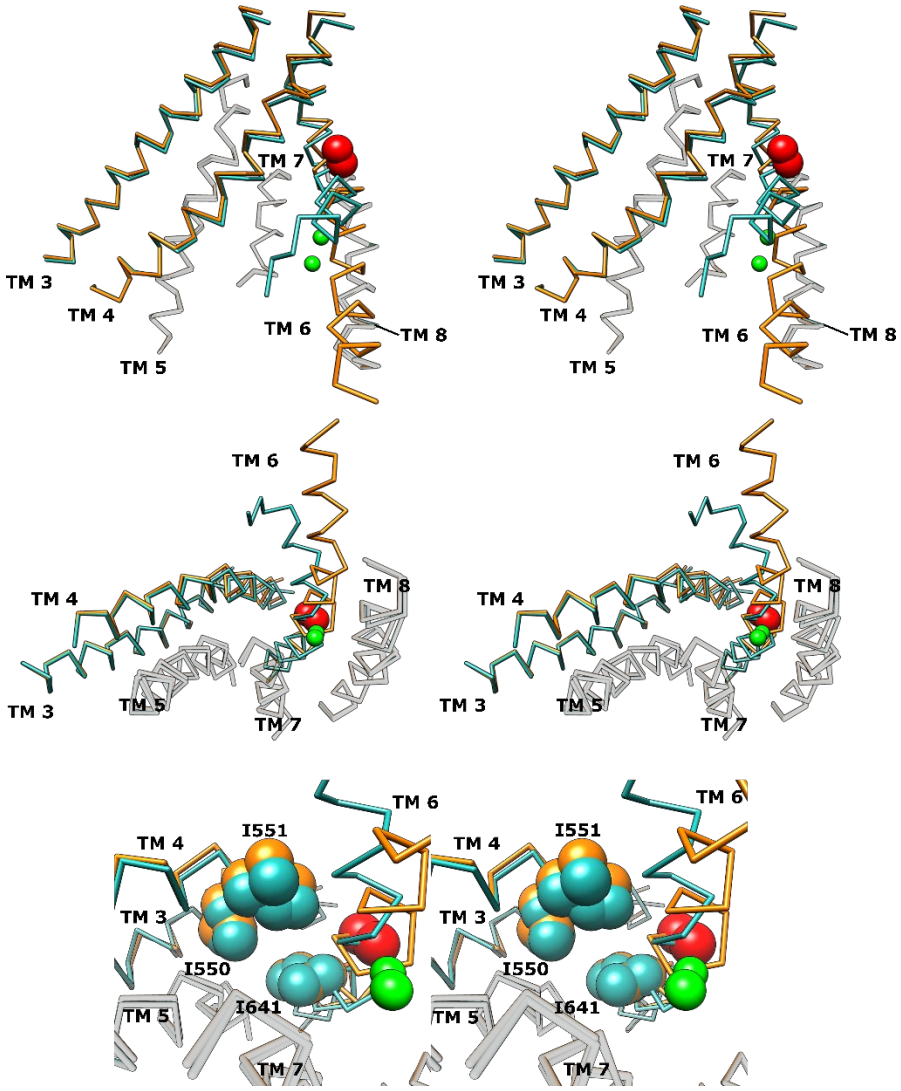

Figure 1.8. (Top) Stereoview of the pore from the side of Ca^{2+}-free (Cyan, PDB: 5OYG) and Ca^{2+}-bound TMEM16A (Orange, PDB: 5OYB) [96]. (Middle) View from intracellular to top of the pore. (Bottom) The pore constriction with residues (spacefill) protruding into the pore. The glycine hinge (G644) is presented as a red sphere in all stereo pairs, and green spheres are Ca^{2+} ions. UCSF Chimera was used for structure alignments for figures 1.8-1.12 [138].

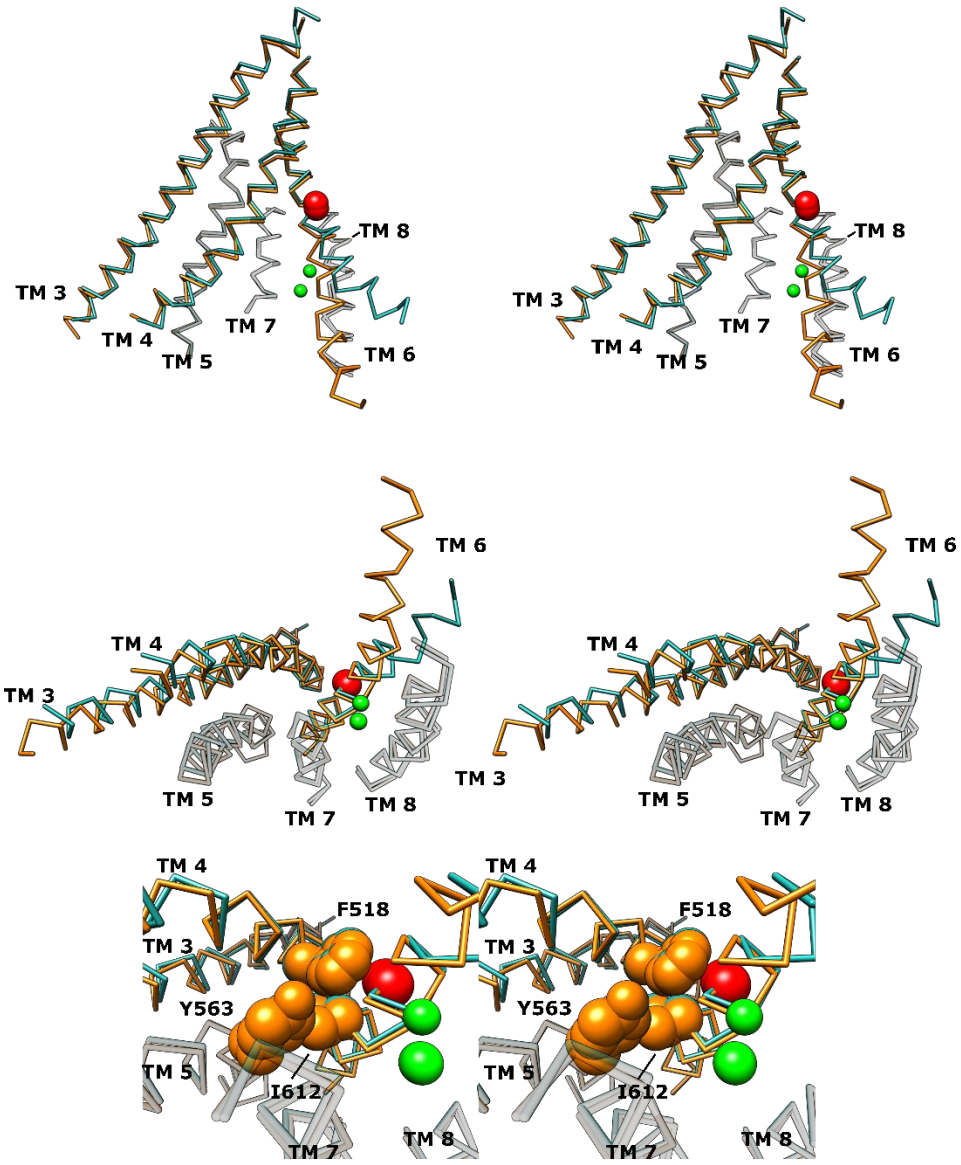

Figure 1.9. (Top) Stereoview of the pore from the side of Ca^{2+}-free (Cyan, PDB: 6QPB) and Ca^{2+}-bound TMEM16F (Orange, PDB: 6QP6) [95]. (Middle) View from intracellular to top of the pore. (Bottom) The pore constriction with residues (spacefill) protruding into the pore. The glycine hinge (G615) is presented as a red sphere in all stereo pairs, and green spheres are Ca^{2+} ions.

In 2019, Alvadia et al. published structures of Ca^{2+}-free and Ca^{2+}-bound TMEM16F (**Fig. 1.9**) [95]. In the absence of Ca^{2+}, TM 6 bends away from TM 4, 7, 8, and the Ca^{2+}-binding site. As seen with TMEM16A, experimental data suggest that three hydrophobic residues (F518, I612, and Y563) protrude into the phospholipid transport pathway and reduce the scramblase activity of TMEM16F (**Fig. 1.9**, bottom panel) [111]. The Ca^{2+}-bound structure of TMEM16F shows a straight TM 6 that forms part of the Ca^{2+}-binding site. Like TMEM16A, Ca^{2+} binding causes TM 6 to bend at the glycine hinge (G615). The overall conformational change upon Ca^{2+} binding is smaller in TMEM16F than in TMEM16A.

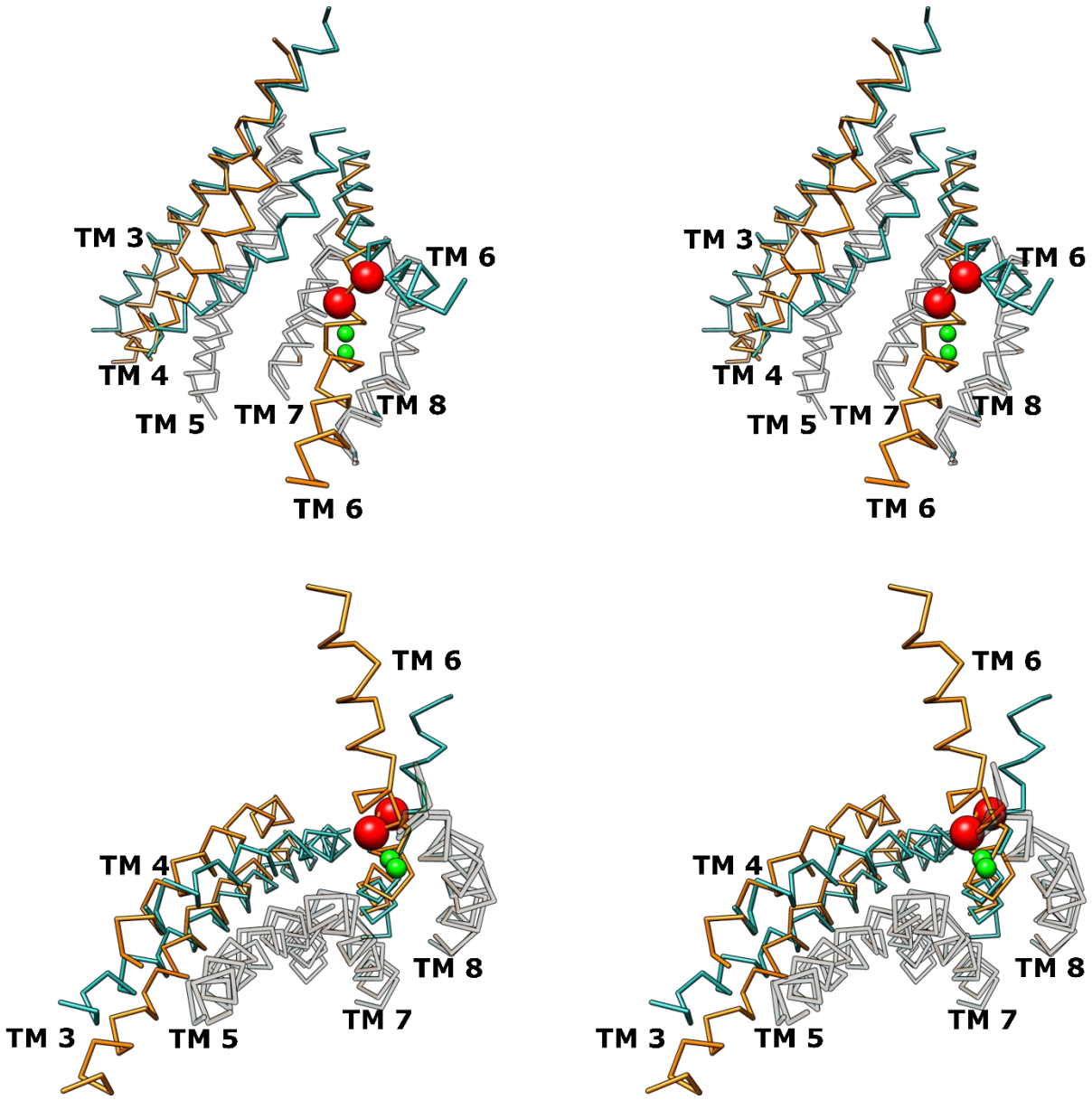

Figure 1.10. (Top) Stereoview of the pore of Ca^{2+}-free (Cyan, PDB: 6DZ7) and Ca^{2+}-bound afTMEM16 (Orange, PDB: 6E0H) [90]. (Bottom) View from intracellular to top of the pore. G441 is presented as a red sphere in all stereo pairs, and green spheres are Ca^{2+} ions.

In 2019, Falzone et al. published structures of Ca^{2+}-free and Ca^{2+}-bound afTMEM16 (**Fig. 1.10**) [90]. In the absence of Ca^{2+}, TM 6 bends away from TM 4, 7, 8, and the Ca^{2+}-binding site. In the presence of Ca^{2+}, TM 6 is straightened by bending at G441, bringing it closer to TM 7-8 to form the Ca^{2+}-binding site. Unlike TMEM16A and TMEM16F, the activation of afTMEM16 involves a significant conformational change of TM 3 and 4 that widens the protein's intracellular vestibule.

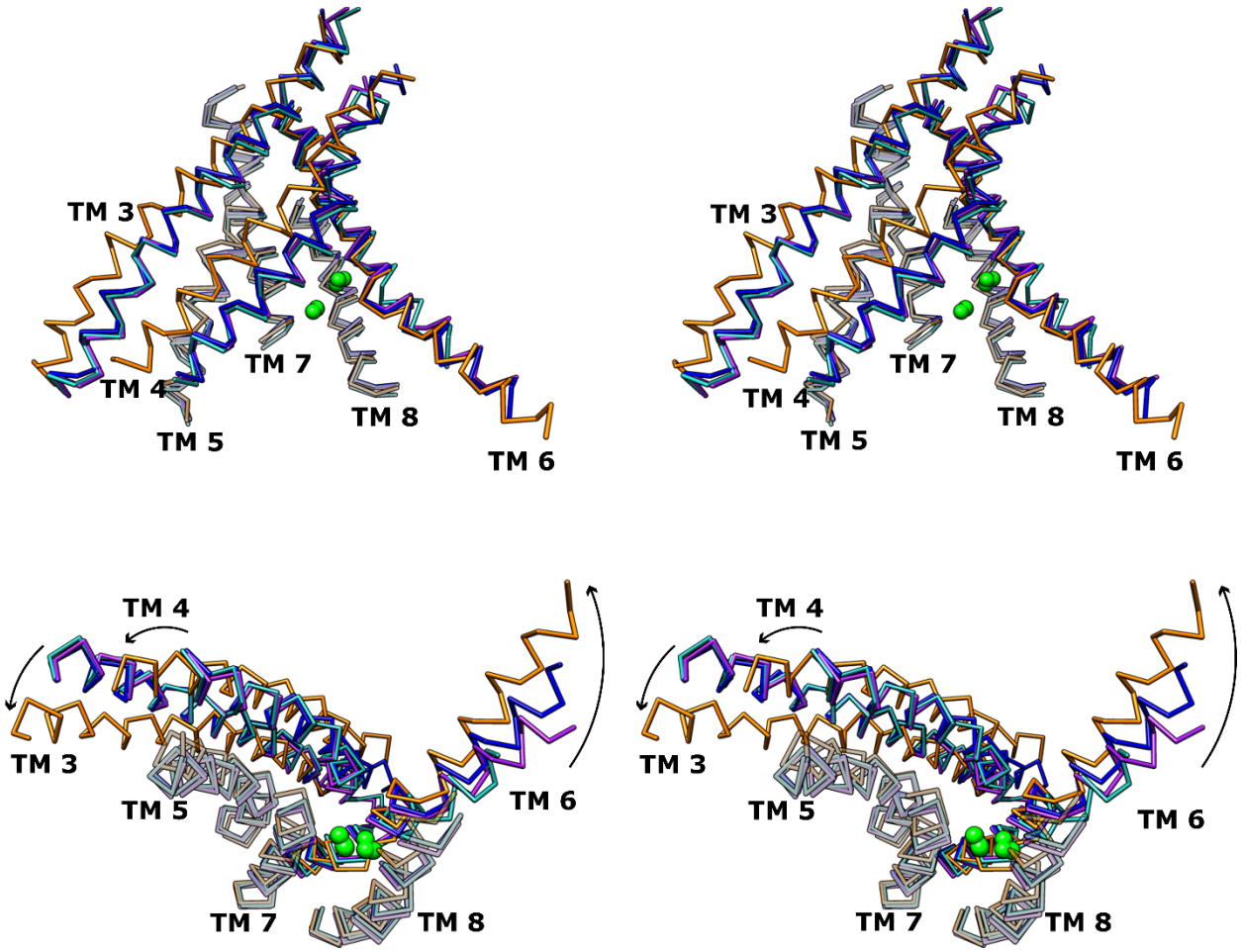

Figure 1.11. (Top) Stereoview of the pore of Ca^{2+}-free (Cyan, PDB: 6QM4) and Ca^{2+}-bound (Violet, PDB: 6QMB; Blue, PDB: 6QMA; Orange, PDB: 6QM9) nhTMEM16 [91]. TM 6 of the Ca^{2+}-free structure is partially unresolved. Green spheres are Ca^{2+} ions. (Bottom) Intracellular view of the pore. The conformational transition arrows are speculative. Note that more than two Ca^{2+} ions are visible because the location of the Ca^{2+} ions varies between the Ca^{2+}-bound structures. However, only two Ca^{2+} ions are present at any one time.

In 2019, Kalienkova et al. published structures of nhTMEM16 at various stages of activation (**Fig. 1.11**) [91]. The structure of Ca^{2+}-free nhTMEM16 purified with n-Dodecyl-B-D-maltoside (DDM) is different from the structure of Ca^{2+}-free nhTMEM16 in lipid nanodiscs. TM 4 of nhTMEM16 is closer to TM 6-8 in nanodiscs than in DDM. Consequently, the intracellular vestibule of nhTMEM16 is more shielded from the membrane core in nanodisc. In the absence of Ca^{2+}, TM 6 bends away from TM4 and the Ca^{2+}-binding site. Interestingly, TM 6 of nhTMEM16 has an alanine in place of the glycine hinge seen in TMEM16A and TMEM16F. In the presence of Ca^{2+}, a slight rotation of TM 6 brings it closer to the Ca^{2+}-binding site and TM 4. Similar to the activation of afTMEM16, the activation of nhTMEM16 involves a significant movement of TM 3-4. Upon Ca^{2+} binding, TM 3 and TM 4 shift away from the Ca^{2+}-binding site and widen the intracellular vestibule. Also, Kalienkova et al. were able to solve the structure of two potential intermediate states that show a partial movement of TM 6, which partially widens the intracellular vestibule.

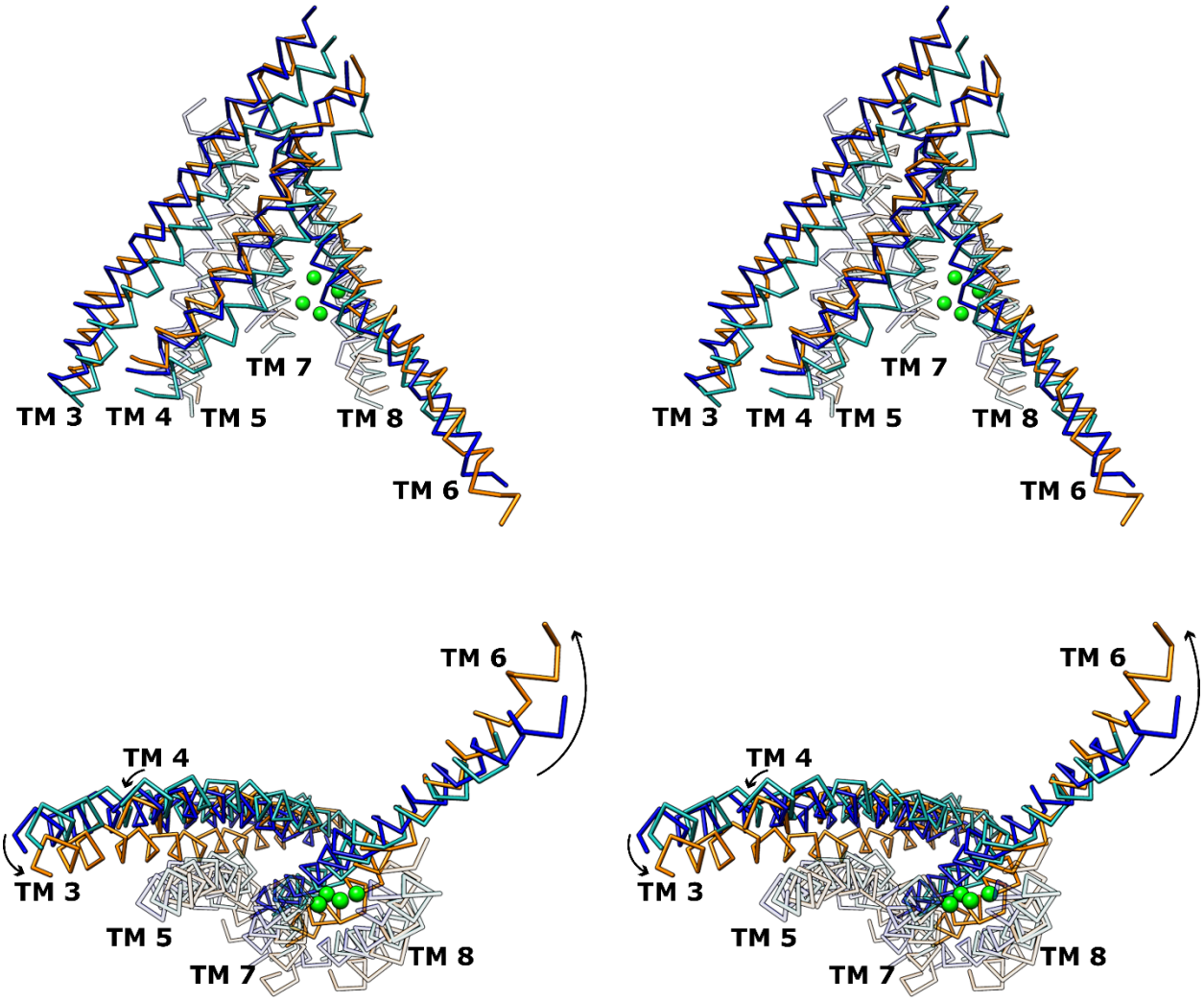

Figure 1.12. (Top) Stereoview of the pore of Ca^{2+}-free (Cyan, PDB: 6R7Z) and Ca^{2+}-bound (Blue, PDB: 6R7Y; Orange, PDB: 5OC9) TMEM16K [82]. TM 6 of the Ca^{2+}-free structure is partially unresolved. Green spheres are Ca^{2+} ions. (Bottom) Intracellular view of the pore. The conformational transition arrows are speculative. Note that more than two Ca^{2+} ions are visible because the location of the Ca^{2+} ions varies between the Ca^{2+}-bound structures. However, only two Ca^{2+} ions are present at any one time.

In 2019, Bushell et al. published structures of Ca^{2+}-free and Ca^{2+}-bound TMEM16K (**Fig. 1.12**) [82]. The activation of TMEM16K resembles the activation of nhTMEM16. In the presence of Ca^{2+}, TM 6 shifts toward the Ca^{2+}-binding site, and TM 3-4 shifts away from the Ca^{2+}-binding site widening the intracellular vestibule. Interestingly, Bushell et al. also reported a Ca^{2+}-bound structure of TMEM16K structurally like the Ca^{2+}-free structure. This structure could represent an intermediate state or a rundown state.

In summary, the activation of these TMEM16 proteins involves a significant conformational change of transmembrane helices exposed to membrane phospholipids. The activation of TMEM16 proteins that have a glycine hinge involves a larger movement of TM 6 toward the Ca^{2+}-binding site and a relatively smaller movement of TM 3-4. In contrast, the activation of TMEM16 proteins that lack a glycine hinge involves a smaller movement of TM 6 toward the Ca^{2+}-binding site and a relatively larger movement of TM 3-4 that clearly widens the intracellular vestibule. Several questions involving the activation of TMEM16 proteins remain unanswered. Experimentally, TMEM16 proteins undergo desensitization (a decrease in Ca^{2+} affinity) and rundown (significant attenuation or disappearance of Ca^{2+} activated current). We do not have a clear picture of the conformational changes associated with these processes. Likewise, the conformational change associated with phospholipid transport, especially for TMEM16 phospholipid scramblases that also conduct ionic current, is not well

understood. In order to accommodate phospholipids, TMEM16 phospholipid scramblases likely have a wider intracellular vestibule than TMEM16 CaCCs. However, the interaction of the ion/lipid transport pathway with the intracellular leaflet of the cell membrane is very dynamic. As discussed earlier, the type of stabilizing agent (DDM or phospholipids in nanodisc) was shown to affect the structure of nhTMEM16 [91]. Thus, other less stable intermediate conformations (between Ca^{2+}-free and Ca^{2+}-bound conformations) of TMEM16 protein likely exist.

1.4 Regulation of TMEM16 proteins

1.4.1 Calmodulin

Several studies have examined how calmodulin (CaM), a Ca^{2+}-binding messenger protein, regulates TMEM16 CaCCs. The regulation of TMEM16A and TMEM16B by CaM has been controversial. Tian et al. (2011) showed that trifluoperazine, a CaM inhibitor, reduces the activation of TMEM16A and that the channel can be co-immunoprecipitated with CaM [139]. However, Vocke et al. (2013) showed that trifluoperazine and N-8-aminooctyl-5-iodo-naphthalenesulfonamide, another CaM inhibitor, have no significant effect on the activation of both TMEM16A and TMEM16B [140]. Interestingly, the two CaM inhibitors can suppress the inactivation (defined as the Ca^{2+}-induced loss of channel activity) of TMEM16B. They also showed that the overexpression of CaM mutants with only two instead of four Ca^{2+}-binding sites decreases TMEM16A currents. Initially, they postulated that CaM

mutants with only two Ca^{2+}-binding sites compete with endogenous CaM to reduce TMEM16A currents. However, they showed that CaM mutant with no Ca^{2+}-binding sites, which should also compete with endogenous CaM, does not affect TMEM16A currents. In agreement with Tian et al., Vocke et al. show that both TMEM16A and TMEM16B can be co-immunoprecipitated with CaM.

In disagreement with both Tien et al. and Vocke et al., Terashima et al. (2013) and Yu et al. (2014) reported the activation of TMEM16A in the presence of Ca^{2+} alone [141, 142]. They also challenged the idea that CaM and TMEM16A form a stable complex. Terashima et al. showed that CaM and TMEM16A do not elute at the same time when run together on a size-exclusion chromatography column [141]. Also, Yu et al. showed that CaM co-immunoprecipitated with Ca^{2+}-activated K^+ (SK2) channel but not TMEM16A.

In 2013, Jung et al. suggested that CaM enhances the channel permeability to HCO_3^-. In HEK293 cells, exposing TMEM16A to purified CaM on the intracellular side causes a reversible shift in the P_{HCO3}/P_{Cl} from ~0.3-0.4 to ~0.9-1 [143]. However, Yu et al. (2014) could not reproduce this ion permeability shift [142]. Yu et al. attributed the observed shift in ion permeability to technical issues associated with patch clamping, namely series resistance and ion accumulation, rather than to CaM. As many structures of TMEM16 molecules have been solved, the previously identified

potential CaM binding domains via mutagenesis studies appear to be not readily accessible to intracellular CaM, making it less likely that CaM binds to and modulates TMEM16 proteins.

1.4.2 Phospholipids and Ion permeation

The cell membrane influences the structure and function of TMEM16 proteins. A cryo-electron microscopy study of afTMEM16 shows that the protein causes phospholipid bilayer bending at its dimer interface, resulting in phospholipid bilayer thinning near the ion permeation/phospholipid transport pathway [90]. The mismatch in height between TM 3/TM 5 of one subunit and TM 1/TM 2 of the other subunit deforms the cell membrane [90]. Also, molecular simulations of nhTMEM16 and afTMEM16 suggest that membrane thinning lowers the energy barrier for phospholipids/ions transport [109, 144]. Experimentally, increasing membrane thickness reduces the phospholipid scrambling rate of afTMEM16 [11].

Prolong exposure to Ca^{2+} seems to change the Ca^{2+}-affinity of TMEM16 proteins. Ta et al. (2017) showed that phosphatidylinositol 4,5-bisphosphate diC8 (diC8-PIP2) increases TMEM16A currents and inhibits TMEM16B currents at non-saturating concentration of Ca^{2+} but not at saturating concentration of Ca^{2+} [145]. Using *Danio rerio* voltage-sensitive phosphatase (Dr-VSP) to cleave PIP2 and phosphatidylinositol phosphate kinase to replenish PIP2, they also showed that endogenous PIP2 affects TMEM16A and TMEM16B in a similar manner to diC8-PIP2 [145]. In agreement with Ta

et al., De Jesús-Pérez et al. (2018) showed that the activation of Dr-VSP triggers a decrease in TMEM16A currents. They also showed that diC8-PIP2 prevents or partially reverses the current decay caused by prolonged Ca^{2+} exposure [127]. Subsequently, Le et al. (2019) reported that the EC50 of diC8-PIP2 in preventing TMEM16A desensitization is ~4 μM at 100 μM Ca^{2+} [146]. As with TMEM16A, prolong exposure to Ca^{2+} also decreases the Ca^{2+} affinity of TMEM16F. Ye et al. (2018) showed that prolong exposure to 1 mM Ca^{2+} shifts the EC50 of TMEM16F from 7.0 ± 0.8 μM to 45 ± 5 μM at +80 mV [147]. The desensitization of TMEM16 proteins likely involves PIP2 depletion from the cell membrane. Poly-L-lysine, which acts as a PIP2 scavenger, decreases the Ca^{2+} affinity of TMEM16F, which can be reversed with the application of exogenous PIP2 [147]. Similarly, poly-L-lysine is also able to trigger desensitization in TMEM16A at 0.25 μM Ca^{2+} [146]. The neutralization of several basic residues in the first intracellular loop (N-terminus) of TMEM16F seems to generate a desensitized protein [147]. Thus, this region of TMEM16F may interact with PIP2.

Le et al. (2019) identified several key basic residues in the TM 2-3 linker and TM 3-5 that alter the desensitization kinetics of TMEM16A when mutated [146]. Also, Yu et al. (2019) identified twelve basic residues that hinder diC8-PIP2 ability to increase TMEM16A currents when neutralized [148]. These residues are in the N-terminus, TM 2, TM 2-3 linker, TM 5, and TM 6-7 linker. They also identified several other residues associated with the

diC8-PIP2 effect on TMEM16A current. Together, these two studies suggest that TMEM16A appears to have multiple PIP2 binding sites. Currently, there is no high-resolution structure of PIP2-bound TMEM16A. However, one PIP2 molecule can be docked into a region form by TM 3-5 (**Fig. 1.13**) [146, 149]. Besides PIP2, fatty acids and phosphatidylserine were shown to inhibit TMEM16A, but the exact mechanism of inhibition requires further investigation [127].

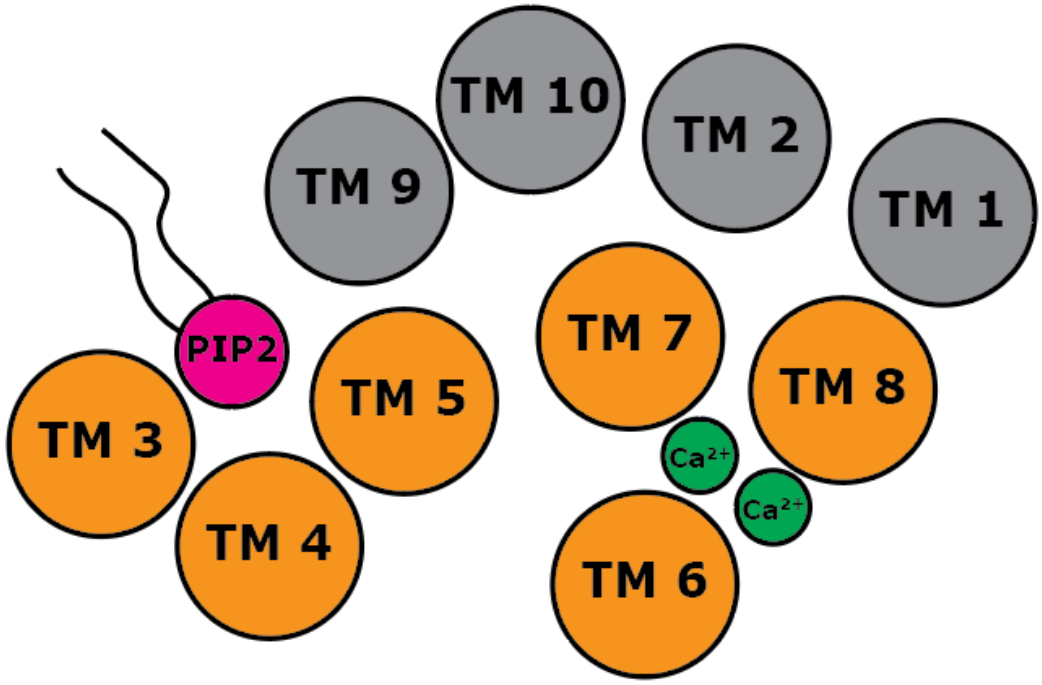

Figure 1.13. Illustration of a potential PIP2 binding site for TMEM16A revealed by molecular docking [146, 149].

1.4.3 Calcium-activated chloride channel regulator 1

Interest in the calcium-activated chloride channel regulator 1 (CLCA1) stems from its association with chronic obstructive pulmonary disease and mucus cell metaplasia [150, 151]. Even though CLCA1 was annotated as an ion channel initially, several studies have indicated that CLCA1 is a soluble protein rather than a transmembrane protein and that it can modulate CaCC [152-154]. Thus, several studies have examined the modulation of TMEM16A by CLCA1. Sala-Rabanal et al. (2015) showed that CLCA1 increases the surface expression of TMEM16A, which then increases calcium-activated Cl^- currents [155]. They postulated that secreted CLCA1 stabilizes the assembly of TMEM16A at the membrane surface and hinders either TMEM16A internalization or degradation. However, The exact mechanism requires further clarification. CLCA1 contains five domains: a metalloprotease catalytic domain, a cysteine-rich domain, a von Willebrand factor type A domain (VWA), a β sheet-rich domain, and a fibronectin type III domain (FnIII) [156]. Secreted CLCA1 undergoes self-cleavage at position 695, and the N-terminal fragment (N-CLCA1) itself (residues 1-695, no FnIII) can modulate TMEM16A [155, 157]. In the presence of Mg^{2+}, the VWA (residue 297-482 in the N-CLCA1) alone can modulate TMEM16A [156]. The VWA seems to require Mg^{2+} specifically because Berry et al. (2020) reported that Mg^{2+} but not Ca^{2+} stabilizes this domain [158]. They also suggest that the most probable site for CLCA1-TMEM16A interaction is on

the extracellular side of TMEM16A. How and if CLCA1 modulates other TMEM16 proteins besides TMEM16A requires further investigation.

1.5 Pharmacology

1.5.1 Inhibitors

Out of all TMEM16 proteins, TMEM16A has been the primary drug target. Multiple TMEM16A inhibitors have been identified (**Fig. 1.14**). Even before the discovery of TMEM16A, niflumic acid (NFA) has been used to study CaCCs in *Xenopus laevis* oocytes, dog and cow airways, rabbit portal veins, and rat cerebral arteries [159-162]. NFA inhibits TMEM16A currents with an EC50 of ~18-20 μM over a wide range of voltages, consistent with a voltage-independent mechanism of inhibition [115]. However, the EC50 of NFA inhibition increases when Cl^- is replaced with more permeant ions like Br^-, I^-, and SCN^- [115]. Besides TMEM16A, NFA also affects other ion channels, such as γ-Aminobutyric acid type A receptor, Slo2.1 channel, CLC-1 channel, and BK channel, making it a poor TMEM16A-selective inhibitor [163-166]. NFA inhibits TMEM16B with no reported EC50 and TMEM16F with an EC50 of 213 μM [114, 135]. Several groups have set out to discover TMEM16A-selective inhibitors. Namkung et al. identified four inhibitors for TMEM16A: $T16A_{inh}$-A01 (EC50 = 1.1 μM), $CaCC_{inh}AO1$ (EC50 = 2.1 μM), digallic acid (EC50 = 3.6 μM), and tannic acid (EC50 = 6.4 μM) [167]. Using a high throughput screening assay, Huang et al. (2012) discovered three

TMEM16A inhibitors: dichlorophen (EC50 = 5.49 μM), benzbromarone (EC50 = 9.97 μM), and hexachlorophene (EC50 = 10.00 μM) [168]. Oh et al. (2013) discovered another TMEM16A inhibitor, N-((4-methoxy)-2-naphthyl)-5-nitroanthranilic acid (MONNA), with an EC50 of 0.08 μM [169]. Seo et al. (2016) identified 2-(4-chloro-2-methylphenoxy)-N-[(2-methoxyphenyl)methylideneamino]-acetamide (Ani9) as an TMEM16A inhibitor with an EC50 of 77 ± 1.1 nM [170]. Miner et al. (2019) identified several additional TMEM16A inhibitors such as niclosamide (EC50 = 132 nM) and nitazoxanide (EC50 = 1.23 μM) [171].

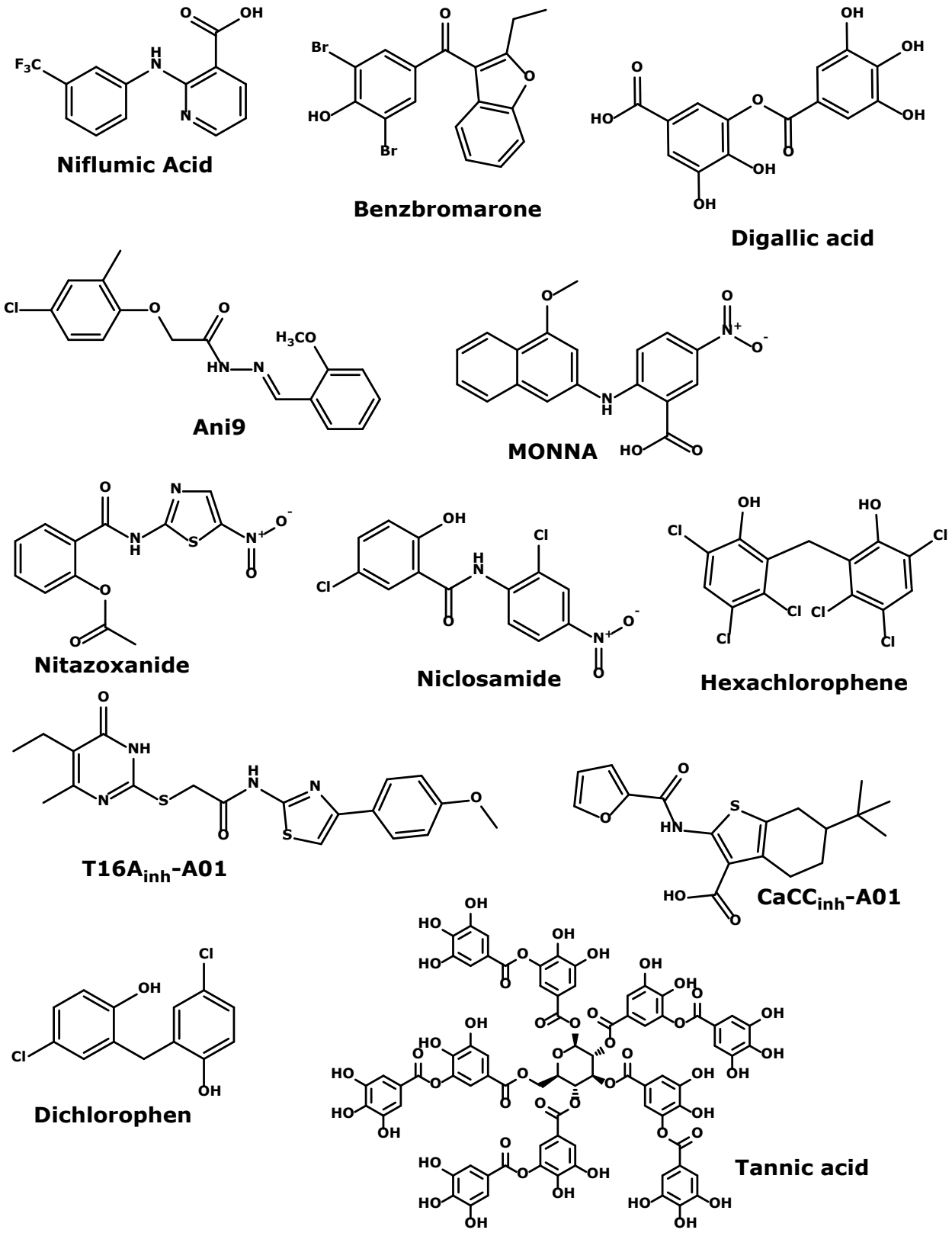

Figure 1.14. TMEM16A inhibitors.

1.5.2 Activators and Potentiators

Namkung et al. (2011b) identified several TMEM16A potentiators such as 3,4,5-trimethoxy-N-(2-methoxyethyl)-N-(4-phenylthiazol-2-yl)benzamide (E_{act}), which activates TMEM16A with an EC50 of 3 μM in the absence of Ca^{2+} (**Fig. 1.15**) [172]. E_{act} was also found to activate TMEM16B but no EC50 was reported [172]. They also discovered several potentiators that enhance TMEM16A affinity for Ca^{2+} but cannot activate the channel by itself. An example of a TMEM16A potentiator is N-(4-bromophenyl)-3-(1H-tetrazol-1-yl)benzamide with an EC50 of 37 μM (**Fig. 1.15**) [172]. Danahay et al. (2020) discovered ETX001, which potentiates TMEM16A with an EC50 of 116 nM [173]. They did not publish the structure of ETX001.

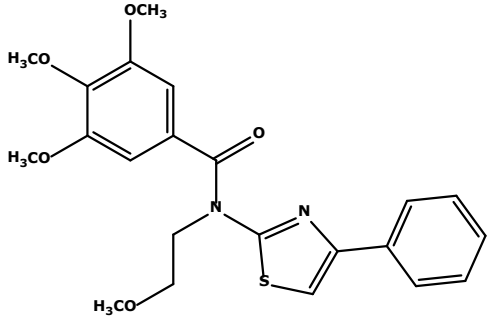

3,4,5-trimethoxy-*N*-(2-methoxyethyl)-*N*-(4-phenylthiazol-2-yl)benzamide (Activator)

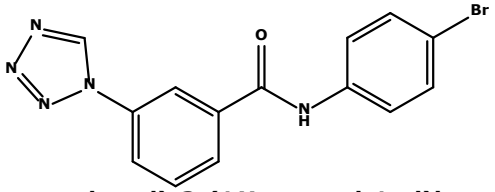

***N*-(4-bromophenyl)-3-(1*H*-tetrazol-1-yl)benzamide (Potentiator)**

Figure 1.15. Representative TMEM16A activator and potentiator.

1.5.3 Concluding remarks

The specificity of these pharmacological agents still needs to be examined. For example, Boedtkjer et al. (2015) have questioned the specificity of $T16A_{inh}$-A01, $CaCC_{inh}$-A01, and MONNA for TMEM16A. They showed that these compounds, which were reported to target CaCCs, can induce vasorelaxation in rat arteries in the absence of Cl^- [174]. Many TMEM16A activators affect endogenous TMEM16A and overexpressed TMEM16A differently [171, 172], and different cell types may respond to these compounds differently. For example, micromolar of Ani9, a TMEM16A inhibitor (EC50 = 77 nM) initially tested in Fischer Rat Thyroid cells [170], has no effect on endogenous TMEM16A in HT_{29} (human colorectal adenocarcinoma) cells, minor effect on endogenous TMEM16A in M1 (mouse myeloid leukemia) cells and in Cal33 (human tongue squamous cell carcinoma) cells [124]. Also, how these compounds interact with other TMEM16 proteins besides TMEM16A needs to be examined. Inhibiting multiple TMEM16 proteins can have an adverse effect. For example, niclosamide, which inhibits TMEM16A, also inhibits TMEM16F [175]. Since TMEM16F plays a role in thrombosis, niclosamide may also cause abnormal blood clotting when used as a therapeutic.

1.6 Dissertation aims

The current-voltage relationship of TMEM16 CaCCs and TMEM16 phospholipid scramblases differ from each other. TMEM16A, a CaCC, exhibits a linear I-V relationship at a saturating concentration of Ca^{2+} [7, 8, 107, 115], whereas TMEM16F, a phospholipid scramblase that can conduct ion current, exhibits an outwardly rectified I-V relationship [49]. In chapter 2, our group explored the molecular mechanism behind the I-V relationship of TMEM16A and TMEM16F. Mutating a pore residue, K584, into glutamine altered the I-V relationship of TMEM16A [107]. Thus, this residue may exert an electrostatic control on ion permeation in TMEM16A. We tested whether this residue influences the I-V relationship of TMEM16A through an electrostatic mechanism and whether this residue's charge will correlate with the degree of current rectification. In addition, we tested whether the charge of the analogous residue in TMEM16F, Q559, can alter the channel's I-V relationship.

High-resolution structures of TMEM16F and TMEM16K reveal another Ca^{2+}-binding site besides the high-affinity Ca^{2+}-binding site [82, 95]. The biphasic Ca^{2+} dose-response curve of TMEM16A hints at the existence of undiscovered, low-affinity, Ca^{2+}-binding sites for TMEM16 proteins [106, 107]. In chapter 3, we characterized how Co^{2+} affects ion permeation in TMEM16A. Next, we tested whether this potential allosteric binding site is within the membrane electrostatic field by testing for voltage dependence.

Finally, we tested whether Co^{2+} increases the current going through the pore of TMEM16A by mutating a pore residue, Y589, and seeing if the Co^{2+} effect on ion permeation is altered.

Generally, TMEM16 CaCCs and TMEM16 phospholipid scramblases have different cation permeability. However, they share a similar general structure in that the intracellular vestibule is partially exposed to membrane phospholipids. Ions interacting with phospholipids near the intracellular vestibule of TMEM16A and TMEM16F may influence ion permeation in these proteins. In chapter 4, we explored how divalent and monovalent cations affect ion permeation in TMEM16A and TMEM16F. Next, we addressed the apparent controversial ion selectivity of TMEM16F in the literature. Finally, we explored how manipulating membrane phospholipids, especially PIP2, affects ion permeation in TMEM16A and TMEM16F.

Chapter 2: Comparison of Ion Transport Determinants Between a TMEM16 Chloride Channel and Phospholipid Scramblase

Dung M. Nguyen[1], Louisa S. Chen[2], Wei-Ping Yu[2], and Tsung-Yu Chen[2,3]

Graduate Group of Pharmacology and Toxicology[1], Center for Neuroscience[2] and Department of Neurology[3], University of California, Davis, Davis, CA 95618.

This chapter has been adapted from a publication in *J. Gen. Physiol.* (Volume 151, issue 4, page 518-531).

2.1 Abstract

Two TMEM16 family members, TMEM16A and TMEM16F, have different ion-transport properties. Upon activation by intracellular Ca^{2+}, TMEM16A—a Ca^{2+}-activated Cl^- channel—is more selective for anions than cations, whereas TMEM16F—a phospholipid scramblase—appears to transport both cations and anions. Under saturating Ca^{2+} conditions, the current-voltage (I-V) relationships of these two proteins also differ; the I-V curve of TMEM16A is linear while that of TMEM16F is outwardly rectifying. We previously found that mutating a positively charged lysine residue (K584) in the ion-transport pathway to glutamine converted the linear I-V curve of TMEM16A to an outwardly rectifying curve. Interestingly, the corresponding residue in the outwardly rectifying TMEM16F is also a glutamine (Q559). Here we examine the ion transport functions of TMEM16 molecules and compare the roles of K584 of TMEM16A and Q559 of TMEM16F in controlling the rectification of their respective I-V curves. We find that rectification of TMEM16A is

regulated electrostatically by the side-chain charge on the residue at position 584, whereas the charge on residue 559 in TMEM16F has little effect. Unexpectedly, mutation of Q559 to aromatic amino acid residues significantly alters outward rectification in TMEM16F. These same mutants show reduced Ca^{2+}-induced current rundown (or desensitization) compared with wild-type TMEM16F. A mutant that removes the rundown of TMEM16F could facilitate the study of ion transport mechanisms in this phospholipid scramblase in the same way that a CLC-0 mutant in which inactivation (or closure of the slow gate) is suppressed was used in our previous studies.

2.2 Introduction

The TMEM16 family of transmembrane proteins consists of Ca^{2+}-activated ion channels, such as TMEM16A and TMEM16B, and phospholipid scramblases, such as TMEM16F [176, 177]. TMEM16A [6-8] and TMEM16B [43, 178] control Cl^- transport across cell membranes and thus play important physiological roles in various functions, such as transepithelial fluid transport, intestinal smooth muscle contraction, and signal transduction in sensory neurons [3]. The physiological role of TMEM16F, on the other hand, is different. After its activation by Ca^{2+}, TMEM16F scrambles phospholipids in the lipid membrane, resulting in the exposure of phospholipids normally residing in the inner leaflet of cell membranes (such as phosphatidylserine) to the extracellular environment [9, 66, 108], a process critical for many physiological functions [176, 179]. For example,

the presence of phosphatidylserine in the outer leaflet of platelet cell membranes attracts blood coagulation factors to the surface of platelet cells, thus facilitating the blood coagulation process. A defective function of TMEM16F, therefore, can cause a bleeding disorder called Scott syndrome [9, 180].

Recent x-ray crystallography and cryo-electron microscopy studies have revealed the atomic structures of TMEM16 molecules [10, 96, 97, 103]. The X-ray structure of a fungus phospholipid scramblase, nhTMEM16, displays a dimeric structure formed by two identical subunits (Fig. 2.1 A, right panel). Within each subunit, transmembrane helices 3-7 form an open aqueduct (or groove), residing distantly from the molecule's twofold symmetry axis, and this aqueduct is thought to be the lipid transport pathway [10]. The cryo-electron microscopy structure of TMEM16A (Fig. 2.1 A, left panel) shows a similar molecular architecture to that of nhTMEM16 except that transmembrane helix 4 of TMEM16A (helix colored in green in Fig. 2.1 B) is more tilted and partially covers the aforementioned aqueduct structure [96, 97, 103]. Consequently, the extracellular half of the aqueduct in TMEM16A is completely enclosed by helices 3-7 (compare the left and right panels in Fig. 2.1 B), forming a pore-like structure. Experimental evidence has suggested that this pore-like structure in TMEM16A is likely the pathway that conducts the current carried by Cl^- [97, 103, 106, 107]. Meanwhile, Ca^{2+}-activated TMEM16F molecules also conduct ionic currents in

addition to the phospholipid scramblase activity [108, 134]. It has been suggested that ion transport and phospholipid transport in TMEM16F share the same pathway [108, 109]. However, while an aqueduct with the sidewall open can transport lipid molecules via a “credit-card” sliding mechanism [176, 181], a structure without an enclosed protein conduit raises questions about the ion transport mechanism in phospholipid scramblases.

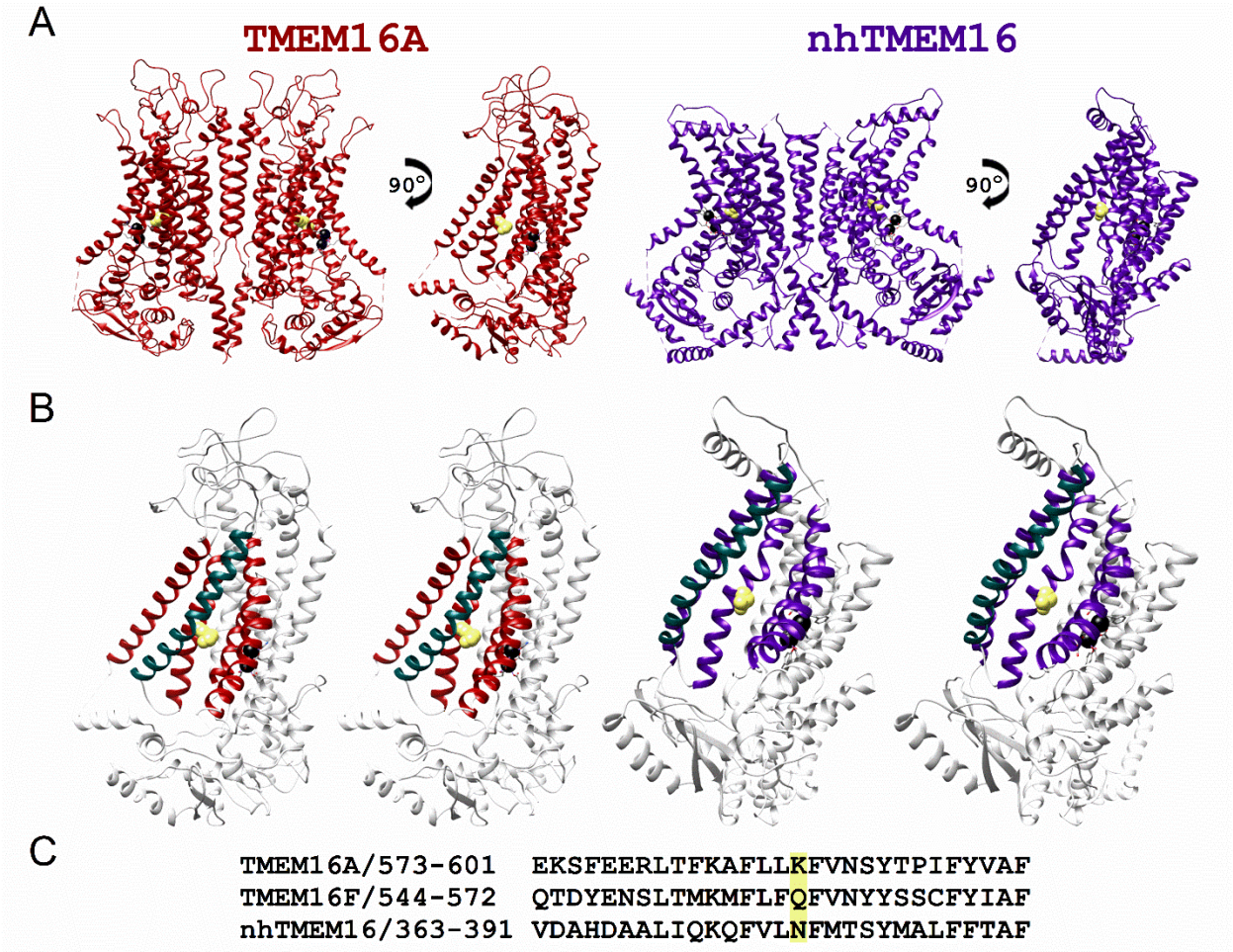

Figure 2.1. Atomic structures of TMEM16 proteins. (A) Structures of TMEM16A *(red)* and nhTMEM16 *(purple)*. In each structure, the right subunit of the molecule rotated by 90° along the twofold symmetry axis is depicted on the right. Black spheres represent Ca^{2+} ions. (B) Stereo views of single TMEM16A *(left)* and nhTMEM16 *(right)* subunits highlighting the arrangement of helices 3-7. The view angle is the same as that of viewing the single subunit in A. Helix 3 and helices 5-7 of TMEM16A and TMEM16F are colored in red and purple, respectively, while helix 4 is in green in both molecules. (C) Sequence alignment of helix 5 of TMEM16A, TMEM16F, and

nhTMEM16. $K584_{16A}$, $Q559_{16F}$, and the corresponding residue N378 in nhTMEM16 (highlighted in yellow) are located in this helix. $K584_{16A}$ and N378 of nhTMEM16 are also depicted as a space-filled residue (colored in yellow) in the structures shown in A and B.

Although both TMEM16A and TMEM16F conduct currents upon activation by intracellular Ca^{2+} ($[Ca^{2+}]_i$), their selectivity of the transported ions differs. The pores of TMEM16A are more selective for anions [107, 115] while those of TMEM16F poorly discriminate cations from anions [108, 135]. In saturating $[Ca^{2+}]_i$, the I-V curve of TMEM16A is quite linear, while that of TMEM16F is very outwardly rectifying [108, 135]. In structural-functional studies of TMEM16 molecules, functional roles of pore residues have been examined [49, 96, 97, 106, 107]. In particular, one residue was thought to be critical for controlling the anion/cation selectivity in TMEM16A and TMEM16F [49]. In TMEM16A, this pore residue is a positively charged lysine residue (K584, abbreviated as $K584_{16A}$) in the alternatively spliced isoform "a" (or K588 in the "a, c" isoform), while it is a glutamine residue in TMEM16F ($Q559_{16F}$). These corresponding residues are highlighted in the sequence alignment in Fig. 2.1 C, and their locations are depicted in Fig. 2.1 A & B as a space-filled residue. It has been suggested that the positive charge from this residue in TMEM16A helps select anions over cations in TMEM16A, while the neutral residue in TMEM16F renders this phospholipid

scramblase less selective for anions [49]. In another aspect of ion transport function, we and others showed that mutating $K584_{16A}$ into glutamine ($K584Q_{16A}$) generated a prominent outward rectification in the I-V curve of TMEM16A [106, 107].

The role of $Q559_{16F}$ in regulating the I-V curve rectification of TMEM16F has not been rigorously examined, although the $Q559K_{16F}$ mutant was shown to remain outwardly rectifying [49]. In this study, we compared the residues $K584_{16A}$ and $Q559_{16F}$ in controlling the rectification of their respective I-V curves. We found that the side-chain charge of amino acid at position 584 of TMEM16A appears to control the rectification of TMEM16A's I-V curve electrostatically. However, charge manipulation of residue 559 of TMEM16F was not consistent with an electrostatic regulation. Instead, we discovered that placing aromatic amino acids at position 559 of TMEM16F significantly reduced the outward rectification in this phospholipid scramblase. Furthermore, mutating $Q559_{16F}$ into an aromatic amino acid also greatly reduced the rundown of TMEM16F current. We thus took advantage of the mutant with a more linear I-V curve and less current rundown to evaluate the properties of ion transport in TMEM16F.

2.3 Materials and Methods

2.3.1 Molecular biology and channel expression

The alternatively spliced isoform "a" of the wild-type (WT) mouse TMEM16A cDNA (available from GenBank under accession no.

NM_001242349.1) was a gift from L.Y. Jan (University of California, San Francisco, San Francisco, CA). We also obtained from Addgene the WT mouse TMEM16F tagged with mCherry on the C-terminus (Addgene plasmid # 62554), initially deposited by Han Renzhi (Loyola University Chicago Health Science Division, Maywood, IL). The WT TMEM16A (abbreviated as WT_{16A}) and the mCherry-removed WT TMEM16F (WT_{16F}) cDNAs, as well as their mutant cDNA constructs, were subcloned in pEGFP-N3 or pIRES2 expression vectors (Takara Bio). Mutations of cDNAs were made using the QuikChange II site-directed mutagenesis kit (Agilent Technologies), and were verified by commercial DNA sequencing services. These cDNA constructs produced channels with a GFP attached to the C-terminus of the channel proteins (from pEGFP-N3 constructs) or channels without a GFP tag but with a separate GFP protein (from pIRES2 constructs). The functional properties of these two types of constructs were indistinguishable. In this study, we used the GFP-tagged construct in all TMEM16A experiments. For the TMEM16F experiments, the dose-response curve was obtained from the GFP-tagged molecule while the I-V curves were obtained from the untagged TMEM16F. WT_{16A}, WT_{16F}, and all mutants were expressed in human embryonic kidney (HEK) 293 cells. Transfections of cDNAs to HEK 293 cells were performed using the lipofectamine transfection method [107, 142]. Transfected cells were identified by the green fluorescence under an inverted

microscope (DM IRB; Leica) equipped with a fluorescent light source and a GFP filter cube (Chroma Technology).

2.3.2 Electrophysiological experiments

All experiments were excised inside-out patch recordings and were conducted 24–72 h after transfections. The pipette solution contained 140 mM NaCl, 10 mM HEPES, and 0.1 mM EGTA at pH 7.4 (adjusted with NaOH). This solution, which will also be called "Solution A," was considered to have nominally "zero" free $[Ca^{2+}]$. Solutions containing various free $[Ca^{2+}]$ were made by adding $CaCl_2$ to solution A followed by adjusting the pH. The required amounts of total Ca^{2+} for generating specific free $[Ca^{2+}]$ were calculated using the MaxChelator program [182], if the desired free $[Ca^{2+}] \leq 10$ μM. In experiments where various intracellular pH (pH_i) (5.4–8.4) were necessary, the NaOH was also used to adjust the pH. For solutions containing free $[Ca^{2+}] \geq 20$ μM, the total $[Ca^{2+}]$ added to Solution A was equal to the desired free $[Ca^{2+}]$ plus 0.1 mM. If the total added $[CaCl_2]$ was >0.5 mM, [NaCl] was reduced accordingly to maintain a total $[Cl^-]$ at 140 mM. Free $[Ca^{2+}]$ in the intracellular side of excised inside-out patches will be abbreviated as $[Ca^{2+}]_i$. In all experiments, the recording pipettes were made from borosilicate glass capillaries (World Precision Instruments) using the PP830 electrode puller (Narishige), and the electrode resistance was between ~1.5 and ~3.0 MΩ when filled with Solution A. All experiments were conducted using an Axopatch 200B amplifier, and the signals, filtered at 1

kHz, were digitized at 2 kHz by the Digidata analogue/digital signal converting board controlled by the pClamp software (Molecular Devices). Solutions were delivered to the intracellular side of the excised inside-out patch using the SF-77 solution exchanger (Warner Instruments), which can switch solutions within a few milliseconds [183].

To construct $[Ca^{2+}]$-dependent activation curves, we used the previously described three-pulse protocol to minimize Ca^{2+}-induced current rundown. The apparent Ca^{2+} affinity of activating TMEM16F was significantly lower than that of activating TMEM16A, so we used 900 μM $[Ca^{2+}]_i$ as the saturating $[Ca^{2+}]_i$. The experimental protocol included a direct delivery to the cytoplasmic side of the membrane of 900 μM $[Ca^{2+}]_i$, a test $[Ca^{2+}]_i$ (1-500 μM $[Ca^{2+}]_i$), and finally 900 μM $[Ca^{2+}]_i$ again. The leak current, measured in the zero-Ca^{2+} solution (Solution A), was subtracted from the current in the presence of Ca^{2+}. The current activated by the test $[Ca^{2+}]_i$ pulse was normalized to the average of the two flanking saturating currents obtained in 900 μM $[Ca^{2+}]_i$. For the dose-response activation curve of $Q559W_{16F}$ and other aromatic mutants of TMEM16F, the three-pulse protocol described above was also employed. Due to these mutants' resistance to rundown, current activated with 0.1-1 mM $[Ca^{2+}]_i$ was normalized to current activated with 2 mM $[Ca^{2+}]_i$ instead of 900 μM $[Ca^{2+}]_i$. With $Q559W_{16F}$, we also used another protocol to construct a dose-response curve, in which we sequentially applied various $[Ca^{2+}]_i$, and normalized the Ca^{2+}-induced

current to the current activated by the maximal $[Ca^{2+}]_i$. The purpose of using this latter protocol was to compare the results with those reported in the literature obtained with similar methods. In both types of experiments, normalized values of the Ca^{2+}-induced current (I_{norm}) were plotted against $[Ca^{2+}]_i$ to construct dose-response curves.

I-V curves were constructed using a 1.6-s voltage ramp from −80 mV to +80 mV applied to the excised inside-out patches. For each patch, the recordings in Ca^{2+} free intracellular solutions were subtracted from that obtained in the presence of $[Ca^{2+}]_i$, and the resulting leak-subtracted I-V curves were used to determine the reversal potential (E_{rev}). To average I-V curves from different membrane patches, the digitized data points from the ramp protocol were normalized to the last digitized point obtained at +80 mV, and the normalized values from different patches were averaged. All TMEM16A constructs were activated with 20 μM or 20 mM $[Ca^{2+}]_i$. Additional I-V curves for WT_{16A} and $K584H_{16A}$ were measured at pH 5.4, 6.4 and 7.4 with 400 μM $[Ca^{2+}]_i$. All TMEM16F constructs were activated with 1 mM $[Ca^{2+}]_i$. Additional I-V curves for $Q559H_{16F}$ was constructed at pH 6.4, 7.4, and 8.4. To evaluate the degree of the I-V curve rectification, we defined a parameter called the rectification index (RI), which is the ratio of the absolute current amplitudes at −80 mV versus that at +80 mV ($RI = |I_{-80mV}/I_{+80mV}|$). Thus, positive or negative deviation in RI from 1 indicates inward or outward rectification, respectively.

To measure E_{rev} under reduced NaCl conditions, the extracellular solution was Solution A, containing 140 mM NaCl. The intracellular NaCl concentration ($[NaCl]_i$) was made by mixing the 140 mM NaCl solution with the same concentration of $(NMDG)_2SO_4$ solution, both containing identical [HEPES], [EGTA], [Ca^{2+}-EGTA], and free [Ca^{2+}] [107]. I-V curves of WT_{16A}, $K584Q_{16A}$, WT_{16F}, and $Q559W_{16F}$ were measured in the presence of various intracellular solutions containing 100% (~140 mM $[NaCl]_i$), 60% (~84 mM $[NaCl]_i$), or 30% (~42 mM $[NaCl]_i$) of Solution A, whereas the reduced $[NaCl]_i$ was replaced with the same concentration of $(NMDG)_2SO_4$ solution. We also conducted the same experiments without adding $(NMDG)_2SO_4$ to replace the reduced $[NaCl]_i$. To estimate the anion permeability sequence, E_{rev} was measured under bi-ionic conditions: $[NaCl]_i$ was replaced with identical concentrations of NaI or NaSCN. The liquid junction potentials in these various experiments were less than 2 mV except when reducing $[NaCl]_i$ without adding $(NMDG)_2SO_4$. In experiments without adding $(NMDG)_2SO_4$, the junction potentials were 2.6 mV and 6 mV for 84 mM and 42 mM $[NaCl]_i$, respectively. All the reported E_{rev} values have been corrected for liquid junction potentials.

To alter the charge of the introduced cysteine residue, we used methanethiosulfonate (MTS) reagents to modify the free thiol group of the cysteine side chain. MTS reagents such as sulfonatoethyl MTS (MTSES) and ethyltrimethylammonium MTS (MTSET) were purchased from Toronto

Research Chemicals. High concentrations of MTS reagents were made in double-distilled H_2O and were stored at -80°C. Upon use, stock solutions of MTS reagents were thawed and placed on ice and were directly diluted into the working solution. To modify the channels in excised inside-out patches, WT_{16A} and $K584C_{16A}$ were activated with 20 μM $[Ca^{2+}]_i$ at -40 mV before the application of MTS reagents. I-V curves of the channels before and after MTS modification were obtained as previously described.

2.3.3 Data Analysis

Experimental data were analyzed using the Clampfit 10 software (Molecular Devices) and Origin software (OriginLab).

To evaluate the apparent Ca^{2+} affinity for activating TMEM16 molecules, data points of the normalized current (I_{norm}) in the dose-response plot were fitted to the Hill equation:

$$I_{norm} = 1/[1 + (K_{1/2}/[Ca^{2+}]_i)^h],$$

where $K_{1/2}$ and h are the fitted half-effective concentration and the Hill coefficient, respectively.

Permeability ratios of Na^+ versus Cl^- (P_{Na}/P_{Cl}) were calculated according to the Goldman-Hodgkin-Katz equation:

$$E_{rev} = (RT/F)\ln[(P_{Na}[Na^+]_o + P_{Cl}[Cl^-]_i)/(P_{Na}[Na^+]_i + P_{Cl}[Cl^-]_o)],$$

where R, T, and F are the ideal gas constant, absolute temperature, and Faraday constant, respectively.

All averaged data were presented as means ± SEM. Student's *t* test was used for statistical comparisons among the data sets of fixed-charge mutations. For MTS modification experiments, a paired Student's *t* test was employed to compare the datasets before and after 12-s MTS modifications. Differences were considered statistically significant if $p < 0.05$.

2.4 Results

2.4.1 Roles of $K584_{16A}$ in the rectification of TMEM16A's I-V curve

TMEM16A is a dimeric Cl^- channel [101, 102, 184] with two distinct pores. The two-pore architecture was first suggested based on the observations that mutating $K584_{16A}$ (or $K588_{16A}$ of the "a,c" isoform of TMEM16A) into a neutral residue, glutamine, generated an outwardly rectifying I-V curve, and that this mutation effect was subunit-specific [106, 107]. The high-resolution structure of TMEM16A confirms the location of this positively charged residue in the pore [96, 97, 103]. Therefore, TMEM16A's I-V curve rectification, caused by the $K584Q_{16A}$ mutation, might reflect an electrostatic effect of losing a positive charge on Cl^- conduction. Such an electrostatic control has been documented in CLC-0, in which the mutation of K519 of this *Torpedo* Cl^- channel can alter the anion permeation electrostatically [185, 186]. A recent study also showed that Ca^{2+} binding to the binding sites of TMEM16A, which are close to the location of $K584_{16A}$, can

electrostatically influence anion permeation in the pore [126]. To verify this possibility, we mutated $K584_{16A}$ into amino acids with different side-chain charges. Fig. 2.2 A shows that placing any neutral amino acids at this position caused a significant outward rectification of the I-V curve obtained in saturating $[Ca^{2+}]_i$ with symmetrical 140 mM $[Cl^-]$. When a negatively charged residue, such as glutamate or aspartate, was introduced at this position, the I-V curves were even more outwardly rectifying. On the other hand, introducing a positively charged residue at this position, i.e. the $K584R_{16A}$ mutation, only affected the rectification slightly. To compare the degree of rectification, we defined the rectification index (RI) as the ratio of the absolute value of the current at -80 mV to that at +80 mV. The mutation experiments revealed that the value of the RI followed with the side-chain charge of the residue 584: mutants with a negatively charged side chain had the smallest RI, while those with the positively charged residues had the largest RI. However, since the I-V curve of the WT_{16A} exhibits outward rectification in nonsaturating $[Ca^{2+}]_i$ [8, 104, 187], we also conducted the experiments with 20 mM $[Ca^{2+}]_i$ to ensure maximum activation of all TMEM16A mutants. As shown in Fig. 2.2 B, the pattern of the electrostatic influence on RI is preserved for I-V curves obtained at 20 mM $[Ca^{2+}]_i$.

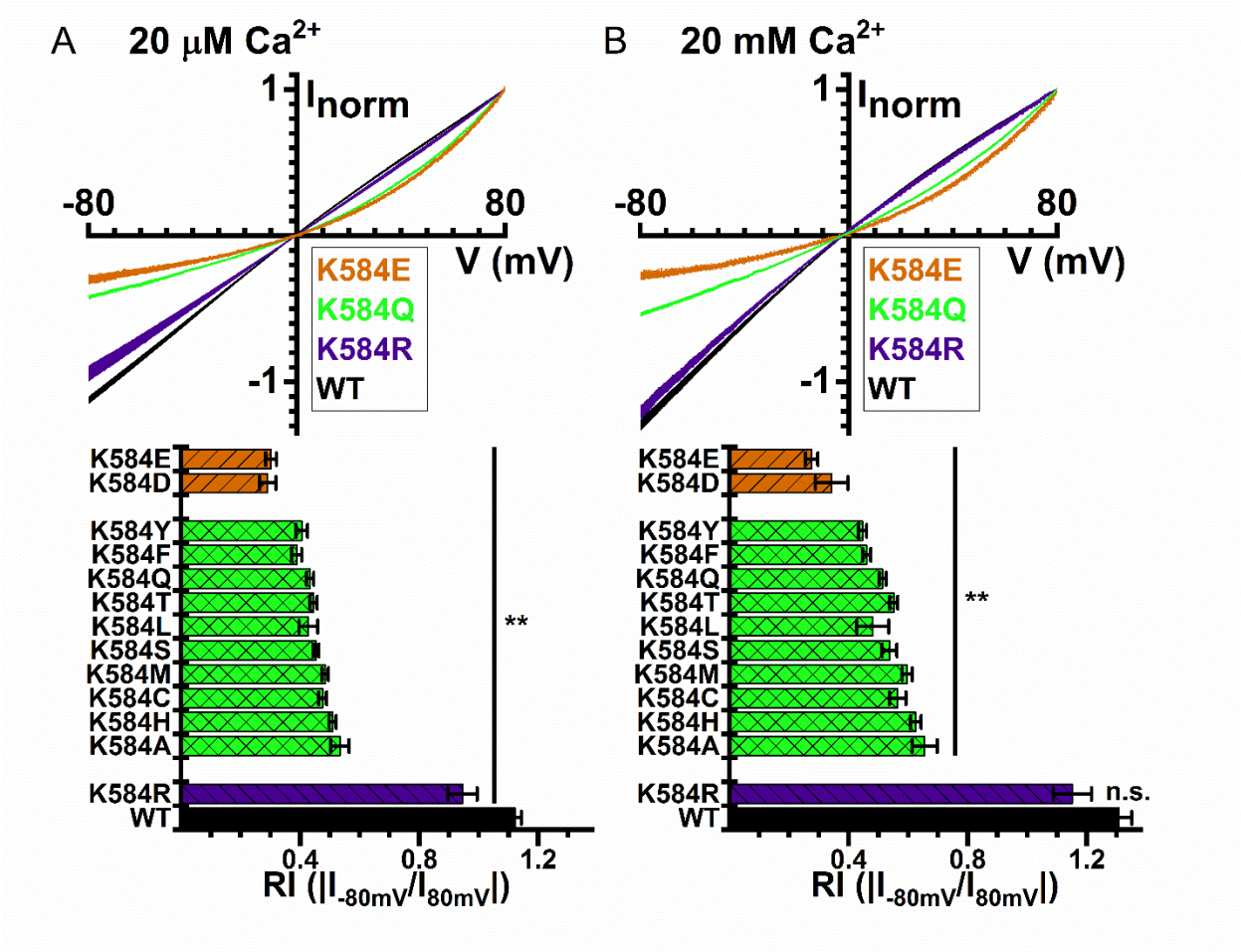

Figure 2.2. I-V curves of WT TMEM16A and mutants. I-V curves in the presence of (A) 20 μM and (B) 20 mM $[Ca^{2+}]_i$. Symmetrical 140 mM $[Cl^-]$. In both (A) & (B), averaged I-V curves of WT_{16A}, $K584Q_{16A}$, $K584R_{16A}$, and $K584E_{16A}$ are depicted on top, while the averaged RI values (mean ± SEM, n = 3-36) of the WT_{16A} and various mutants are shown at the bottom. *P < 0.05 and **P < 0.005 by Student's t-test comparing to WT_{16A}. n.s., not significant.

To examine the electrostatic control of ion transport in TMEM16A more rigorously, we adopted two other methods to alter the side-chain charge of residue 584. First, we placed histidine at this position ($K584H_{16A}$) and measured the effect of intracellular pH (pH_i) on the I-V curve [185]. Lowering pH_i, however, may reduce the channel affinity for Ca^{2+} because the Ca^{2+}-binding site of TMEM16A consists of several acidic residues such as E698, E701, E730, and D734 [10, 96, 97, 104, 105]. The I-V curve of TMEM16A in nonsaturating $[Ca^{2+}]_i$ is known to be outwardly rectifying, which could complicate the interpretation of the results. Therefore, we used a higher $[Ca^{2+}]_i$ (400 μM) to activate the current in this experiment. Lowering the pH_i does not cause a decrease of RI in WT_{16A} (Fig. 2.3 A), indicating that 400 μM $[Ca^{2+}]_i$ is high enough to fully open the channel even at lower pH_i conditions. For $K584H_{16A}$, a reduction of pH_i from 7.4 to 5.4 incrementally increases the RI value in $K584H_{16A}$ (Fig. 2.3 B), likely due to the more positively charged side chain of histidine. Another approach to alter the sidechain charge is to modify a cysteine residue at position 584 ($K584C_{16A}$ mutation) with charged MTS reagents, such as MTSES or MTSET, which add a negative and a positive charge to the cysteine side chain, respectively [185, 186]. The WT_{16A} channel contains endogenous cysteine residues. However, neither 10 mM MTSES nor 2 mM MTSET alters the Ca^{2+}-activated current in WT_{16A} (Fig. 2.3, C & D, left panel). In contrast, MTSES and MTSET, decreases and increases the current of $K584C_{16A}$, respectively (Fig. 2.3 C &

D, middle panel), although the current alteration effect of MTSET appears to be larger. It is also worth noting that millimolar concentrations of MTS reagents are required to alter current within several seconds, so their modification rates of $K584C_{16A}$ are at least 30 times slower than the corresponding modifications of K519C of CLC-0 [188]. The modification by 10 mM MTSES for 12 s renders the I-V curve more outwardly rectifying (Fig. 2.3 C, right), albeit the effect on the RI reduction is small. In contrast, MTSET modification generates a greater effect on altering the RI value, and the modification by 2 mM MTSET for 12 sec generates a nearly linear I-V curve (Fig. 2.3 D, right), suggesting that such an MTSET exposure likely modifies most of the $K584C_{16A}$ mutants. The smaller MTSES modification effect is consistent with the observation that the RI difference between constructs with a neutral and a negatively charged residue at position 584 is smaller than the difference between those with a neutral and a positively charged mutation (Fig. 2.2). In addition, exposing the membrane patch for the same duration to 10 mM MTSES, which has an intrinsic reactivity 12-fold lower than that of MTSET [189], is not enough to fully modify all $K584C_{16A}$ mutants. This is shown by separate experiments in which MTSET induces current in patches pre-exposed to 10 mM MTSES for 12 s, and thus increases RI (Fig. 2.S1). Regardless of the slow MTS modification rates, the I-V curves become more outwardly rectifying in every individual patch after the application of 10 mM MTSES for 12 sec (Fig. 2.3 C, right), whereas

outward rectification was decreased after MTSET modification (Fig. 2.3 D, right). These MTS modification results and the pH titration effects shown above mimic those shown in CLC-0 where a positively charged residue, K519, electrostatically controls the efflux of Cl^- in the CLC-0 pore [185, 186].

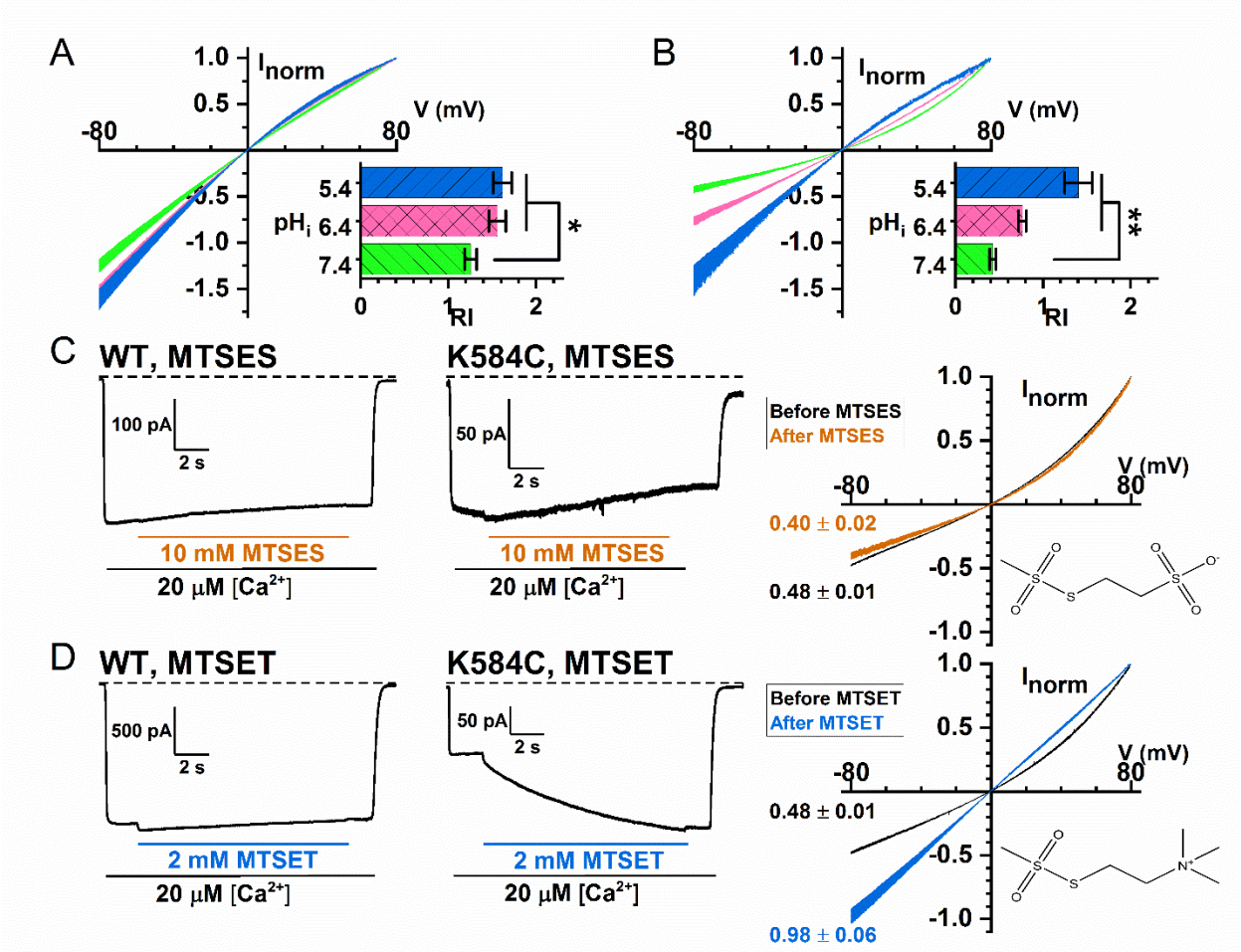

Figure 2.3. Side-chain charge modifications of the residue at position 584 of TMEM16A. (A and B) I-V curves of WT_{16A} (A) and $K584H_{16A}$ (B) with 400 μM $[Ca^{2+}]_i$ at pH 5.4 (blue), 6.4 (pink), and 7.4 (green). Insets show averaged

rectification indices (n = 6, *P < 0.05 and **P < 0.005 by Student's t-test). (C and D) Manipulation of the side-chain charge of $K584C_{16A}$ by MTSES (C) and MTSET (D) modifications. In each panel, recording traces of MTS modifications of WT_{16A} and $K584C_{16A}$ at -40 mV are depicted on the left and middle, respectively. The dashed line represents zero current level. The structures of the MTS molecules and the I-V curves of $K584C_{16A}$ before and after MTS modification are shown on the right. The RI values are displayed next to each I-V curve. The RI values after MTSES (n = 9) and MTSET (n = 6) modifications were significantly different from those before the modifications (p < 0.05, paired Student's t test).

2.4.2 Roles of $Q559_{16F}$ in the rectification of TMEM16F's I-V Curve

TMEM16F, a phospholipid scramblase in the TMEM16 family, can also conduct ionic current upon activation by $[Ca^{2+}]_i$. We were thus curious whether the charge of residue 559 of TMEM16F also controls the rectification of its I-V curve. Before answering this question, we evaluated the apparent Ca^{2+} affinity of the WT_{16F} to determine a saturating $[Ca^{2+}]_i$ suitable for the experiments (Fig. 2.4 A). With excised inside-out patch recordings, the TMEM16F current appeared almost immediately upon the application of intracellular Ca^{2+}, and the current induced by high $[Ca^{2+}]_i$ ran down quickly (Fig. 2.4 A). We thus constructed the $[Ca^{2+}]_i$-dependent activation curve using the standard three-pulse methods, and normalized the current in

tested $[Ca^{2+}]_i$ to the mean of the saturated current (induced by 900 μM $[Ca^{2+}]_i$) immediately before and after the tested $[Ca^{2+}]_i$ [115]. Such a dose-response relationship shows that at +40 mV the $K_{1/2}$ for Ca^{2+} was 34 μM and the Hill coefficient was 1.2 (Fig. 2.4 B). Since TMEM16F currents run down within several seconds, the dose-response curve in Fig. 2.4 B likely comes from the partially rundown TMEM16F, which has a lower Ca^{2+} affinity than the pre-rundown TMEM16F [147]. As the dose-response curve indicated that it requires more than ~100 μM $[Ca^{2+}]_i$ for a near saturation of Ca^{2+} activation, we obtained I-V curves at a ten-fold higher $[Ca^{2+}]_i$ (1 mM) to ensure full activation of TMEM16F. WT_{16F} contains a neutral residue (glutamine) at position 559, but mutating $Q559_{16F}$ into charged amino acid residues did not drastically alter the rectification of its I-V curve—$Q559E_{16F}$ and $Q559D_{16F}$ mutations did not significantly alter the values of RI while $Q559R_{16F}$ and $Q559K_{16F}$ mutations only caused a small increase in RI (Fig. 2.5 A, and B). Furthermore, titrating the side-chain charge of $Q559H_{16F}$ with pH_i generated a result inconsistent with an electrostatic control—lowering pH_i from 7.4 to 5.4 actually decreases RI in the $Q559H_{16F}$ mutant (Fig. 2.5, C and D). Therefore, we conclude that there is no clear pattern of a significant electrostatic control of the I-V curve rectification by the charge from residue 559 in TMEM16F.

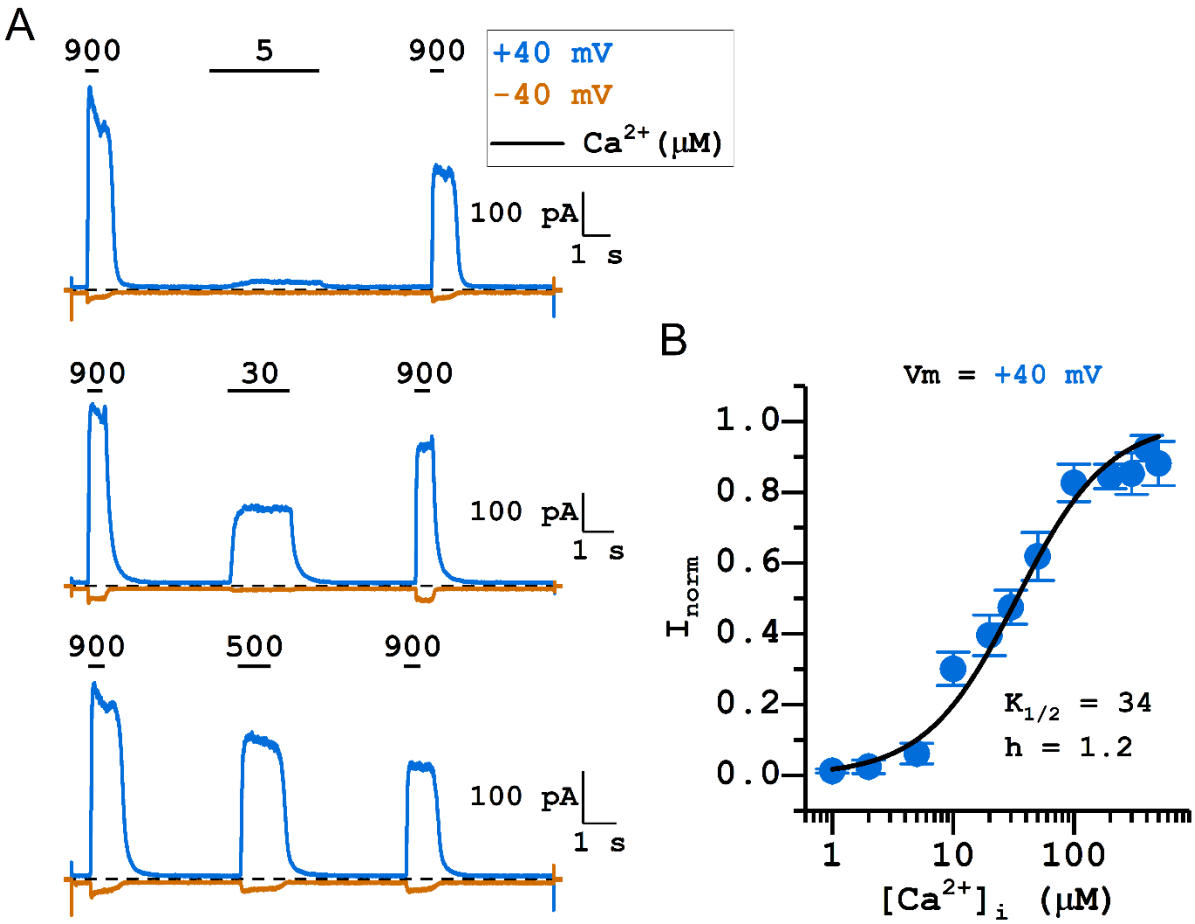

Figure 2.4. $[Ca^{2+}]_i$-dependent activation of WT_{16F}. Symmetrical 140 mM [Cl^-]. (A) Representative traces obtained at +40 mV *(blue)* and -40 mV *(orange)* showing the three-pulse protocol. Dashed lines are zero current level. Numbers and horizontal bars on top of the traces indicate the application of indicated $[Ca^{2+}]_i$ (in μM). Notice the rapid current rundown of TMEM16F. (B) $[Ca^{2+}]_i$-dependent activation curve of TMEM16F. All current was normalized to that obtained with 900 μM $[Ca^{2+}]_i$. Data points were the average of 3-12 independent measurements (mean ± SEM). The fitted values of $K_{1/2}$ and Hill coefficient (h) are shown next to the fitted curve.

Among the various mutations of $Q559_{16F}$, we found unexpectedly that introducing an aromatic amino acid at position 559 significantly reduces the I-V curve outward rectification. Fig. 2.5 (A and B) shows that the I-V curves of $Q559W_{16F}$, $Q559H_{16F}$, $Q559Y_{16F}$ and $Q559F_{16F}$ all have a significant increase in their RI, which were 0.45 ± 0.03 (n = 10), 0.23 ± 0.03 (n = 11), 0.22 ± 0.04 (n = 10), 0.19 ± 0.03 (n = 9), respectively. In comparison, the RI of WT_{16F} was 0.05 ± 0.01 (n = 15). Although other possibilities exist, the simplest interpretation for these findings is that the region near $Q559_{16F}$, like the corresponding region in TMEM16A, could be involved in the ion transport of this phospholipid scramblase.

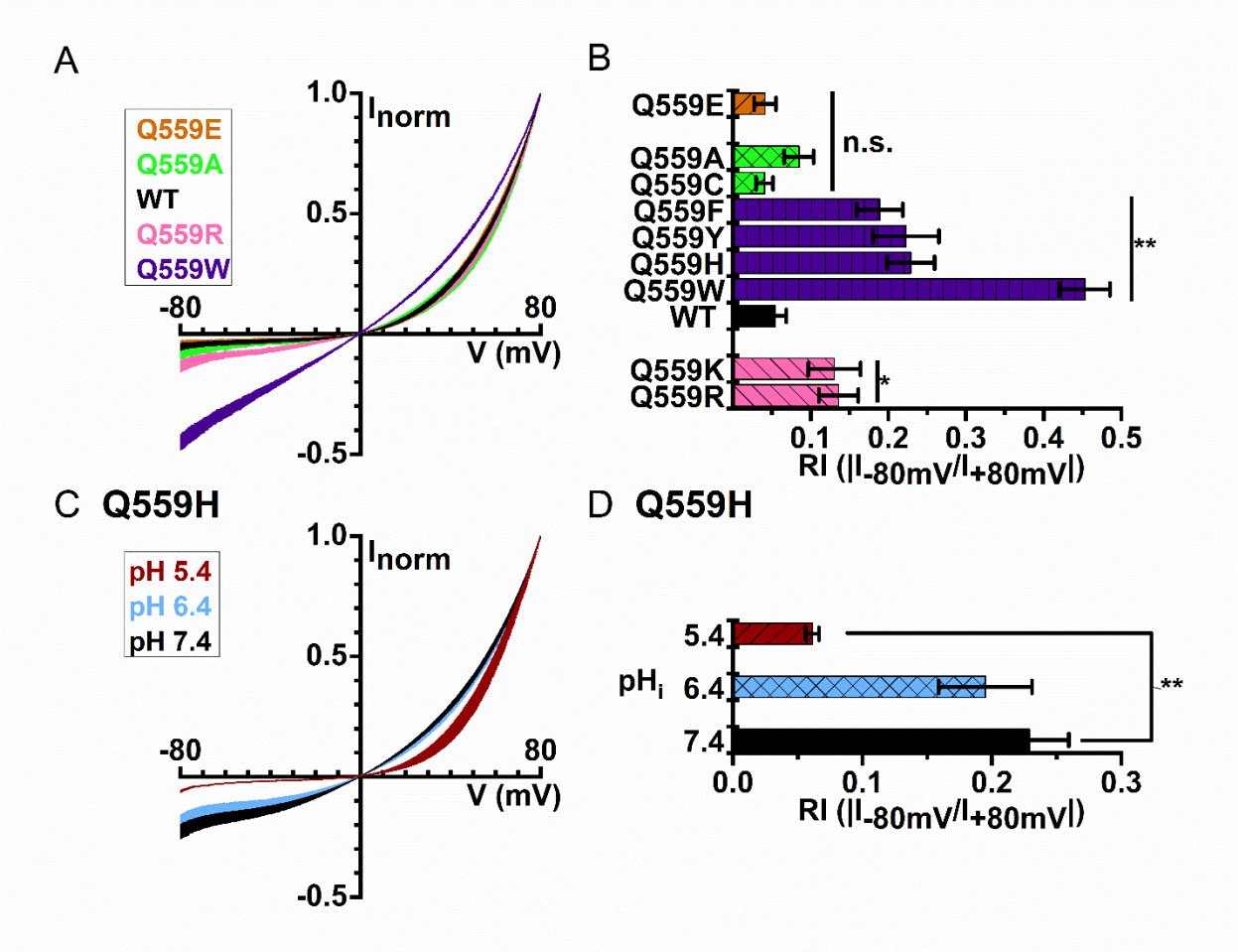

Figure 2.5. I-V curves of WT_{16F} and mutants in symmetrical 140 mM [Cl^-] and with 1 mM $[Ca^{2+}]_i$. (A) Averaged I-V curves of $Q559E_{16F}$ *(orange)*, $Q559A_{16F}$ *(green)*, WT_{16F} *(black)*, $Q559R_{16F}$ *(pink)*, and $Q559W_{16F}$ *(purple)* (n = 4-11). (B) Rectification indices of WT_{16F} and various mutants. (C) I-V curves of $Q559H_{16F}$ at pH_i 7.4 *(black)*, 6.4 *(blue)*, and 5.4 *(red)*. (D) Averaged rectification indices of $Q559H_{16F}$ at different pH_i. *P < 0.05 and **P < 0.005 by Student's t-test comparing to WT_{16F} at pH_i = 7.4.

2.4.3 $Q559_{16F}$ is critical for the rundown of TMEM16F currents

The second interesting finding of placing an aromatic amino acid at position 559 of TMEM16F is that these mutants show little current rundown induced by high $[Ca^{2+}]_i$! As shown in Fig. 2.6 (top trace), the WT TMEM16F current activated by 2 mM $[Ca^{2+}]_i$ runs down significantly within several seconds. On the other hand, $Q559W_{16F}$, $Q559H_{16F}$, $Q559Y_{16F}$ and $Q559F_{16F}$ do not exhibit significant current rundown from the same $[Ca^{2+}]_i$ application (Fig. 2.6). For comparison, introducing neutral amino acids such as alanine and cysteine, or negatively charged amino acids such as glutamate still maintains the quick rundown response. On the other hand, introducing positively charged amino acids does not cause rundown in the same high $[Ca^{2+}]_i$. Instead, a slowly increased current upon $[Ca^{2+}]_i$ application was observed in $Q559K_{16F}$ and $Q559R_{16F}$ mutants. We also tested the rundown for a more prolonged time in $Q559W_{16F}$, and found little rundown in this mutant even with 2 mM $[Ca^{2+}]_i$ for 3 min (Fig. 2.7 A). These results reveal that residue 559 of TMEM16F is critical for controlling the rundown of TMEM16F.

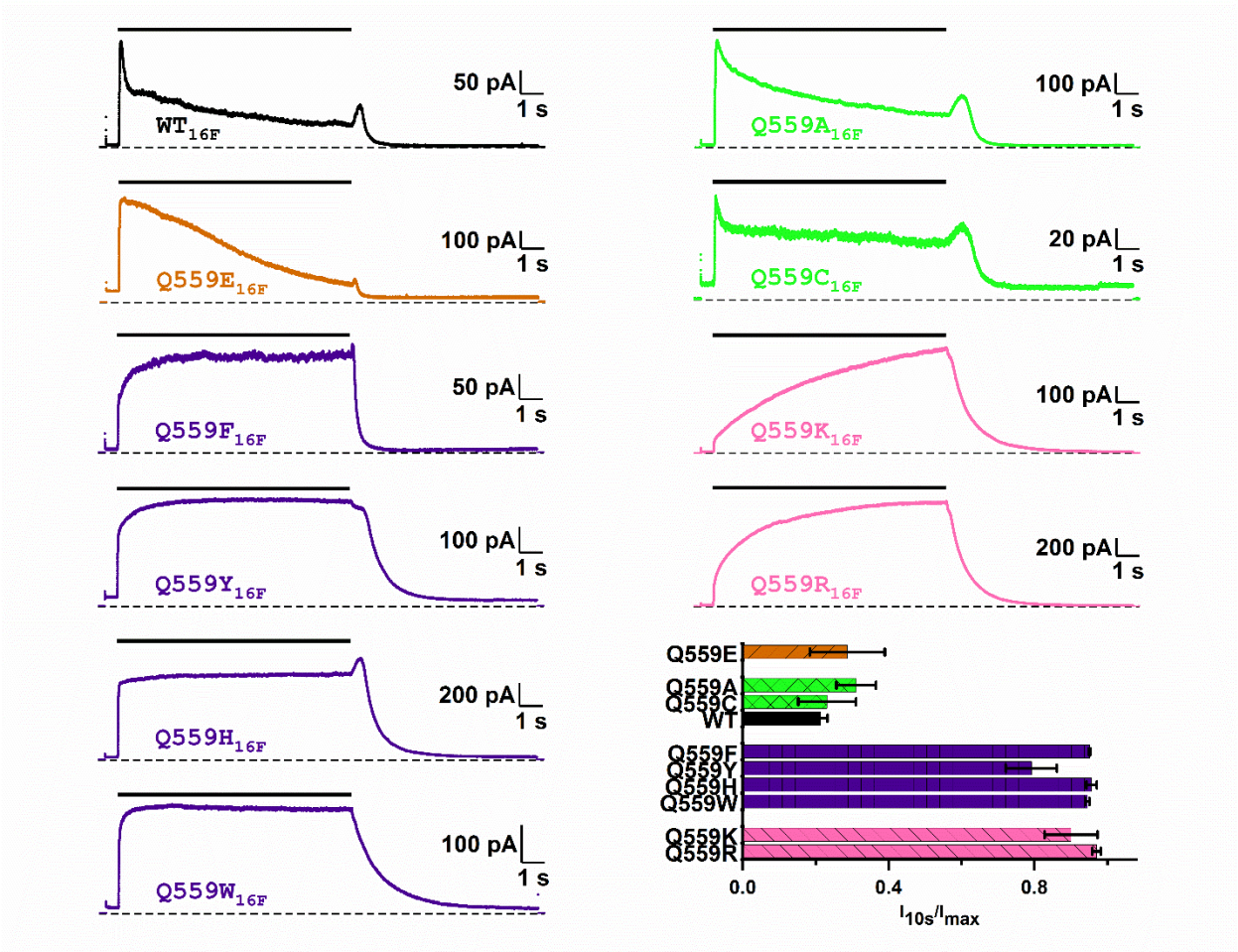

Figure 2.6. Mutation of $Q559_{16F}$ alters the Ca^{2+}-dependent rundown of TMEM16F. WT_{16F} *(black)* and various mutants of $Q559_{16F}$ were activated by 2 mM $[Ca^{2+}]_i$ at +40 mV in symmetrical 140 mM $[Cl^-]$. Dashed lines are zero current level. Black horizontal line segments above the traces indicate the 10-sec application of 2 mM $[Ca^{2+}]_i$. To evaluate the degree of Ca^{2+}-induced rundown, the current measured at the end of the 10-sec $[Ca^{2+}]_i$ exposure (I_{10s}) was divided by the maximal current (I_{max}) in the same 10-sec recording in $[Ca^{2+}]_i$. Bar graph shows the averaged values of I_{10s}/I_{max},

indicating the non-desensitized current fraction after exposure to 2 mM $[Ca^{2+}]_i$ for 10 sec (n = 3-8).

The unexpected findings that the $[Ca^{2+}]_i$-induced rundown in TMEM16F can be prevented and that the I-V curves are more linear in mutants with aromatic amino acids at position 559 provide an opportunity for more reliable assessment of the functional properties of TMEM16F. A more linear I-V curve allows a better estimate of the E_{rev} while little current rundown makes the construction of $[Ca^{2+}]_i$-dependent activation curve less prone to rundown-induced errors [115]. We thus characterized the apparent Ca^{2+} affinity and ion permeability functions in these mutants. We employed two different protocols to construct $[Ca^{2+}]_i$-dependent activation curves of $Q559W_{16F}$ (Fig. 2.7, B and C). While the Hill coefficient of WT_{16F} and that of the $Q559W_{16F}$ mutant are similar, the $K_{1/2}$ of the dose-response activation curve in the $Q559W_{16F}$ is significantly different from that of the WT_{16F} (Fig. 2.7), but similar to that of the pre-rundown WT_{16F} reported in the literature [147]. Other mutants with an aromatic residue at position 559 also have apparent Ca^{2+} affinities similar to that of the pre-rundown WT_{16F} as well (Table 2.1). For $Q559K_{16F}$ and $Q559R_{16F}$, although the current rundown was also suppressed, a slow continuous increase of the Ca^{2+}-induced current generated a technical uncertainty to determine the steady-state current.

Therefore, we did not construct $[Ca^{2+}]_i$-dependent activation curves for these two mutants.

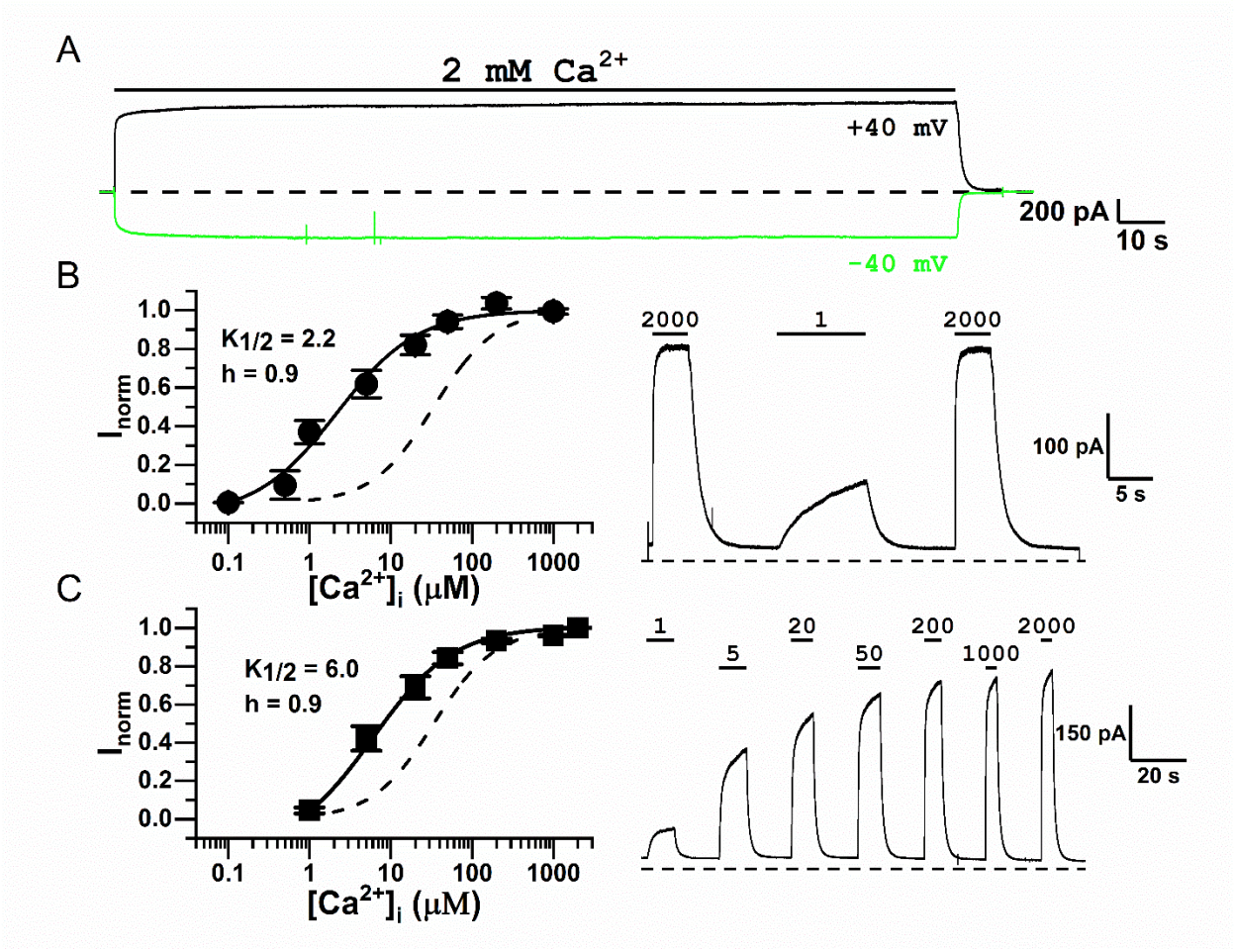

Figure 2.7. Ca^{2+}-dependent activation of $Q559W_{16F}$. (A) Exposure of $Q559W_{16F}$ to 2 mM $[Ca^{2+}]_i$ for 3 min (indicated by the black line on top) revealed little current rundown. (B) Examining $[Ca^{2+}]_i$-dependent activation of $Q559W_{16F}$ (at +40 mV) in symmetrical 140 mM $[Cl^-]$ using the three-pulse protocol. A representative trace of the experiment using this protocol is shown on the right. The dotted line is the zero-current level. Numbers and horizontal segments above the trace represent the application of the applied

$[Ca^{2+}]_i$ in μM. (C) Dose-response curve of Ca^{2+}-activation of $Q559W_{16F}$ in symmetrical 140 mM Cl^-. Various $[Ca^{2+}]_i$ were sequentially applied as shown by the recording trace shown on the right. In B and C, all currents were normalized to that obtained with 2 mM $[Ca^{2+}]_i$ (n = 10-15). The dashed curve was the fitted dose-response curve of WT_{16F} shown in Fig. 2.4.

Table 2.1. Ca^{2+}-dependent activation of WT TMEM16F and aromatic Q559 mutants using the three-pulse protocol.

	Ca^{2+} Dose-response	
Channel	$K_{1/2}$ (μM)	Hill Coefficient
WT_{16F}*	34 ± 3	1.2 ± 0.1
$Q559F_{16F}$	10 ± 1	1.5 ± 0.1
$Q559Y_{16F}$	7.9 ± 0.9	1.3 ± 0.1
$Q559H_{16F}$	3.2 ± 0.6	1.9 ± 0.2
$Q559W_{16F}$	2.2 ± 0.7	0.9 ± 0.2

*Channel likely in partially rundown state

2.4.4 The $Q559W_{16F}$ mutation does not significantly alter ion permeation of TMEM16F

To further characterize the rundown-resistant TMEM16F mutants, we compared ion permeation functions between WT_{16A} and WT_{16F} in two aspects: the anion/cation selectivity, and the permeability of I^-, and SCN^-

relative to that of Cl^-. The former was assessed by measuring the E_{rev} in reduced $[NaCl]_i$ conditions: 60% (84 mM) and 30% (42 mM) of the extracellular [NaCl] (Fig. 2.8, A and B), while the latter was evaluated by experiments in which $[Cl^-]_i$ was replaced with equal concentrations of a different anion (Fig. 2.8, C and D). Unlike our previous results in WT_{16A} with the same ionic conditions [107], reducing $[NaCl]_i$ to 42 mM (30 % of the control concentration) resulted in only a small shift of the E_{rev}. The values of E_{rev} were 0.7 ± 0.7 mV and 1.3 ± 0.8 mV for WT_{16F} and 2.8 ± 0.4 mV and 4.3 ± 0.9 mV for $Q559W_{16F}$ in 84 mM and 42 mM $[NaCl]_i$, respectively (Fig. 2.8 B), in the experiments where the reduced $[NaCl]_i$ was replaced with $(NMDG)_2SO_4$. Comparing these measured E_{rev} values with a perfect Cl^- Nernstian curve indicates that the pore of WT_{16F} does not selectively conduct Cl^-, and the $Q559W_{16F}$ mutation does not change this property (Fig. 2.8 B). Because the permeability of TMEM16F for the ions that replace $[NaCl]_i$ (namely, $NMDG^+$ and SO_4^{2-}) were not certain, we further conducted similar experiments in reduced $[NaCl]_i$ solutions without $(NMDG)_2SO_4$. The E_{rev} values were 1.7 ± 0.7 mV and 5.4 ± 1.8 mV for WT_{16F} and -0.2 ± 0.7 mV and -1.4 ± 2.9 mV for $Q559W_{16F}$ in 84 mM and 42 mM $[NaCl]_i$, respectively (Fig. 2.8 B). The calculated P_{Na}/P_{Cl} permeability ratios were estimated to be ~1.3 and ~ 1.0 for WT_{16F} and $Q559W_{16F,}$ respectively, based on the values of E_{rev} obtained with 84 mM $[NaCl]_i$.

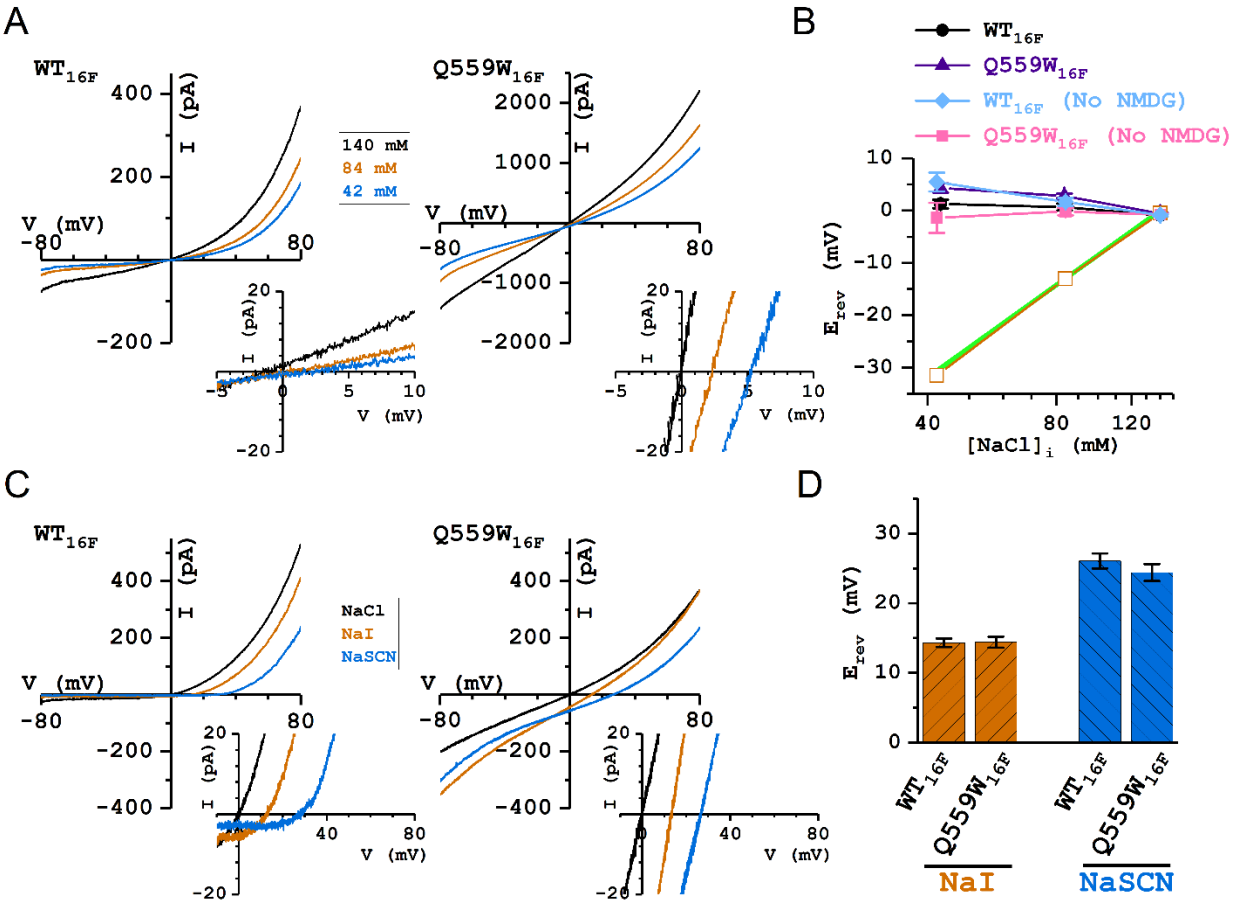

Figure 2.8. Comparing ion selectivity between WT_{16F} and $Q559W_{16F}$. All recordings were with 1 mM $[Ca^{2+}]_i$ and 140 mM $[NaCl]_o$. (A) Representative I-V curves of WT_{16F} and $Q559W_{16F}$ in 140 mM (*black*), 84 mM (*orange*), and 42 mM (*blue*) $[NaCl]_i$. Insets show the expansion of the I-V curves near the zero-current level. (B) Values of E_{rev} plotted against $[NaCl]_i$ in experiments of reducing $[NaCl]_i$ with and without the replaced $(NMDG)_2SO_4$. Green line depicts a perfect Nernstian relation for Cl^-. Orange squares were the mean E_{rev} of WT_{16A} in the same ionic conditions reproduced from Jeng et al. [107]. (C) Representative I-V curves of WT_{16F} and $Q559W_{16F}$ in 140 mM $[NaCl]_i$

(black), $[NaI]_i$ *(orange)*, and $[NaSCN]_i$ *(blue)*. (D) Comparing bi-ionic potentials between WT_{16F} and $Q559W_{16F}$. The values of E_{rev} show no statistically significant difference between WT_{16F} and $Q559W_{16F}$.

The permeability of I^- and SCN^- relative to that of Cl^- were evaluated from bi-ionic experiments shown in Fig. 2.8 C. In both WT_{16F} and $Q559W_{16F}$, replacing $[NaCl]_i$ with equal concentrations of $[NaI]_i$ or $[NaSCN]_i$ generated significant shifts of E_{rev} toward more positive potentials (~14 mV and ~25 mV, respectively) (Fig. 2.8 C & D), suggesting that I^- and SCN^- are more permeable than Cl^- in TMEM16F. The shifts of E_{rev} in WT_{16F} and $Q559W_{16F}$ were not statistically different, indicating the $Q559W_{16F}$ mutation did not alter the selectivity among these anions.

2.5 Discussion

TMEM16 family members play important roles in various physiological functions. TMEM16A participates in transmembrane Cl^- transport, while TMEM16F scrambles membrane phospholipids. Although ion transport across lipid membranes appears unnecessary for the known physiological role of TMEM16F, this protein also conducts ionic current upon activation by Ca^{2+}. It has been shown that the scramblase activity and the current conduction of TMEM16F accompany each other, suggesting that ion transport in TMEM16F may be involved in the process of phospholipid transport [108]. High-

resolution structural studies show that the mouse TMEM16A molecule and the fungus phospholipid scramblase, nhTMEM16, adopt a similar structural architecture, including the conserved Ca^{2+}-binding sites [10, 96, 97, 103]. Nonetheless, the potential ion-transport pathways appear to be slightly different between these two molecules. In TMEM16A, the extracellular half of the ion-transport pathway is enclosed by several helices (see the left stereo pair in Fig. 2.1 B). On the other hand, the corresponding pathway in nhTMEM16 appears to be an open "aqueduct," in which the sidewall of the entire pathway is open (right stereo pair in Fig. 2.1 B). To understand the ion transport mechanisms of TMEM16 members with or without an enclosed pore, we compared the functional properties between TMEM16A and TMEM16F. In excised inside-out patches, both molecules conducted ionic currents almost immediately after Ca^{2+} was applied to the intracellular side of the membrane, although a delayed current activation of TMEM16F was previously reported in whole-cell recording conditions [108, 133]. An easily identified difference between the two molecules is that TMEM16A appears to be more sensitive to Ca^{2+} activation than TMEM16F. Only sub-micromolar $[Ca^{2+}]_i$ is required to open the pore of TMEM16A, while micromolar $[Ca^{2+}]_i$ is necessary to induce current in TMEM16F.

2.5.1 Roles of $K584_{16A}$ and $Q559_{16F}$ in the I-V curve rectification

Another difference between WT_{16A} and WT_{16F} is the rectification of their I-V curves. In symmetrical 140 mM $[Cl^-]$ with a saturated $[Ca^{2+}]_i$, the I-V

curve of WT_{16A} is linear (Fig. 2.2), while that of WT_{16F} is very outwardly rectifying (Fig. 2.5). Previous experiments have shown that when a positively charged residue, $K584_{16A}$ (in the "a" alternatively spliced variant, corresponding to $K588_{16A}$ in the "a, c" spliced variant), is mutated to glutamine, the linear I-V curve of WT_{16A} becomes outwardly rectifying in $K584Q_{16A}$ [106, 107]. Interestingly, WT_{16F}, which has an outwardly rectifying I-V curve, contains a glutamine residue at the corresponding position ($Q559_{16F}$). To understand the roles of $K584_{16A}$ and $Q559_{16F}$ in regulating the I-V curve rectification, we first examined if the outward rectification observed in $K584Q_{16A}$ resulted from the removal of a positive charge. We mutated $K584_{16A}$ into various amino acids and showed that the sidechain charge from the introduced residue correlated with the degree of outward rectification in TMEM16A—the more negative the sidechain charge, the more outwardly rectifying the I-V curve. We also adopted two other methods to change the sidechain charge: titrating the sidechain charge of a histidine residue with pH_i, and modifying the free thiol group of a cysteine residue by charged MTS reagents (Fig. 2.3). The results from these experiments support the idea of an electrostatic regulation of the I-V curve rectification in TMEM16A by the charge from residue 584. One somewhat surprising observation from MTS modification experiments of $K584C_{16A}$ is that the modification rates are slow, compared to the rates of modifying K519C of CLC-0. Although the position of $K584_{16A}$ appears accessible from the

intracellular aqueous solution based on the molecular structure of mouse TMEM16A, the MTS modification rates may be reduced by factors not favoring the modification. These factors, however, cannot be electrostatic in nature because both MTSES and MTSET modification rates are equally reduced. The interfering factors thus could be due to physical obstruction to reduce the accessibility of MTS reagents or due to a reduced reactivity of the thiol group of the introduced cysteine.

An electrostatic control of ion permeation in TMEM16A has recently also been reported through the analysis of I-V curve rectification in various saturation levels of the Ca^{2+}-binding site. It was concluded that binding of Ca^{2+} to the binding sites, which are located at the sidewall of the intracellular pore entrance near $K584_{16A}$, removes the electrostatic barrier for anion permeation exerted by those negatively-charged residues forming the binding sites [126]. Using a noise analysis approach, Lim et al. [106] have previously shown that the $K588Q_{16A}$ mutation (in the "a, c" isoform) reduces the TMEM16A channel conductance. Therefore, the mechanism of the electrostatic control from residue 584 is likely similar to that of K519 of CLC-0 in which replacing a positively charged residue with a neutral or a negatively charged residue at the intracellular pore entrance decreases the outward Cl^- flux [185, 186]. On the other hand, the side-chain charge on residue 559 of TMEM16F does not show a significant correlation with the I-V curve rectification. Mutating Q559 to negatively charged residues does not

change the RI of TMEM16F, while mutating Q559 to positively charged residues only slightly increases the RI. However, this small increase of the RI is not consistent with the results from the pH_i titration of $Q559H_{16F}$; lowering the pH_i (and thus increasing the positivity of a histidine sidechain) appears to decrease the RI in $Q559H_{16F}$ (Fig. 2.4). Therefore, there is no clear pattern of an electrostatic control of the I-V curve rectification by the sidechain charge of residue 559 in TMEM16F. Furthermore, we discovered that when Q559 is mutated to an aromatic amino acid, the RI significantly increases. For example, the value of the RI from 10 independent patches of $Q559W_{16F}$ ranged from 0.24 to 0.61, in comparison with the range of 0.01-0.23 from 15 independent recordings of WT_{16F}. To our knowledge, this is the first report that mutations of TMEM16F can alter the I-V curve rectification in TMEM16F. The finding supports the idea that ion transport in TMEM16F is more likely achieved through a specific structure, possibly involving the region near $Q559_{16F}$, rather than a non-specific leak. The results also support the idea that the open aqueduct in the lipid scramblase may mediate the ion transport [108, 109].

2.5.2 Rundown of TMEM16F alters the apparent Ca^{2+} affinity

Another unexpected finding from replacing Q559 with aromatic amino acids is that these mutants are resistant to $[Ca^{2+}]_i$-induced current rundown. The rundown of TMEM16 proteins has been well documented [115, 147,

190], and has been a hurdle in studying TMEM16 molecules. Previously, we adopted a three-pulse protocol to evaluate the apparent Ca^{2+} affinity of TMEM16A [115]. This method exposes the membrane patch to test and saturating $[Ca^{2+}]_i$ within ~10-15 s. Because the rundown of TMEM16A in such a time frame is minimal, normalizing the current induced by the test $[Ca^{2+}]_i$ to those obtained in saturating $[Ca^{2+}]_i$ provides a reasonably accurate determination of the current fraction activated by the test $[Ca^{2+}]_i$ [115]. For WT_{16F}, however, the current induced by a saturating $[Ca^{2+}]_i$ (900 μM) already shows prominent rundown within several seconds (Fig. 2.4). Therefore, the two saturated currents before and after the test $[Ca^{2+}]_i$ in the three-pulse protocol are always significantly different, creating uncertainty on the precision of the dose-response curve. Furthermore, Ye et al. [147] recently showed that the apparent $K_{1/2}$ of the rundown (or desensitized) TMEM16F for Ca^{2+} (~45 μM) was significantly higher than that of the TMEM16F before rundown (~7 μM), although the rundown of TMEM16A did not affect the apparent Ca^{2+} affinity of TMEM16A [97, 115]. Our finding that $Q559W_{16F}$ shows very little rundown for several minutes provides an excellent model for the pre-rundown TMEM16F. Indeed, we show that the $K_{1/2}$ of WT_{16F} obtained from using the three-pulse protocol was ~ 34 μM (Fig. 2.4 & Table 2.1), while the $K_{1/2}$ of $Q559W_{16F}$ mutant and other mutants with aromatic amino acids were ~ 2-10 μM (Fig. 2.7 & Table 2.1). This difference

in the apparent $K_{1/2}$ between WT_{16F} and aromatic mutants is likely due to a decrease of Ca^{2+} affinity in the rundown WT_{16F} molecules.

2.5.3 The rundown resistant mutation $Q559W_{16F}$ did not significantly alter ion permeation of TMEM16F

Previous studies have shown that TMEM16A conducts mostly anions, while TMEM16F is less discriminating of cations from anions [107, 108, 115]. Measuring E_{rev} for evaluating ion permeation functions, however, is not without challenges. In recording a large current, series resistance may render the measured E_{rev} inaccurate [142, 191], while determining the zero-current voltage for a highly rectified I-V curve could be less certain than for a more linear I-V curve. The I-V curves of TMEM16A and TMEM16F show different degrees of rectification. In saturating $[Ca^{2+}]_i$ and symmetrical 140 mM $[Cl^-]$, WT_{16A} has a linear I-V curve with an RI ($-I_{-80\ mV}/I_{+80\ mV}$) close to unity (Fig. 2.2), while the RI of WT_{16F} is very small, at ~0.05 (Fig. 2.5). If the inward current of WT_{16F} is further reduced (for example, by reducing the concentration of conducting ions), precise measurements of E_{rev} can be challenging (see Fig. 2.8 A, left panel). In mutants with an aromatic amino acid at position 559, the RI was between ~0.2-0.5, providing an I-V curve better than that of WT_{16F} for determining the zero-current voltage (compare left and right panels in Fig. 2.8 A). Although we were more confident on the

accuracy of the results measured from $Q559W_{16F}$ than from WT_{16A}, the values of E_{rev} obtained in reduced $[NaCl]_i$ and those in $[NaI]_i$ or $[NaSCN]_i$ ended up being reasonably similar for WT_{16F} and $Q559W_{16F}$ (Fig. 2.8, B and D). This indicates that the $Q559W_{16F}$ mutations did not significantly alter the ion permeation functions of TMEM16F. The results also affirm the previous conclusion that TMEM16F does not selectively conduct Cl^-. One concern in our TMEM16F experiments of reducing $[NaCl]_i$ is that the two ions used to replace the reduced $[NaCl]_i$ (namely, $NMDG^+$ and SO_4^{2-}) may permeate through TMEM16F. We chose to use $(NMDG)_2SO_4$ to replace the reduced [NaCl] so that the results obtained here can be directly compared with those from our previous studies on TMEM16A (see Fig. 2.8 B). For the experiments of assessing anion permeation, we did not use $NMDG^+$ or SO_4^{2-}, and thus the comparison of bi-anion potentials (and thus the anion selectivity) may be more direct. The results show that the anion selectivity of WT_{16F} and $Q559W_{16F}$ still follows the type I Eisenman sequence [192], namely, $P_{SCN} > P_I > P_{Cl,}$ similar to the previous observations in TMEM16F [133] and in TMEM16A [115, 193].

2.5.4 Conclusion and Speculation

The I-V curve rectification presented here are more interpretable for TMEM16A than for TMEM16F. TMEM16A appears to be a classical ligand-gated anion channel. It is reasonable that $K584_{16A}$ exerts an electrostatic

control on the outward Cl^- flux, because numerous studies have documented that a charge alteration at the pore entrance can increase or decrease the ion flux [185, 186, 194, 195]. In TMEM16F, however, the mechanisms underlying the change of rectification and underlying the rundown resistance in mutants with aromatic residues at position 559 remain obscure. A recent study by Ye et al. [147] suggests that the rundown of TMEM16F may involve phospholipids. Furthermore, it has been proposed that the ion conduction pathway of TMEM16 proteins is partly composed of lipids [196], and molecular dynamic studies of the fungus TMEM16 protein suggest that the lipid bilayer is deformed near the aqueduct [109, 144]. The existing literature thus prompts us to speculate whether the aromatic amino acids we placed at position 559 of TMEM16F may alter the interaction of phospholipids with the protein molecule. If so, are phospholipids also present in the intracellular vestibule of TMEM16A, and does the very low MTS modification rate of $K584C_{16A}$ result from obstruction by nearby phospholipids? It will require further studies to explore these speculations and to understand the role of phospholipids in the ion transport of TMEM16 molecules.

2.6 Acknowledgement

We thank Drs. Robert Fairclough, Tzyh-Chang Hwang, Takashi Kurahashi and Hiroko Takeuchi for helpful discussion and critical reading of the manuscript. This work was supported by an NIH grant R01GM065447,

and by the Jong L. Chen Family Neuroscience Research Fund. Additionally, we thank Osaka University's International Joint Research Promotion Program for providing international travel support. The authors declare no competing financial interests.

2.7 Supplementray material

Fig. 2.S1 shows MTS ET modification effects of K584C16A after pre-exposing the mutant channels to MTS ES intracellularly.

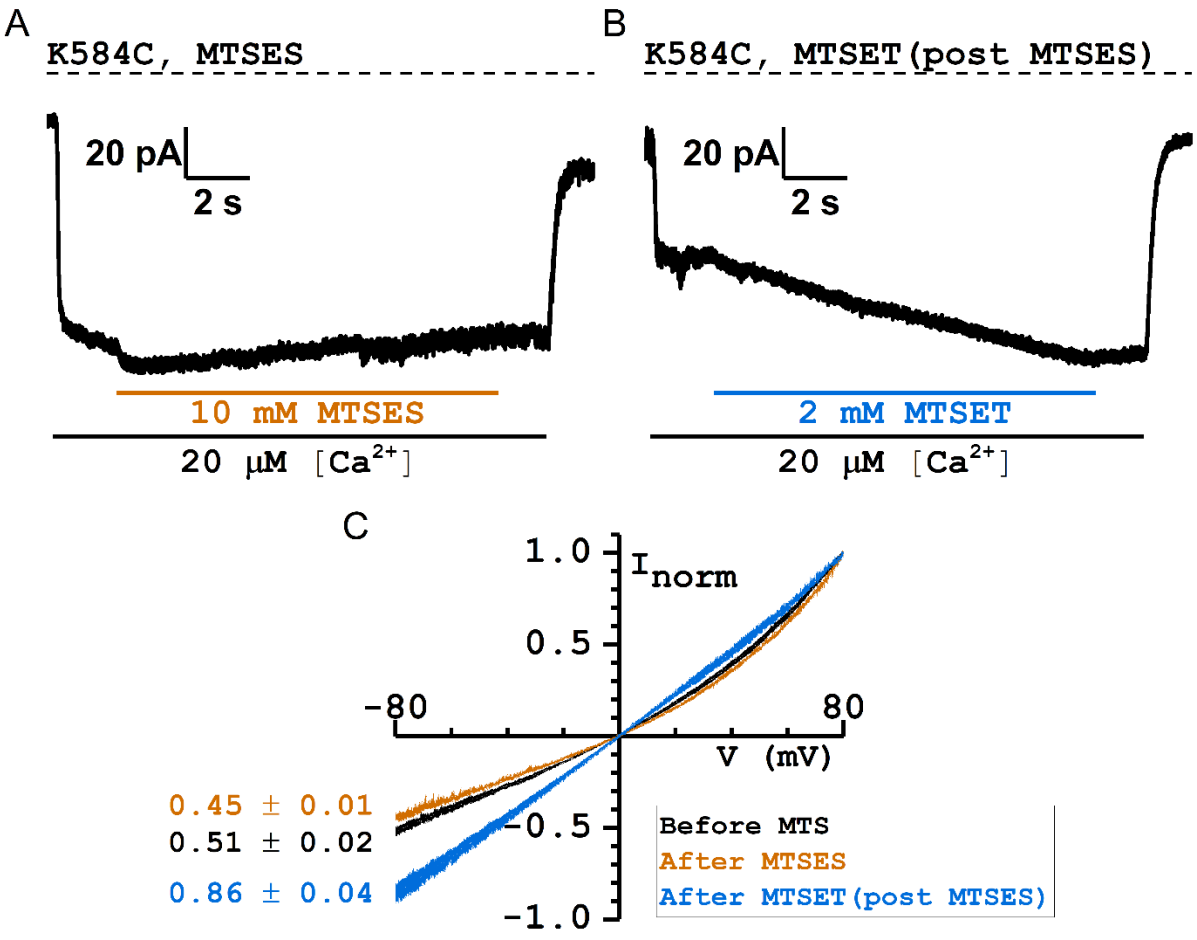

Figure 2.S1. MTSET modification effects of $K584C_{16A}$ after pre-exposing the mutant channels to MTSES intracellularly. (A) Representative recording trace

of MTSES modifications of $K584C_{16A}$ at -40 mV. (B) Recording trace of intracellular MTSET modification of $K584C_{16A}$ (same patch as that shown in A) after the patch was treated with 10 mM MTSES for 12 sec. (C) Averaged I-V curves of $K584C_{16A}$ before MTS modification *(black)*, after MTSES modification *(orange)*, and after MTSET modification, post-MTSES treatment *(blue)*. The values of RI (mean ± SEM, n = 3) are displayed next to each I-V curve.

Chapter 3: Cobalt Ion Interaction with TMEM16A Calcium-Activated Chloride Channel: Inhibition and Potentiation

Dung M. Nguyen[1], Louisa S. Chen[1], Grace Jeng[1], Wei-Ping Yu[1] and Tsung-Yu Chen[1,2]

[1] Center for Neuroscience, University of California, Davis, California, United States of America

[2] Department of Neurology, University of California, Davis, California, United States of America

This chapter has been adapted from a publication in *PLoS ONE* (Volume 15, issue 4).

3.1 Abstract

TMEM16A, a Ca^{2+}-sensitive Cl^- channel, plays key roles in many physiological functions related to Cl^- transport across lipid membranes. Activation of this channel is mediated via binding intracellular Ca^{2+} to the channel with a relatively high apparent affinity, roughly in the sub-μM to low μM concentration range. Recently available high-resolution structures of TMEM16 molecules reveal that the high-affinity Ca^{2+} activation sites are formed by several acidic amino acids, using their negatively charged sidechain carboxylates to coordinate the bound Ca^{2+}. In this study, we examine the interaction of TMEM16A with a divalent cation, Co^{2+}, which by itself cannot activate current in TMEM16A. This divalent cation, however, has two effects when applied intracellularly. It inhibits the Ca^{2+}-induced TMEM16A current by competing with Ca^{2+} for the aforementioned high-

affinity activation sites. In addition, Co^{2+} also potentiates the Ca^{2+}-induced current with a low affinity. This potentiation effect requires high concentration (mM) of Co^{2+}, similar to our previous findings that high concentrations (mM) of intracellular Ca^{2+} ($[Ca^{2+}]_i$) can induce more TMEM16A current after the Ca^{2+}-activation sites are saturated by tens of μM $[Ca^{2+}]_i$. The degrees of potentiation by Co^{2+} and Ca^{2+} also roughly correlate with each other. Interestingly, mutating a pore residue of TMEM16A, Y589, alters the degree of potentiation in that the smaller the sidechain of the replaced residue, the larger the potentiation induced by divalent cations. We suggest that the Co^{2+} potentiation and the Ca^{2+} potentiation share a similar mechanism by increasing Cl^- flux through the channel pore, perhaps due to an increase of positive pore potential after the binding of divalent cations to phospholipids in the pore. A smaller sidechain of a pore residue may allow the pore to accommodate more phospholipids, thus enhancing the current potentiation caused by high concentrations of divalent cations.

3.2 Introduction

The TMEM16 gene family consists of two types of transmembrane proteins with distinct molecular functions: ion channels and phospholipid scramblases [176, 177]. TMEM16A, the first identified member in this gene family [6-8], is a Ca^{2+}-activated Cl^- channel. It is highly expressed in the apical membrane of ductal epithelial cells, and one well-documented physiological function of this channel known for decades is its critical roles in

transepithelial Cl^- transport [3]. Another Ca^{2+}-activated Cl^- channel from the TMEM16 family is TMEM16B, which helps transduce odor stimuli into electrical signals in olfactory receptor neurons [43, 178]. Physiologically, these two anion channels conduct Cl^- across the lipid membrane in response to sub-μM or low μM concentrations of intracellular Ca^{2+} ($[Ca^{2+}]_i$). The other type of TMEM16 family members, such as fungus nhTMEM16, afTMEM16 and mammalian TMEM16F, are phospholipid scramblases. One documented physiological role of TMEM16F is to scramble phospholipids in platelet cell membranes and thus expose phosphatidylserine to the extracellular environment, an important step in the signaling cascade for blood coagulation [9, 66, 108]. A defect in the scrambling activity of TMEM16F has been known to result in a bleeding disorder called Scott syndrome [9, 180]. Interestingly, activation of phospholipid scramblases by $[Ca^{2+}]_i$ not only leads to scrambling of membrane phospholipids but also causes ionic conduction across lipid membranes. The physiological roles of the current conduction in these phospholipid scramblases remain to be identified.

Although the physiological functions of ion channels and phospholipid scramblases appear to be quite different, the structures of these two types of TMEM16 proteins are similar to each other [10, 90, 95-97, 103]. These TMEM16 molecules are homodimeric proteins [101], with 10 transmembrane helices (helix 1-10) present in one subunit. In each subunit, helices 3-8 form a conduit thought to be the pathway for the substrate (ions or

phospholipids) transport across lipid membranes (Fig 3.1). Structural studies of fungus TMEM16 proteins (such as nhTMEM16 and afTMEM16) show that the conduit thought to be the substrate-transport pathways appears as an open groove [10, 90], raising the possibility that phospholipid transport may resemble swiping a credit card through a card reader [10, 108, 109, 144, 197]. However, recent cryo-EM studies on the mammalian TMEM16F protein revealed that the extracellular half of helix 4 (the helix colored in orange in Fig 3.1) slants more towards the transport pathway than the corresponding helix in fungus scramblases [95, 198], and therefore the extracellular half of the transport pathway appears to be fully enclosed by helices 3-8 (Fig 3.1A). The intracellular half of the transport pathway in mammalian TMEM16F, however, is still open, making room for membrane phospholipids to contribute to the wall-lining. This structure of the transport pathway in mammalian TMEM16F, namely, an enclosed ion-permeation conduit only in the extracellular half of the pathway is shared by TMEM16A (Fig 3.1B), which functions as a conventional ion channel but not a phospholipid scramblase [96, 97, 103]. The implication from the pore structures of various TMEM16 molecules with respect to their abilities of transporting phospholipids remains to be determined [95, 198].

A

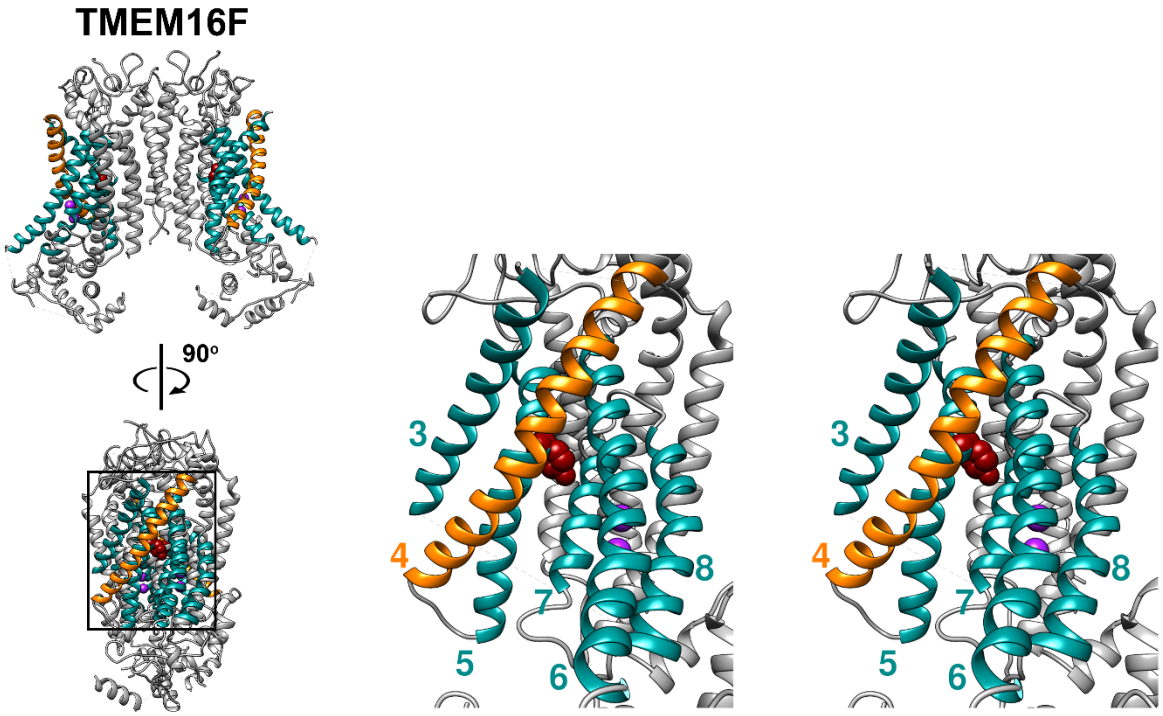

B

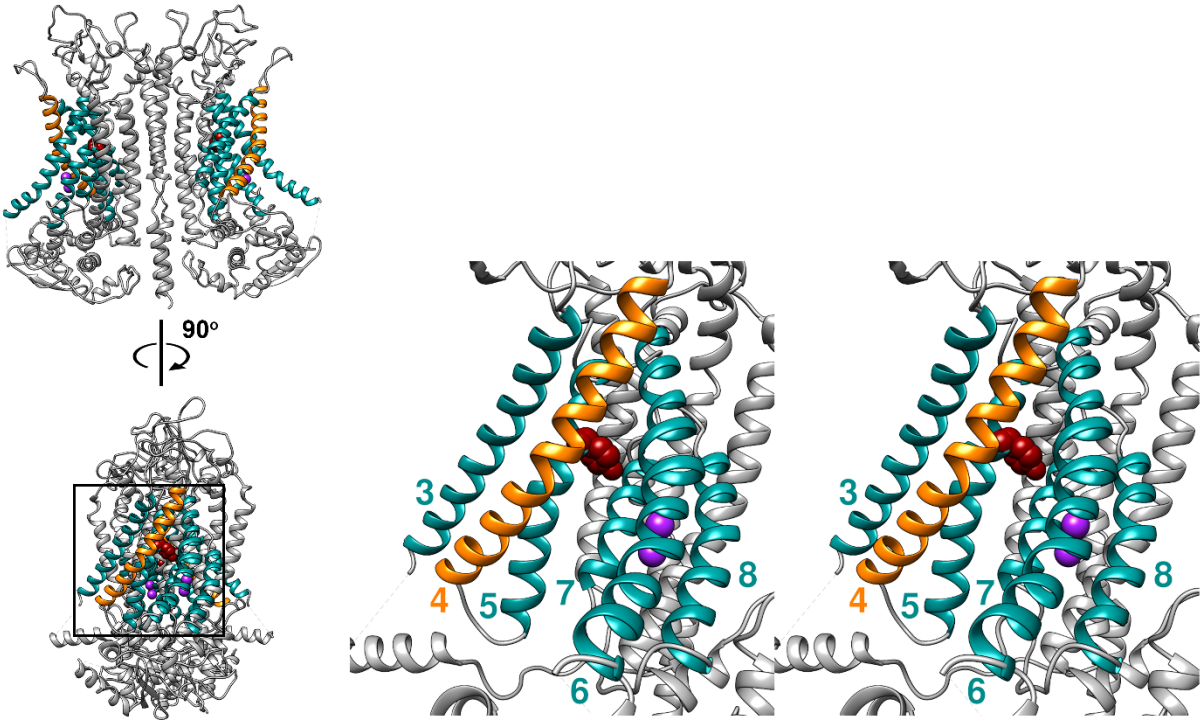

Fig 3.1. Structures of TMEM16A and TMEM16F with bound Ca^{2+}. (A) TMEM16F structure (PDB: 6QPC). (B) TMEM16A structure (PDB: 5OYB). On the left part of both A & B, the top view is from within the phospholipids for seeing both subunits. The view below is obtained by rotating the structure 90° clockwise around the two-fold axis. The boxed area in the lower view is expanded on the right using a stereo pair, and the subunit in the back is hidden for clarity. Purple spheres represent calcium ions, and the space-filled residue in red represents Y589 of TMEM16A or Y564 of TMEM16F. Helices in color are labeled with numbers representing the six transmembrane helices (TM3-8) encompassing the transport pathway.

In addition to the transport pathways for anions and phospholipids, the Ca^{2+}-activation sites have also been identified in the high-resolution structures of TMEM16 molecules [10, 90, 95-97, 103, 198]. In both types of TMEM16 molecules, each protein subunit possesses two Ca^{2+}-binding sites, in which several acidic residues use their sidechain carboxylates to coordinate the bound Ca^{2+}. Functional studies have shown that activation of one subunit of TMEM16A still generates a dose-response activation curve with a Hill coefficient greater than unity [107], consistent with the structural findings that multiple Ca^{2+} can bind to the activation sites of a subunit and that one subunit contains one pore. Mutations of these acidic residues dramatically alter the half-effective Ca^{2+} concentration ($[Ca^{2+}]$) in activating

the channel—mutation of a single glutamate or aspartate residue increases the intracellular [Ca^{2+}] ([Ca^{2+}]$_i$) required for channel activation by three orders of magnitude [104, 105, 107]. Thus, coordination of Ca^{2+} in the channel activation sites by multiple carboxylates from these acidic residues underlies the relatively high apparent affinity of Ca^{2+} in activating the channel. In TMEM16A, it has been shown that Ca^{2+} binding to the activation sites can also have an effect on ion permeation—the binding reduces the negative charge from these acidic Ca^{2+}-coordinating residues, thus altering the rectification of the Cl^- flux through the channel pore [126]. This is consistent with the structural finding that the Ca^{2+} activation sites are located not far from the pore. Our previous experiments also showed that altering the sidechain charge of a pore residue affects the rectification of the I-V curve, directly supporting an electrostatic control of Cl^- flux in the pore [107, 125].

While the structural features reasonably explain some of the molecular properties of the TMEM16 proteins, the mechanisms of other functional phenomena of TMEM16 molecules remain unclear. For example, the biphasic dose-response activation curve for the activation of TMEM16A by Ca^{2+} is still puzzling [106, 107]. It is well documented that intracellular Ca^{2+} activates TMEM16A with a half-activation concentration in the range of sub-μM to low μM [8, 99, 115, 117]. Therefore, the activation of TMEM16A should be saturated by 10-20 μM [Ca^{2+}]$_i$. Yet, if [Ca^{2+}]$_i$ is increased to hundreds of μM

or to mM concentrations, TMEM16A current can be further increased—the current induced by 20 mM $[Ca^{2+}]_i$ was ~30-40 % larger than that activated by 20 μM $[Ca^{2+}]_i$ [106, 107]. If the Ca^{2+}-activation sites have already been saturated by 20 μM $[Ca^{2+}]_i$, what is the mechanism responsible for the current induced by mM $[Ca^{2+}]_i$? Is the current induced by mM $[Ca^{2+}]_i$ mediated by different Ca^{2+}-activation sites or is the mechanism of this low affinity Ca^{2+} effect mediated by the high affinity Ca^{2+}-binding sites formed by the aforementioned negatively-charged residues? To further examine the properties of TMEM16A, we initially aimed at using cobalt ions (Co^{2+}), to interact with the channel activation sites on this Cl^- channel. We found that intracellular Co^{2+} is a competitive inhibitor for the Ca^{2+} activation of TMEM16A. The experiments also lead to a serendipity finding that high concentrations (hundreds of μM or above) of intracellular Co^{2+} ($[Co^{2+}]_i$) potentiate the Ca^{2+}-induced TMEM16A current. The results suggest that the TMEM16A current potentiation by mM $[Co^{2+}]_i$ and that by mM $[Ca^{2+}]_i$ described above may come from the same mechanism, thus explaining the biphasic dose-dependent activation curve of TMEM16A. Interestingly, mutating a pore residue of TMEM16A affects the degree of potentiation, suggesting that the relatively low affinity potentiation site(s) for these two cations may reside in or near the anion transport pathway.

3.3 Materials and Methods

3.3.1 Reagents and cDNA clones

The cDNA of the "*a*" alternative splice variant [99] of the TMEM16A (NCBI reference sequence: NM_001242349.1), subcloned in the pEGFP-N3 or pIRES expression vector (Clontech/Takara Bio), was used throughout the study. The cDNA constructs produced channels with (from the pEGFP-N3 construct) or without (from the pIRES construct) a green fluorescent protein (GFP) attached to the C terminus of the channel proteins. The results obtained from the GFP-tagged and un-tagged TMEM16A were not distinguishable. To create mutations, the QuikChange II Site-Directed Mutagenesis Kit (Agilent Technologies) was used according to manufacturer's instruction. Channel expression was achieved by transiently transfecting the channel cDNAs to human embryonic kidney (HEK) 293 cells using the lipofectamine transfection method [107, 115, 142]. Under an inverted microscope (DM IRB; Leica) equipped with a fluorescent light source and a GFP filter (Chroma Technology), HEK293 cells expressing transfected channels were identified by the green fluorescence from the cells. The chemicals used in this study were all reagent grade. Regular salts such as NaCl and $CoCl_2$ were obtained from MilliporeSigma and MP Medicals. HEPES was obtained from Sigma/Aldrich.

3.3.2 Electrophysiological methods

Twenty-four to forty-eight hours after transfection, patch-clamp recordings were conducted on HEK293 cells with green fluorescence. All experiments were from excised inside-out membrane patches. The pipette (extracellular) solution contained 140 mM NaCl, 10 mM HEPES, and 0.1 mM EGTA (pH 7.4). This solution was also used as the intracellular solution containing "zero Ca^{2+}." For the intracellular solutions containing specified $[Ca^{2+}]_i$, EGTA was not included because of two considerations. First, including a Ca^{2+} buffer (such as EGTA) in solutions containing both Ca^{2+} and Co^{2+} would alter the free concentration of each ion in a complicated manner. Second, most of the solutions used in this study contained $[Ca^{2+}]_i$ in μM to mM range, which is way beyond the buffering range of EGTA. Without the added EGTA, the free $[Ca^{2+}]_i$ was assumed to be equal to the total added $[Ca^{2+}]_i$. Nonetheless, it should be noticed that when the indicated $[Ca^{2+}]_i$ was low (such as 2 or 5 μM), the real $[Ca^{2+}]_i$ was likely slightly higher because of the contaminating Ca^{2+}. Based on the current of a TMEM16F mutant induced by an intraceullar solution containing neither EGTA nor Ca^{2+}, the contaminating $[Ca^{2+}]_i$ in this nominal zero-Ca^{2+} solution was less than 1 μM (see 3.S1 Fig.). Such a small contaminating $[Ca^{2+}]_i$ should not alter the major conclusions in this paper as most of our experiments were performed on the TMEM16A current induced by much higher $[Ca^{2+}]_i$. All intracellular solutions also contained 10 mM HEPES (pH 7.4) and had a final $[Cl^-]$ of 140

mM. In the experiments of assessing Co^{2+} effects, the intracellular solutions contained Co^{2+} up to 20 mM. Because the source of Co^{2+} was from $CoCl_2$, the concentration of NaCl in the intracellular solution was reduced according to the extra $[Cl^-]$ from the added $[CoCl_2]$. For example, the solution containing 20 mM $[Co^{2+}]$ included 100 mM [NaCl] and 20 mM $[CoCl_2]$. In experiments using high $[Ca^{2+}]_i$, the intracellular [NaCl] was also adjusted accordingly if the total $[CaCl_2]$ in the solution was more than 0.5 mM. These adjustments, likely would alter the ionic strength of the solution, and therefore, the measurements obtained with high divalent cation concentrations (such as 5 - 20 mM) may be less accurate.

The recording electrodes were made from borosilicate glass capillaries (World Precision Instruments) using a PP830 electrode puller (Narishige). The electrode tip was ~1-2 μm in diameter, and the electrode resistance was between ~1.5 MΩ and ~3 MΩ when filled with the extracellular solution. Voltage clamp experiments were conducted using the Axopatch 200B amplifier (Molecular Devices), and the current was digitized via a Digidata1440 analog-digital signal-converting board controlled by the pClamp10 software (Molecular Devices). Exchanging solutions on the intracellular side of the excised inside-out patch was achieved using the SF-77 solution exchanger (Warner Instruments). Except where indicated, the recording was initiated by stepping the membrane voltage to ±20 mV in the EGTA-containing zero-Ca^{2+} solution. $[Ca^{2+}]_i$ was then applied to open the

TMEM16A channel, followed by the application of a particular $[Co^{2+}]_i$ (with the same $[Ca^{2+}]_i$) for 6 sec, which allowed the Co^{2+} effect to reach a steady state. Co^{2+} was then removed by changing the solution back to the one before applying $[Co^{2+}]_i$. Finally, the intracellular Ca^{2+} was removed using the EGTA-containing zero-Ca^{2+} solution. In evaluating the kinetics of the current activation or deactivation upon applying or removing $[Ca^{2+}]_i$ (such as those in Fig 3.4), the recordings were made in the presence of the indicated $[Co^{2+}]_i$ throughout the whole recording course. For these experiments, $[Co^{2+}]_i$ was first applied, and the voltage was then stepped to ±20 mV followed by applying and then removing $[Ca^{2+}]_i$ in the presence of the same $[Co^{2+}]_i$.

To assess the current potentiation by high $[Ca^{2+}]_i$, we employed a three-pulse protocol described previously [115]. The cytoplasmic side of the patch was sequentially exposed to a control solution containing 20 μM $[Ca^{2+}]_i$, a test solution containing $[Ca^{2+}]_i$ from 50 μM to 20 mM, and then again the 20 μM $[Ca^{2+}]_i$ solution. We used this experimental protocol to minimize the effect of current rundown so that a dose-response effect of the test $[Ca^{2+}]_i$ can be more precisely evaluated. The current induced by the test $[Ca^{2+}]$ was then normalized to the average of the two currents obtained in 20 μM $[Ca^{2+}]$, and the normalized values were used for generating dose-response curves.

3.3.3 Data Analysis

We analyzed the experimental data using the combination of pClamp (Molecular Devices) and Origin (OriginLab, Co.) software. For data analyses, the background leak current in the absence of $[Ca^{2+}]$ was first subtracted from the current obtained in the presence of $[Ca^{2+}]_i$. Upon the application of $[Co^{2+}]_i$, the Ca^{2+}-induced current of TMEM16A was potentiated almost immediately followed by a slower process of inhibition. We named I_0 as the control current immediately before the application of $[Co^{2+}]_i$. The peak of the current potentiation was defined as I_{peak}, while the current measured at the end of the 6-sec Co^{2+} application was defined as I_{Co}. We performed the same experiments on the wild-type (WT) TMEM16A channel as well as on more than 10 point mutants of residue Y589. To evaluate the degrees of potentiation and inhibition, a Co^{2+} potentiation coefficient was calculated by dividing I_{peak} by I_0, while a Co^{2+} inhibition coefficient was calculated by I_{Co}/I_{peak}. All averaged results are presented as mean ± S.E.M.

To analyze the dependence of the degree of inhibition on $[Co^{2+}]$, the values of I_{Co}/I_{peak} were plotted against $[Co^{2+}]_i$, and the dose-dependent Co^{2+} inhibitions were fitted to a Langmuir equation to evaluate the apparent Co^{2+} affinity:

$$I_{norm} = \frac{I_{Co}}{I_{peak}} = \frac{1}{1+\frac{[Co^{2+}]}{K_{1/2}}} \qquad (1)$$

where $K_{1/2}$ is the fitted half-inhibition concentration. For the current potentiation, because the potentiation effect appeared to be voltage dependent and because the effect of the highest $[Co^{2+}]_i$ (20 mM) at +20 mV appeared unsaturated, we did not fit the $[Co^{2+}]_i$-dependent potentiation to any type of binding isotherm equations. The data points were connected by line segments.

To evaluate the apparent Ca^{2+}-dissociation rate from the Ca^{2+}-activation site, the time course of the current reduction upon the final washout of $[Ca^{2+}]_i$ was fit to a single-exponential decay function:

$$I(t)=(I_{peak}\text{-}I_{Co})\times\left(1\text{-}\exp\left(-\frac{t}{\tau_{off}}\right)\right) \qquad (2)$$

where I(t) is the TMEM16A current at time t and the meaning of I_{peak} and I_{Co} are as defined above. The time constant of the current reduction process (τ_{off}) was used to correlate with the degrees of Co^{2+} inhibition or Co^{2+} potentiation. Two other parameters, the sidechain hydrophobicity and the molecular volume of the amino acid placed at position 589, were also used to correlate with the Co^{2+} inhibition or the Co^{2+} potentiation. The values of the sidechain hydrophobicity and the molecular volume of the amino acid were obtained, respectively, from Kyte and Doolittle [199] and Zamyatnin [200].

3.4 Results

Examples of the intracellular Co^{2+} effects on the WT TMEM16A are shown in Fig 3.2. Intracellular Co^{2+} (up to 20 mM) by itself does not activate any current in WT TMEM16A (Fig 3.2A, left panel), while a robust current can be induced by intracellular Ca^{2+} from the same membrane patch (Fig 3.2A, right panel). However, as illustrated by the recording traces shown in Fig 3.2B, intracellular Co^{2+} (from 50 μM to 5 mM shown in these traces) appears to have dual effects on the Ca^{2+}-induced TMEM16A current. In these recordings, TMEM16A currents were first activated by 30 μM $[Ca^{2+}]_i$. Upon applying $[Co^{2+}]_i$ (in the presence of 30 μM $[Ca^{2+}]_i$), the currents were first potentiated, then inhibited, although the potentiation of the current by 50 μM Co^{2+} was not observed. It appears that the degrees of the current potentiation and inhibition depend on $[Co^{2+}]_i$.

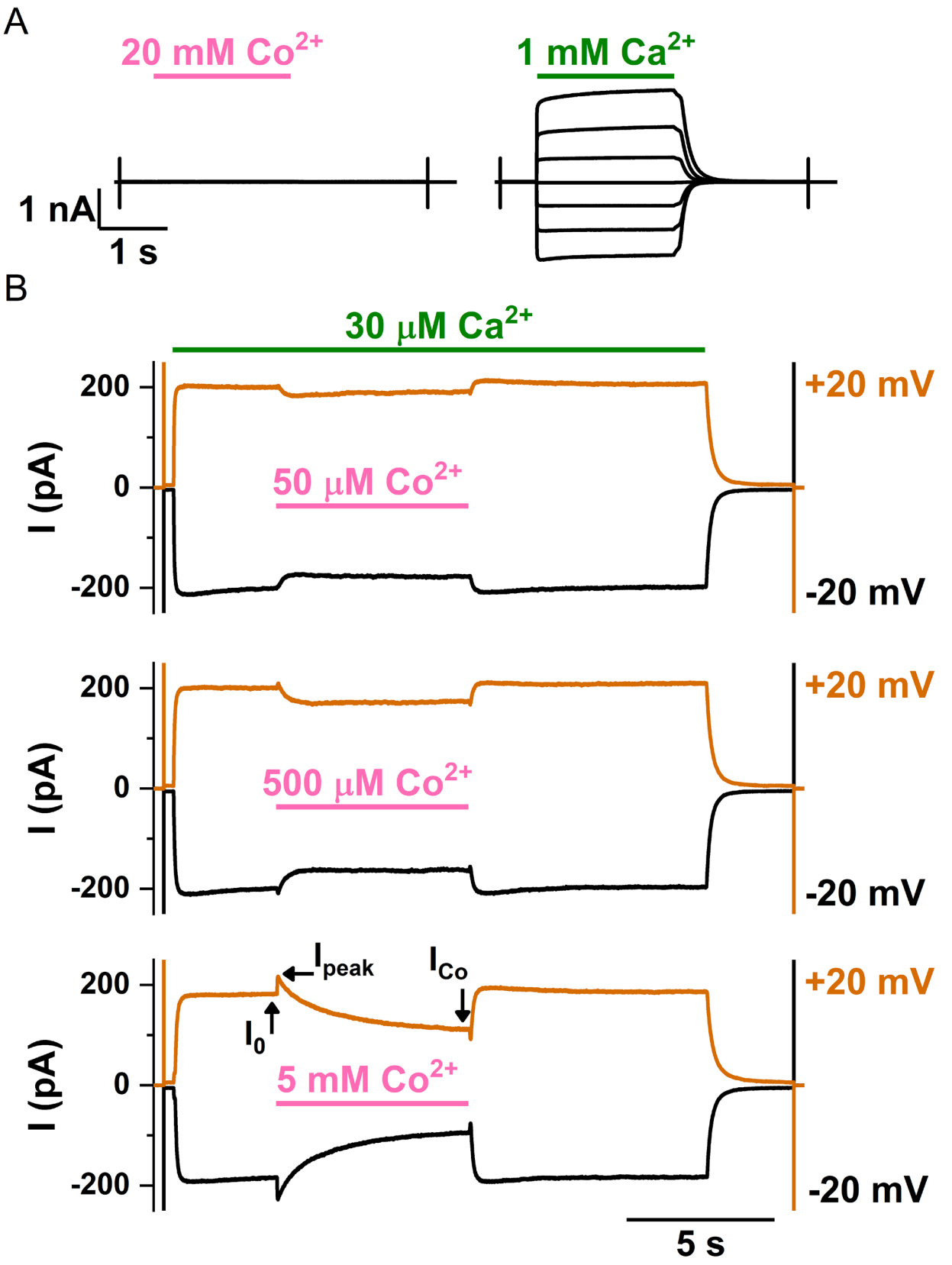
A
20 mM Co2+
1 mM Ca2+
1 nA
1 s
B
30 μM Ca2+
200
0
-200
I (pA)
50 μM Co2+
+20 mV
-20 mV
500 μM Co2+
5 mM Co2+
Ipeak
ICo
I0
5 s

Fig 3.2. Effects of Co^{2+} on the WT TMEM16A channel. (A) Effects of intracellular Co^{2+} (left) and Ca^{2+} (right) when applied alone. The membrane voltage began at 0 mV, and was then stepped from -60 mV to +60 mV in +20 mV steps. $[Co^{2+}]_i$ (pink line) and $[Ca^{2+}]_i$ (green line) were applied as indicated on the same membrane patch. (B) Effects of various $[Co^{2+}]_i$ on the TMEM16A current activated by 30 μM $[Ca^{2+}]_i$. The membrane voltage was 0 mV at the start of the recording and then stepped to -20 mV (black traces) and +20 mV (orange traces), respectively, at the time indicated by the capacitive spikes. $[Ca^{2+}]_i$ (30 μM) was then applied, followed by applying Co^{2+} in the presence of the same $[Ca^{2+}]_i$ as indicated by horizontal lines. I_{peak}, I_0 and I_{Co} are defined as in the Data Analysis section in METHODS.

To understand the Co^{2+} effects on TMEM16A, we first examined the mechanism of inhibition. Fig 3.3A shows Co^{2+} inhibition on the TMEM16A current activated by different saturating concentrations of $[Ca^{2+}]_i$ (from 10-300 μM). Although $[Co^{2+}]_i$ in all these recordings is the same (2 mM), the degree of inhibition decreases with an increase of $[Ca^{2+}]_i$ used for activating the current. Fig 3.3B shows that at both +20 mV (upper panel) and -20 mV (lower panel), the $K_{1/2}$ of $[Co^{2+}]_i$-dependent inhibition (shown in Table 3.1) was shifted in parallel to higher values by increased $[Ca^{2+}]_i$. These results suggest that Co^{2+} may inhibit the current by competing with Ca^{2+} for the activation sites. This competition can also be directly appreciated from the

kinetics of TMEM16A current induction by $[Ca^{2+}]_i$. Fig 3.4A and 3.4B show two sets of the TMEM16A current activation time course in the presence of 0, 0.5, 2, and 5 mM $[Co^{2+}]_i$. Both the rate of the current activation upon applying $[Ca^{2+}]_i$ and that of the current reduction after removing $[Ca^{2+}]_i$ are decreased in the presence of $[Co^{2+}]_i$. Thus, Co^{2+} slows down the kinetics of Ca^{2+} binding to the activation sites.

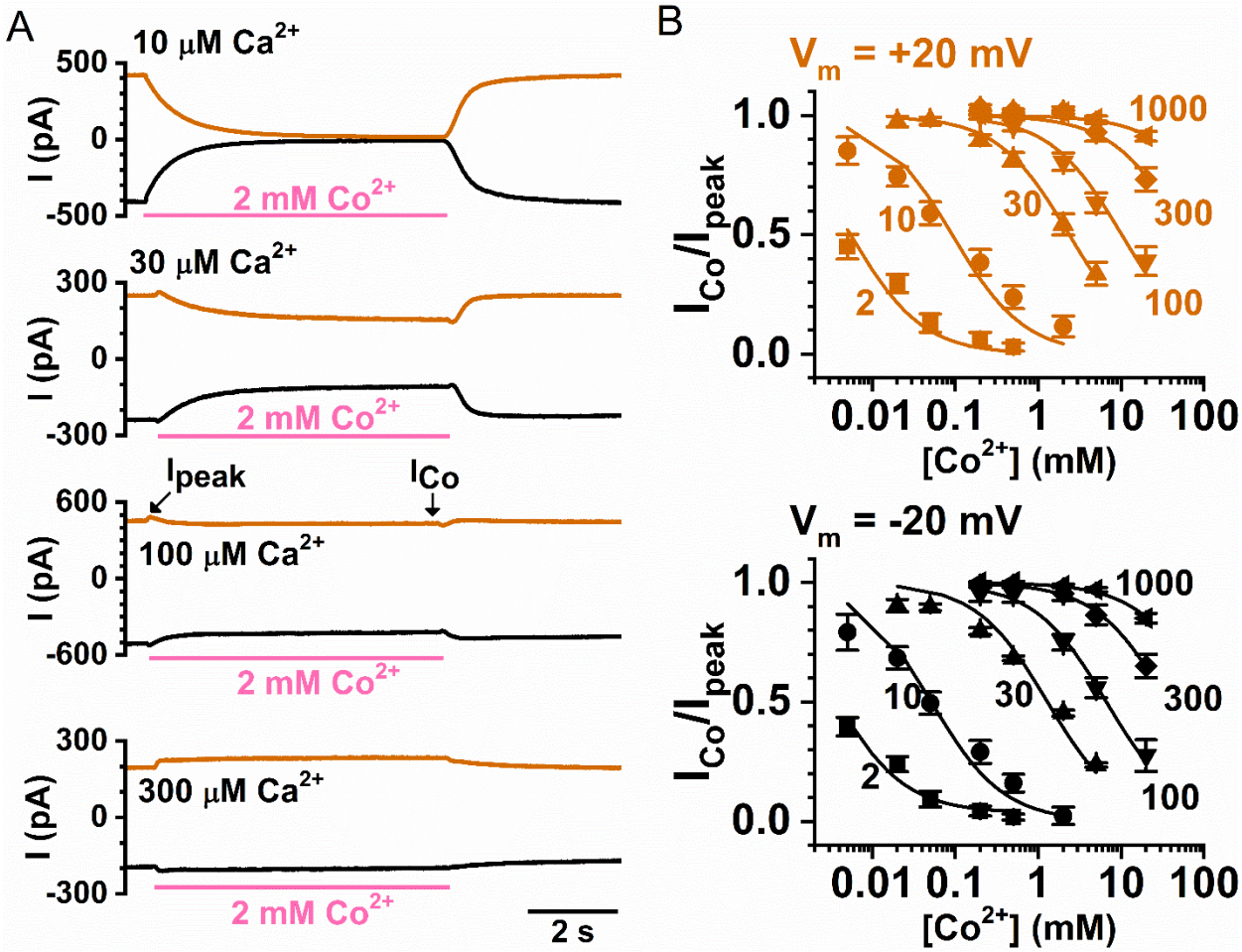

Fig 3.3. Competitive inhibition by Co^{2+} on $[Ca^{2+}]_i$-induced TMEM16A current. (A) Inhibition by 2 mM Co^{2+} of the TMEM16A current activated by

various $[Ca^{2+}]_i$ at -20 mV (black) and +20 mV (orange). **(B)** Concentration-dependent Co^{2+} inhibition of the TMEM16A current activated by various $[Ca^{2+}]_i$ at +20 mV (upper panel) and -20 mV (lower panel). Numbers next to each individual dose-response curves represent the $[Ca^{2+}]_i$ (in μM) used in activating the current. Data points were fitted to the Langmuir function defined in METHODS (Eq 1). The fitted $K_{1/2}$ values of Co^{2+} inhibition at -20 mV and +20 mV in various $[Ca^{2+}]_i$ are presented in Table 3.1.

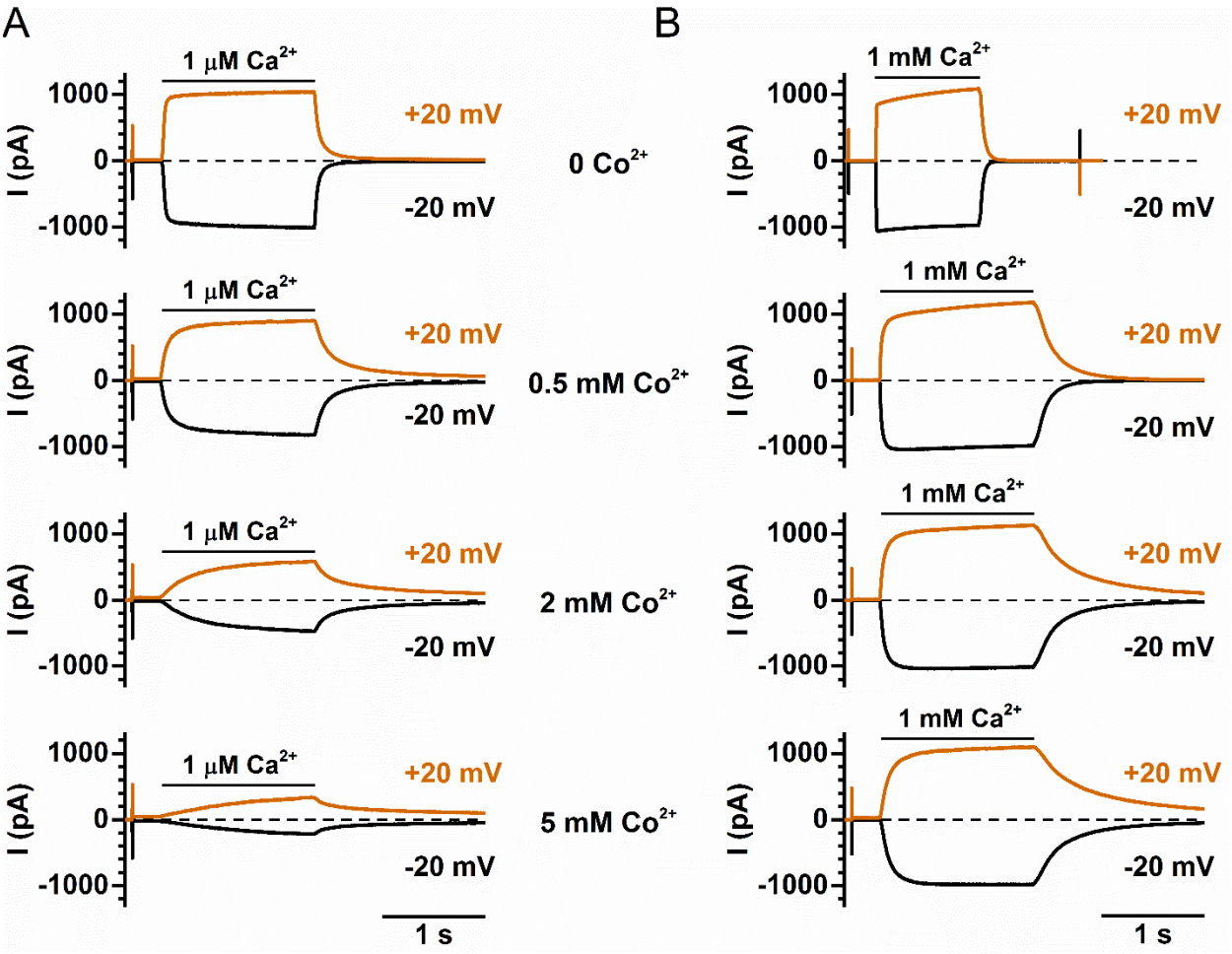

Fig 3.4. Effects of Co^{2+} on the kinetics of TMEM16A activation/deactivation. The indicated $[Co^{2+}]_i$ was present throughout the entire recording period in all recordings. TMEM16A current was induced by (A) 1 μM $[Ca^{2+}]_i$ and (B) 1 mM $[Ca^{2+}]_i$. All recording traces in A were from the same patch, while the recording traces in B were from another patch. Notice intracellular Co^{2+} slows down the current activation upon applying $[Ca^{2+}]_i$ and the current reduction upon $[Ca^{2+}]_i$ washout in a dose-dependent way. At the same time Ca^{2+} antagonizes the effects of Co^{2+} on the activation/deactivation kinetics. Similar results were observed in another 4 patches (two patches each with 1 μM $[Ca^{2+}]_i$ and 1 mM $[Ca^{2+}]_i$).

Table 3.1. $K_{1/2}$ of Co^{2+} inhibition of the TMEM16A current induced by various $[Ca^{2+}]_i$.

$[Ca^{2+}]_i$ (μM)	$K_{1/2}$ (mM) of Co^{2+} inhibition	
	-20 mV	+20 mV
2	0.003 ± 0.001	0.005 ± 0.001
10	0.05 ± 0.01	0.09 ± 0.02
30	1.3 ± 0.2	2.4 ± 0.1
100	6.6 ± 0.4	10 ± 1.1
300	36 ± 1.3	59 ± 9.6
1000	118 ± 7	223 ± 37

If Co^{2+} and Ca^{2+} compete for the Ca^{2+}-activation sites, the potency of Co^{2+} inhibition may decrease in mutant channels with slower Ca^{2+} dissociation rates. This indeed appears to be the case. Fig 3.5A depicts

recording traces of applying 50 μM, 500 μM, and 5 mM $[Co^{2+}]_i$ to a TMEM16A mutant, Y589A, while Fig 3.5B shows a comparison of the $[Co^{2+}]_i$-dependent inhibition curves between WT TMEM16A and the Y589A mutant at -20 mV (upper panel) and +20 mV (lower panel), respectively. The Y589A mutant has been reported to have a greater apparent affinity for Ca^{2+} activation than WT channels [97]. Our recordings show that the rate of the current reduction upon $[Ca^{2+}]_i$ removal in this mutant is significantly slower (τ_{off} of the current reduction process is larger) than in the WT channel (Fig 3.5C), consistent with a greater Ca^{2+} affinity in this mutant. In comparison with the effect on the WT channel, a higher $[Co^{2+}]_i$ is required to inhibit the Y589A current induced by the same concentration of $[Ca^{2+}]_i$. Meanwhile, the degree of current potentiation by $[Co^{2+}]_i$ is larger in Y589A than in the WT channel (Fig 3.5D). We thus constructed more mutants of Y589 and analyzed Co^{2+} inhibition more extensively. Fig 3.6 depicts recording traces of the Co^{2+} effects in ten Y589 mutants. These Y589 mutants have different Ca^{2+} dissociation rates as judged from the current reduction time (τ_{off}) after removing $[Ca^{2+}]_i$ near the end of the recordings. For example, the current reduction upon washout of $[Ca^{2+}]_i$ appears slower in Y589G, Y589S, Y589V, and Y589C than in Y589W, Y589H, Y589F and Y589K (Fig 3.6).

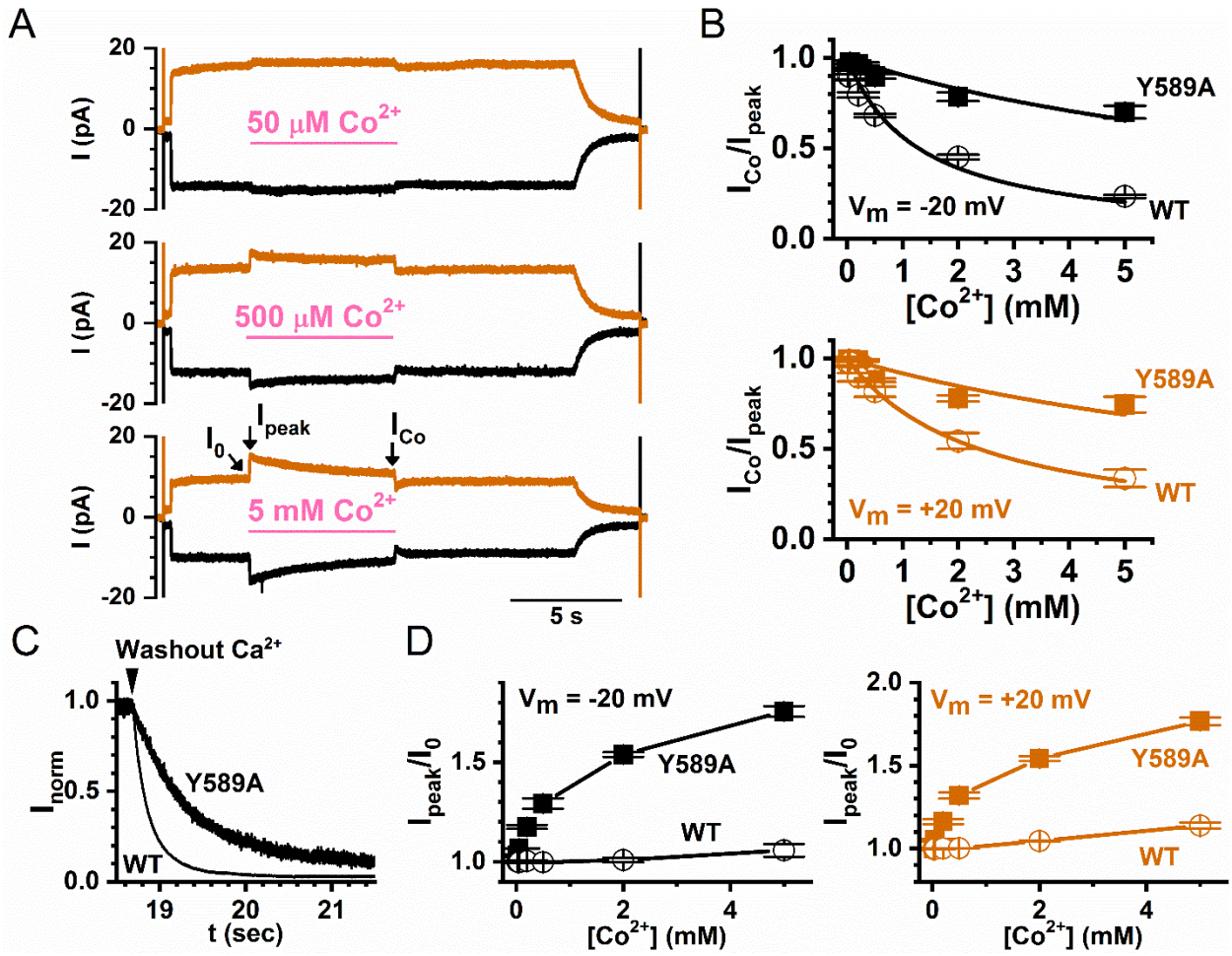

Fig 3.5. Comparing Co^{2+} effects between WT TMEM16A and the Y589A mutant. (A) Effects of various $[Co^{2+}]_i$ on the Y589A mutant. $[Ca^{2+}]_i$ = 30 μM for all patches. (B) Comparison of the dose-response curves of Co^{2+} inhibition between WT TMEM16A and the Y589A mutant. (C) Representative traces comparing the current-reduction process upon washout of $[Ca^{2+}]_i$ at +20 mV between WT TMEM16A and the Y589A mutant. Recorded currents were normalized to the current right before the washout of $[Ca^{2+}]_i$. The current reduction processes were fitted to Eq 2 with the averaged τ_{off} of 144 ± 5 ms (n = 6) and 601 ± 29 ms (n = 4) for the WT channel and the Y589A

mutant, respectively. (D) Comparison of the dose-response curves of Co^{2+} potentiation between WT TMEM16A and the Y589A mutant at -20 mV (left) and +20 mV (right).

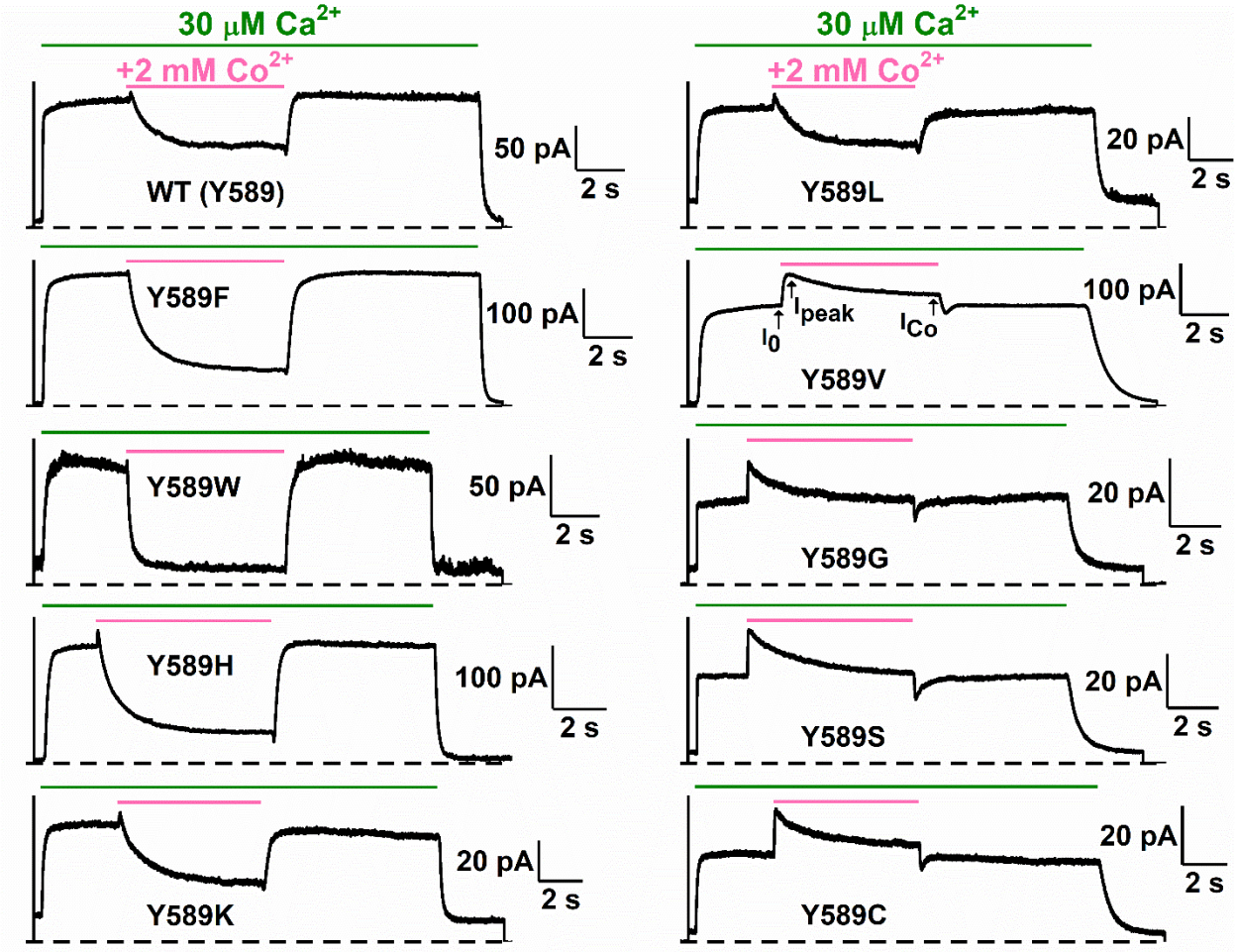

Fig 3.6. Dependence of Co^{2+} inhibition on the current reduction time (τ_{off}) upon Ca^{2+} washout. Recording traces illustrate the effects of 2 mM Co^{2+} on various Y589 mutants activated by 30 μM $[Ca^{2+}]_i$ at +20 mV. Dissociation rates of Ca^{2+} were evaluated from the current reduction process upon Ca^{2+} washout at the end of each recording by fitting the current

reduction process with a single-exponential decay function (Eq 2). Notice that the degree of Co^{2+} inhibition was reduced with the increase of the time constant (τ_{off}) of the current reduction upon removing $[Ca^{2+}]_i$ (see correlation plot in the left panel of Fig 3.7A).

The correlations between Co^{2+} inhibition and the current reduction time (τ_{off}) are shown in Fig 3.7A and 3.7B (left panel). Plotting the fraction of remaining current after 2 mM Co^{2+} inhibition (I_{Co}/I_{peak}) against the value of τ_{off} confirms that the potency of Co^{2+} inhibition decreases with the increase of τ_{off}; namely, the slower the Ca^{2+} dissociation rate, the weaker the Co^{2+} inhibition. We also correlated the Co^{2+} inhibition (I_{Co}/I_{peak}) obtained at +20 mV (Fig 3.7A) and at -20 mV (Fig 3.7B) against two other parameters: the sidechain hydrophobic index (Fig 3.7A and B, middle panel) and the molecular volume (Fig 3.7A and B, right panel) of the amino acid at position 589. Visual inspection of these correlation plots suggests that Co^{2+} inhibition decreases with the increase of τ_{off} (Fig 3.7A and B, left panel), while the correlations of Co^{2+} inhibition with the sidechain hydrophobicity Fig 3.7A and B, middle panel) and with the molecular volume (Fig 3.7A and B, right panel) are weak. The inverse correlation of the potency of Co^{2+} inhibition with the Ca^{2+}-dissociation rate supports the idea that Co^{2+} and Ca^{2+} compete for the high-affinity Ca^{2+}-activation sites on the channel.

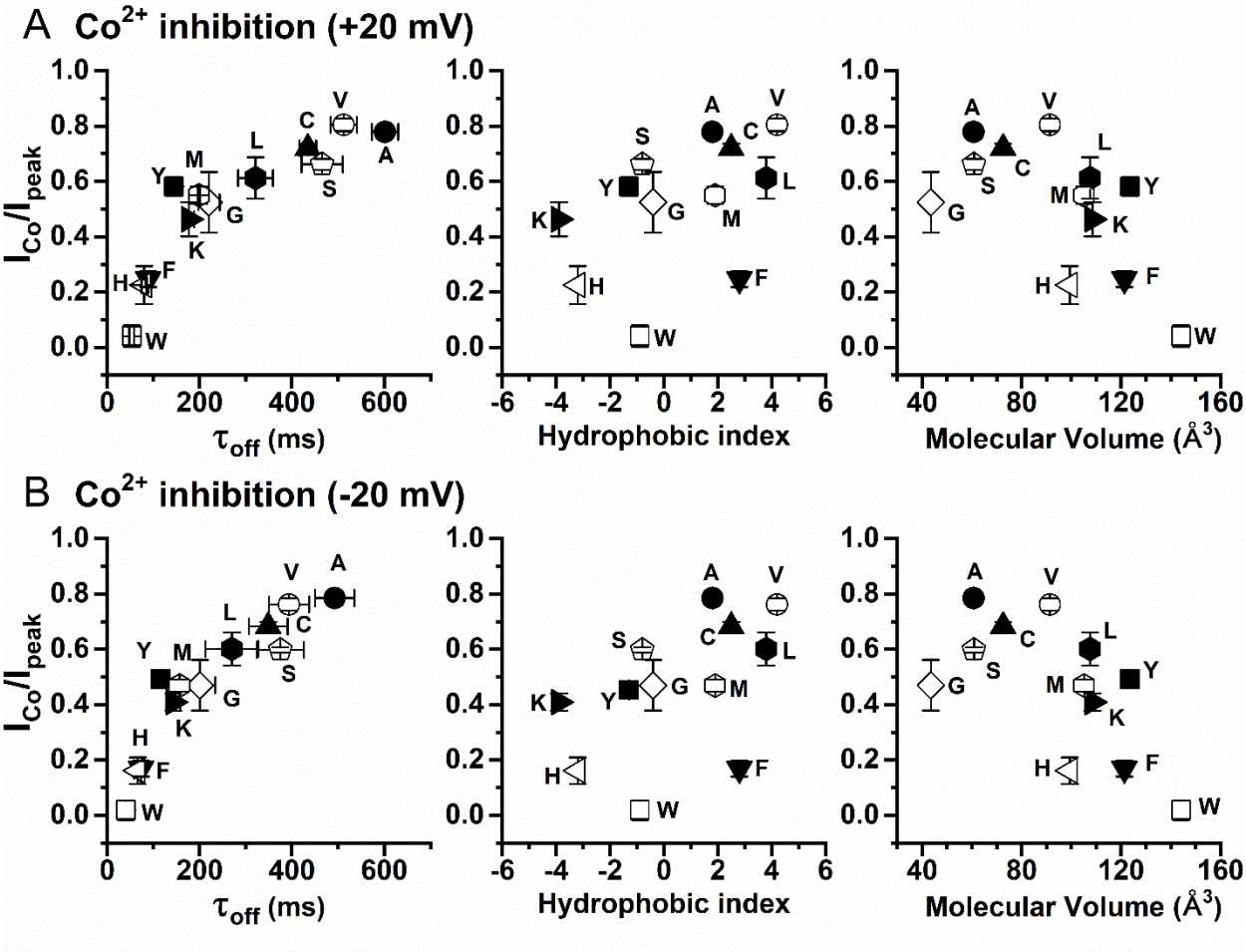

Fig 3.7. Correlation of Co^{2+} inhibition with τ_{off}, the hydrophobicity index, or the molecular volume of the amino acid placed at position 589. Here, experiments were similar to those shown in Fig 3.6. the remaining current fraction after 6-sec Co^{2+} application (I_{Co}/I_{peak}) was calculated and was plotted against the three different parameters. (A) Results obtained at +20 mV. (B) Results obtained at -20 mV. All data points were obtained from the effects of 2 mM $[Co^{2+}]_i$ on the WT TMEM16A current induced by 30 μM $[Ca^{2+}]_i$.

As shown in the original recording traces (for example, see Fig 3.2B or 3.6), intracellular Co^{2+} also potentiates the channel current. To extend data analyses, we also plot the degree of potentiation against the τ_{off} of current deactivation, the sidechain hydrophobicity, and the molecular volume of the introduced amino acid at position 589 (Fig 3.8). Unexpectedly, the potentiation was found to correlate best with the molecular volume of the amino acid—the Co^{2+} potentiation was larger in mutants with a smaller amino acid sidechain at position 589 (Fig 3.8A and 3.8B, right panel). On the other hand, the correlations between the degree of Co^{2+} potentiation with τ_{off} (Fig 3.8A and 3.8B, left panel) and with the sidechain hydrophobicity (Fig 3.8A and 3.8B, middle panel) were weak.

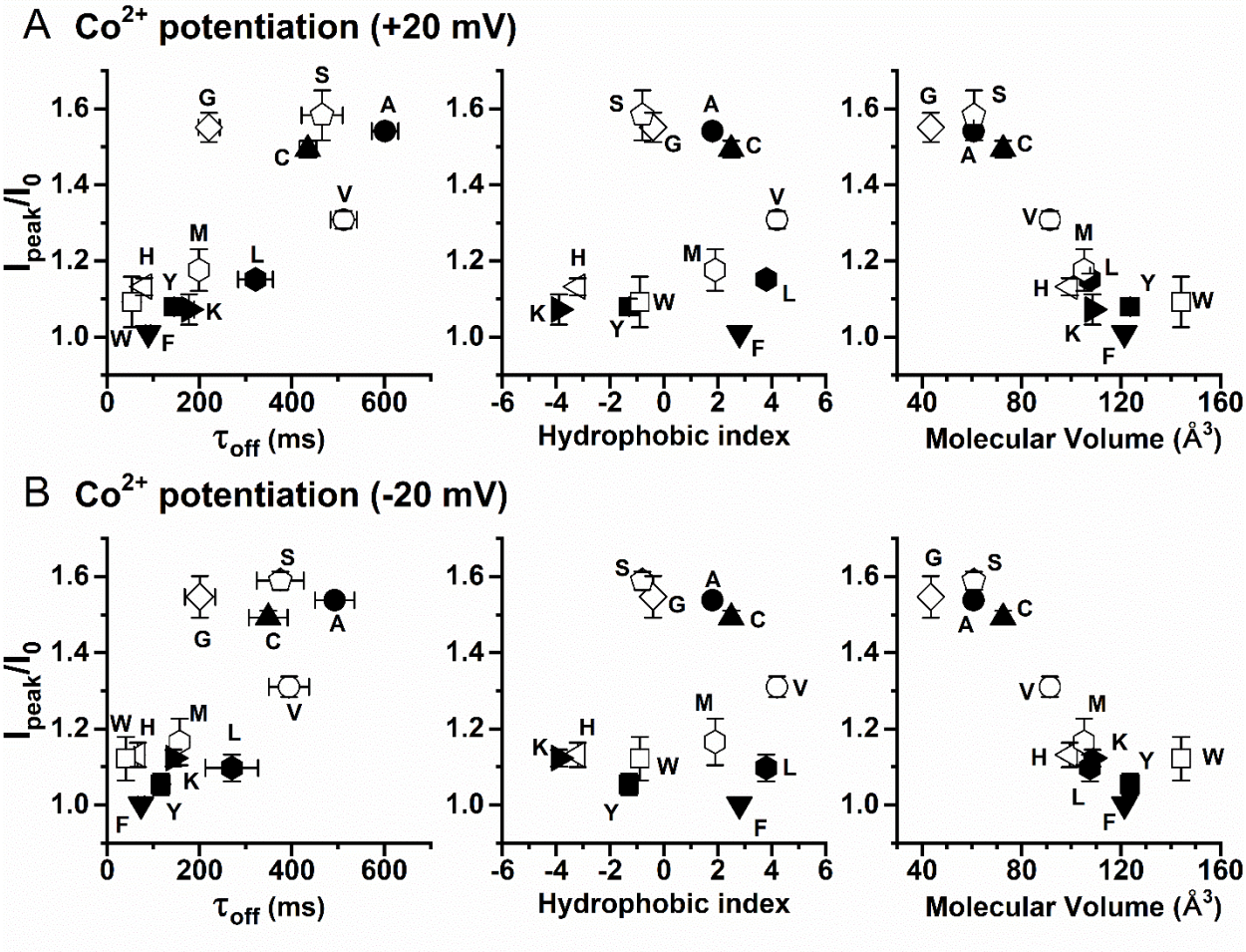

Fig 3.8. Correlation of Co^{2+} potentiation with τ_{off}, the hydrophobicity index, or the molecular volume of the amino acid at position 589. (A) Results obtained at +20 mV. (B) Results obtained at -20 mV. All data points were obtained from the effects of 2 mM $[Co^{2+}]_i$ on the 30 μM $[Ca^{2+}]_i$-induced TMEM16A current. The degree of Co^{2+} potentiation was defined as I_{peak}/I_0. Notice a rough correlation between the potentiation and the volume of the amino acid placed at position 589—the larger the side-chain volume, the smaller the Co^{2+} potentiation.

To study the Co^{2+} potentiation more closely, we examined the concentration-dependent effect of Co^{2+}. For the recording traces shown in Fig 3.9A, the WT TMEM16A currents were respectively induced by 100, 300 and 1000 μM $[Ca^{2+}]_i$. $[Co^{2+}]_i$ of various concentrations were applied at +20 mV (orange traces) and -20 mV (black traces), and the concentration-dependent Co^{2+} potentiation was shown in Fig 3.9B. The potentiation was minimal at sub-mM $[Co^{2+}]_i$. At the highest $[Co^{2+}]_i$ (20 mM), the potentiation was ~10% and ~35-45% of the control current at -20 mV and +20 mV, respectively. The results reveal a voltage dependence of Co^{2+} potentiation: the degree of potentiation at +20 mV is significantly larger than that at -20 mV, with this voltage-dependent difference most clearly observed at $[Co^{2+}]_i$ = 20 mM. It is also clear from these results that the affinity of Co^{2+} for the potentiation effect is low—the potentiation effect at +20 mV was not saturated even at 20 mM $[Co^{2+}]_i$! At -20 mV, the dose-dependent curve appears to have an apparent half-effective concentration of several mM.

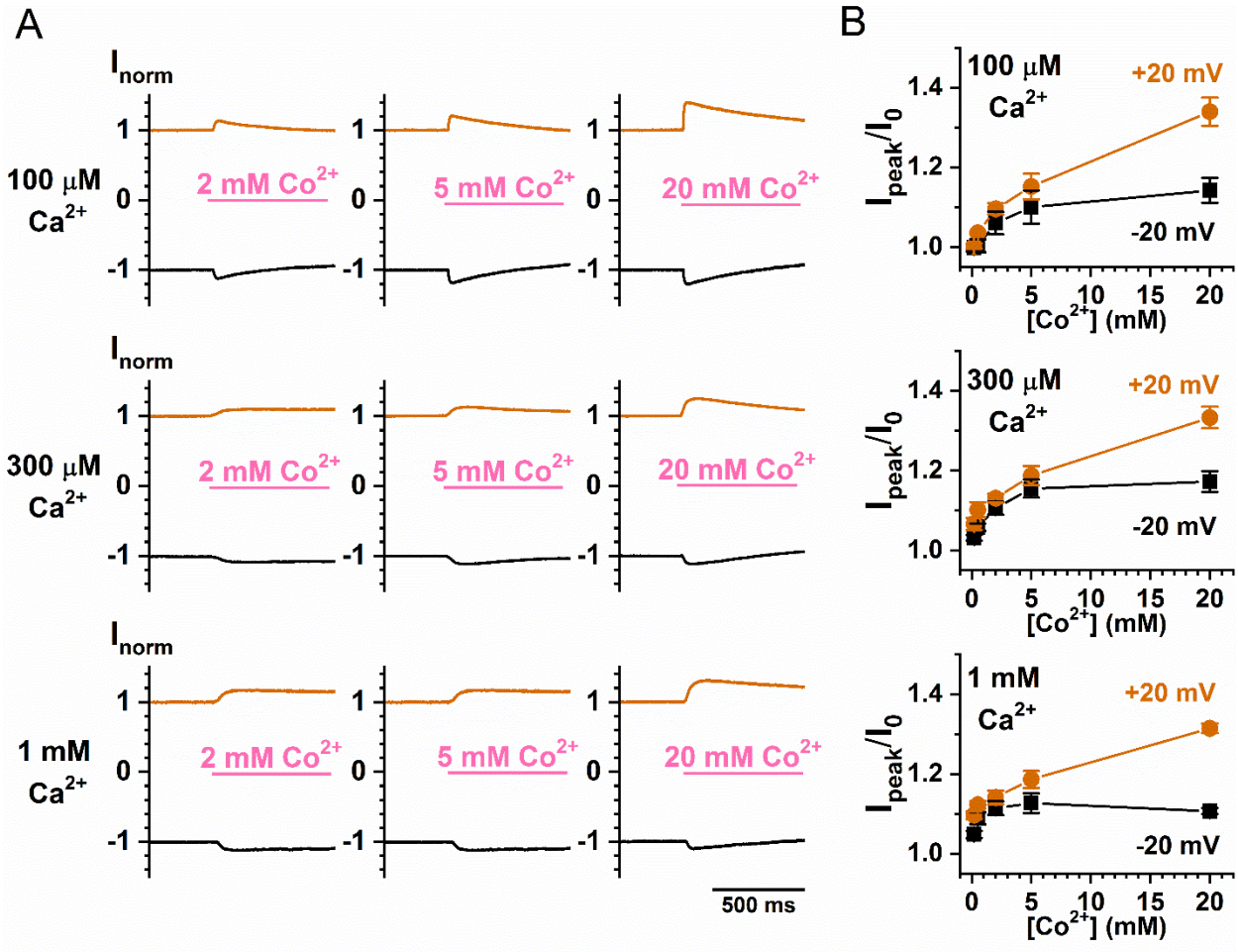

Fig 3.9. Dose-dependent Co^{2+} potentiation of the WT TMEM16A current. (A) Recording traces depicting Co^{2+} potentiation of the TMEM16A current activated by 100 μM, 300 μM, and 1 mM $[Ca^{2+}]_i$, respectively. To focus on the Co^{2+} potentiation effect, only the traces from 450 ms before to 550 ms after the application of Co^{2+} are shown. (B) Averaged Co^{2+} potentiation of the WT TMEM16A current as a function of $[Co^{2+}]_i$. Notice the difference in the degree of potentiation between the experiments at -20 mV and +20 mV.

The observation that mM $[Co^{2+}]_i$ is required for potentiation is reminiscent of the finding that $[Ca^{2+}]_i$ in the mM concentration range induces more TMEM16A current even though the channel opening has already been saturated by low μM $[Ca^{2+}]_i$ [106, 107]. The dose-response curve of Ca^{2+} activation of TMEM16A thus appeared as biphasic. Fig 3.10A shows an experiment on the WT TMEM16A, using the three-pulse protocol to compare the current induced by high $[Ca^{2+}]_i$ (2 or 20 mM) with that by 20 μM $[Ca^{2+}]_i$, a concentration thought to already saturate the high-affinity Ca^{2+}-activation sites [8, 99, 115, 117]. The recording traces reveal that the current induced by 2 or 20 mM $[Ca^{2+}]_i$ is significantly larger than the current induced by 20 μM $[Ca^{2+}]_i$. Furthermore, the current reduction process upon removing mM $[Ca^{2+}]_i$ shows two exponential decays, and the remaining current after the first exponential decay matches the amplitude of the current induced by 20 μM $[Ca^{2+}]_i$. These recording traces thus indicate that the current induced by mM $[Ca^{2+}]_i$ likely consists of two different components. We suspected that the extra current induced by mM $[Ca^{2+}]_i$ may have the same underlying mechanism for the Co^{2+} potentiation as both potentiation effects are mediated by relatively low-affinity binding of these two divalent cations (mM concentrations). Accordingly, we examined the high $[Ca^{2+}]_i$-induced current in various Y589 mutants more closely. The exemplary recording traces shown in Fig 3.10B indicate that the current reduction of the Y589A mutant upon washout of $[Ca^{2+}]_i$ also consists of two components: a fast and a slow

current-decaying component. The fraction of the fast current-decaying component (the low-affinity component) is larger than that in the WT channel, consistent with a larger Co^{2+} potentiation in Y589A than in the WT channel. The dose-response curves of Ca^{2+} potentiation in the WT channel and in various Y589 mutants obtained with high $[Ca^{2+}]_i$ (from 50 μM to 20 mM) are depicted in Fig 3.11. In comparison with the potentiation on the WT channel (which has a tyrosine residue at 589 position), some mutants (such as Y589A, Y589C, and Y589W) show greater potentiation, and some have a similar degree of potentiation (such as Y589H and Y589L) while others show a smaller effect. To compare the potentiation by Ca^{2+} and Co^{2+}, we plot the potentiation by 20 mM $[Ca^{2+}]_i$ (relative to the current induced by 20 μM $[Ca^{2+}]_i$) against the potentiation by 20 mM $[Co^{2+}]_i$ (the current was activated by 300 μM $[Ca^{2+}]_i$) for all the Y589 mutants we have created (Fig 3.12). The results show that the Ca^{2+} potentiation and the Co^{2+} potentiation are roughly correlated with each other—the higher the Ca^{2+} potentiation, the larger the Co^{2+} potentiation. These results suggest that Ca^{2+} and Co^{2+} may act through the same mechanism to generate the potentiation effects.

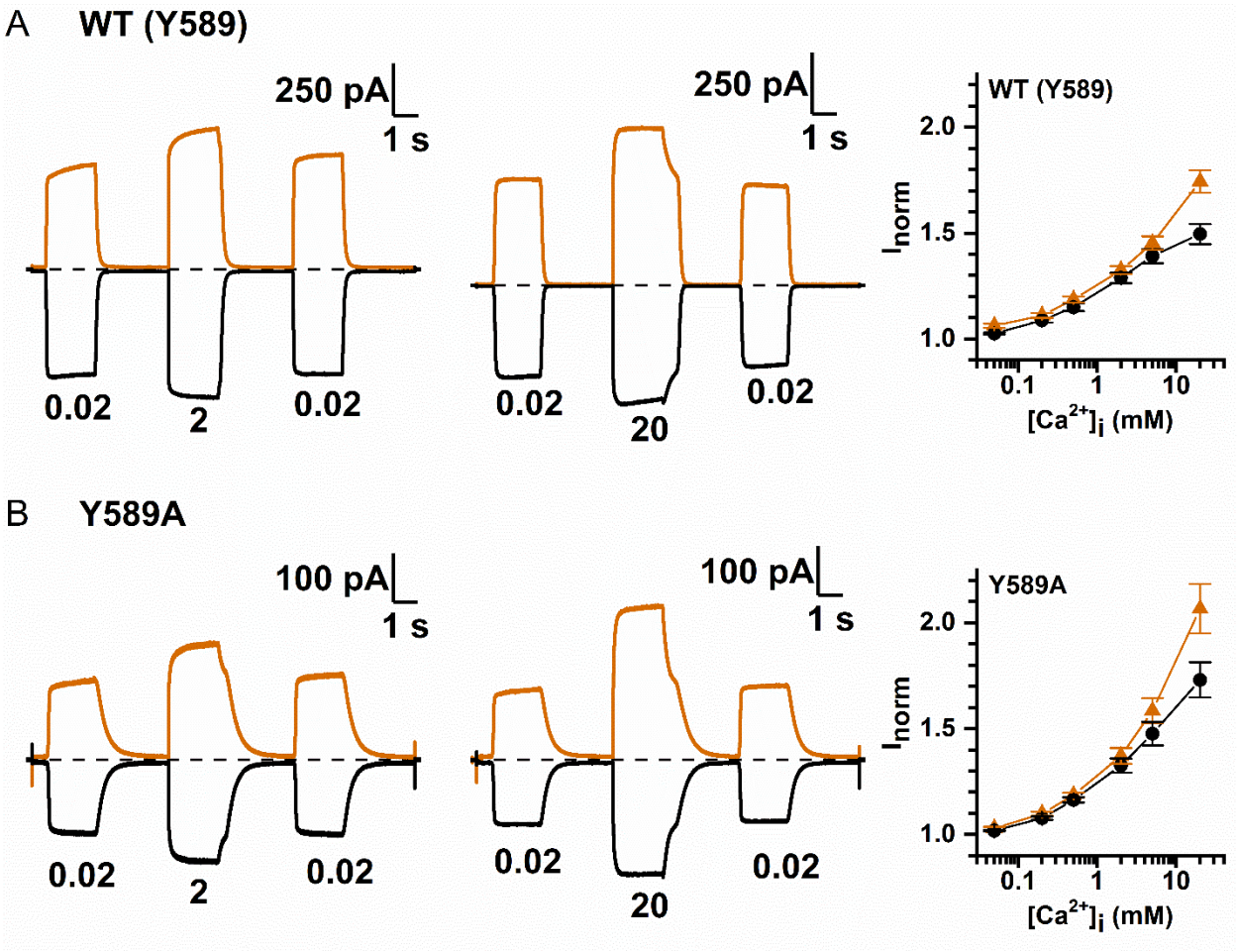

Fig 3.10. Potentiation of TMEM16A current by mM concentrations of $[Ca^{2+}]_i$. Recording traces of (A) WT TMEM16A and (B) Y589A. Both panels show a larger current induced by 2 mM (left panel) or 20 mM $[Ca^{2+}]_i$ (middle panel) than that induced by 20 μM $[Ca^{2+}]_i$. Numbers below each pulse represent $[Ca^{2+}]_i$ in mM. Orange and black traces are from +20 mV and -20 mV, respectively. Notice the fast and the slow current reduction upon washout of 2 or 20 mM $[Ca^{2+}]_i$. Right panels show dose-dependent Ca^{2+} potentiation of WT TMEM16A and Y589A at ±20 mV compared to the current induced by 20 μM $[Ca^{2+}]_i$. Current activated by various test $[Ca^{2+}]_i$ (middle

pulse) was normalized to the average of the control currents at 20 μM $[Ca^{2+}]_i$ before and after the test $[Ca^{2+}]_i$.

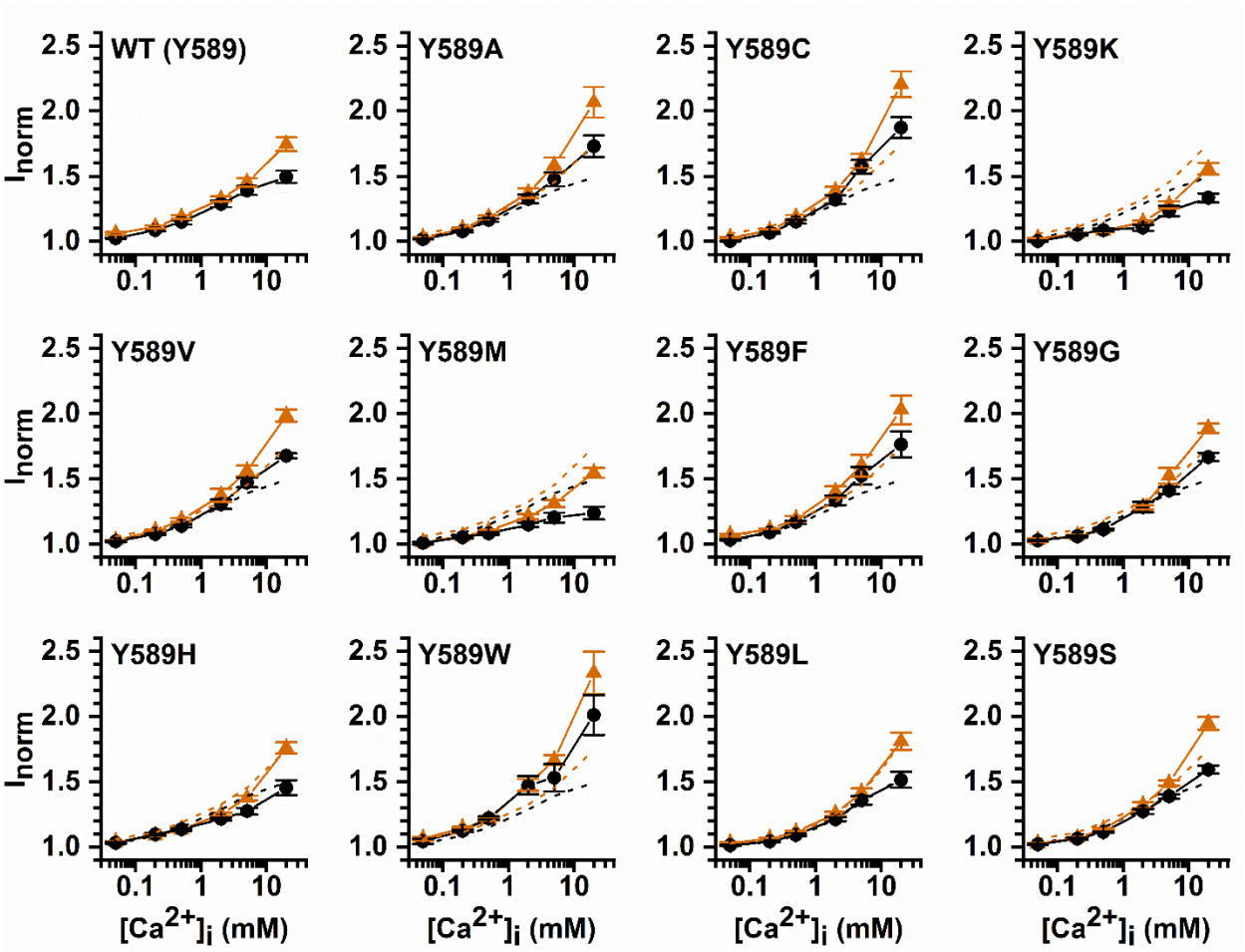

Fig 3.11. Current potentiation in various Y589 mutants by high $[Ca^{2+}]_i$. Dose-response curves at +20 mV (orange triangle) and -20 mV (black circle) were constructed from data obtained by the three-pulse protocol as that shown in Fig 3.10 (A & B). The dose-response curves of WT TMEM16A are plotted as dash curves in other panels for comparison.

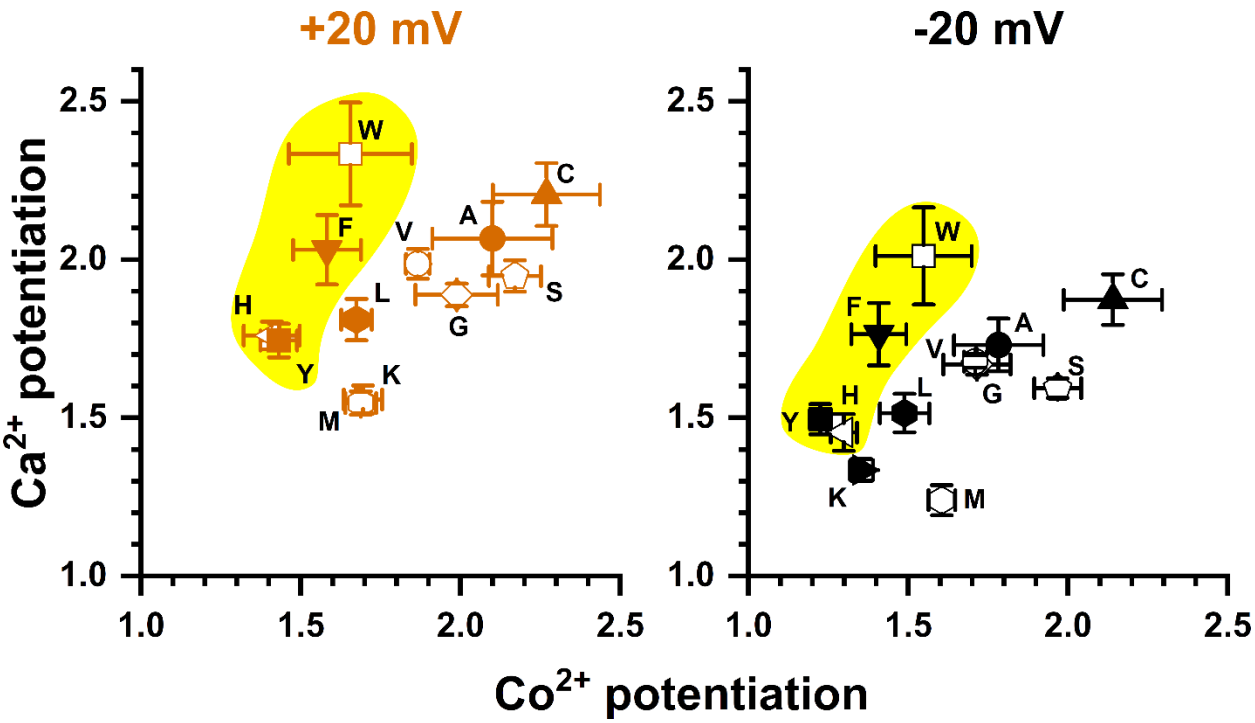

Fig 3.12. Correlation of Ca^{2+} potentiation with Co^{2+} potentiation for various Y589 mutants. Y-axis represents the potentiation by 20 mM $[Ca^{2+}]_i$ (namely, $I_{20\ mM}/I_{20\ \mu M}$) while X-axis is the potentiation of the $[Ca^{2+}]_i$ (300 μM)-induced current by 20 mM $[Co^{2+}]_i$. Aromatic mutants are highlighted in yellow.

3.5 Discussion

TMEM16A is expressed in various tissues and plays many physiological roles, including mediating transepithelial anion transport [201, 202], modulating the mucin secretion and smooth muscle contraction in airways

[168, 203], and controlling the motility of intestine [204, 205]. High-resolution structures of TMEM16 molecules show that multiple acidic residues use their sidechain carboxylates to coordinate the physiological ligand, Ca^{2+}, in the Ca^{2+}-binding sites [10, 90, 95-97, 103], thus opening the channel. Although other alkaline earth divalent cations can bind to the activation sites, only Sr^{2+} and Ba^{2+} can induce current while Mg^{2+} cannot. The binding of Mg^{2+} to the activation sites was previously suggested through the observation that Mg^{2+} shifts the Ca^{2+}-activation curve [115], suggesting a competition of Mg^{2+} and Ca^{2+} for the activation sites. In the absence of other divalent cations, the apparent affinities of Ca^{2+}, Sr^{2+}, and Ba^{2+} in activating TMEM16A were shown to be in the range of ~0.5-1 μM, ~5-10 μM, and ~200-500 μM, respectively, while mM [Mg^{2+}] is needed to shift the apparent Ca^{2+} affinity by only twofold [115]. It is not surprising that the relative apparent affinities for these divalent cations in binding to TMEM16A appear to be qualitatively similar to those of their binding to EGTA, because the divalent cation-coordinating groups in TMEM16A and EGTA are carboxylates, providing a relatively high affinity for Ca^{2+} binding. The activation of TMEM16A by sub-μM to low μM $[Ca^{2+}]_i$ is physiologically important because the channel can perfectly respond to the change of $[Ca^{2+}]_i$ from the resting state (~0.1 μM) to the excited state (sub μM to low μM) of cells.

In the present study, we demonstrate that another divalent cation, Co^{2+}, can also interact with TMEM16A, although intracellular Co^{2+} up to 20 mM cannot induce current in WT TMEM16A (Fig 3.2A). Intracellular Co^{2+}, however, has two effects on the Ca^{2+}-induced TMEM16A current: an immediate potentiation of the Ca^{2+}-induced current followed by an inhibition of the current (Fig 3.2B). The degree of Co^{2+} inhibition depends on the $[Ca^{2+}]_i$ used to induce the current—with a higher $[Ca^{2+}]_i$, a larger $[Co^{2+}]_i$ is required to exert the same degree of inhibition (Fig 3.3A). In fact, Ca^{2+} shifts the dose-dependent Co^{2+} inhibition curve in parallel towards the direction of higher $[Co^{2+}]_i$ (Fig 3.3B), and the rate of the Ca^{2+} activation of TMEM16A decreases with the presence of Co^{2+} (Fig 3.4A and 3.4B). Furthermore, mutant TMEM16A channels with a slower Ca^{2+}-dissociation rate from the activation sites show weaker Co^{2+} inhibition—the longer the current deactivation time (τ_{off}) upon removing $[Ca^{2+}]_i$, the weaker the Co^{2+} inhibition (Fig 3.6 and 3.7). We thus conclude that Co^{2+} inhibition of the Ca^{2+}-induced current in TMEM16A likely results from the competition of Co^{2+} with Ca^{2+} for the high-affinity Ca^{2+}-activation sites. The apparent affinity of Co^{2+} inhibition is quite high, likely due to its interaction with the sidechain carboxylate of multiple acidic residues in the Ca^{2+}-activation sites. For example, the $K_{1/2}$ of Co^{2+} inhibition of the current induced by 2 μM $[Ca^{2+}]_i$ is only ~3-5 μM (Fig 3.3 & Table 3.1). In comparison, the Mg^{2+} inhibition of the TMEM16A current activated by ~0.7 μM $[Ca^{2+}]_i$ has a $K_{1/2}$ of ~5 mM [115].

Besides inhibiting the Ca^{2+}-induced TMEM16A current, intracellular Co^{2+} also potentiates the current, and this effect occurs before the inhibition appears. In all Co^{2+} concentrations used, we cannot discern the difference between the rate of potentiation and the rate of solution exchange. Because the time courses of potentiation and inhibition can be clearly distinguished, and because the degree of potentiation does not significantly change in various $[Ca^{2+}]_i$ used in inducing current (Fig 3.9), Co^{2+} potentiation is less likely to be a phenomenon mediated via high-affinity Ca^{2+} activation sites. The current potentiation requires high $[Co^{2+}]_i$. Generating even a slight potentiation effect requires at least hundreds of μM of $[Co^{2+}]_i$. The potentiation appears to be voltage dependent: a clear difference in the degree of potentiation is observed between -20 mV and +20 mV when 20 mM $[Co^{2+}]_i$ was used to potentiate the current (Fig 3.9). Furthermore, the degree of Co^{2+} potentiation is affected by mutation of Y589 (Figs 3.6 and 3.88), a pore residue. We thus suspect that the potentiation may result from an increase of the Cl^- flux mediated by the binding of Co^{2+} to the pore region.

Previous experiments have shown a biphasic Ca^{2+} activation of TMEM16A [106, 107]. Namely, the TMEM16A activation is saturated at the concentration range from several μM to ~100-200 μM of $[Ca^{2+}]_i$. However, as $[Ca^{2+}]_i$ is further increased, more TMEM16A current can be induced [106, 107]. Recording traces in Fig 3.10A and 3.10B reveal that the current

reduction upon removing mM $[Ca^{2+}]_i$ consists of a fast and a slow current-deactivation process, and the amplitude of the slower component is equivalent to the amplitude of the current induced by 20 μM $[Ca^{2+}]_i$. Thus, the fast-decaying component is the extra current induced by mM $[Ca^{2+}]_i$. Fig 3.10A and 3.10B also show that the amplitude of this low-affinity component in Y589A is larger than that in the WT channel, consistent with a larger Co^{2+} potentiation in the Y589A mutant. We systematically compared over ten Y589 mutants for the degree of potentiation by Ca^{2+} and Co^{2+}. The results indicate that the degree of potentiation by 20 mM $[Co^{2+}]_i$ (300 μM $[Ca^{2+}]_i$-activated current) roughly correlates with the degree of 20 mM $[Ca^{2+}]_i$-induced potentiation (relative to the 20 μM $[Ca^{2+}]_i$-activated current), except perhaps in two mutants, Y589W and Y589F (Fig 3.12). The less than perfect correlation in these two mutants could have two reasons. As shown in Fig 3.6, Y589W and Y589F have the shortest time constants (τ_{off}) of current deactivation upon removing $[Ca^{2+}]_i$, so their affinity for Ca^{2+} activation are low. Perhaps the 20 μM $[Ca^{2+}]_i$ used to induce the current in these two mutants was not a saturating concentration. Therefore, the current potentiation by 20 mM $[Ca^{2+}]_i$ (compared to the current induced by 20 μM $[Ca^{2+}]_i$) may include a further opening of the channel by a more saturating $[Ca^{2+}]_i$. A second possibility for the disproportionally higher Ca^{2+} potentiation than the Co^{2+} potentiation in Y589W and Y589F may be a true difference of the potentiation due to, for example, a different binding of these two

divalent cations to mutants with an aromatic sidechain. The less than perfect correlation between Ca^{2+} and Co^{2+} potentiation in Y589F and Y589W does not undermine the observations that the affinities for the Ca^{2+} and Co^{2+} potentiation are low, and the degrees of the potentiation by these two cations are similar to each other.

It is intriguing that mutating the pore residue Y589 affects the degree of Ca^{2+} and Co^{2+} potentiation. The fact that the mutants Y589K, Y589L, and Y589M exhibit a similar degree of potentiation indicates that sidechain charge plays little role in the potentiation. The correlation between sidechain hydrophobicity and the degree of potentiation is also weak. Rather, the potentiation appears to best correlate with the sidechain volume of the amino acid at position 589. We suspect that the sidechain of residue 589 probably does not directly interact with Ca^{2+} or Co^{2+}. The potentiation requiring hundreds of μM or mM of Ca^{2+} or Co^{2+} further indicates that binding of these two divalent cations to generate the effect is of low affinity, and therefore could be non-specific. Recent experiments from our laboratory have revealed that introducing an aromatic residue at the Q559 position of TMEM16F, which corresponds to K584 of TMEM16A (a pore residue), significantly reduces the rundown of TMEM16F [125]. We speculated that this reduction of rundown in the Q559W mutant may involve phospholipids because membrane phosphatidylinositol diphosphate (PIP2) were shown to affect the rundown of TMEM16 molecules [127, 147]. Interaction of the

fungus scramblase protein with phospholipids has been shown to thin the lipid bilayer near the transport pathway [90, 144]. Structures of TMEM16 molecules also suggest phospholipids may exist in the pore region [10, 90, 96, 97, 103], or may even form the wall of the substrate-transport pathways [196]. Interestingly, divalent cations are known to bind to phospholipids with binding affinities of mM or above [206-208]. It is thus possible that Co^{2+} and Ca^{2+} bind to the phospholipids located at the intracellular pore entrance to increase Cl^- flux through the channel pore.

We and others have also shown that the sidechain charge from K584 (or K588 of the "a, c" alternatively spliced isoform) of TMEM16A electrostatically controls the Cl^- flux [106, 107, 125]. The binding of divalent cations to the nearby regions would increase local [Cl^-] via an electrostatic effect. The degree of the Co^{2+} potentiation best correlates with the volume of the amino acid placed at position 589—a larger Co^{2+} potentiation appears in the mutants with a smaller sidechain (Fig 3.8). Such a dependence on the sidechain volume of the introduced amino acid is reminiscent of previous studies on the *Torpedo* CLC-0 Cl^- channel where the sidechain volume of a residue deep in the pore (E166 of CLC-0) affects the blocking affinity of amphiphlic pore blockers such as parachlorophenoxy acetate or octanoate [183, 209]. In those experiments, it was concluded that the charged end of the blockers "dock" at the pore entrance while the hydrophobic end of the blockers directly interact with the sidechain of the amino acid at the E166

position. If phospholipids contribute forming the pore wall of TMEM16A [196], the hydrophilic (or charged) end of phospholipids should be located at the pore entrance while the hydrophobic tail would be at a deeper position of the pore. Perhaps a smaller sidechain of residue 589 would allow the pore vestibule to accommodate more phospholipids for binding more divalent cations.

In summary, we have shown that intracellular Co^{2+}, like Mg^{2+}, competes with Ca^{2+} for the channel activation sites and thus inhibits the Ca^{2+}-induced current in TMEM16A. Co^{2+} at higher concentrations can also potentiate the Ca^{2+}-induced TMEM16A current. Potentiation of the TMEM16A current by Co^{2+} is likely mediated by the same mechanism of the current potentiation by mM $[Ca^{2+}]_i$. We suggest that this potentiation may occur via the binding of divalent cations near or within the pore because of the voltage dependence of the potentiation and because pore residue mutations affect this potentiation. We suspect this potentiation effect may be related to the phospholipids near the intracellular pore region. It will require further experiments to refute or further support this conjecture that membrane phospholipids indeed involve in the Ca^{2+} and Co^{2+} potentiation of the TMEM16A current.

3.6 Supporting Information

A

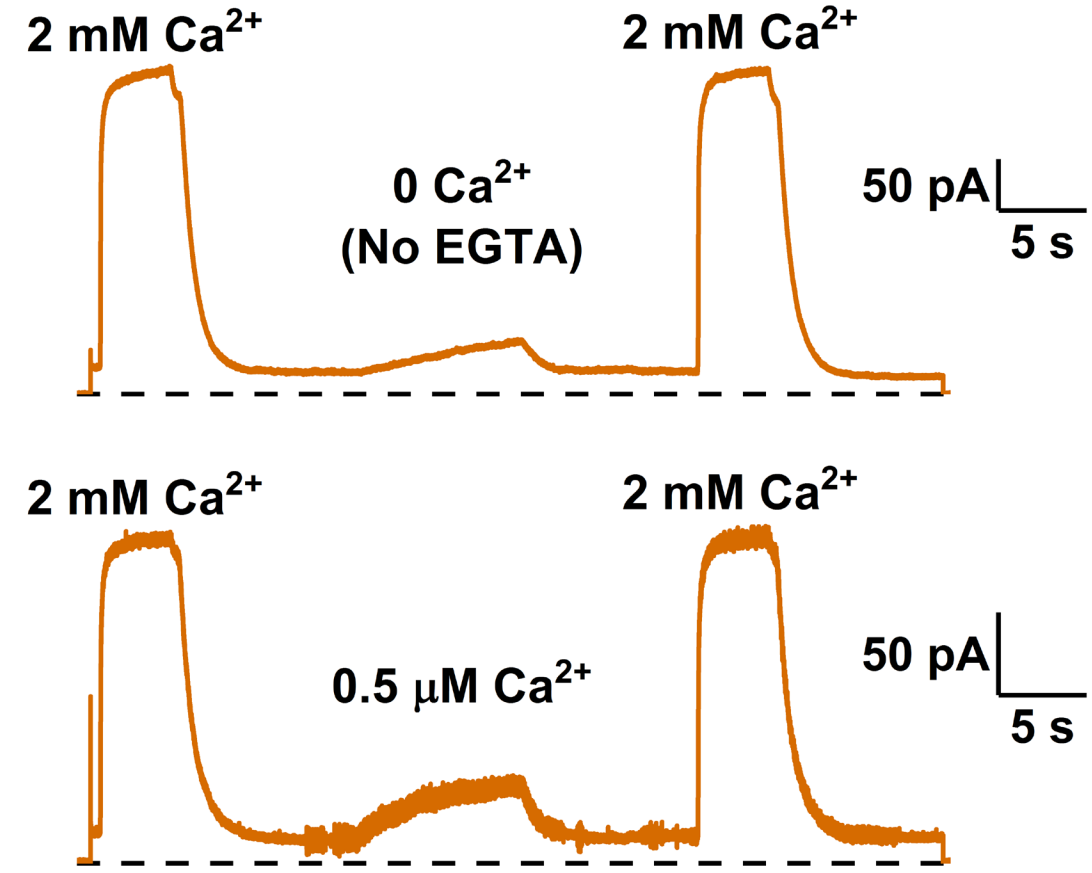
2 mM Ca2+
2 mM Ca2+
0 Ca2+
(No EGTA)
50 pA
5 s
2 mM Ca2+
2 mM Ca2+
0.5 μM Ca2+
50 pA
5 s

B

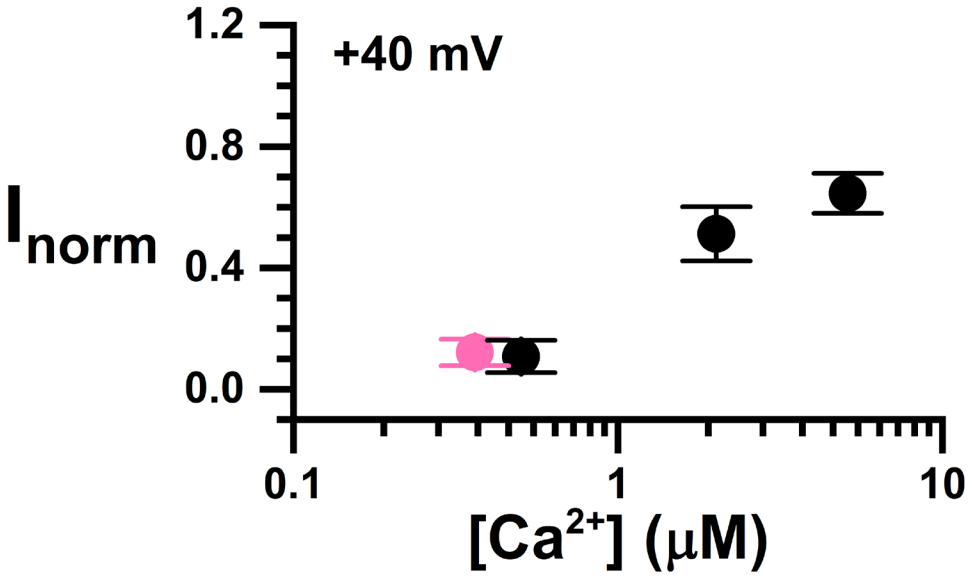
1.2
0.8
0.4
0.0
+40 mV
Inorm
0.1
1
10
[Ca2+] (μM)

3.S1 Fig. Estimation of the concentration of contaminating Ca^{2+}. (A) Recording traces of the currents of the TMEM16F Q559W mutant induced by various $[Ca^{2+}]_i$ using a three-pulse protocol. The dash line represents zero-current level. V_m = +40 mV. $[Ca^{2+}]_i$ in the first and the third pulse was 2 mM, a saturating concentration. For the second pulse in the top trace, a solution containing neither EGTA nor any added $[Ca^{2+}]_i$ (called nominal zero-Ca^{2+} solution) was used, while a solution containing a calculated free $[Ca^{2+}]_i$ of ~0.5 μM was used for the second pulse in the lower trace. The nominal zero-Ca^{2+} solution used in the top trace contains only 140 mM NaCl and 10 mM HEPES (pH = 7.4 adjusted with NaOH), while the solution used for the second pulse in the lower trace contains extra 100 μM EGTA and an added $[Ca^{2+}]_i$ of 89.8 μM. Free $[Ca^{2+}]_i$ in the solution was calculated using the MaxChelator program (http://maxchelator.stanford.edu/CaEGTA-NIST.htm). (B) Normalized currents of a TMEM16F mutant, Q559W, activated by various $[Ca^{2+}]_i$. The amplitudes of all recorded currents were normalized to that induced by 2 mM $[Ca^{2+}]_i$. Solid black circles represent the data from using solutions containing calculated $[Ca^{2+}]_i$ of 0.5 μM, 2.0 μM, and 5.1 μM free $[Ca^{2+}]_i$ (n = 4-11), and the data match the dose-response curve for TMEM16F Q559W mutant reported in Nguyen et al. [125]. The solid pink circle represents the data from using the 0 Ca^{2+} solution containing only the contaminating $[Ca^{2+}]_i$ (n = 11).

3.7 Acknowlegement

We thank Dr. Robert Fairclough for helpful suggestions and critical reading of the manuscript.

3.8 Author Contributions

Conceived and designed the experiments: DMN, TC. Performed the electrophysiological experiments: DMN, LSC, GJ, TC. Analyzed the data, DMN, LSC, GJ, TC; Contributed reagents/materials/analysis tools: WY, TC. Wrote the paper: DMN, LSC, TC.

Chapter 4: Divalent Cation Modulation of Ion Permeation in TMEM16 Proteins

Dung M. Nguyen[1,3], Hwoi Chan Kwon[1,4] and Tsung-Yu Chen[1,2]*

[1] Center for Neuroscience, University of California, Davis, California, 95616, United States of America; tycchen@ucdavis.edu

[2] Department of Neurology, University of California, Davis, California, 95616, United States of America.

[3] Pharmacology and Toxicology Graduate Program, University of California, Davis, California, 95616, United States of America; dmanguyen@ucdavis.edu

[4] Biophysics Graduate Program, University of California, Davis, California, 95616, United States of America; hwckwon@ucdavis.edu

This chapter has been adapted from a publication in *Int. J. Mol. Sci.* (Volume 22, issue 4, page 2209).

4.1 Abstract

Intracellular divalent cations control the molecular function of transmembrane protein 16 (TMEM16) family members. Both anion channels (such as TMEM16A) and phospholipid scramblases (such as TMEM16F) in this family are activated by intracellular Ca^{2+} in the low μM range. In addition, intracellular Ca^{2+} or Co^{2+} at mM concentrations have been shown to further potentiate the saturated Ca^{2+}-activated current of TMEM16A. In this study, we found that all alkaline earth divalent cations in mM concentrations can generate similar potentiation effects in TMEM16A when applied intracellularly, and that manipulations thought to deplete membrane

phospholipids weaken the effect. In comparison, mM concentrations of divalent cations minimally potentiate the current of TMEM16F but significantly change its cation/anion selectivity. We suggest that divalent cations may increase local concentrations of permeant ions via a change in pore electrostatic potential, possibly acting through phospholipid head groups in or near the pore. Monovalent cations appear to exert a similar effect, although with a much lower affinity. Our findings resolve controversies regarding the ion selectivity of TMEM16 proteins. The physiological role of this mechanism, however, remains elusive because of the nearly constant high cation concentrations in cytosols.

4.2 Introduction

The TMEM16 family encompasses transmembrane proteins functioning as Ca^{2+}-sensitive Cl^- channels and phospholipid scramblases [176, 177]. TMEM16A is a Ca^{2+}-activated Cl^- channel [6-8], and its activation is important for anion transport across cell membranes in many types of cells [3, 210]. On the other hand, upon activation by Ca^{2+}, TMEM16F and other fungal TMEM16 molecules scramble membrane phospholipids, as well as conducting ionic currents [9, 49, 66, 108]. Recent structural-functional studies of TMEM16 molecules have revealed that the homodimeric architecture is conserved between anion channels and phospholipid scramblases, and helices 3-8 appear to form a conduit thought to be the

pathway for ion and/or phospholipid transport [10, 90, 95-97, 103]. However, the substrate-transport pathways of the two types of TMEM16 phospholipid scramblases may be slightly different. In fungal phospholipid scramblases, the entire conduit appears as a groove with an open sidewall [10, 90]. This conduit in mammalian TMEM16F, however, has an intact protein sidewall at its extracellular half as shown in recent cryo-EM studies [95, 198]. The difference in the degree of sidewall opening of this conduit between fungus and mammalian phospholipid scramblases raises a question regarding the molecular mechanism by which these scramblases transport phospholipids [198]. The ion-conducting pore of TMEM16A is similar to that of mammalian TMEM16F; namely, the pore is fully enclosed for the extracellular half but is missing part of the protein sidewall at the intracellular half [96, 97, 103]. As TMEM16A and TMEM16F are membrane proteins, the open cavity at the intracellular end of the conduit could consist of membrane phospholipids. Indeed, interactions of phospholipids and TMEM16 proteins have been suggested in structural and calculation studies [90, 91, 109, 144, 148, 198]. Functional effects of phospholipids on the activation and rundown of TMEM16 molecules have also been experimentally documented [127, 145, 147, 148].

Various studies generally agree that after activation by intracellular Ca^{2+}, TMEM16A conducts mostly anions [8, 106, 115, 141, 142, 211]. On the other hand, the cation versus anion selectivity for TMEM16F's current

conduction has been controversial. In TMEM16F, some experiments showed that TMEM16F non-selectively conducts cations and anions with only a slightly higher selectivity towards anions [133-135], whereas in other studies the selectivity was found to significantly favor cations [49]. This controversy may depend on experimental conditions. For example, experiments using whole-cell recording methods tend to report that TMEM16F is less cation-selective [133-135], whereas experiments with excised inside-out patch recordings have shown very different Na^+ versus Cl^- permeability ratios (P_{Na}/P_{Cl}) [49, 125]. Recently, Ye et al. [116] reported that the P_{Na}/P_{Cl} ratio of TMEM16F depends on the intracellular Ca^{2+} concentration ($[Ca^{2+}]_i$) used to activate the current: the ratio was ~0.5 (more anion selective) and ~6-7 (more cation selective) when the TMEM16F current was activated by 1 mM and 15 μM $[Ca^{2+}]_i$, respectively. It was suggested that this effect could result from a change in the pore electrostatic potential due to Ca^{2+} binding to the pore. Our laboratory has shown that the electrostatic control of Cl^- flux through the TMEM16A pore can be achieved via altering the sidechain charge of a pore residue [107, 125]. The binding of Ca^{2+} to the high-affinity channel activation sites has also been shown to electrostatically affect the ion conduction of TMEM16A [126], presumably because Ca^{2+}-activation sites are near the intracellular pore entrance. The electrostatic control of Ca^{2+} in altering the P_{Na}/P_{Cl} ratio of TMEM16F is thus conceivable, although the nature of this Ca^{2+}-modulation effect on the

P_{Na}/P_{Cl} ratio in TMEM16F is still murky. For example, if TMEM16F activated by 15 μM and by 1 mM $[Ca^{2+}]_i$ have different P_{Na}/P_{Cl} ratios, the difference cannot be mediated by Ca^{2+} binding to the activation sites of TMEM16F, which have an apparent Ca^{2+} affinity < 10 μM. Meanwhile, though Ye et al. [116] showed that TMEM16F was quite cation-selective (P_{Na}/P_{Cl} ~6-7) when the current was activated by low $[Ca^{2+}]_i$ (15 μM), various studies in the literature revealed that $[Ca^{2+}]_i$ at similarly low concentrations activates a non-selective TMEM16F current [125, 133-135].

We have reported that a high concentration (hundreds of μM or above) of intracellular Co^{2+} ($[Co^{2+}]_i$) potentiates the TMEM16A current induced by saturating $[Ca^{2+}]_i$ [212]. This Co^{2+} potentiation effect (see Figure 4.1A) appeared to be similar to the current potentiation by mM $[Ca^{2+}]_i$ after the activation of TMEM16A is saturated (see Figure 4.1B). We suggested that Ca^{2+} and Co^{2+} may bind to the pore region of TMEM16A to potentiate Cl^- currents [212]. In the present study, we further examined this current potentiation mechanism. We found that besides Ca^{2+} and Co^{2+}, alkaline earth divalent cations such as Mg^{2+}, Sr^{2+} and Ba^{2+} can all potentiate the TMEM16A current with a roughly similar low affinity. In addition, treating the patch intracellularly with poly-L-lysine reduces the potentiation effect, whereas lowering ionic strength enhances the potentiation. On the other hand, the same high concentrations of divalent cations had a minimal effect in potentiating the current of TMEM16F, but changed its P_{Na}/P_{Cl} ratio, as

reported by Ye et al. [116]. The P_{Na}/P_{Cl} ratio of TMEM16F also depends on the concentration of intracellular monovalent cations. These results show a modulation on the ion permeation of TMEM16 molecules by a rather nonspecific cation binding. We suggest that divalent and monovalent cations congregate around phospholipid head groups near or within the ion-transport pathway of TMEM16 proteins with low affinities, thus changing the electrostatic potential near the pore region. These observations are significant because they explain the controversy in the literature regarding the cation versus anion selectivity of TMEM16 molecules.

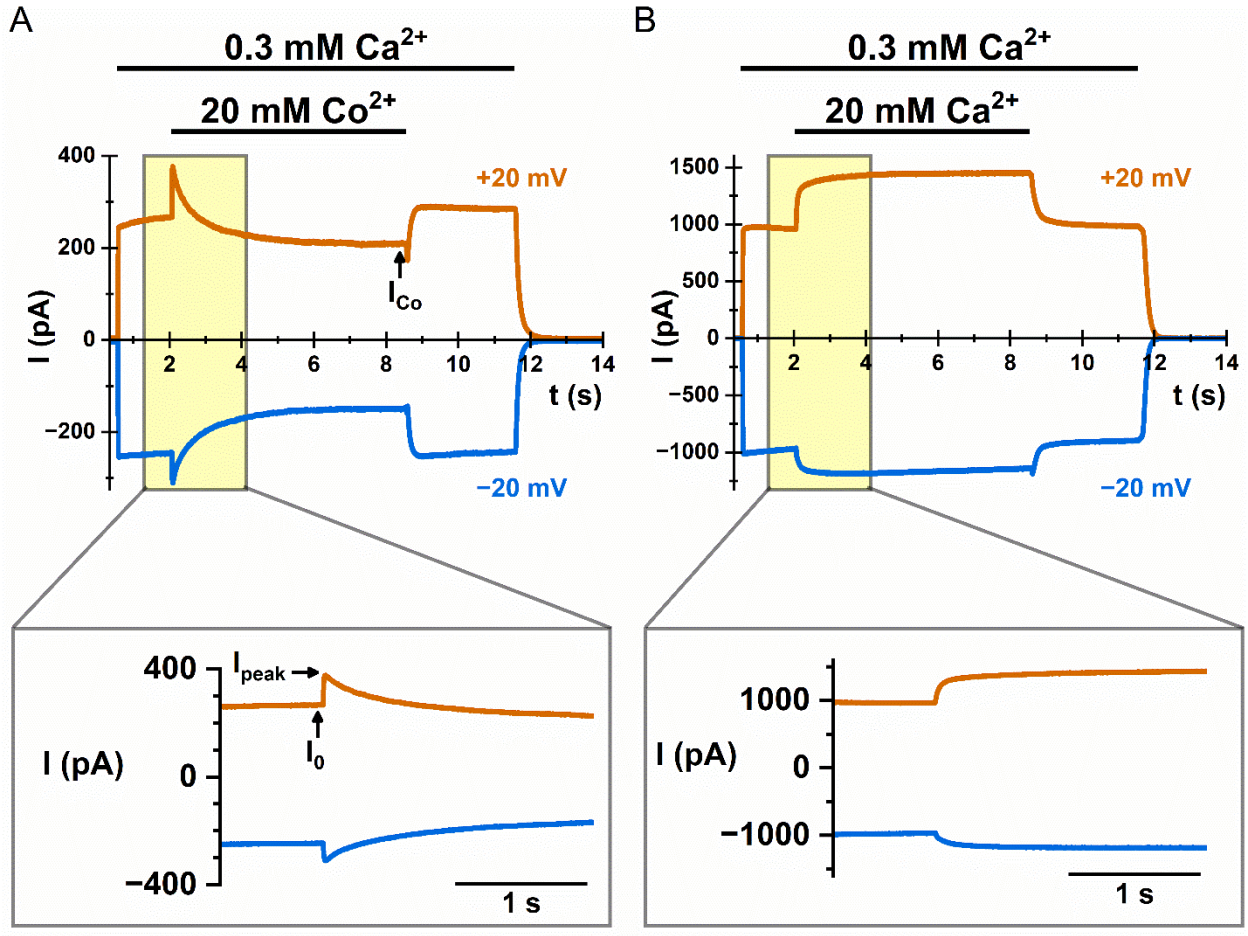

Figure 4.1. Potentiation of the TMEM16A current by intracellular Co^{2+} and Ca^{2+}. TMEM16A currents were obtained at voltages clamped at -20 mV (blue traces) and +20 mV (orange traces). Currents were activated by 0.3 mM intracellular calcium concentration($[Ca^{2+}]_i$). (**A**) Recording traces showing the dual effects, inhibition and potentiation, on the wild-type TMEM16A (WT_{16A}) current by 20 mM intracellular cobalt concentration ($[Co^{2+}]_i$). (**B**) Recording traces showing potentiation of WT_{16A} by 20 mM $[Ca^{2+}]_i$. In the bottom panel of both A and B, an expanded view of the yellow shaded area in the upper panel is depicted to focus on the current potentiation. I_0 represents the control current before the application of divalent cations, whereas I_{peak} and I_{Co} represent the peak current after the application of Co^{2+} and the quasi-steady-state current at the end of the Co^{2+} application, respectively.

4.3 Materials and Methods

4.3.1 Molecular biology and channel expression

The cDNAs of the TMEM16 family members and their mutants were generated as described recently in Nguyen et al [212]. Briefly, the wild-type TMEM16A (WT_{16A}) (NCBI reference sequence: NM_001242349.1) [99] and the wild-type TMEM16F (WT_{16F}) cDNA (Addgene plasmid # 62554) were subcloned in pEGFP-N3 or pIRES2 expression vectors (Clontech/Takara Bio, Mountain View, California, USA). Mutants of TMEM16 molecules were created

using the QuikChange II site-directed mutagenesis kit (Agilent Technologies, Santa Clara, California, USA), and the mutations were verified with commercial DNA sequencing services. The E166A mutant of CLC-0 (abbreviated as $E166A_{CLC0}$), which was reported previously [209], was constructed in the pIRES2 vector (Clontech/Takara Bio). Transfections of cDNAs to human embryonic kidney (HEK) 293 cells were performed using the Lipofectamine 3000 kit (MilliporeSigma, St. Louis, Missouri, USA) according to the manufacturer's instructions. The cells that expressed channels were identified by the green fluorescence with an inverted microscope (DM IRB; Leica) equipped with a fluorescent light source and a GFP filter (Chroma Technology, Bellows Falls, Vermont, USA).

4.3.2 Electrophysiological recordings

All electrophysiological recordings were performed on inside-out membrane patches excised from GFP-positive cells 24–72 h after transfections. Except where indicated, the pipette (extracellular) solution was the same as the intracellular zero-Ca^{2+} solution, which contained 140 mM NaCl, 10 mM HEPES, and 0.1 mM EGTA at pH 7.4 (adjusted with NaOH). Solutions with 20 μM Ca^{2+} were the same as the intracellular zero-Ca^{2+} solution except for the addition of 120 μM $CaCl_2$ (pH adjusted to 7.4 after the addition of $CaCl_2$). The experiments for evaluating the degree of current potentiation were performed in symmetrical [Cl^-] (140 mM or 40 mM). For experiments in symmetrical 140 mM [Cl^-] with intracellular solutions

containing high concentrations (> 20 μM) of divalent ions (Ca^{2+}, Mg^{2+}, Ba^{2+}, or Co^{2+}), EGTA was not included in the solution, and the total concentration of the divalent cations added to the solution was considered as the free concentration. Because these divalent cations were from chloride salts, the amount of NaCl was reduced accordingly to maintain a total [Cl^-] of 140 mM. For experiments testing the potentiation in symmetrical 40 mM Cl^-, the extracellular (pipette) solution contains 40 mM [NaCl] and 100 mM D-mannitol (VWR Chemicals, Radnor, Pennsylvania, USA). The intracellular solution was of two kinds, containing 100 mM D-mannitol and 40 mM $[NaCl]_i$ or 20 mM divalent cations (chloride salts). For experiments evaluating the reversal potential of TMEM16F, the extracellular solution was the zero-Ca^{2+} solution (140 mM [NaCl]). For measuring reversal potentials in asymmetrical [NaCl] conditions, if $[NaCl]_i$ was lower than 140 mM (such as 15-70 mM), D-mannitol was used to replace the reduced $[NaCl]_i$. All experiments were performed at room temperature (20 °C–22 °C). Poly-L-lysine-hydrochloride (MW 15000-30000, MilliporeSigma, St. Louis, Missouri, USA) was dissolved in ddH_2O to make 150-300 mg/ml stock solutions, which were kept at -20 °C and were diluted into working solutions right before use. The intracellular side of the membrane patch was treated with poly-L-lysine (0.3 mg/mL) for 5 s. PIP2 of porcine brain origin (ammonium salt) was purchased from Avanti Polar Lipids (Alabaster, Alabama, USA). Upon use, the organic solvent in the vial (20:9:1, chloroform:methanol:water) was evaporated with

nitrogen gas and immediately dissolved into the zero-Ca^{2+} working solution. The PIP2 solution (20 μM) was applied to the intracellular side of the membrane patch for 1 min.

Recording electrodes were made from borosilicate glass capillaries (World Precision Instruments) using the PP830 electrode puller (Narishige, Amityville, New York, USA). When filled with the zero-Ca^{2+} solution, the resistance of the electrodes was between ~1.5 and ~2.5 MΩ. All experiments were performed using the Axopatch 200B amplifier and the Digidata1440 analogue-digital signal-converting board controlled using pClamp10 software (Molecular Devices, San Jose, California, USA). Solutions were delivered to intracellular side of the excised membrane patch using the SF-77 solution exchanger (Warner Instruments, Holliston, Massachusetts, USA). In all experiments, the ground electrode was immersed in 3-M KCl solution well, which was then connected to the bath solution with a 1% agarose salt bridge made out of 3-M KCl. Giga-ohm seal formations and patch excisions were always achieved in an identical bath and pipette solution. Liquid junction potentials were not corrected with the assumption that the potential difference among various intracellular solutions connected to 3-M KCl reference remain constant during recordings.

Except where indicated, all experiments of divalent cation-induced potentiation were initiated by clamping the membrane voltage to ±20 mV in the EGTA-containing zero-Ca^{2+} solution. The currents of TMEM16A or

TMEM16F were activated by 0.3 mM $[Ca^{2+}]_i$. Intracellular divalent cations of various concentrations were then applied (in the presence of $[Ca^{2+}]_i$ used for channel activation) until the recorded current reached a steady state. The potentiating divalent cations were then removed (see Figure 4.1). Before analyzing the experimental results, the leak current in the absence of $[Ca^{2+}]_i$ was first subtracted from the recorded currents. For evaluating the degree of potentiation, the peak current in the presence of potentiating agents (I_{peak}) was divided by the control current (I_0) immediately before adding the potentiating agents (see Figure 4.1). In some experiments, the degree of current inhibition by divalent cations was also evaluated. In this case, the quasi-steady-state current at the end of the application of divalent cations was defined as $I_{Divalent}$ (for example, I_{Co} or I_{Mg}) (see Figure 4.1), and the ratio of $I_{Divalent}/I_{peak}$ was used to reflect the degree of inhibition. Data points from the dose-dependent divalent cation potentiation were not fitted to any binding curves because the potentiation by the highest concentration (20 mM) of divalent cations did not reach saturation. To estimate the Na^+ and Cl^- permeability ratio (P_{Na}/P_{Cl}), the asymmetrical [NaCl] conditions were created by changing $[NaCl]_i$ to 15, 40, 70 or 280 mM while $[NaCl]_o$ was kept at 140 mM. When $[NaCl]_i$ was reduced, the reduced $[NaCl]_i$ was replaced with the same concentration of D-mannitol (VWR Chemicals, Radnor, Pennsylvania, USA). The current-voltage (I-V) relationship was generated using a 1.6-s ramp protocol from -80 mV to +80 mV. For each patch, the leak current

obtained in Ca^{2+} free solutions was subtracted from the current obtained in the presence of Ca^{2+}, and the resulting leak-subtracted I-V curve was used to determine the reversal potential (E_{rev}). I-V curves under symmetrical 140 mM [NaCl] were always recorded before $[NaCl]_i$ was changed. If the reversal potential in symmetrical [NaCl] was more than 2 mV away from 0 mV, the patch was discarded. The P_{Na}/P_{Cl} ratio was calculated from E_{rev} according to the Goldman-Hodgkin-Katz equation:

$$E_{rev} = \frac{RT}{F} \ln \frac{P_{Na}[Na^+]_o + P_{Cl}[Cl^-]_i}{P_{Na}[Na^+]_i + P_{Cl}[Cl^-]_o} \quad (1)$$

where R, T and F are the universal gas constant, absolute temperature and Faraday constant, respectively.

For the recording of $E166A_{CLC\text{-}0}$ (Supplemental Information), because this mutant is open constantly, the tight seal of the excised patch was evaluated by taking advantage of the fact that the current of $E166A_{CLC\text{-}0}$ was blocked by μM para-chlorophenoxy acetate (CPA) at negative membrane potentials [209]. Thus, for every excised patch, the currents at -160 mV in the absence and presence of 10 mM CPA (Sigma/Aldrich) were first compared before Mg^{2+} potentiation experiments were conducted. If the steady-state current in the presence of CPA was larger than 5% of the current in the absence of CPA, the tight seal was considered not to be optimal and the patch was discarded.

4.3.3 Data Analysis

Experimental data were analyzed using Clampfit software (Molecular Devices, San Jose, California, USA), OriginPro 2018 software (OriginLab, Co., Northampton, Massachusetts, USA), and in-house script in Python 3.7 (Python 3.7, first released in 27 June 2018, was downloaded from http://www.python.org); the Python script was used to find the peak current (I_{peak}) in recordings. In brief, I_{peak} was detected with a moving average based algorithm, which alleviates a bias detection of the peak from noise of the recording trace. All averaged data are presented as mean ± SEM. The one-way ANOVA followed by Bonferroni's multiple comparisons was used for hypothesis testing in statistical comparisons. Symbols of * and ** indicate the statistically significance levels of 0.05 and 0.005, respectively.

4.4 Results

We have previously shown that intracellular Co^{2+} (up to 20 mM) by itself does not activate current in WT_{16A}. However, intracellular Co^{2+} potentiates the Ca^{2+}-induced WT_{16A} current, followed by an inhibition effect [212]. Co^{2+} inhibition on the WT_{16A} current (see Figure 4.1A) is easier to understand—Co^{2+} competes with intracellular Ca^{2+} for the high-affinity Ca^{2+}-activation sites [212]. The current potentiation by Co^{2+}, however, is a different mechanism because the potentiation occurs before the inhibition. A high $[Ca^{2+}]_i$ also potentiates the current of WT_{16A} (Figure 4.1B), just like the

potentiation generated by high $[Co^{2+}]_i$. For both Co^{2+} and Ca^{2+}, at least hundreds of μM are required for generating a detectable potentiation effect. As the potentiation appears almost immediately upon the application of Co^{2+} or Ca^{2+}, the effect likely results from a potentiation of Cl^- conduction through the TMEM16A pore [212].

To further explore the mechanism underlying Co^{2+} and Ca^{2+} potentiation, we examined whether other divalent cations also potentiate TMEM16A current. Figure 4.2A compares the dose-dependent potentiation of Mg^{2+} (upper panels) and Ca^{2+} (lower panels) on the WT_{16A} current. In these experiments, the current was induced by 300 μM $[Ca^{2+}]_i$ at +20 mV (colored in orange) and -20 mV (colored in blue), followed by the application of the indicated concentrations of extra divalent cations (2 mM to 20 mM). To compare the potentiation effects among different experiments, all currents were normalized to the control current (I_0) right before the addition of the potentiating divalent cations. The degree of current potentiation, I_{peak}/I_0, was calculated, and was plotted against the concentration of the potentiating agents (Mg^{2+} or Ca^{2+}). As shown in the right panels of Figure 4.2A, the current potentiation by Mg^{2+} and Ca^{2+} was qualitatively similar, both in the concentration range required for generating the effect, as well as in the degree of the potentiation. Figure 4.2B depicts the degree of potentiation of each individual patch (circle symbols) and the averaged potentiation (columns) by various divalent cations at 20 mM. The results show that

alkaline earth divalent cations all potentiate the current of WT_{16A} to a roughly similar degree. Approximately 40%-60% increase at +20 mV and 20%-40% increase at -20 mV of the control current (activated by 0.3 mM $[Ca^{2+}]_i$) can be further induced by 20 mM divalent cations.

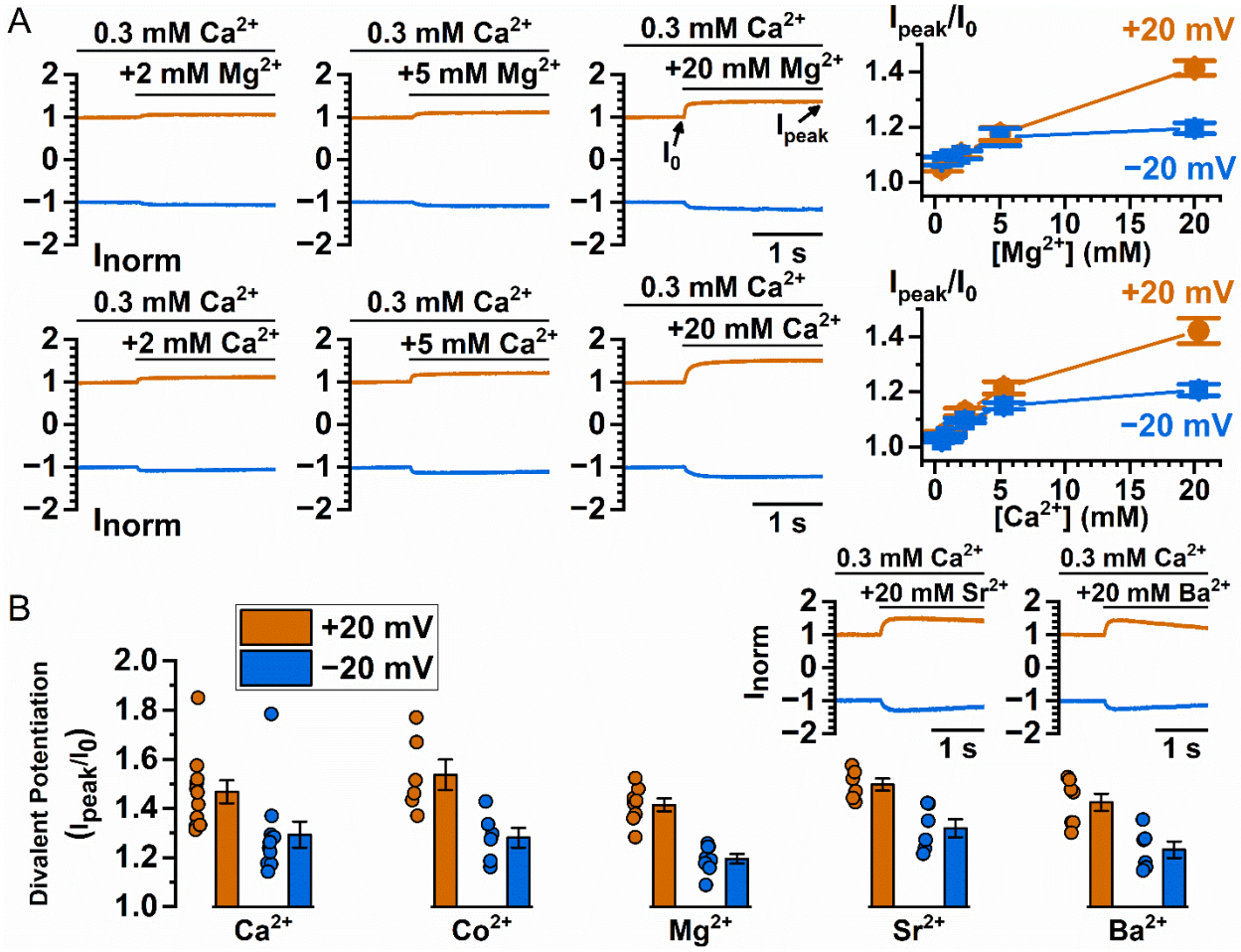

Figure 4.2. Potentiation of WT_{16A} current by various divalent cations. (**A**) Dose-dependent Mg^{2+} and Ca^{2+} potentiation of the WT_{16A} current. Left three panels show raw recording traces of Mg^{2+} or Ca^{2+} potentiation of WT_{16A}

current. The currents were normalized to the current immediately before the application of mM intracellular concentration of magnesium ([Mg^{2+}]) or [Ca^{2+}]. Right panel shows averaged potentiation of WT_{16A} current as a function of [Mg^{2+}] (*n* = 5-8) or [Ca^{2+}] (*n* = 6-7). (**B**) Averaged potentiation of 0.3 mM $[Ca^{2+}]_i$-induced WT_{16A} current by 20 mM Ca^{2+}, Co^{2+}, Mg^{2+}, Sr^{2+}, or Ba^{2+} (*n* = 6-11). Insets show raw recording traces of Sr^{2+} or Ba^{2+} potentiation of WT_{16A} current.

The above results indicate that these various divalent cations potentiate the current of WT_{16A} with low different—all require at least hundreds of μM to mM to start generating the effect. This is different from the higher and very distinct apparent affinities of these divalent cations in activating the current of WT_{16A} [115]. The low affinity suggests that the potentiation might involve phospholipids because the binding affinities between the divalent cations and phospholipids are known to be in the range of hundreds of μM to mM, or above [207, 208, 213]. To explore whether the potentiation mechanism might involve phospholipids, we took advantage of the report that poly-L-lysine depletes membrane phospholipids [147]. Figure 4.3A,B illustrate Co^{2+} and Ca^{2+} potentiation, respectively, before and after poly-L-lysine treatment of the membrane patch expressing WT_{16A}, or two Y589 mutants of TMEM16A with larger Co^{2+} potentiation, Y589V and Y589A (abbreviated as $Y589V_{16A}$ and $Y589A_{16A}$, respectively) [212]. Figure 4.3C,D

show that exposing the membrane patches to intracellular poly-L-lysine (0.3 mg/mL) for only 5 s reduces the potentiation of Co^{2+} and Ca^{2+}. On the other hand, after poly-L-lysine treatment, supplying the membrane patch with 20 μM L-α-phosphatidylinositol-4,5-bisphosphate (PIP2) for 1 min appears to recover the loss of potentiation caused by poly-L-lysine (Figure 4.3E,F).

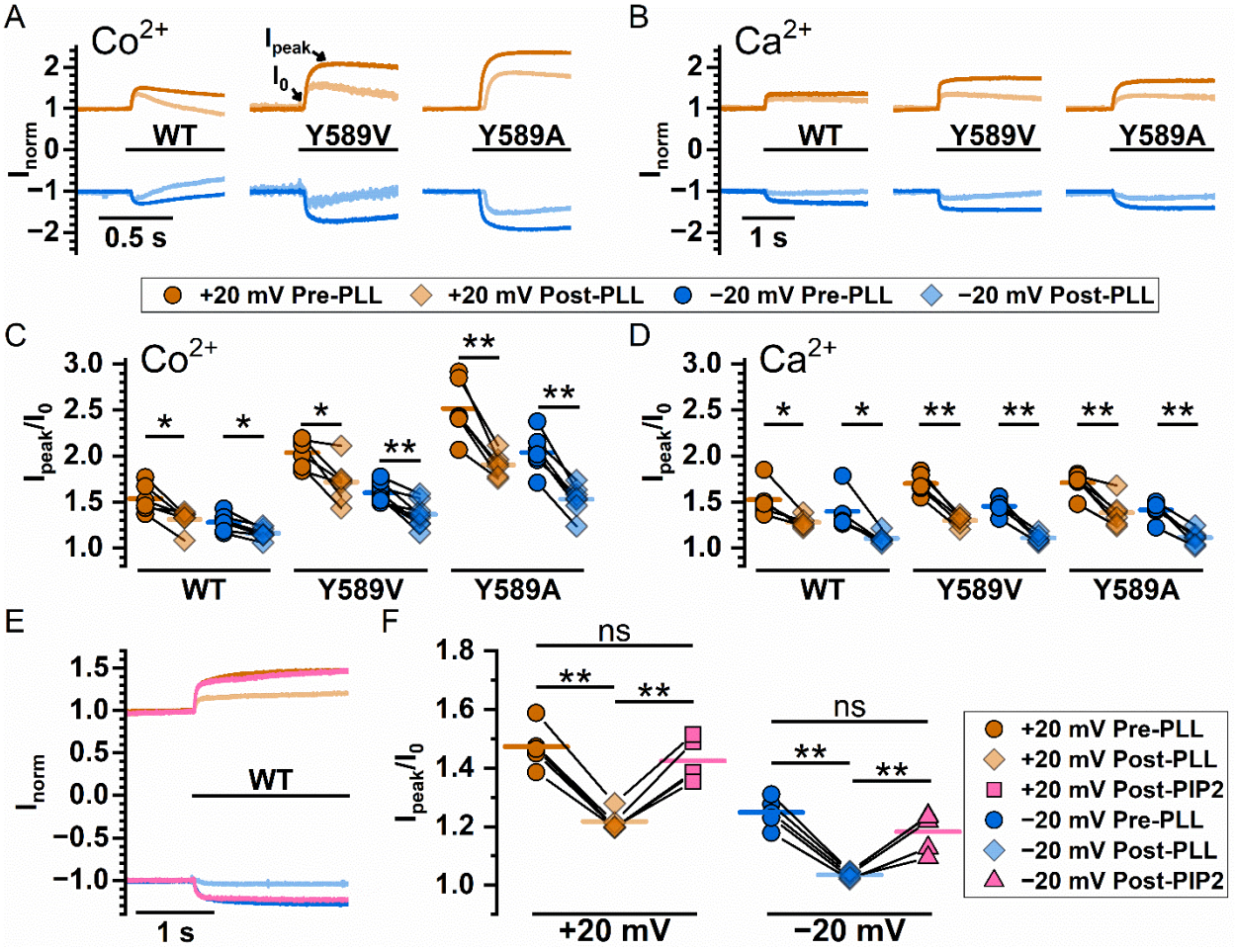

Figure 4.3. Manipulating Co^{2+} and Ca^{2+} potentiation of WT_{16A}, $Y589V_{16A}$, and $Y589A_{16A}$ by intracellular reagents that affect membrane phospholipids. (**A**,**B**) Representative recordings showing Co^{2+} and Ca^{2+} potentiation,

respectively, before and after treating the patch with poly-L-lysine (PLL, 0.3 mg/mL) for 5 sec. All currents were induced by 0.3 mM $[Ca^{2+}]_i$ and potentiated with an additional 20 mM Co^{2+} or Ca^{2+} (black bars underneath phenotype labels). (**C**,**D**) Degree of Co^{2+} and Ca^{2+} potentiation, respectively, before and after poly-L-lysine treatment. Orange (+20 mV) and blue (-20 mV) circles are the potentiation before poly-L-lysine treatment while light orange (+20 mV) and light blue (-20 mV) diamonds are the potentiation after poly-L-lysine. (**E,F**) Effects of PIP2 for reversing the effect of poly-L-lysine on the Ca^{2+}-induced potentiation of the WT_{16A} current. Degree of Ca^{2+} potentiation was measured before poly-L-lysine treatment, after poly-L-lysine treatment, and after PIP2 treatment. In (**C**,**D**,**F**), data points from the same patch are connected by solid lines, and colored horizontal line segments represent the mean of the data set. ns $p > 0.05$; * $p < 0.05$; ** $p < 0.005$ by one-way ANOVA followed by Bonferroni's multiple comparisons.

The results shown in Figure 4.2B and in Figure 4.3 C,D,F reveal a significant variation in the degree of potentiation among different membrane patches even before the treatment with poly-L-lysine. TMEM16 currents are known to undergo significant rundown, and poly-L-lysine facilitates the rundown process, an effect attributed to a depletion of phospholipids [146, 147]. We thus examined if the degree of the potentiation correlates with channel rundown. Figure 4.4A shows an experiment on a TMEM16A mutant,

$Y589A_{16A}$. Here, the Mg^{2+} potentiation was tested every one minute at +20 mV and -20 mV. The rundown of the TMEM16A current can be directly observed from the time-dependent reduction of I_0 from the recording traces in Figure 4.4A and from the averaged I_0 in Figure 4.4B (circles). Figure 4.4B also shows that the averaged degree of the Mg^{2+} potentiation (I_{peak}/I_0, squares) was reduced during the current rundown. We also tested if mutations that reduce the binding of phosphatidylinositol-(4, 5)-biphosphate (PIP2) to TMEM16A [146, 148] alter the degree of potentiation. Figure 4.4C,D confirm that the current potentiation by 20 mM $[Mg^{2+}]_i$ is significantly smaller in $P566A_{16A}$ and $D481A_{16A}$ mutants than that in WT_{16A} whether the effects were examined at +20 mV or -20 mV. On the other hand, the mutation effects of $K678Q_{16A}$ and $R437Q_{16A}$ appear to be less pronounced—the potentiation in these two mutants is more similar to that in WT_{16A}. Only the potentiation at -20 mV in R437Q is significantly smaller than that in WT_{16A}. We speculated that the variation of these mutation effects in different mutants might be related to the physical distance of the mutated residues from the pore (see Discussion).

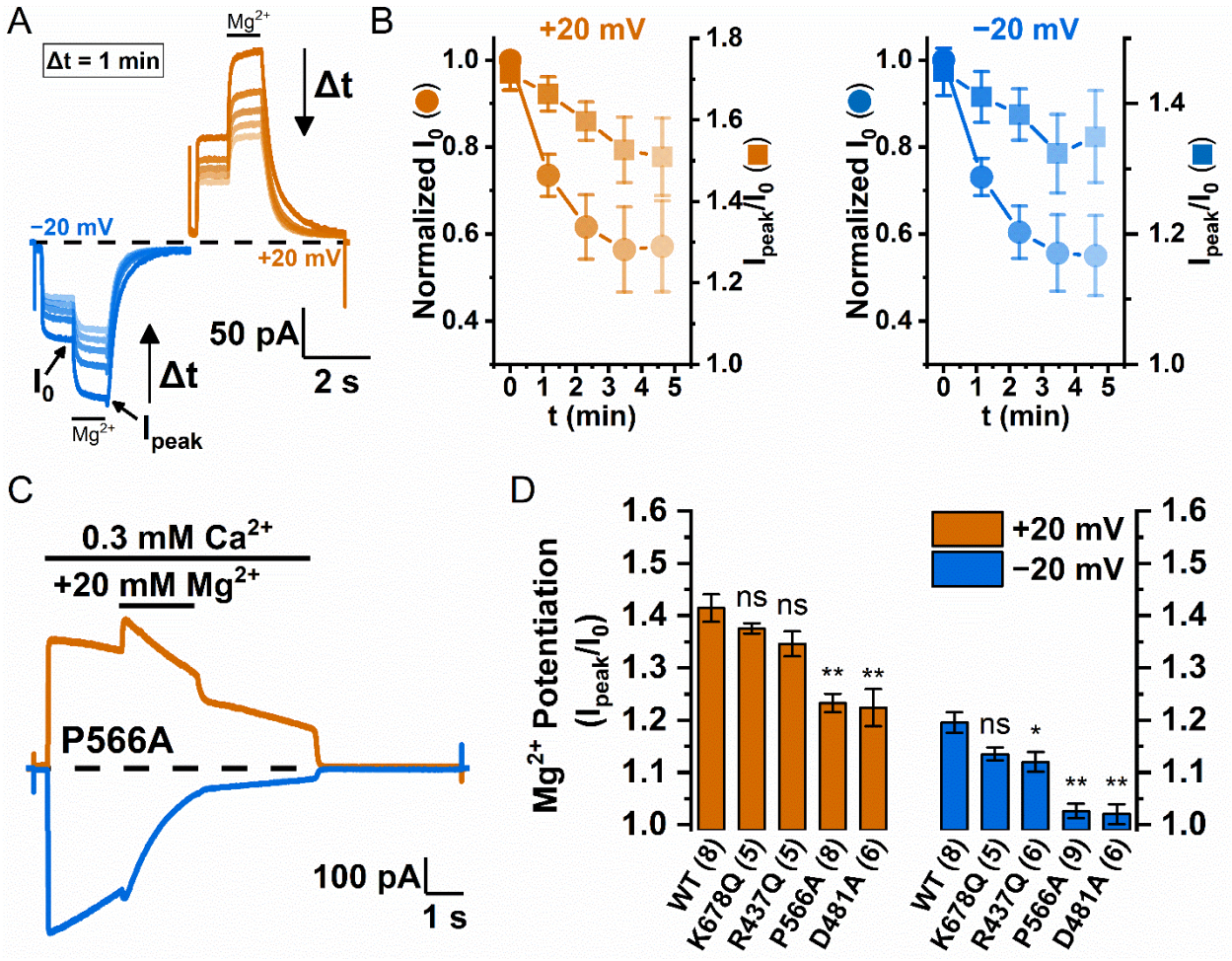

Figure 4.4. Involvement of Phospholipids in divalent cation-induced potentiation. (**A**) Representative recording traces are depicted to illustrate the decrease in Mg^{2+} potentiation of $Y589A_{16A}$ after channel rundown. For every minute, current was elicited with 100 μM Ca^{2+} (a concentration chosen for reducing the speed of rundown), and 20 mM Mg^{2+} were applied subsequently for 1 s (black bar above traces). (**B**) Reduction of Mg^{2+} potentiation (I_{peak}/I_0) over time at +20 mV (left panel, orange) and -20 mV (right panel, blue) (*n* = 6-9). The rundown of the control current (I_0 normalized to the I_0 of the trace at t = 0 min) is shown by circles whereas

the reduction of the Mg^{2+} potentiation is shown by squares. (**C**) Mg^{2+} potentiation of a PIP2 binding-site mutant $P566A_{16A}$ at ±20 mV. The $P566A_{16A}$ current was easier to run down and the degree of potentiation was also smaller compared to that in WT_{16A}. (**D**) Comparing Mg^{2+} potentiation at ±20 mV between WT_{16A} (replotted from Figure 4.1) and four mutants (numbers below each column are number of patches). ns $p > 0.05$; * $p < 0.05$; and ** $p < 0.005$ by one-way ANOVA followed by Bonferroni's multiple comparisons.

One well-documented mechanism underlying the effect of divalent cation binding to membrane phospholipids on ion channels is an alteration of the surface potential of the membrane [214, 215]. Altering membrane surface potential affects the voltage-dependent activation of voltage-gated channels [216, 217] as well as changing the conductance of various ion channels [218, 219]. In altering the channel conductance, the effect depends on the distance of the surface charge from the pore due to the Columbic potential—the closer the charge to the pore, the larger the effect. A large groove cavity is found at the intracellular pore entrance of TMEM16 molecules, and various studies have suggested the presence of phospholipids in the nearby region [90, 91, 109, 144, 198]. As the open groove is exposed to phospholipids, divalent cations may bind to low-affinity binding sites formed by phospholipid head-groups near the pore, thus

affecting ion transport. In comparison, the ion-transport pathways of CLC channel/transporters are completely enclosed by protein structures [220, 221]. Therefore, membrane phospholipids are likely located further away from the pore entrance in CLC channels than in TMEM16A. We thus examined the degree of current potentiation by intracellular Mg^{2+} on a gate-opened mutant of CLC-0, a Cl^- channel expressed in a *Torpedo* electric organ. Indeed, the potentiation effects by intracellular Mg^{2+} in $E166A_{CLC0}$ were much smaller than those observed in WT_{16A} (Supplementary Materials, Figure 4.S1), consistent with the idea that phospholipids are located closer to the ion-transport pathway in TMEM16 molecules than in CLC channels. If the nature of the current potentiation is electrostatic, another prediction is that the potentiation will be enhanced in low ionic strength solutions [214, 215]. Figure 4.5 shows that in symmetrical 40 mM [Cl^-], the degrees of potentiation at +20 mV (outward current or inward Cl^- flux) by Co^{2+} and Mg^{2+} were greatly enhanced compared to those in the symmetrical 140 mM [Cl^-] condition. However, lowering the ionic strength appears to have little effect on the potentiation of the inward current at -20 mV (see Discussion for the interpretation of these results).

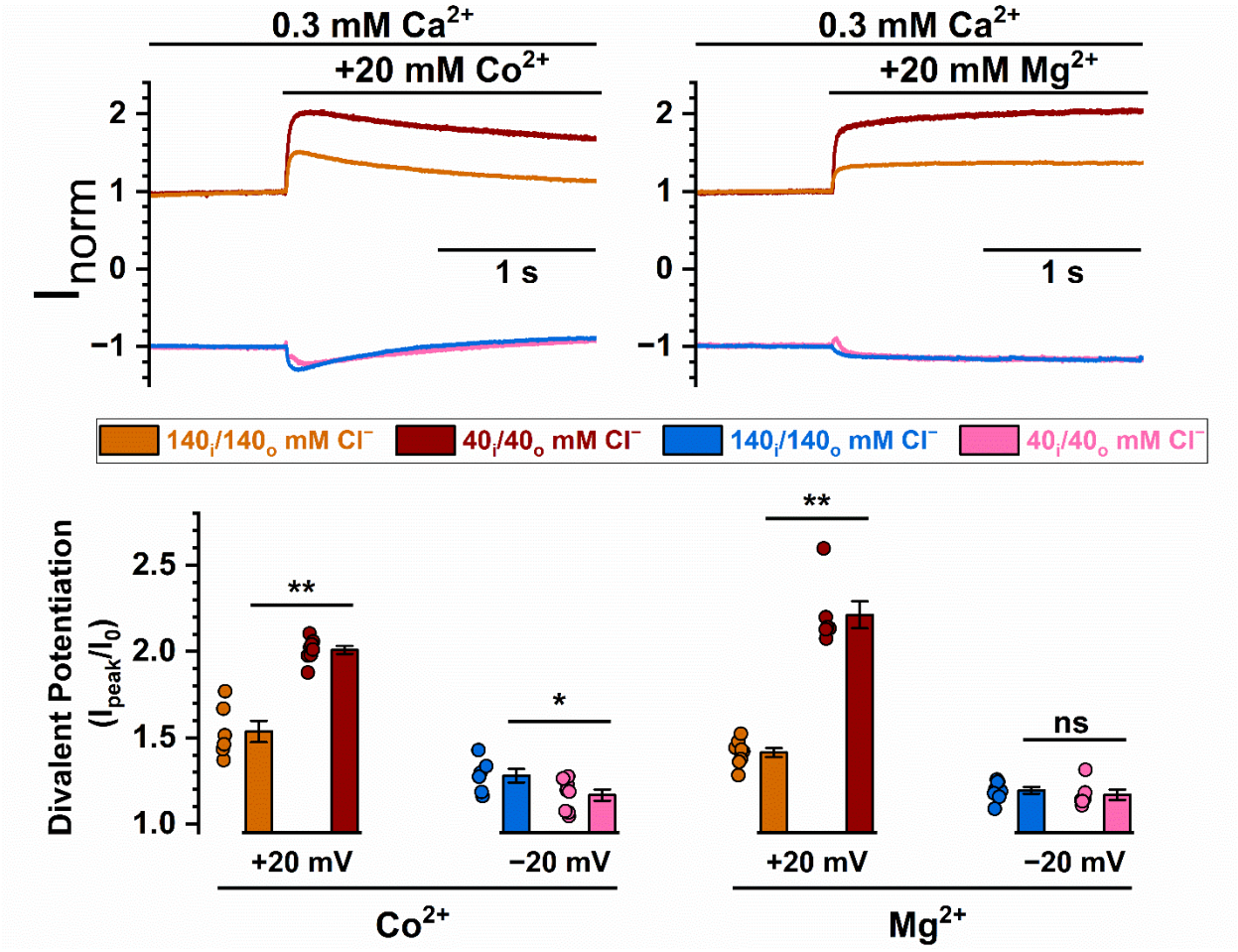

Figure 4.5. Enhanced divalent cation potentiation of WT_{16A} in low ionic strength solutions. (Top) Recording traces comparing the Co2+ or Mg2+ potentiation of WT16A between conditions of symmetrical 140 mM and 40 mM NaCl. The 40 mM NaCl solution also contains 100 mM D-mannitol. All currents were induced by 0.3 mM [Ca2+]i. (Bottom) Bar graph summarizing Co2+ and Mg2+ potentiation under symmetrical 140 mM or 40 mM NaCl (*n* = 6-8). ns $p > 0.05$; * $p < 0.05$; ** $p < 0.005$ by one-way ANOVA followed by Bonferroni's multiple comparisons.

The electrostatic control of channel conductance is thought to result from an increase of the local concentration of the counter-charged ions or a decrease in the concentration of the ions with the same charge near the pore [214, 215, 218]. Because TMEM16F conducts both cations and anions, we expected that the current potentiation in TMEM16F by divalent cations would be smaller than that in TMEM16A because TMEM16F conducts cations as well as anions. To study current potentiation in TMEM16F, we performed experiments on the Q559W mutant of TMEM16F (abbreviated as $Q559W_{16F}$) due to the technical advantage of slower current rundown in this mutant [125]. The recording traces shown in Figure 4.6A and the averaged data in Figure 4.6B indeed indicate that 20 mM Mg^{2+} or Co^{2+} generates very little current potentiation in $Q559W_{16F}$. On the other hand, Mg^{2+} and Co^{2+} inhibit the $Q559W_{16F}$ current (Figure 4.6A,C), likely by competing with Ca^{2+} for the high-affinity activation sites as that shown in TMEM16A [115, 212].

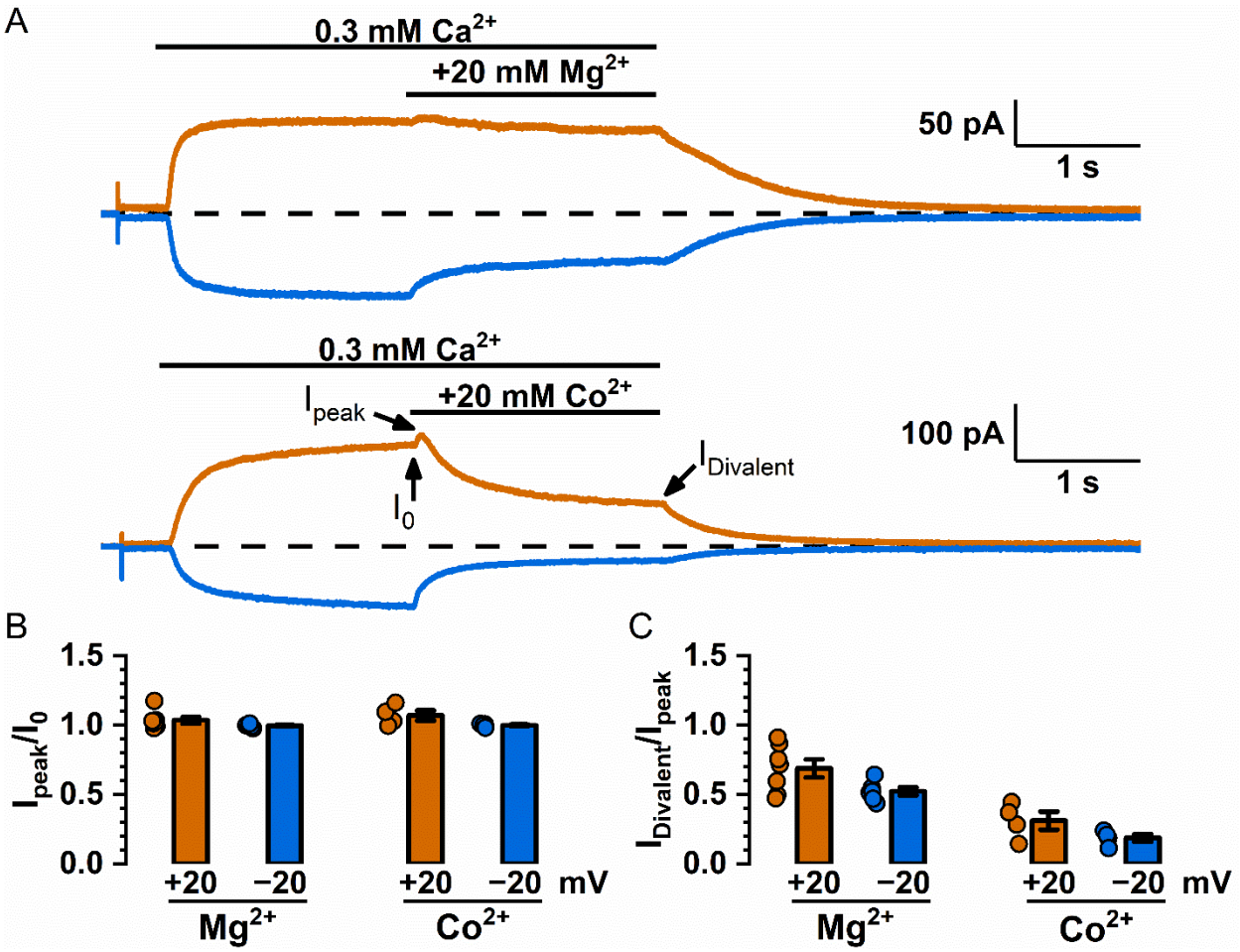

Figure 4.6. Potentiation and inhibition of the Q559W$_{16F}$ current by Mg^{2+} and Co^{2+}. (**A**) Representative recording traces for the Mg^{2+} and Co^{2+} effects on the Q559W$_{16F}$ current (induced by 0.3 mM $[Ca^{2+}]_i$). (**B**) Averaged potentiation (I_{peak}/I_0) of Mg^{2+} and Co^{2+} on the Q559W$_{16F}$ current. (**C**) Averaged inhibition ($I_{Divalent}/I_{peak}$, i.e., I_{Mg}/I_{peak} or I_{Co}/I_{peak}) of Mg^{2+} and Co^{2+} on the Q559W$_{16F}$ current.

The electrostatic potential that increases local $[Cl^-]_i$ and reduces local $[Na^+]_i$ near the pore entrance could alter the calculated Na^+ versus Cl^-

permeability ratio (P_{Na}/P_{Cl}). Controlling the channel's ion selectivity by surface potential has been previously suggested from experimental data [222], as well as by theoretical analyses [223]. Recently, altering the P_{Na}/P_{Cl} ratio of TMEM16F by intracellular Ca^{2+} has been reported [116]. To study the effects of divalent cations on the ion selectivity of TMEM16F, we employed $Q559W_{16F}$ again because a more linear I-V curve in this mutant provides a better tool than WT_{16F} for measuring the reversal potential under asymmetrical ionic conditions [125]. The I-V curves of WT_{16A} and $Q559W_{16F}$ shown in Figure 4.7A,B, respectively, were obtained from currents activated by 20 μM or 1 mM $[Ca^{2+}]_i$, using a voltage ramp from -80 mV to +80 mV. Compared to the symmetrical 140 mM [NaCl] condition, the reversal potentials with 40 mM or 15 mM $[NaCl]_i$ were shifted towards the negative voltage direction for WT_{16A}, but were shifted towards the positive voltage direction for $Q559W_{16F}$, indicating that WT_{16A} is more Cl^- selective, whereas $Q559W_{16F}$ is more Na^+ selective. Interestingly, the calculated P_{Na}/P_{Cl} ratio in $Q559W_{16F}$ showed a large difference between the currents activated by 20 μM $[Ca^{2+}]_i$ and those activated by 1 mM $[Ca^{2+}]_i$—the P_{Na}/P_{Cl} ratios for the currents activated by 20 μM $[Ca^{2+}]_i$ were ~5.5-6.2 versus ~1.3-1.5 for the current activated by 1 mM $[Ca^{2+}]_i$ (Figure 4.7C). In WT_{16A}, the P_{Na}/P_{Cl} ratios between currents induced by 20 μM and 1 mM $[Ca^{2+}]_i$ appeared to be different as well, although the difference was much smaller (Figure 4.7C &

Table 4.1). A significant difference of the P_{Na}/P_{Cl} ratio between low and high $[Ca^{2+}]_i$ conditions is consistent with the previous finding of Ye et al. [116].

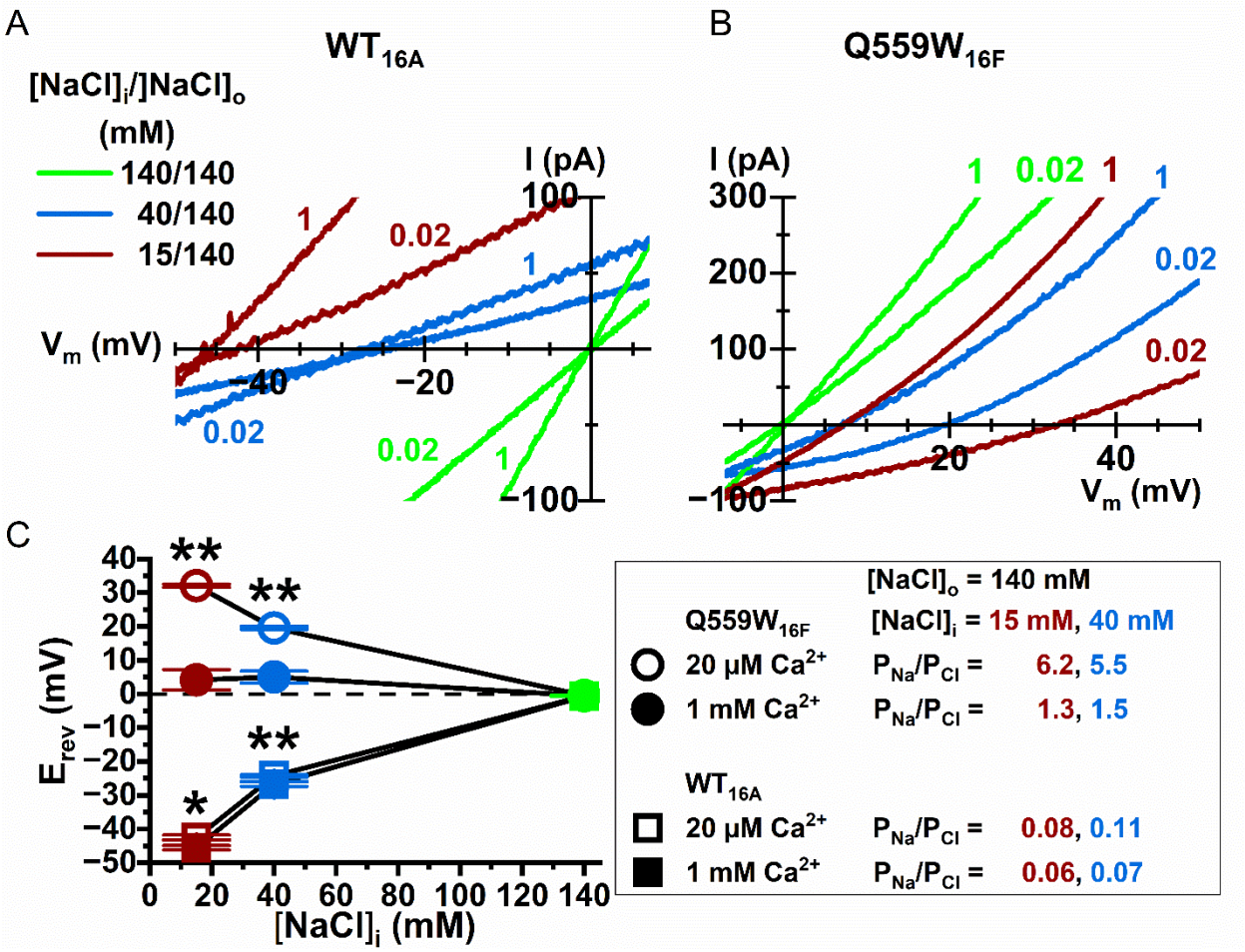

Figure 4.7. Intracellular Ca^{2+} effect on the Na^+ versus Cl^- permeability ratios (P_{Na}/P_{Cl}) of TMEM16 currents. Representative I-V curves for (**A**) WT_{16A} and (**B**) $Q559W_{16F}$ under asymmetrical [NaCl]. $[NaCl]_o$ = 140 mM in all recordings, whereas $[NaCl]_i$ was 140 mM (green), 40 mM (blue) and 15 mM (red), respectively. The reduced $[NaCl]_i$ in the 40 and 15 mM $[NaCl]_i$ solutions was replaced with D-mannitol. Currents were elicited with either

0.02 mM or 1 mM $[Ca^{2+}]_i$, indicated by the colored numbers next to each curve. (**C**) Summary of reverse potential (E_{rev}) measured under asymmetrical [NaCl] for WT_{16A} (squares) and $Q559W_{16F}$ (circles). The P_{Na}/P_{Cl} ratios (calculated based on the Goldman-Hodgkin-Katz equation, see equation 1 in Materials and Methods) of WT_{16A} and $Q559W_{16F}$ are shown in the box on the right and in Table 4.1 (n = 5-15). * $p < 0.05$; ** $p < 0.005$ by one-way ANOVA followed by Bonferroni's multiple comparisons.

Table 4.1. Calculated P_{Na}/P_{Cl} of WT_{16A} and $Q559W_{16F}$.

$[NaCl]_i$‡ (mM)	**$[Ca^{2+}]_i$ (mM)**	**P_{Na}/P_{Cl}**	
		WT_{16A}	**$Q559W_{16F}$**
15	0.02	0.08 ± 0.005	6.2 ± 0.2
	1	0.06 ± 0.004	1.3 ± 0.2
40	0.02	0.11 ± 0.006	5.5 ± 0.4
	1	0.07 ± 0.01	1.5 ± 0.2
70	0.02	--	2.8 ± 0.3
	1	--	--
280	0.02	--	1.7 ± 0.1
	1	--	--

‡ Does not include extraneous Na^+ from NaOH for clarity. However, the extraneous Na^+ was included for the calculation of the P_{Na}/P_{Cl} ratio.

Motivated by the effects of intracellular poly-L-lysine and PIP2 on the divalent-cation activated TMEM16A current (Figure 4.3), we also examined whether the same reagents could alter the P_{Na}/P_{Cl} ratio of $Q559W_{16F}$. Figure

4.8A,B show that treating the intracellular side of the membrane patches with poly-L-lysine (0.3 mg/mL for 5 seconds) reduces the P_{Na}/P_{Cl} ratio of $Q559W_{16F}$, whereas PIP2 (20 μM for 1 min) can reverse the effect of poly-L-lysine. These results demonstrate that the current of TMEM16A and the P_{Na}/P_{Cl} ratio in TMEM16F are both modulated by membrane phospholipid manipulation.

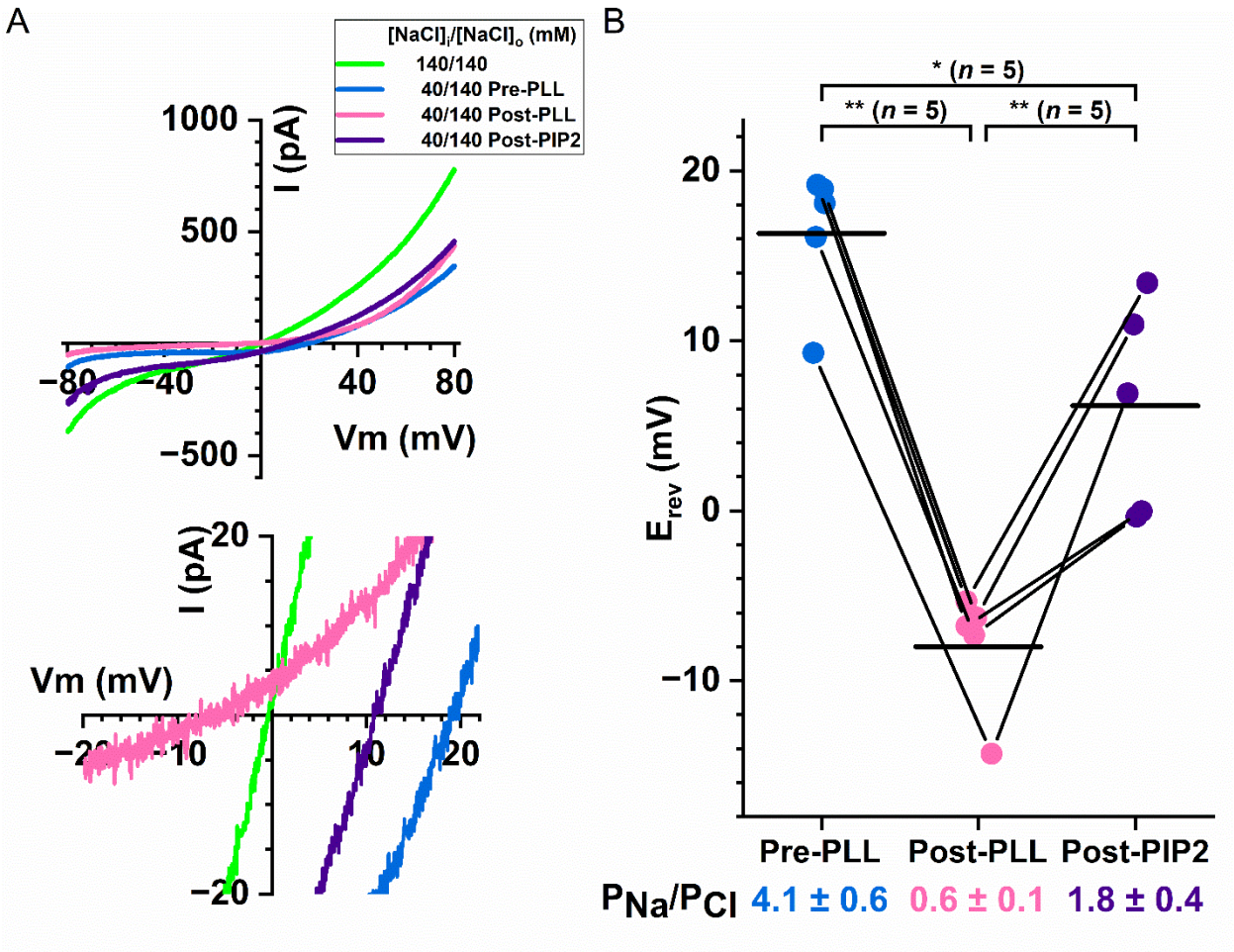

Figure 4.8. Effects of manipulating membrane phospholipids on the P_{Na}/P_{Cl} ratio of $Q559W_{16F}$. All experiments were performed with 20 μM $[Ca^{2+}]_i$. $[NaCl]_o$ = 140 mM in all experiments. (**A**) Representative I-V curves of

$Q559W_{16F}$ in various intracellular solutions; -80 mV to +80 mV are shown in the top panel, whereas the expanded traces near reversal potentials are depicted at the bottom. Experiments were first performed in 140 mM $[NaCl]_i$ (green traces), followed by experiments in 40 mM $[NaCl]_i$ before (blue traces) and after (pink traces) 0.3 mg/mL intracellular poly-L-lysine treatment for 5 s. Finally, the I-V curve was obtained after the patch was intracellularly treated with 20 μM PIP2 for 1 min (purple traces). (**B**) Altering the P_{Na}/P_{Cl} ratio of $Q559W_{16F}$ after treating membrane patches with intracellular poly-L-lysine or PIP2. Results are from experiments like those shown in (A) and data points from the same patch are connected by line segments. Horizontal lines depict the averaged reversal potentials from individual data set. The mean P_{Na}/P_{Cl} ratios (± SEM) at the bottom of the plot were calculated according to equation 1. * $p < 0.05$; ** $p < 0.005$ by one-way ANOVA followed by Bonferroni's multiple comparisons.

Because the degree of current potentiation of TMEM16A induced by divalent cations (such as Mg^{2+}) is roughly similar to that induced by Ca^{2+}, we asked whether intracellular Mg^{2+} can also change the P_{Na}/P_{Cl} ratio of $Q559W_{16F}$. Figure 4.9A,B show experiments in which 20 μM of $[Ca^{2+}]_i$ was used to activate the current. In an asymmetric Cl^- condition in which $[NaCl]_o$ = 140 mM and $[NaCl]_i$ = 40 mM, the P_{Na}/P_{Cl} ratio of $Q559W_{16F}$ was 4.9 ± 0.2 in the absence of Mg^{2+} but was reduced to 2.3 ± 0.1 in the presence of 1

mM $[Mg^{2+}]_i$, a result roughly similar to the effect of 1 mM $[Ca^{2+}]_i$. These results demonstrate that divalent cations other than Ca^{2+} can also alter the P_{Na}/P_{Cl} ratio of $Q559W_{16F}$.

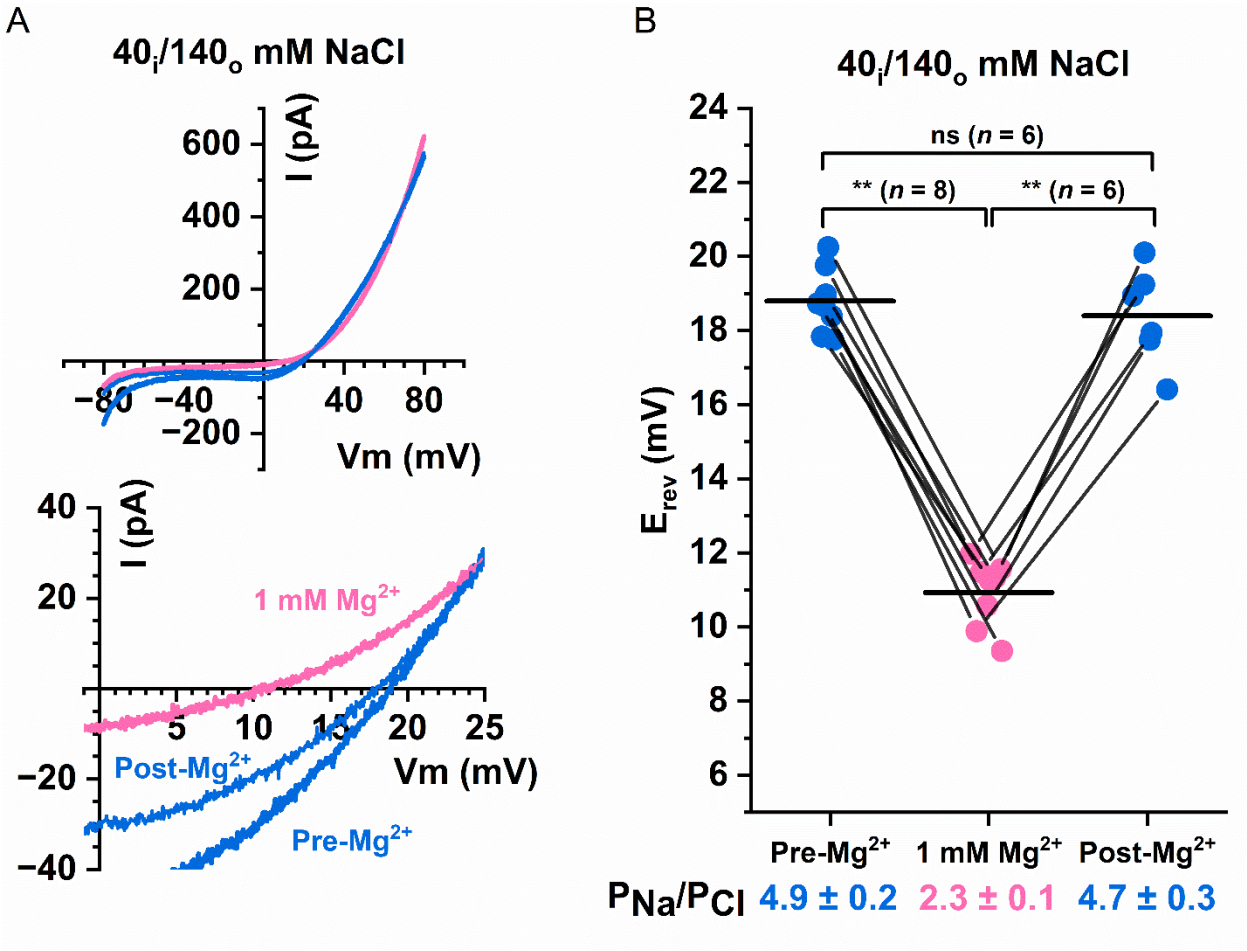

Figure 4.9. Effects of $[Mg^{2+}]_i$ on the P_{Na}/P_{Cl} ratio of $Q559W_{16F}$. (**A**) Representative I-V curves of $Q559W_{16F}$ under asymmetrical [NaCl] in the presence and absence of 1 mM Mg^{2+}. Currents were activated by 20 μM $[Ca^{2+}]_i$. Bottom panel shows the same I-V curves expanded around E_{rev}. (**B**) Paired data showing the values of E_{rev} in the presence (pink circles) of 1 mM

Mg^{2+}, and the values of E_{rev} before Mg^{2+} wash-in and after Mg^{2+} wash-out (blue circles). Horizontal black lines indicate the mean value for each data set. Calculated P_{Na}/P_{Cl} ratios are shown at the bottom of the plot. ns $p >$ 0.05; ** $p <$0.005 by one-way ANOVA followed by Bonferroni's multiple comparisons.

In measuring the P_{Na}/P_{Cl} ratios of $Q559W_{16F}$ with asymmetric [NaCl], we noticed that the P_{Na}/P_{Cl} ratio appears to be affected by $[NaCl]_i$, especially in the experiments with low $[Ca^{2+}]_i$ (20 μM). For example, with 15 mM $[NaCl]_i$, the current induced by 20 μM $[Ca^{2+}]_i$ has a P_{Na}/P_{Cl} ratio of 6.2 ± 0.2, which is significantly larger than the P_{Na}/P_{Cl} ratio of 5.5 ± 0.4 for the current induced by the same $[Ca^{2+}]_i$ in 40 mM $[NaCl]_i$ (Table 4.1). Since the controversial P_{Na}/P_{Cl} ratios from different laboratories were obtained with different intracellular concentrations of monovalent ions [49, 116, 125, 133-135], we examined the effect of $[NaCl]_i$ on the P_{Na}/P_{Cl} ratio more rigorously. In this experiment, we used a non-charged molecule, mannitol, to replace $[NaCl]_i$, and systemically changed $[NaCl]_i$ in intracellular solutions containing 20 μM $[Ca^{2+}]_i$ (Figure 4.10A). The P_{Na}/P_{Cl} ratios of the $Q559W_{16F}$ current at 70 mM and 280 mM of $[NaCl]_i$ were reduced to 2.8 ± 0.3 and 1.7 ± 0.1, respectively, in the same 20 μM $[Ca^{2+}]_i$ (Table 4.1). Figure 4.10 B & C show that the ratio of P_{Na}/P_{Cl} of $Q559W_{16F}$ reduced with an increase of $[NaCl]_i$, suggesting a reduction of cation selectivity in high $[NaCl]_i$. It should be

emphasized that except for the indicated $[NaCl]_i$ the intracellular solutions in these experiments did not include other salts (mannitol was used to replace the reduced $[NaCl]_i$). Although the affinities of phospholipid binding with monovalent cations are lower than those with divalent cations, the monovalent cation Na^+ is likely the culprit rendering the pore of $Q559W_{16F}$ less cation-selective.

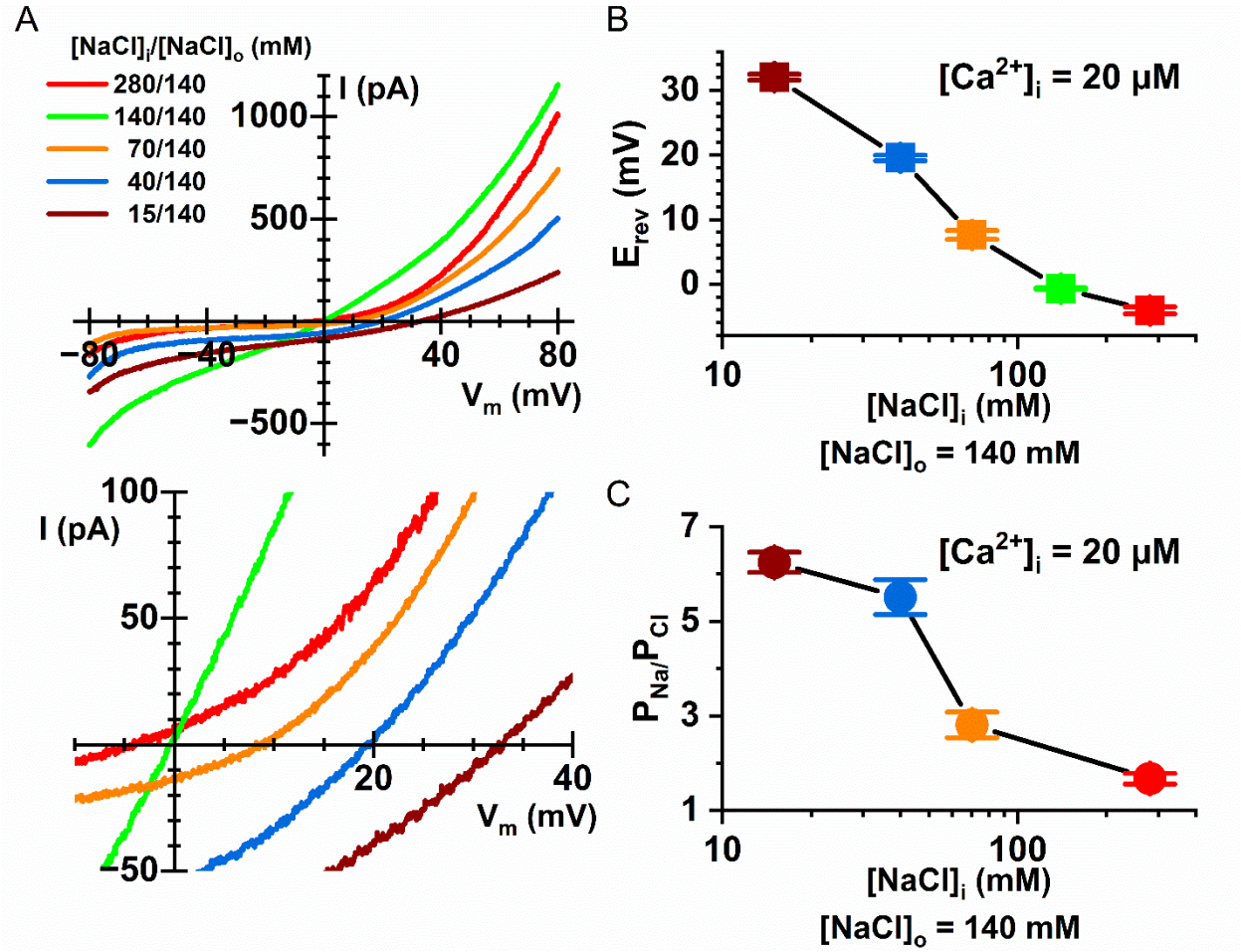

Figure 4.10. Dependence of the P_{Na}/P_{Cl} ratio of $Q559W_{16F}$ on $[NaCl]_i$. (**A**) Representative I-V curves for $Q559W_{16F}$ in various $[NaCl]_i$ (from 15 to 280

mM). In all recordings, $[NaCl]_o$ = 140 mM and the currents were activated by 20 μM $[Ca^{2+}]_i$. The same I-V curves expanded around the E_{rev} are shown in the bottom panel. (**B**) Averaged E_{rev} as a function of $[NaCl]_i$ from the recordings like those shown in A. (**C**) P_{Na}/P_{Cl} ratio as a function of $[NaCl]_i$. Notice the reduction of P_{Na}/P_{Cl} ratio as the $[NaCl]_i$ increases (*n* = 6-22).

The above results are again consistent with the idea that cations bind to membrane phospholipids, alter pore potential and thus change the concentrations of permeant ions near the pore. This electrostatic control exists in both TMEM16A and TMEM16F. For TMEM16F, a change in the local ion concentration results in an alteration of the P_{Na}/P_{Cl} ratio. However, since TMEM16A is much more selective for anions, the effect manifests as a potentiation of the anion flux through the pore. The phospholipids could reside within the pore, or at locations outside the pore within a distance short enough for an electrostatic effect (such as a position confined by helices 3, 4 and 5, see Figure 4.11), or both. The fact that the P_{Na}/P_{Cl} ratio depends on divalent and monovalent cations and that the affinities of these cations to generate the effects are low (mM or above) further suggest that the binding of these cations is rather non-specific.

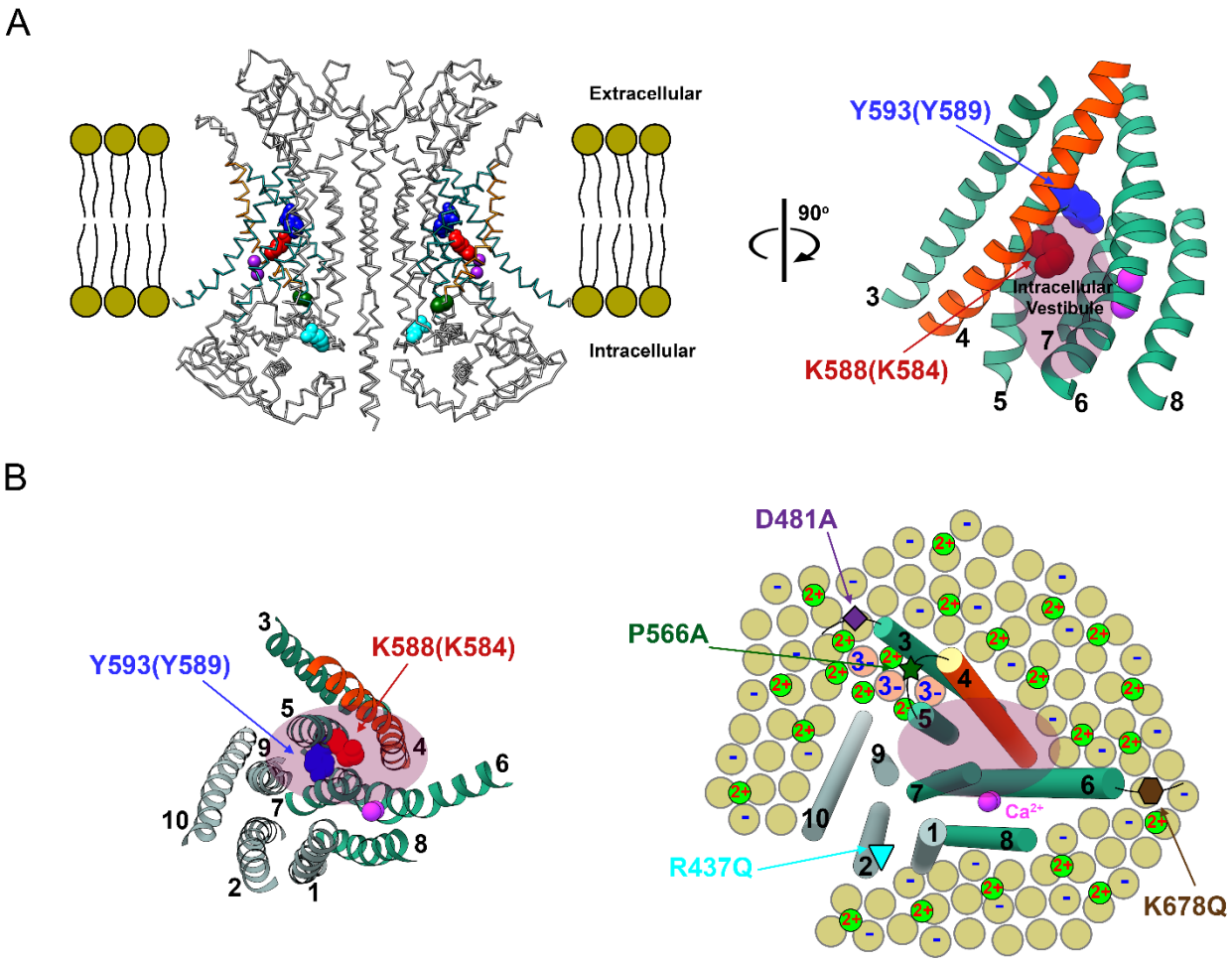

Figure 4.11. Illustration of divalent cation effects on TMEM16 molecules. (**A**) High resolution structure of the "ac" alternatively spliced variant of TMEM16A (left, PDB:5OYB). The six transmembrane helices (helices 3-8) of a single subunit forming the ion-conduction pathway are rotated 90° clockwise along the axis perpendicular to the cell membrane (right). Helix 4 is colored in orange, whereas all other helices are colored in green. Residue K584 of the alternatively-spliced "a" variant of TMEM16A (used in our experiments) and residue Q559 of TMEM16F corresponds to residue K588 of

the TMEM16A “ac” variant (colored in red). Y589 of the TMEM16A “a” variant mentioned in the text corresponds to Y593 in the TMEM16A “ac” variant (colored in blue). Light purple oval roughly depicts the intracellular pore vestibule. (**B**) Intracellular view perpendicular to the cell membrane of a single subunit. (Left) all transmembrane helices (with helix numbers) are shown. (Right) Cartoon model of the six pore-forming helices depicted as cylinders (same orientation as that in the left panel). Intracellular leaflet of cell membranes contains negatively charged phospholipids (yellow circles labeled with “-”) as well as neutral ones (yellow circles without “-”). PIP2 molecules are depicted as salmon-color circles with “3-”. The Ca^{2+} ions at the activation sites are colored in pink. Monovalent (not shown), divalent (depicted as small green circles) or even multivalent cations (not shown) can bind to phospholipid head groups, consequently decreasing the negative potential from phospholipids. Four mutations associated with PIP2 regulations of TMEM16A studied in this paper are shown. Notice that residues P556 (dark green star) and D481 (purple diamond) appear to be closer to the intracellular pore vestibule than residues R437 (cyan down triangle) and K678 (brown hexagon).

4.5 Discussion

Ion channels reside in lipid membranes, and thus membrane phospholipids can control the function of ion channels in multiple ways. PIP2,

for example, directly interacts with various ion channels to regulate their functions [224]. The stabilization of the activity of voltage-gated Na^+ channels by extracellular divalent cations was attributed to a membrane surface potential effect resulting from divalent cations binding to membrane phospholipids [216, 217, 225]. It has also been well documented that membrane surface potential can control the conductance of ion channels via altering the local ion concentrations near the cell membrane [214, 218, 219, 226]. For TMEM16 proteins, depletion of PIP2 from the recorded membrane patches has been shown to reduce the apparent Ca^{2+} affinity for the activation of TMEM16F [147]. PIP2 also affects the rundown of TMEM16A and TMEM16F, perhaps by binding to domains formed by helices 3-5, as well as other parts of the molecules [127, 146-148]. These examples underlie the critical interaction between membrane phospholipids and channel proteins. Here, we suggest that phospholipids that are tightly associated with TMEM16 molecules may participate in forming cation-binding sites in or near the intracellular ion-transport pathway and that the binding of intracellular cations to the phospholipids alters pore potential and thus modulates ion permeation.

4.5.1 Divalent cations potentiate the current of TMEM16A

All divalent cations and even the monovalent cations tested in the present study modulate the ion permeation of TMEM16 proteins at low affinities. In TMEM16A, generating the current potentiation requires at least

hundreds of μM to mM Co^{2+} and alkaline earth divalent cations (Figure 4.1, also see [212]). The apparent affinity for monovalent cations (such as Na^+) to modulate the ion permeation of TMEM16 molecules appears to be even lower, based on the observation that the calculated P_{Na}/P_{Cl} ratios of TMEM16F at 15-40 mM $[NaCl]_i$ are significantly different from those obtained at 70-280 mM $[NaCl]_i$ (Figure 4.10). These very low affinities are similar to the binding affinities between phospholipids and various cations documented in the literature [207, 208]. We thus suspected that divalent cations may bind to membrane phospholipids and mediate the effects by altering the membrane surface potential [214, 215, 227]. To examine whether the potentiation of TMEM16A current by divalent cations involves phospholipids, we conducted several lines of experiments. We first found that treating excised membrane patches with intracellularly applied poly-L-lysine for only 5 s reduced the potentiation of TMEM16A by divalent cations, whereas applying PIP2 can reverse the effect of poly-L-lysine (Figure 4.3). Secondly, the rundown of the TMEM16A current, a phenomenon thought to be due to phospholipid depletion, was correlated with a reduction in the current potentiation (Figure 4.4A,B). Finally, mutations thought to decrease PIP2 binding to TMEM16A also reduce divalent cation-induced potentiation (Figure 4.4D). These results support the idea that phospholipids are involved in the divalent cation-mediated potentiation of the TMEM16A current. It is possible that phospholipids are located at positions close to the pore of TMEM16A,

and thus the binding of divalent cations can attract more Cl^- to the intracellular pore entrance. A depletion of negatively charged phospholipids (for example, PIP2) would thus result in less divalent cation binding to the pore region and weaken the current potentiation.

Because divalent cation-mediated potentiation appears to involve phospholipids, we further examined if the control is electrostatic in nature. Our results revealed that the potentiation of the outward TMEM16A current was significantly enhanced in solutions with a lower ionic strength (Figure 4.5), a phenomenon consistent with an electrostatic mechanism. We also compared the degree of potentiation between TMEM16A and a CLC channel because of the difference of the pore structures between these two types of Cl^- channels (Figure 4.S1). Indeed, the same concentration of intracellular Mg^{2+} had a significantly smaller potentiation effect in a CLC channel compared to that in TMEM16A (Figure 4.S1C), a phenomenon that is likely due to the closer location of phospholipids to the intracellular pore vestibule of TMEM16A. It is interesting that the various mutations thought to alter the interaction of PIP2 with TMEM16 molecules reduce the Co^{2+}-induced potentiation with different strengths (Figure 4.4D). Based on the cartoon in Figure 4.11B (right), where the locations of these four mutated residues relative to the pore vestibule are depicted, the strengths of the mutation effects may depend on the distance of these residues to the intracellular pore entrance. For example, mutations of D481 and P556 are known to

affect the PIP2 located within a cavity formed by helices 3, 4 and 5 [146], a location quite close to the intracellular pore vestibule. Therefore, mutations reducing the amount of phospholipids at these positions are expected to exert a larger effect than the mutations located farther away (such as R437 and K678). Although other speculations may also exist, an electrostatic mechanism is consistent with the observation that larger effects occur at those two mutations closer to the pore vestibule.

4.5.2 Intracellular cations alter the ion selectivity of TMEM16F

If the TMEM16A current potentiation is mediated by a change of the potential near or within the pore, binding of divalent cations to the pore region is expected to cause an increase of local $[Cl^-]_i$ and a decrease of local $[Na^+]_i$. In an ion transport pathway that conducts both cations and anions (such as TMEM16F), an increase in Cl^- conductance would be canceled out by a decrease in Na^+ conductance. Our experiments indeed show that the current potentiation by high concentrations (20 mM) of divalent cations is much smaller in $Q559W_{16F}$ (Figure 4.6 A,B). Nonetheless, the changes in local anions and cations are expected to alter the calculated cation versus anion selectivity, as shown elegantly in a theoretical analysis [223]. Our experimental results confirm that the cation selectivity of $Q559W_{16F}$ in 1 mM $[Ca^{2+}]_i$ (P_{Na}/P_{Cl} = ~1.3-1.5) was significantly smaller than that in 20 μM $[Ca^{2+}]_i$ (P_{Na}/P_{Cl} = ~5-6) (Figure 4.7 and Table 4.1). Such effects of Ca^{2+} on

the P_{Na}/P_{Cl} ratio of $Q559W_{16F}$ are consistent with those observed in WT_{16F} reported by Ye et al. [116].

Monovalent ions appeared to modulate the ion selectivity of TMEM16 proteins as well, as shown by the dependence of the P_{Na}/P_{Cl} ratio of $Q559W_{16F}$ on $[NaCl]_i$ (Figure 4.10 and Table 4.1). With $[Ca^{2+}]_i$ = 20 μM, the P_{Na}/P_{Cl} ratios of $Q559W_{16F}$ were ~5-6 in 15-40 mM $[NaCl]_i$. When $[NaCl]_i$ was increased to 70-280 mM, the calculated P_{Na}/P_{Cl} ratio was reduced to ~2. The binding affinities of phospholipids with monovalent cations have been shown to be lower than those with divalent cations and could be in the range of tens to hundreds of mM [207, 208]. The observation that the P_{Na}/P_{Cl} ratios at 15 and 40 mM $[NaCl]_i$ were more similar to each other than to those at 70 mM $[NaCl]_i$ is consistent with such a very low binding affinity between phospholipids and monovalent cations.

4.5.3 Modulations of TMEM16A and TMEM16F ion permeations result from the same mechanism

Although divalent cations significantly alter the P_{Na}/P_{Cl} ratio of TMEM16F, their effects on TMEM16A are manifested as an increase in the Cl^- current because Na^+ flux through TMEM16A is nearly negligible. The degree of potentiation of the WT_{16A} current by divalent cations was larger at +20 mV (inward Cl^- flux) than at -20 mV (outward Cl^- flux). Since it was the intracellular divalent cations that were manipulated, the change in the surface charge should have been more prominent on the intracellular side of

the membranes. A weaker potentiation of the inward current (outward Cl^- flux) therefore contradicts to the classical Gouy-Chapman theory [214]. However, a more realistic surface potential model normally requires taking the location of the surface charge into account, as elaborated by the Stern theory [214, 215, 218, 228]. The anomaly of a larger potentiation at +20 mV, for example, could result from the voltage-dependent binding of these modulating divalent cations if the binding sites are located within the membrane electric field. Interestingly, the effect of $[Ca^{2+}]_i$ on the P_{Na}/P_{Cl} ratio of TMEM16F was also shown to be voltage dependent—in the same $[Ca^{2+}]_i$, the TMEM16F pore was more selective for anions at more positive membrane voltages [116]. In the present study (Figure 4.5), the potentiation of TMEM16A current was enhanced at +20 mV but not at -20 mV in symmetrical 40 mM [NaCl], a phenomenon that can also be explained by the idea that monovalent cations (such as Na^+) modulate the pore potential of TMEM16A in a voltage-dependent way.

Although the divalent cation effects on altering TMEM16F's P_{Na}/P_{Cl} ratio have been reported by Ye et al [116], our results here provide a more general insight underlying the modulation of the ion permeation of TMEM16 molecules. In both TMEM16A and TMEM16F, we observed several common features. First, we observed that all divalent cations and even monovalent cations can exert the effect with very low affinities, suggesting a non-specific binding. Second, we showed that phospholipids are involved in the

modulation mechanisms. Third, the degree of modulation is different in solutions with different ionic strengths. These results led us to conclude that the potentiation of the TMEM16A current and the alteration of P_{Na}/P_{Cl} ratio of TMEM16F result from the same electrostatic mechanism—intracellular divalent and monovalent cations likely bind to membrane phospholipids, thus modulating ion fluxes by altering the pore potential.

4.5.4 Implication of the modulation of TMEM16 current by intracellular cations

The insight from the present study led us to recover a coherent picture from the apparently controversial results of TMEM16F's ion permeability in the literature—experiments with high concentrations of cations (including monovalent cations) on the intracellular side all showed a small P_{Na}/P_{Cl} ratio (less cation selective). In fact, this phenomenon is not limited to TMEM16F, but appears to be also present in TMEM16A. When using 20 μM $[Ca^{2+}]_i$ to activate the current of WT_{16A}, for example, the reversal potentials in solutions containing only 40 mM $[NaCl]_i$ in this study (~-26 mV, see blue open squares in Figure 4.7A) were significantly smaller than those values (~-30 to -31 mV) when the reduced $[NaCl]_i$ was replaced with NMDG-Cl [107]. Thus, even in a quite anion-selective channel such as WT_{16A}, if non-permeant monovalent cations (such as $NMDG^+$) are used to replace the reduced $[Na^+]_i$, the estimated P_{Na}/P_{Cl} ratio is slightly smaller than those from experiments where non-charged molecules (such as D-mannitol) were used

to replace monovalent cations. This insight thus explains why TMEM16F is very cation-selective (P_{Na}/P_{Cl} = 6-7) in excised membrane patch experiments in very low $[NaCl]_i$ (for example, 15 mM) than in whole-cell recording experiments where physiological cation concentrations were present inside the cell.

It should be emphasized that although divalent cations exert a powerful effect on the calculated permeability on TMEM16F, a modulation resulting from altering the pore potential does not change the "intrinsic selectivity" of the channel pore [223]. The electrostatic control of the permeability ratio of two ions will occur if the two ionic species are of different valences. For two permeant ions with opposite charges traversing the pore (such as that in TMEM16F), the calculated permeability can be changed from more cation-selective to more anion-selective by means of a change in surface potential of tens of mV [223]. Such a degree of membrane surface potential perturbation is easily attainable by adding mM divalent cations [217, 228, 229].

Our studies thus clarify the biophysical mechanism of the divalent cation modulation on the ion permeation of TMEM16 molecules. The results, however, raise a question regarding the physiological role of this modulation. In vitro experiments show that the TMEM16F current can have a P_{Na}/P_{Cl} = 6-7 at low $[NaCl]_i$ (such as 15 mM). This high P_{Na}/P_{Cl} ratio only exists if no other monovalent cations are present in the intracellular solution. In a

physiological context, however, a high concentration of monovalent cations (such as K^+) is present in cytosols. At the same time, the cytosolic solution also contains mM Mg^{2+} and other cations with multiple charges. As shown in Table 4.1, even with 70 mM intracellular monovalent cations, the P_{Na}/P_{Cl} ratio is already reduced to ~2 in the absence of $[Mg^{2+}]_i$. A physiological concentration (>100 mM) of intracellular monovalent cations and mM $[Mg^{2+}]_i$ likely maintains a steady surface potential that renders TMEM16F non-selective even with a fluctuation of $[Ca^{2+}]_i$ from the sub-μM to μM level. What then is a possible physiological role for this modulation of ion permeation function of TMEM16 molecules? We speculate that the significance of this electrostatic control may lie in the metabolism of negatively charged phospholipids. For example, activation of G-protein-coupled receptors is known to stimulate phospholipase C activity, leading to the degradation of PIP2 [224]. Such a reduction in the amount of PIP2 in the inner leaflet of cell membranes might alter the electrostatic potential near the pore entrance of TMEM16 molecules and thus modulate ion permeation. It will require experiments in more physiological conditions to confirm or refute this possibility of controlling the ion permeation through TMEM16 molecules via synthesis and degradation of membrane phospholipids.

4.6 Supplementary Materials

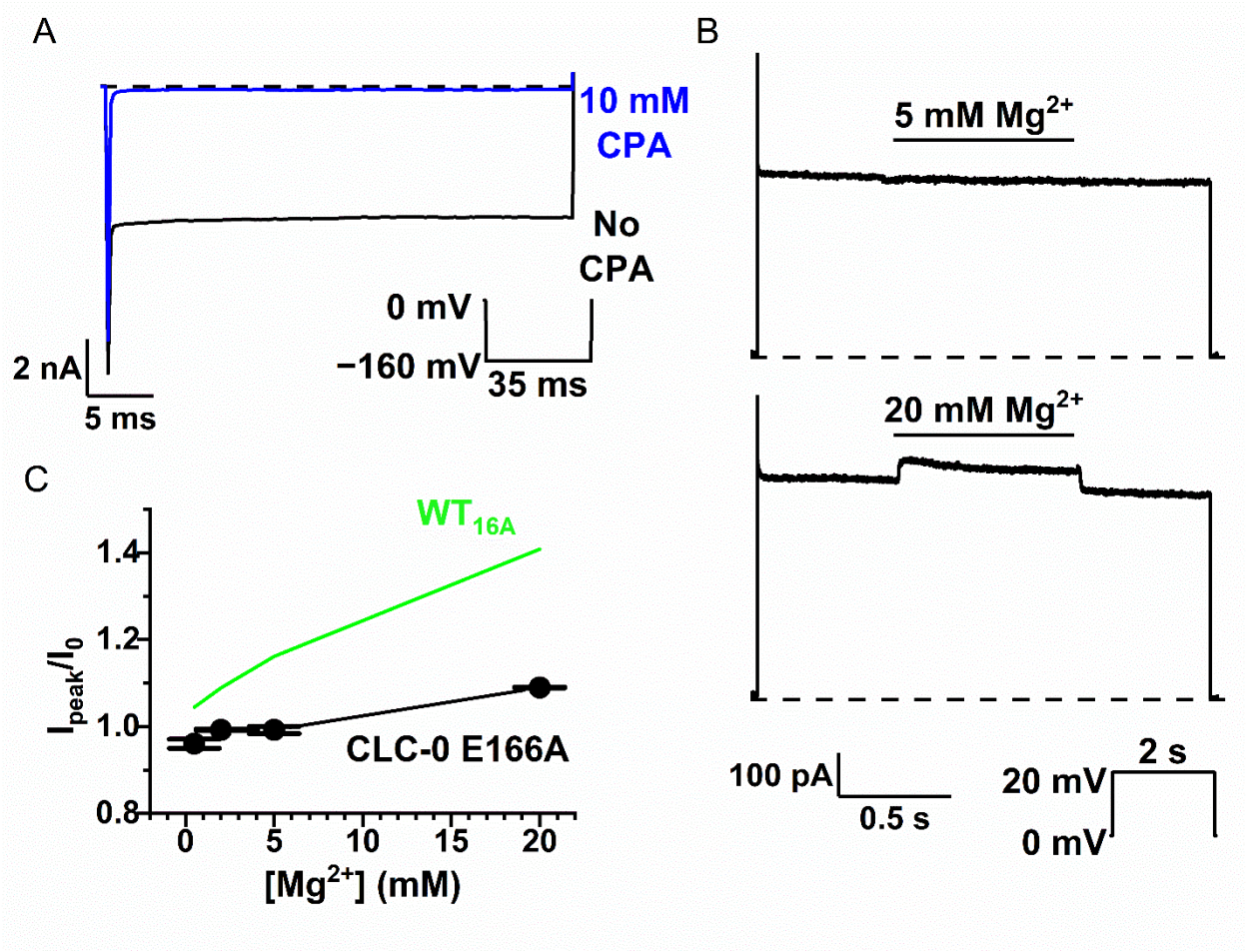

Figure 4.S1. Potentiation of the current of E166A$_{CLC0}$ by intracellular Mg^{2+}. (A) Nearly complete current block of E166A$_{CLC0}$ by 10 mM CPA at -160 mV to ensure that the majority of the current in the recording patch was from the CLC-0 mutant. Horizontal dashed line indicates zero-current level. Inset shows the voltage protocol (from 0 mV to -160 mV) used to induced the current. **(B)** Representative traces showing the effect of 5 mM (upper panel) and 20 mM Mg^{2+} (lower panel) on the current of E166A$_{CLC0}$ at +20

mV. Inset shows the voltage protocol (0 mV to +20 mV) used for the experiments. Dashed lines are the zero-current level. **(C)** Dose-dependent Mg^{2+} potentiation of the $E166A_{CLC0}$ current (n = 3). The solid green line represents the Mg^{2+}-dependent potentiation of WT_{16A}.

4.7 Author Contributions

Conceived and designed the experiments: DMN, TC. Performed the electrophysiological experiments: DMN, HCK, TC. Analyzed the data, DMN, HCK, TC; Contributed reagents/materials/analysis tools: DMN, TC. Wrote the paper: DMN, TC.

4.8 Acknowlegements

Generating the cDNA constructs of the TMEM16A and CLC-0 mutants used in this study by Dr. Wei-Ping Yu is acknowledged. We also thank Dr. Robert Fairclough for his helpful suggestions and critical reading of the manuscript.

Chapter 5: Dissertation Summary and discussion

5.1 Preface

Electrochemical gradients drive ion permeation through ion channel pores. However, ions must overcome several barriers to cross the cell membrane. In solution, water molecules form a solvation shell around ions. Generally, ion transports are facilitated after the solvation shell is stripped. For example, the ion selectivity filter of voltage-gated K^+ channels contains the conserved sequence TVGYG [230]. As K^+ ions travel through the selectivity filter, water molecules in their solvation shell are replaced by the backbone carbonyl of the conserved sequence [230]. This dissertation examines the protein-ion interactions that affect ion permeation in TMEM16A and TMEM16F.

We do not have a complete picture of ion permeation in TMEM16 proteins. Generally, TMEM16 CaCCs are anion-selective, whereas conductive TMEM16 phospholipid scramblases are non-selective. One of the most well-studied TMEM16 CaCCs is TMEM16A. The ion permeability of the unidentified CaCC had been studied extensively even before the discovery of the TMEM16 family. Qu et al. (2000) reported that the endogenous CaCC in *Xenopus laevis* oocyte, later identified as TMEM16A in 2008 [7], is more permeable to larger anions, which require less energy to desolvate than smaller anions [193]. They also show that the channel has a higher conductance when the

permeant anion is smaller and that SCN^- or $C(CN)_3^-$ can block Cl^- current [193]. Therefore, smaller anions can enter the pore easier than larger anions, but larger anions can occupy the pore for a longer time. While weak interactions between ions and pore residues are essential for the ion desolvation process, interactions between ions and pore residues could also hinder ion conduction. Thus, ion channels maintain optimal interactions with permeant ions to achieve high conductivity and selectivity. A similar idea likely applies to phospholipid transport. Phospholipid transporters need to facilitate the movement of phospholipids across the cell membrane without binding to them too tightly. Since most TMEM16 proteins are phospholipid scramblases, phospholipids may also interact with permeant ions and affect ion permeation.

One of the most well-studied TMEM16 phospholipid scramblases is TMEM16F. The anion permeability of TMEM16F resembles that of TMEM16A [7, 115, 123, 130, 133, 135, 136]. In chapter 2, we reproduce the results reported in the literature. Both TMEM16A and TMEM16F have a similar relative anion selectivity sequence, $SCN^- > I^- > Cl^-$. However, TMEM16F is much more permeable to cations than TMEM16A. TMEM16A and TMEM16F also exhibit different current-voltage (I-V) relationships. At saturating concentration of Ca^{2+}, TMEM16A exhibits a linear I-V relationship [7, 8, 107, 115], whereas TMEM16F exhibits an outwardly rectified I-V relationship [49].

This dissertation examines the ion permeation in both TMEM16A and TMEM16F using electrophysiological and biochemical techniques. First, the molecular mechanisms behind the I-V relationships of TMEM16A and TMEM16F are explored. Second, how divalent cations binding to regions outside the high-affinity binding sites affect ion permeation in these proteins is examined. Finally, this dissertation also addresses the controversial ion selectivity of TMEM16F and proposes a potential mechanism of how membrane phospholipids can modulate ion permeation in TMEM16A and TMEM16F.

5.2 Molecular mechanism behind the I-V relationship of TMEM16A

Chapter 2 demonstrates how K584, a pore-lining residue, affects the current-voltage relationship of TMEM16A. In wild-type TMEM16A, K584 seems to attract nearby anions to the intracellular vestibule. Thus, neutralizing this residue eliminates this interaction and reduces the local concentration of anions near the intracellular vestibule. Consequently, anion efflux is reduced, leading to an outwardly rectified I-V relationship. Making this residue more negatively charged has an even more pronounced effect. Both TMEM16A K584E and TMEM16A K584D have a significantly more outwardly rectified I-V curve than wild-type TMEM16A. Similar to charge-altering mutations, the modification of TMEM16A K584C by methanethiosulfonate (MTS) reagents result in a similar shift in the degree of outward rectification. Namely, a positively charged MTS reagent results in

a more linear I-V relationship, whereas a negatively charged MTS reagent results in a more outwardly rectified I-V relationship. Chapter 2 also shows that the intracellular pH controls TMEM16A K584H's I-V curve rectification by controlling the charge of the introduced histidine residue. Consistent with previous manipulations, the I-V relationship of TMEM16A K584H becomes more linear as the intracellular pH decreases.

The electrostatic control of the I-V relationship of TMEM16A by K584 occurs at saturating concentrations of Ca^{2+} and is similar to electrostatic effect that the Ca^{2+} bound to the channel [125] has on ion permeation. Electrostatic control of ion conduction and permeation can be seen with nicotinic acetylcholine receptors (nAChRs), in which rings of negatively charged residues at both the extracellular and intracellular pore entrances influence the conductance and ion selectivity of nAChRs [195, 231, 232]. Similarly, K584 appears to be a determinant of TMEM16A's conductance. Nonstationary noise analysis of TMEM16A K584E and wild-type TMEM16A shows that the charge-reversal mutation reduces the single-channel conductance of TMEM16A by a factor of ~2.5 [106]. Similar to TMEM16A, charge-reversal mutation of the rings of charged residues in the *Torpedo californica* AChR also affects the I-V relationship of the channel [195].

The residue in TMEM16F corresponding to K584 in TMEM16A is Q559. However, this residue's charge does not seem to have the same effect on the I-V relationship of TMEM16F. Thus, the molecular mechanism behind the

outwardly rectified I-V relationship of TMEM16F is different from that of TMEM16A. Placing an aromatic but not a charged amino acid at position 559 alters TMEM16F's I-V relationship. Wild-type TMEM16F has an outwardly rectified I-V relationship, whereas the I-V curves of aromatic Q559 mutants are less outwardly rectified. Interestingly, replacing Q559 with an aromatic or a basic residue also attenuates channel rundown without altering the ion selectivity of TMEM16F. However, the mechanism behind how these Q559 mutants affect ion conduction in TMEM16F is still unresolved.

Nonetheless, the TMEM16F mutants resistant to channel rundown and exhibiting a more linear I-V curve will be helpful in future studies. The high degree of outward rectification makes the identification of reversal potential from I-V curves difficult, and the reduction in conductance over time due to channel rundown introduces confounding variables into electrophysiological experiments. Thus, utilizing rundown-resistant mutants of TMEM16F will allow for more reliable reversal potential measurements. The rundown of TMEM16F currents has been linked to the depletion of PIP2 from the cell membrane [147]. However, it is unclear whether rundown-resistant mutants of TMEM16F reduce the dissociation of PIP2 from the channel or stabilize the conductive state of the channel.

5.3 Divalent cations affect ion permeation in TMEM16A and TMEM16F

Chapters 3 and 4 show that divalent cation binding to locations other than the high-affinity Ca^{2+}-binding sites can modulate ion permeation in

TMEM16A and TMEM16F. Using Co^{2+} as a probe, we found that Co^{2+} serves as a competitive inhibitor for Ca^{2+} binding to the high-affinity Ca^{2+}-binding sites, thus inhibiting the Ca^{2+}-induced current in TMEM16A. This competitive inhibition is similar to the inhibition effect of Mg^{2+}, which also competes with Ca^{2+} and inhibits TMEM16A [115]. Besides serving as competitive inhibitors, Co^{2+} and Mg^{2+} also potentiate the current of TMEM16A with very low affinity (mM or above). This potentiation effect has several characteristics. First, it is not specific to Co^{2+} and Mg^{2+}, and other divalent cations, including (but not limited to) Sr^{2+} and Ba^{2+}, can potentiate TMEM16A currents with similarly low affinities, all at ~mM concentrations. Second, the potentiation occurs even when the channel is saturated with Ca^{2+}, and the degree of potentiation is not affected by the Ca^{2+} concentration used to activate the channel. Therefore, the potentiation effect is likely due to divalent cations binding at sites other than the high-affinity Ca^{2+}-binding sites responsible for channel activation. The low-affinity and non-specific binding of divalent cations led us to conclude that phospholipids may form these binding sites; The affinities of divalent cation binding to phospholipids are also in the mM range [207, 208, 233, 234]. The binding of divalent cations to membrane phospholipids can alter the membrane surface potential [227], which then attracts or repels permeant ions. We believe that the current potentiation elicited by mM divalent cations likely comes from an increase in positive electrostatic potential near the intracellular pore entrance of TMEM16A.

Therefore, divalent cation binding to membrane phospholipids increases the local Cl^- concentrations, leading to additional Cl^- ions going through the pore. To exert such an electrostatic effect on ion permeation, divalent cations need to be near the ion permeation pathway of TMEM16A. In support of these divalent cation binding sites locating within the membrane electric field, chapter 3 shows that the divalent cation potentiation exhibits voltage dependence, with potentiation being favored at depolarized membrane potentials.

In contrast to TMEM16A, divalent cations only inhibit TMEM16F, likely by competing with Ca^{2+}, and do not potentiate the current of TMEM16F. Since TMEM16F is permeable to both cations and anions, we believe that an increase in positive electrostatic potential near the intracellular pore entrance would attract anions to the pore and repel cations away from the pore, leading to little to no net increase in current. Therefore, we postulated the change in electrostatic potential would affect the ion-selectivity of TMEM16F. Indeed, chapter 4 shows that 1 mM of either Ca^{2+} or Mg^{2+} decreases the relative sodium-to-chloride permeability ratio (P_{Na}/P_{Cl}) of TMEM16F. While other explanations for the shift in ion selectivity exist, we attributed the effect to a change in electrostatic potential at the pore entrance.

Thus, chapters 3 and 4 suggest that TMEM16A and TMEM16F may have additional non-selective, low-affinity binding sites for divalent ions.

Since divalent cations bind to phospholipids with low affinity [207, 208, 233, 234], and the intracellular vestibule of TMEM16 proteins are partially exposed to membrane phospholipids, pore-lining phospholipids can potentially act as divalent cation binding sites. However, it is important to note that these binding sites' location remains unresolved, and structures of TMEM16 proteins with membrane phospholipids are not yet available. Thus, the locations of these low-affinity divalent cation binding sites require further clarification.

Also, other factors may contribute to the potentiation effect described above. For instance, divalent cations, especially at mM concentrations, have been shown to have a significant effect on cell membranes' structure [235], and molecular dynamic simulations of lipid translocation in nhTMEM16 suggest that membrane thinning at the ion permeation/phospholipid transport pathway of TMEM16 proteins facilitates the movement of ions and phospholipid head groups [144]. Thus, changes to cell membrane structure may contribute to the potentiation effect. Also, there is a possibility that divalent cations can increase leak current. However, we have addressed this possibility in chapter 3. First, we show that 20 mM Co^{2+} alone can not activate TMEM16A. Second, we show that mutating a pore residue in TMEM16A, Y589, also affects the Co^{2+} potentiation of Ca^{2+}-activated Cl^- currents. Thus, the additional current elicited by divalent cations likely

comes from additional ions going through the pore of TMEM16A rather than elsewhere.

5.4 Factors contributing to the controversial ion selectivity of TMEM16F

Few disagreements exist regarding the ion selectivity of TMEM16 CaCCs. However, the ion selectivity of TMEM16 scramblases has been controversial, with contradicting P_{Na}/P_{Cl} reported in the literature. Chapter 4 focuses on TMEM16F, the most extensively investigated TMEM16 phospholipid scramblase. Initially, K584 in TMEM16A and Q559 in TMEM16F were thought to control the ion selectivity of the two channels [49]. This hypothesis was driven by the fact that only anion-selective TMEM16A and TMEM16B have a positively charged residue at their intracellular vestibule (K584 and K629, respectively), and all other known TMEM16 proteins have an uncharged residue (Gln, Asn, or Tyr) at this location. Indeed, one research group reported that the K584Q mutation renders TMEM16A more permeable to Na^+ and less permeable to Cl^-, whereas the Q599K mutation renders TMEM16F less permeable to Na^+ and more permeable to Cl^- [49]. However, this shift in ion selectivity was not reproduced by others [107, 134].

The idea that electrostatic interaction between pore-lining residues and permeant ions can influence ion selectivity is not new. For example, eukaryotic voltage-gated Na^+ channels' ability to select Na^+ over Ca^{2+} has

been attributed to lysine residues in their selectivity filter [236]. Although Na^+ and Ca^{2+} have a similar ionic radius, ~1.00 Å, Ca^{2+} has a larger charge density [237, 238]. Thus, the electrostatic repulsion between the lysine residues and Ca^{2+} likely allows voltage-gated Na^+ channels to select Na^+ over Ca^{2+}.

If the idea that pore residues can control ion permeation is not out of the ordinary, why are there many conflicting reports on the ion selectivity of TMEM16F in the literature? Studies that support a more cation-selective TMEM16F report a P_{Na}/P_{Cl} between ~1.4 and ~6.8 [49, 95, 108]. In contrast, studies that suggest a more anion-selective TMEM16F report a P_{Na}/P_{Cl} of less than 1 [133-136]. Chapter 4 suggests that the varying ionic conditions between electrophysiological experiments contribute to the controversial ion selectivity of TMEM16F. Consistent with another report [116], chapter 4 shows that TMEM16F is more cation-selective (P_{Na}/P_{Cl} ~6) when activated with 20 μM Ca^{2+}, but is less cation-selective (P_{Na}/P_{Cl} ~1) when activated with 1 mM Ca^{2+}. However, chapter 4 shows that Mg^{2+} also alters the ion selectivity of TMEM16F. In the presence 1 mM Mg^{2+}, a physiological concentration of Mg^{2+}, TMEM16F is also much less cation-selective (P_{Na}/P_{Cl} ~2) when activated with 20 μM Ca^{2+}. Thus, the presence of Mg^{2+} likely contributes to the controversial ion selectivity of TMEM16F since experiments that utilized whole-cell patch-clamp configuration tend to report a less cation-selective channel [108, 133-136]. In whole-cell patch-clamp

experiments, the intracellular solutions usually contain ~1-2 mM Mg^{2+} to mimic the physiological concentration of Mg^{2+}.

The outward rectification of TMEM16F current is another factor that may contribute to the varying P_{Na}/P_{Cl} of TMEM16F in the literature. TMEM16F current is significantly smaller at negative membrane potentials than at positive membrane potentials. As a result, the background current can influence reversal potential measurements. This problem is particularly problematic for inside-out patch-clamp recordings because the absolute current amplitude is often small compared to whole-cell patch-clamp recordings. Background current subtraction can alleviate this problem, but this is not always performed. For example, Yang et al. (2012) reported a P_{Na}/P_{Cl} of 6.8 for TMEM16F [49]. Even though they used a saturating concentration of 0.5 mM Ca^{2+}, they did not perform background current subtraction. Another study that used a similar experimental setup but with 0.2 mM Ca^{2+} and background current subtraction reported a P_{Na}/P_{Cl} of 2.7 [95]. Note that chapter 4 and another study [116] show that using a higher concentration of Ca^{2+} should yield a smaller P_{Na}/P_{Cl}.

Ion permeability experiments involve measuring ion channel currents' reversal potential in an asymmetrical ionic condition. Many studies that examined the ion selectivity of TMEM16F used a 10-fold NaCl concentration gradient to generate a significant shift in reversal potential. However, chapter 4 shows that the actual concentration of NaCl, not just the NaCl

concentration gradient, affects the P_{Na}/P_{Cl} of TMEM16F. The lower the concentration of intracellular NaCl, the higher the P_{Na}/P_{Cl}. This finding may explain why whole-cell patch-clamp experiments where intracellular ions concentration is >100 mM tend to result in a lower P_{Na}/P_{Cl} of TMEM16F. Thus, monovalent cations, in addition to Mg^{2+} and Ca^{2+}, may also affect the ion selectivity of TMEM16F.

In ion permeability experiments, sucrose, D-mannitol, $NMDG_2(SO_4)$, and Cs-Aspartate are a few compounds that are often used to replace NaCl on one side of the cell membrane. Chapters 2 and 4 suggest that the compounds used to adjust NaCl concentration also influence the measured P_{Na}/P_{Cl}. Using either $NMDG_2(SO_4)$, as in chapter 2, or D-mannitol, as in chapter 4, to adjust the intracellular NaCl concentration lead to different reversal potential measurements. TMEM16A is nearly impermeable to $NMDG^+$, whereas TMEM16F is more permeable to $NMDG^+$ [108]. Even though the permeability of $NMDG^+$ is low in TMEM16F, ignoring its permeability may affect the measured P_{Na}/P_{Cl}.

The Ca^{2+}-dependent shift in the ion selectivity of TMEM16F was postulated to have a physiological function [116], but chapter 4 suggests that the dynamic shift in ion selectivity only occurs under non-physiological conditions (no Mg^{2+} and non-physiological concentration of ions). The cytosol of mammalian cells typically contains ~0.8 mM Mg^{2+}, ~139 mM K^+, and ~12 mM Na^+ [239]. At these concentrations of cations, TMEM16F would

most likely be non-selective regardless of the intracellular concentration of Ca^{2+}.

5.5 Phospholipids and ion permeation in TMEM16 proteins

This dissertation suggests that ion permeation in TMEM16A and TMEM16F, and thus TMEM16 proteins in general, involves membrane phospholipids. High-resolution structures of TMEM16 proteins show that the ion/lipid permeation pathway is partially exposed to membrane phospholipids [10, 82, 90, 95-97]. The degree of sidewall opening varies among TMEM16 proteins. Thus, the conformation of phospholipids adjacent to the ion permeation/phospholipid transport pathway of TMEM16 proteins likely varies, and the role that phospholipids play in ion permeation likely varies also. Since the conformation of phospholipids at the intracellular vestibule is poorly understood, we can only speculate how the Q559W mutation influences the I-V relationship of TMEM16F. The phospholipid scrambling domain of TMEM16F contains Q559 [108], and mutating this specific residue into a lysine seems to reduce the phospholipid scramblase activity of TMEM16F significantly [109]. Also, mutating Q559 into aromatic amino acids reduces the degree of outward rectification of TMEM16F currents. Out of all mutations, the Q559W mutation generates the most pronounced effect. The prevalence of tryptophan and other aromatic residues at the water-membrane interface is well documented [240-242]. The indole side chain of tryptophan can form a hydrogen bond with the

carbonyl in phospholipids [243-247]. Thus, placing a tryptophan at the entrance of the intracellular vestibule of TMEM16F may alter the orientation of pore phospholipids and affect ion permeation.

Chapters 3 and 4 show that divalent cations, which can interact with membrane phospholipids [207, 233, 248], potentiate TMEM16A and alter the ion selectivity of TMEM16F. Depleting negatively charged phospholipids from the cell membrane with poly-L-lysine (PLL) reduces the potentiation of TMEM16A by divalent cations and reduces the permeability of Na^+ in TMEM16F. Furthermore, the PLL effect can be reversed by replenishing the cell membrane with PIP2, suggesting membrane phospholipids' involvement in ion permeation. Since Na^+, Mg^{2+}, and Ca^{2+} are all cations, they likely compete with one another to bind to phospholipids. Indeed, isothermal titration calorimetry experiments have shown that Na^+ interferes with Ca^{2+} binding to phosphatidylcholine–phosphatidylserine vesicles [234]. Chapter 4 shows that symmetrically reducing the NaCl concentration on both sides of the cell membrane enhances divalent cations potentiation of TMEM16A. Perhaps lowering the NaCl concentration allows for more divalent cations to bind to phospholipids at the intracellular vestibule of TMEM16A. Likewise, increasing the intracellular NaCl concentration enhances the permeability of anions in TMEM16F, an effect that can also be achieved by increasing the concentration of divalent cations like Ca^{2+} and Mg^{2+}. Thus, Na^+, like Ca^{2+}

and Mg^{2+}, after binding to phospholipids at the intracellular vestibule of TMEM16F, can also change the channel's ion selectivity.

While the orientation of phospholipids surrounding TMEM16 proteins remains unknown, looking at ion permeation in non-biological conical nanopores may shed light on how phospholipids may affect ion permeation in TMEM16 proteins. How hydrophobic/charged surface affects ionic current rectification in conical nanopores has been studied extensively (see [249, 250] for relevant reviews). The pore architecture of conical nanopores roughly resembles that of TMEM16 proteins (a larger intracellular entrance and a smaller extracellular entrance). Chemisorption of hydrocarbon chains to the narrow opening (~100 Å to ~330 Å in diameter) of conical nanopores alters their I-V curve rectification [251]. Similarly, membrane phospholipids' fatty acid tails may act as an ion permeation barrier and alter the I-V relationship of TMEM16 proteins. The location of phospholipid head groups is also relevant because they are polar and can be charged. Phospholipid head groups can block the ion permeation pathway, like how the positively charged spermine blocks CNG channels [252, 253], voltage-gated Na^+ channels [254], voltage-gated Ca^{2+} channels [255], BK channels [256], and a certain type of α-amino-3-hydroxy-5-methyl-4-isoxazolepropionic acid receptor [257, 258]. Alternatively, charged phospholipid head groups might line the pore surface and influence ion permeation directly. This idea was demonstrated with canonical nanopores before. Namely, the chemisorption

of 2-mercaptopropionic acid (negatively charged) or mercaptoethyl ammonium (positively charged) to the surface of gold-coated conical nanopores alters their I-V curve rectification [259]. While conical nanopores may behave like ion channels that exhibit current rectification, they are generally larger than ion channels, usually with diameters in the 100s Å range. Although ion permeation in nanopores and ion channels may differ, smaller conical nanopores exhibit much more pronounced ionic current rectification than larger conical nanopores [260]. Thus, it is likely that much smaller ion channels would be more sensitive to changes to pore surface charge.

If phospholipids cover part of the ion permeation pathway of TMEM16 proteins, then ion binding to pore-lining phospholipids' head groups may influence ion permeation. The idea that ions bound to the pore surface affect ion permeation is not new. In one study, the ionic current rectification of gold-coated conical nanopores was reduced when Cl^- in solutions was replaced with F^- [259]. With K^+ being the primary current carrier, the difference in current rectification between the two solutions is attributed to Cl^- adsorbing onto the gold surface much better than F^- [261, 262]. In another study, the presence of Mg^{2+} or La^{3+} significantly alters ionic current rectification in nanopores with a negatively charged pore surface [263].

Similarly, divalent cations binding to phospholipids near the ion permeation pathway of TMEM16 proteins could affect ion permeation in

these proteins. If that is the case, the phospholipid composition of cell membranes must be considered. Eukaryotic cell membranes are only composed of ~15% of negatively charged phospholipids [264]. Thus, phosphatidylcholine (PC) and phosphatidylethanolamine (PE) (~57% of the cell membrane [264]) are likely more abundant at the intracellular vestibule of TMEM16A and TMEM16F than other phospholipids. While PC and PE are considered neutral phospholipids, they could be positively charged in the presence of Ca^{2+}. Since Ca^{2+} is thought to interact with either the carbonyl group or the phosphate group in phospholipids (**Fig. 5.1**) [248, 265], the normally neutral head group of PC and PE could be positively charged. Beside Ca^{2+}, monovalent cations like Na^{+} can also bind to phospholipids [207, 208]. The idea that ions binding to phospholipids can influence ion permeation is consistent with the data presented in chapter 4. Namely, the ion selectivity of TMEM16F is dependent on the concentration of both Na^{+} and Ca^{2+}, and the potentiation of TMEM16A currents by divalent cations is also dependent on the concentration of Na^{+}.

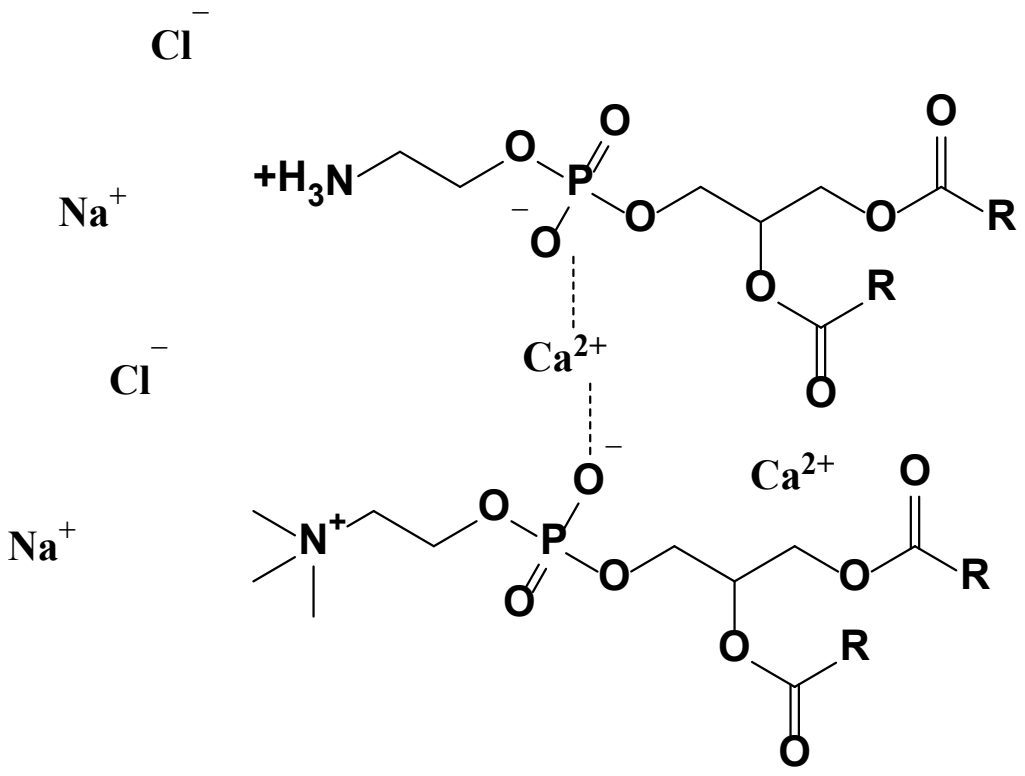

Figure 5.1. An illustration of Ca^{2+} interacting with phosphatidylcholine and phosphatidylethanolamine.

The mechanisms of phospholipid transport in flippases, floppases, and phospholipid scramblases are still under investigation. However, one of the most popular models for phospholipid transport is the "card reader" model. In this model, phospholipids have their fatty acid tails in the cell membrane core and their hydrophilic heads in phospholipid transporters' cavities as they travel between the two membrane leaflets [197]. For TMEM16 proteins, the asymmetric distribution of phospholipids between the two membrane leaflets and the asymmetric architecture of the lipid transport/ion permeation pathway of TMEM16 proteins have important implications. First,

the intracellular half of the phospholipid transport/ion permeation pathway is much more exposed to membrane phospholipids than the extracellular half. Second, the intracellular membrane leaflet is more enriched with negatively charged phospholipids than the extracellular membrane leaflet. Roughly 95% of total phosphatidylserine and 80% of total phosphatidylinositol in the cell membrane are in the intracellular leaflet [264]. The intracellular leaflet also contains a relatively smaller amount of negatively charged phosphatidylinositol 4,5-bisphosphate (PIP2), which has been shown to regulate many ion channels [266], including TMEM16A and TMEM16F [127, 145-148]. Thus, the intracellular side of TMEM16 proteins may be more exposed to charged phospholipids than the extracellular side. This asymmetrical exposure to charged phospholipids may play a role in ion permeation, and further investigation is warranted. One study has explored how other lipids besides PIP2 can affect ion permeation in TMEM16A. De Jesús-Pérez et al. (2018) showed that fatty acids and phosphatidylserine inhibit TMEM16A [127]. Fatty acids are known to affect the structure and function of cell membranes (e.g., induce membrane swelling and disturbing protein-lipid interactions) [267]. Thus, it is plausible that changes to the cell membrane structure could contribute to the inhibitory effect of fatty acids and phosphatidylserine on TMEM16A. Another possibility is that these negatively charged lipids are embedded in the phospholipid regions near the pore of TMEM16A, preventing Cl^- permeation.

Several questions need to be answered before we can fully understand how membrane phospholipids modulate TMEM16 protein function. If TMEM16 phospholipid scramblases utilize the “credit card” model of phospholipid transport, do phospholipids line up along the phospholipid transport pathway with their headgroup in the protein cavity in the absence of Ca^{2+}? Is there a significant difference in the orientation of phospholipids surrounding TMEM16 CaCCs and TMEM16 phospholipid scramblases? Are phospholipid scrambling and ion conduction coupled? We do not have a solid answer for any of these questions. Physiologically, phospholipid metabolism would modulate TMEM16 proteins' function. Thus, understanding how membrane phospholipids interact with TMEM16 proteins can help us understand the physiological role of TMEM16 proteins.

References

1. Barish, M. E., A transient calcium-dependent chloride current in the immature Xenopus oocyte. *J. Physiol.* **1983,** 342, (1), 309-325.

2. Miledi, R., A Calcium-Dependent Transient Outward Current in Xenopus laevis Oocytes. *Proc. R. Soc. Lond. B. Biol. Sci.* **1982,** 215, (1201), 491-497.

3. Hartzell, C.; Putzier, I.; Arreola, J., Calcium-Activated Chloride Channels. *Annu. Rev. Physiol.* **2005,** 67, (1), 719-758.

4. Sun, H.; Tsunenari, T.; Yau, K.-W.; Nathans, J., The vitelliform macular dystrophy protein defines a new family of chloride channels. *Proc. Natl. Acad. Sci. U.S.A.* **2002,** 99, (6), 4008-4013.

5. Hartzell, H. C.; Qu, Z.; Yu, K.; Xiao, Q.; Chien, L.-T., Molecular Physiology of Bestrophins: Multifunctional Membrane Proteins Linked to Best Disease and Other Retinopathies. *Physiol. Rev.* **2008,** 88, (2), 639-672.

6. Caputo, A.; Caci, E.; Ferrera, L.; Pedemonte, N.; Barsanti, C.; Sondo, E.; Pfeffer, U.; Ravazzolo, R.; Zegarra-Moran, O.; Galietta, L. J. V., TMEM16A, A Membrane Protein Associated with Calcium-Dependent Chloride Channel Activity. *Science* **2008,** 322, (5901), 590-594.

7. Schroeder, B. C.; Cheng, T.; Jan, Y. N.; Jan, L. Y., Expression Cloning of TMEM16A as a Calcium-Activated Chloride Channel Subunit. *Cell* **2008,** 134, (6), 1019-1029.

8. Yang, Y. D.; Cho, H.; Koo, J. Y.; Tak, M. H.; Cho, Y.; Shim, W.-S.; Park, S. P.; Lee, J.; Lee, B.; Kim, B.-M.; Raouf, R.; Shin, Y. K.; Oh, U., TMEM16A confers receptor-activated calcium-dependent chloride conductance. *Nature* **2008,** 455, (7217), 1210-1215.

9. Suzuki, J.; Umeda, M.; Sims, P. J.; Nagata, S., Calcium-dependent phospholipid scrambling by TMEM16F. *Nature* **2010,** 468, (7325), 834-838.

10. Brunner, J. D.; Lim, N. K.; Schenck, S.; Duerst, A.; Dutzler, R., X-ray structure of a calcium-activated TMEM16 lipid scramblase. *Nature* **2014,** 516, (7530), 207-212.

11. Malvezzi, M.; Chalat, M.; Janjusevic, R.; Picollo, A.; Terashima, H.; Menon, A. K.; Accardi, A., Ca^{2+}-dependent phospholipid scrambling by a reconstituted TMEM16 ion channel. *Nat. Commun.* **2013,** 4, (1), 2367.

12. Lavieu, G.; Orci, L.; Shi, L.; Geiling, M.; Ravazzola, M.; Wieland, F.; Cosson, P.; Rothman, J. E., Induction of cortical endoplasmic reticulum by dimerization of a coatomer-binding peptide anchored to endoplasmic reticulum membranes. *Proc. Natl. Acad. Sci. U.S.A.* **2010,** 107, (15), 6876.

13. Manford, Andrew G.; Stefan, Christopher J.; Yuan, Helen L.; MacGurn, Jason A.; Emr, Scott D., ER-to-Plasma Membrane Tethering Proteins Regulate Cell Signaling and ER Morphology. *Dev. Cell* **2012,** 23, (6), 1129-1140.

14. Pelz, T.; Drose, D. R.; Fleck, D.; Henkel, B.; Ackels, T.; Spehr, M.; Neuhaus, E. M., An ancestral TMEM16 homolog from Dictyostelium discoideum forms a scramblase. *PLoS ONE* **2018,** 13, (2), e0191219.

15. Benedetto, R.; Ousingsawat, J.; Wanitchakool, P.; Zhang, Y.; Holtzman, M. J.; Amaral, M.; Rock, J. R.; Schreiber, R.; Kunzelmann, K., Epithelial Chloride Transport by CFTR Requires TMEM16A. *Sci. Rep.* **2017,** 7, (1), 12397.

16. Ousingsawat, J.; Martins, J. R.; Schreiber, R.; Rock, J. R.; Harfe, B. D.; Kunzelmann, K., Loss of TMEM16A Causes a Defect in Epithelial Ca2+-dependent Chloride Transport. *J. Biol. Chem.* **2009,** 284, (42), 28698-28703.

17. Plasschaert, L. W.; Žilionis, R.; Choo-Wing, R.; Savova, V.; Knehr, J.; Roma, G.; Klein, A. M.; Jaffe, A. B., A single-cell atlas of the airway epithelium reveals the CFTR-rich pulmonary ionocyte. *Nature* **2018,** 560, (7718), 377-381.

18. Montoro, D. T.; Haber, A. L.; Biton, M.; Vinarsky, V.; Lin, B.; Birket, S. E.; Yuan, F.; Chen, S.; Leung, H. M.; Villoria, J.; Rogel, N.; Burgin, G.; Tsankov, A. M.; Waghray, A.; Slyper, M.; Waldman, J.; Nguyen, L.;

Dionne, D.; Rozenblatt-Rosen, O.; Tata, P. R.; Mou, H.; Shivaraju, M.; Bihler, H.; Mense, M.; Tearney, G. J.; Rowe, S. M.; Engelhardt, J. F.; Regev, A.; Rajagopal, J., A revised airway epithelial hierarchy includes CFTR-expressing ionocytes. *Nature* **2018,** 560, (7718), 319-324.

19. Benedetto, R.; Cabrita, I.; Schreiber, R.; Kunzelmann, K., TMEM16A is indispensable for basal mucus secretion in airways and intestine. *FASEB J.* **2019,** 33, (3), 4502-4512.

20. Zhang, C.-H.; Li, Y.; Zhao, W.; Lifshitz, L. M.; Li, H.; Harfe, B. D.; Zhu, M.-S.; ZhuGe, R., The Transmembrane Protein 16A Ca^{2+}-activated Cl^- Channel in Airway Smooth Muscle Contributes to Airway Hyperresponsiveness. *Am. J. Respir. Crit. Care Med.* **2013,** 187, (4), 374-381.

21. Nelson, M. T.; Brayden, J. E., Regulation of arterial tone by calcium-dependent K^+ channels and ATP-sensitive K^+ channels. *Cardiovasc. Drugs Ther.* **1993,** 7, (3), 605-610.

22. Nelson, M. T.; Patlak, J. B.; Worley, J. F.; Standen, N. B., Calcium channels, potassium channels, and voltage dependence of arterial smooth muscle tone. *Am. J. Physiol. Cell Physiol.* **1990,** 259, (1), C3-C18.

23. Nelson, M. T.; Quayle, J. M., Physiological roles and properties of potassium channels in arterial smooth muscle. *Am. J. Physiol. Cell Physiol.* **1995,** 268, (4), C799-C822.

24. Thorneloe, K. S.; Nelson, M. T., Properties of a tonically active, sodium-permeable current in mouse urinary bladder smooth muscle. *Am. J. Physiol. Cell Physiol.* **2004,** 286, (6), C1246-C1257.

25. Aickin, C. C., Chloride Transport across the Sarcolemma of Vertebrate Smooth and Skeletal Muscle. In *Chloride Channels and Carriers in Nerve, Muscle, and Glial Cells*, Alvarez-Leefmans, F. J.; Russell, J. M., Eds. Springer US: Boston, MA, 1990; pp 209-249.

26. Teixeira, M. C. L.; Coelho, R. R.; Leal-Cardoso, J. H.; Criddle, D. N., Comparative effects of niflumic acid and nifedipine on 5-hydroxytryptamine- and acetylcholine-induced contraction of the rat trachea. *Eur. J. Pharmacol.* **2000,** 394, (1), 117-122.

27. Almaça, J.; Tian, Y.; Aldehni, F.; Ousingsawat, J.; Kongsuphol, P.; Rock, J. R.; Harfe, B. D.; Schreiber, R.; Kunzelmann, K., TMEM16 Proteins Produce Volume-regulated Chloride Currents That Are Reduced in Mice Lacking TMEM16A. *J. Biol. Chem.* **2009,** 284, (42), 28571-28578.

28. Numata, T.; Shimizu, T.; Okada, Y., TRPM7 is a stretch- and swelling-activated cation channel involved in volume regulation in human epithelial cells. *Am. J. Physiol. Cell Physiol.* **2007,** 292, (1), C460-C467.

29. Chachisvilis, M.; Zhang, Y.-L.; Frangos, J. A., G protein-coupled receptors sense fluid shear stress in endothelial cells. *Proc. Natl. Acad. Sci. U.S.A.* **2006,** 103, (42), 15463-15468.

30. Franco, R.; Panayiotidis, M. I.; Ochoa de la Paz, L. D., Autocrine signaling involved in cell volume regulation: The role of released transmitters and plasma membrane receptors. *Journal of Cellular Physiology* **2008,** 216, (1), 14-28.

31. Oh, U.; Jung, J., Cellular functions of TMEM16/anoctamin. *Pflügers Arch.* **2016,** 468, (3), 443-453.

32. Buck, L.; Axel, R., A novel multigene family may encode odorant receptors: a molecular basis for odor recognition. *Cell* **1991,** 65, (1), 175-87.

33. Kleene, S. J.; Gesteland, R. C., Calcium-activated chloride conductance in frog olfactory cilia. *J. Neurosci.* **1991,** 11, (11), 3624.

34. Yu, T. T.; McIntyre, J. C.; Bose, S. C.; Hardin, D.; Owen, M. C.; McClintock, T. S., Differentially expressed transcripts from phenotypically identified olfactory sensory neurons. *J. Comp. Neurol.* **2005,** 483, (3), 251-62.

35. Dibattista, M.; Pifferi, S.; Boccaccio, A.; Menini, A.; Reisert, J., The long tale of the calcium activated Cl^- channels in olfactory transduction. *Channels (Austin)* **2017,** 11, (5), 399-414.

36. Nakamura, T.; Gold, G. H., A cyclic nucleotide-gated conductance in olfactory receptor cilia. *Nature* **1987,** 325, (6103), 442-444.

37. Firestein, S.; Zufall, F.; Shepherd, G. M., Single odor-sensitive channels in olfactory receptor neurons are also gated by cyclic nucleotides. *J. Neurosci.* **1991,** 11, (11), 3565.

38. Kurahashi, T.; Yau, K.-W., Co-existence of cationic and chloride components in odorant-induced current of vertebrate olfactory receptor cells. *Nature* **1993,** 363, (6424), 71-74.

39. Reisert, J.; Lai, J.; Yau, K.-W.; Bradley, J., Mechanism of the Excitatory Cl^- Response in Mouse Olfactory Receptor Neurons. *Neuron* **2005,** 45, (4), 553-561.

40. Kaneko, H.; Putzier, I.; Frings, S.; Kaupp, U. B.; Gensch, T., Chloride Accumulation in Mammalian Olfactory Sensory Neurons. *J. Neurosci.* **2004,** 24, (36), 7931.

41. Nickell, W. T.; Kleene, N. K.; Kleene, S. J., Mechanisms of neuronal chloride accumulation in intact mouse olfactory epithelium. *J. Physiol.* **2007,** 583, (3), 1005-1020.

42. Reisert, J.; Reingruber, J., Ca^{2+}-activated Cl^- current ensures robust and reliable signal amplification in vertebrate olfactory receptor neurons. *Proc. Natl. Acad. Sci. U.S.A.* **2019,** 116, (3), 1053-1058.

43. Stephan, A. B.; Shum, E. Y.; Hirsh, S.; Cygnar, K. D.; Reisert, J.; Zhao, H., ANO2 is the cilial calcium-activated chloride channel that may mediate olfactory amplification. *Proc. Natl. Acad. Sci. U.S.A.* **2009,** 106, (28), 11776.

44. Neureither, F.; Ziegler, K.; Pitzer, C.; Frings, S.; Möhrlen, F., Impaired Motor Coordination and Learning in Mice Lacking Anoctamin 2 Calcium-Gated Chloride Channels. *Cerebellum* **2017,** 16, (5), 929-937.

45. Zhang, Y.; Zhang, Z.; Xiao, S.; Tien, J.; Le, S.; Le, T.; Jan, L. Y.; Yang, H., Inferior Olivary TMEM16B Mediates Cerebellar Motor Learning. *Neuron* **2017,** 95, (5), 1103-1111.e4.

46. Auer, F.; Franco Taveras, E.; Klein, U.; Kesenheimer, C.; Fleischhauer, D.; Möhrlen, F.; Frings, S., Anoctamin 2-chloride channels reduce simple spike activity and mediate inhibition at elevated calcium concentration in cerebellar Purkinje cells. *PLoS ONE* **2021,** 16, (3), e0247801.

47. Wang, L.; Simms, J.; Peters, C. J.; Tynan-La Fontaine, M.; Li, K.; Gill, T. M.; Jan, Y. N.; Jan, L. Y., TMEM16B Calcium-Activated Chloride Channels Regulate Action Potential Firing in Lateral Septum and Aggression in Male Mice. *J. Neurosci.* **2019,** 39, (36), 7102.

48. Li, K.-X.; He, M.; Ye, W.; Simms, J.; Gill, M.; Xiang, X.; Jan, Y. N.; Jan, L. Y., TMEM16B regulates anxiety-related behavior and GABAergic neuronal signaling in the central lateral amygdala. *eLife* **2019,** 8, e47106.

49. Yang, H.; Kim, A.; David, T.; Palmer, D.; Jin, T.; Tien, J.; Huang, F.; Cheng, T.; Coughlin, Shaun R.; Jan, Yuh N.; Jan, Lily Y., TMEM16F Forms a Ca^{2+}-Activated Cation Channel Required for Lipid Scrambling in Platelets during Blood Coagulation. *Cell* **2012,** 151, (1), 111-122.

50. Harayama, T.; Riezman, H., Understanding the diversity of membrane lipid composition. *Nat. Rev. Mol. Cell Biol.* **2018,** 19, (5), 281-296.

51. Daleke, D. L., Regulation of transbilayer plasma membrane phospholipid asymmetry. *J Lipid Res* **2003,** 44, (2), 233-242.

52. Suzuki, J.; Denning, D. P.; Imanishi, E.; Horvitz, H. R.; Nagata, S., Xk-Related Protein 8 and CED-8 Promote Phosphatidylserine Exposure in Apoptotic Cells. *Science* **2013,** 341, (6144), 403-406.

53. Bevers, E. M.; Williamson, P. L., Phospholipid scramblase: An update. *FEBS Lett.* **2010,** 584, (13), 2724-2730.

54. Kodigepalli, K. M.; Bowers, K.; Sharp, A.; Nanjundan, M., Roles and regulation of phospholipid scramblases. *FEBS Lett.* **2015,** 589, (1), 3-14.

55. Lentz, B. R., Exposure of platelet membrane phosphatidylserine regulates blood coagulation. *Prog. Lipid Res.* **2003,** 42, (5), 423-438.

56. Weiss, H. J.; Lages, B., Family Studies in Scott Syndrome. *Blood* **1997,** 90, (1), 475-476.

57. Zwaal, R. F. A.; Comfurius, P.; Bevers, E. M., Scott syndrome, a bleeding disorder caused by defective scrambling of membrane phospholipids. *Biochim. Biophys. Acta Mol. Cell Biol. Lipids* **2004,** 1636, (2), 119-128.

58. Zhang, Y.; Le, T.; Grabau, R.; Mohseni, Z.; Kim, H.; Natale, D. R.; Feng, L.; Pan, H.; Yang, H., TMEM16F phospholipid scramblase mediates trophoblast fusion and placental development. *Sci. Adv.* **2020,** 6, (19), eaba0310.

59. Wu, N.; Cernysiov, V.; Davidson, D.; Song, H.; Tang, J.; Luo, S.; Lu, Y.; Qian, J.; Gyurova, I. E.; Waggoner, S. N.; Trinh, V. Q.-H.; Cayrol, R.; Sugiura, A.; McBride, H. M.; Daudelin, J.-F.; Labrecque, N.; Veillette, A., Critical Role of Lipid Scramblase TMEM16F in Phosphatidylserine Exposure and Repair of Plasma Membrane after Pore Formation. *Cell Rep.*

2020, 30, (4), 1129-1140.e5.

60. Bricogne, C.; Fine, M.; Pereira, P. M.; Sung, J.; Tijani, M.; Wang, Y.; Henriques, R.; Collins, M. K.; Hilgemann, D. W., TMEM16F activation by Ca^{2+} triggers plasma membrane expansion and directs PD-1 trafficking. *Sci. Rep.* **2019,** 9, (1), 619.

61. Han, T. W.; Ye, W.; Bethel, N. P.; Zubia, M.; Kim, A.; Li, K. H.; Burlingame, A. L.; Grabe, M.; Jan, Y. N.; Jan, L. Y., Chemically induced vesiculation as a platform for studying TMEM16F activity. *Proc. Natl. Acad. Sci. U.S.A.* **2019,** 116, (4), 1309-1318.

62. Fujii, T.; Sakata, A.; Nishimura, S.; Eto, K.; Nagata, S., TMEM16F is required for phosphatidylserine exposure and microparticle release in activated mouse platelets. *Proc. Natl. Acad. Sci. U.S.A.* **2015,** 112, (41), 12800-12805.

63. Sims, P. J.; Wiedmer, T.; Esmon, C. T.; Weiss, H. J.; Shattil, S. J., Assembly of the platelet prothrombinase complex is linked to vesiculation of the platelet plasma membrane. Studies in Scott syndrome: an isolated defect in platelet procoagulant activity. *J. Biol. Chem.* **1989,** 264, (29), 17049-17057.

64. Ehlen, H. W.; Chinenkova, M.; Moser, M.; Munter, H.-M.; Krause, Y.; Gross, S.; Brachvogel, B.; Wuelling, M.; Kornak, U.; Vortkamp, A., Inactivation of anoctamin-6/Tmem16f, a regulator of phosphatidylserine scrambling in osteoblasts, leads to decreased mineral deposition in skeletal tissues. *Journal of Bone and Mineral Research* **2013,** 28, (2), 246-259.

65. Headland, S. E.; Jones, H. R.; Norling, L. V.; Kim, A.; Souza, P. R.; Corsiero, E.; Gil, C. D.; Nerviani, A.; Dell'Accio, F.; Pitzalis, C.; Oliani, S. M.; Jan, L. Y.; Perretti, M., Neutrophil-derived microvesicles enter cartilage and protect the joint in inflammatory arthritis. *Sci. Transl. Med.* **2015,** 7, (315), 315ra190-315ra190.

66. Suzuki, J.; Fujii, T.; Imao, T.; Ishihara, K.; Kuba, H.; Nagata, S., Calcium-dependent Phospholipid Scramblase Activity of TMEM16 Protein Family Members. *J. Biol. Chem.* **2013,** 288, (19), 13305-13316.

67. Pedemonte, N.; Galietta, L. J. V., Structure and Function of TMEM16 Proteins (Anoctamins). *Physiol. Rev.* **2014,** 94, (2), 419-459.

68. Briones, N.; Dinu, V., Data mining of high density genomic variant data for prediction of Alzheimer's disease risk. *BMC Med. Genet.* **2012,** 13, (1), 7.

69. Athanasiu, L.; Mattingsdal, M.; Kähler, A. K.; Brown, A.; Gustafsson, O.; Agartz, I.; Giegling, I.; Muglia, P.; Cichon, S.; Rietschel, M.; Pietiläinen, O. P. H.; Peltonen, L.; Bramon, E.; Collier, D.; Clair, D. S.; Sigurdsson, E.; Petursson, H.; Rujescu, D.; Melle, I.; Steen, V. M.; Djurovic, S.; Andreassen, O. A., Gene variants associated with schizophrenia in a Norwegian genome-wide study are replicated in a large European cohort. *J. Psychiatr. Res.* **2010,** 44, (12), 748-753.

70. Ross, K. A., Evidence for somatic gene conversion and deletion in bipolar disorder, Crohn's disease, coronary artery disease, hypertension, rheumatoid arthritis, type-1 diabetes, and type-2 diabetes. *BMC Med.* **2011,** 9, (1), 12.

71. Huang, F.; Wang, X.; Ostertag, E. M.; Nuwal, T.; Huang, B.; Jan, Y.-N.; Basbaum, A. I.; Jan, L. Y., TMEM16C facilitates Na^+-activated K^+ currents in rat sensory neurons and regulates pain processing. *Nat. Neurosci.* **2013,** 16, (9), 1284-1290.

72. Di Zanni, E.; Gradogna, A.; Scholz-Starke, J.; Boccaccio, A., Gain of function of TMEM16E/ANO5 scrambling activity caused by a mutation associated with gnathodiaphyseal dysplasia. *Cellular and Molecular Life Sciences* **2018,** 75, (9), 1657-1670.

73. Tsutsumi, S.; Kamata, N.; Vokes, T. J.; Maruoka, Y.; Nakakuki, K.; Enomoto, S.; Omura, K.; Amagasa, T.; Nagayama, M.; Saito-Ohara, F.; Inazawa, J.; Moritani, M.; Yamaoka, T.; Inoue, H.; Itakura, M., The Novel Gene Encoding a Putative Transmembrane Protein Is Mutated in Gnathodiaphyseal Dysplasia (GDD). *Am. J. Hum. Genet.* **2004,** 74, (6), 1255-1261.

74. Kaikkonen, E.; Rantapero, T.; Zhang, Q.; Taimen, P.; Laitinen, V.; Kallajoki, M.; Jambulingam, D.; Ettala, O.; Knaapila, J.; Boström, P. J.; Wahlström, G.; Sipeky, C.; Pursiheimo, J.-P.; Tammela, T.; Kellokumpu-Lehtinen, P.-L.; Consortium, P.; Fey, V.; Maehle, L.; Wiklund, F.; Wei, G.-H.; Schleutker, J., ANO7 is associated with aggressive prostate cancer. *Int. J. Cancer* **2018,** 143, (10), 2479-2487.

75. Bera, T. K.; Das, S.; Maeda, H.; Beers, R.; Wolfgang, C. D.; Kumar, V.; Hahn, Y.; Lee, B.; Pastan, I., NGEP, a gene encoding a membrane protein detected only in prostate cancer and normal prostate. *Proc. Natl. Acad. Sci. U.S.A.* **2004,** 101, (9), 3059.

76. Jha, A.; Chung, W. Y.; Vachel, L.; Maleth, J.; Lake, S.; Zhang, G.; Ahuja, M.; Muallem, S., Anoctamin 8 tethers endoplasmic reticulum and plasma membrane for assembly of Ca^{2+} signaling complexes at the ER/PM compartment. *EMBO J.* **2019,** 38, (12), e101452.

77. Secondo, A.; Bagetta, G.; Amantea, D., On the Role of Store-Operated Calcium Entry in Acute and Chronic Neurodegenerative Diseases. *Front. Mol. Neurosci.* **2018,** 11, (87).

78. Rock, J. R.; Harfe, B. D., Expression of TMEM16 paralogs during murine embryogenesis. *Dev. Dyn.* **2008,** 237, (9), 2566-2574.

79. Kim, H.; Kim, H.; Lee, J.; Lee, B.; Kim, H.-R.; Jung, J.; Lee, M.-O.; Oh, U., Anoctamin 9/TMEM16J is a cation channel activated by cAMP/PKA signal. *Cell Calcium* **2018,** 71, 75-85.

80. Li, C.; Cai, S.; Wang, X.; Jiang, Z., Identification and characterization of ANO9 in stage II and III colorectal carcinoma. *Oncotarget* **2015,** 6, (30).

81. Jun, I.; Park, H. S.; Piao, H.; Han, J. W.; An, M. J.; Yun, B. G.; Zhang, X.; Cha, Y. H.; Shin, Y. K.; Yook, J. I.; Jung, J.; Gee, H. Y.; Park, J.

S.; Yoon, D. S.; Jeung, H.-C.; Lee, M. G., ANO9/TMEM16J promotes tumourigenesis via EGFR and is a novel therapeutic target for pancreatic cancer. *Br. J. Cancer* **2017,** 117, (12), 1798-1809.

82. Bushell, S. R.; Pike, A. C. W.; Falzone, M. E.; Rorsman, N. J. G.; Ta, C. M.; Corey, R. A.; Newport, T. D.; Christianson, J. C.; Scofano, L. F.; Shintre, C. A.; Tessitore, A.; Chu, A.; Wang, Q.; Shrestha, L.; Mukhopadhyay, S. M. M.; Love, J. D.; Burgess-Brown, N. A.; Sitsapesan, R.; Stansfeld, P. J.; Huiskonen, J. T.; Tammaro, P.; Accardi, A.; Carpenter, E. P., The structural basis of lipid scrambling and inactivation in the endoplasmic reticulum scramblase TMEM16K. *Nat. Commun.* **2019,** 10, (1), 3956.

83. Chamova, T.; Florez, L.; Guergueltcheva, V.; Raycheva, M.; Kaneva, R.; Lochmüller, H.; Kalaydjieva, L.; Tournev, I., ANO10 c.1150_1151del is a founder mutation causing autosomal recessive cerebellar ataxia in Roma/Gypsies. *J. Neurol.* **2012,** 259, (5), 906-911.

84. Renaud, M.; Anheim, M.; Kamsteeg, E.-J.; Mallaret, M.; Mochel, F.; Vermeer, S.; Drouot, N.; Pouget, J.; Redin, C.; Salort-Campana, E.; Kremer, H. P. H.; Verschuuren-Bemelmans, C. C.; Muller, J.; Scheffer, H.; Durr, A.; Tranchant, C.; Koenig, M., Autosomal Recessive Cerebellar Ataxia Type 3 Due to ANO10 Mutations: Delineation and Genotype-Phenotype Correlation Study. *JAMA Neurology* **2014,** 71, (10), 1305-1310.

85. Vermeer, S.; Hoischen, A.; Meijer, R. P. P.; Gilissen, C.; Neveling, K.; Wieskamp, N.; de Brouwer, A.; Koenig, M.; Anheim, M.; Assoum, M.; Drouot, N.; Todorovic, S.; Milic-Rasic, V.; Lochmüller, H.; Stevanin, G.; Goizet, C.; David, A.; Durr, A.; Brice, A.; Kremer, B.; van de Warrenburg, B. P. C.; Schijvenaars, M. M. V. A. P.; Heister, A.; Kwint, M.; Arts, P.; van der Wijst, J.; Veltman, J.; Kamsteeg, E.-J.; Scheffer, H.; Knoers, N., Targeted Next-Generation Sequencing of a 12.5 Mb Homozygous Region Reveals ANO10 Mutations in Patients with Autosomal-Recessive Cerebellar Ataxia. *Am. J. Hum. Genet.* **2010,** 87, (6), 813-819.

86. Lee, B.-C.; Menon, Anant K.; Accardi, A., The nhTMEM16 Scramblase Is Also a Nonselective Ion Channel. *Biophys. J.* **2016,** 111, (9), 1919-1924.

87. Wong, X. M.; Younger, S.; Peters, C. J.; Jan, Y. N.; Jan, L. Y., Subdued, a TMEM16 family Ca^{2+}-activated Cl^- channel in Drosophila melanogaster with an unexpected role in host defense. *eLife* **2013,** 2, e00862.

88. Le, T.; Le, S. C.; Yang, H., Drosophila Subdued is a moonlighting transmembrane protein 16 (TMEM16) that transports ions and phospholipids. *J. Biol. Chem.* **2019,** 294, (12), 4529-4537.

89. Jang, W.; Kim, J. Y.; Cui, S.; Jo, J.; Lee, B.-C.; Lee, Y.; Kwon, K.-S.; Park, C.-S.; Kim, C., The Anoctamin Family Channel Subdued Mediates Thermal Nociception in Drosophila. *J. Biol. Chem.* **2015,** 290, (4), 2521-2528.

90. Falzone, M. E.; Rheinberger, J.; Lee, B.-C.; Peyear, T.; Sasset, L.; Raczkowski, A. M.; Eng, E. T.; Di Lorenzo, A.; Andersen, O. S.; Nimigean, C. M.; Accardi, A., Structural basis of Ca^{2+}-dependent activation and lipid transport by a TMEM16 scramblase. *eLife* **2019,** 8, e43229.

91. Kalienkova, V.; Clerico Mosina, V.; Bryner, L.; Oostergetel, G. T.; Dutzler, R.; Paulino, C., Stepwise activation mechanism of the scramblase nhTMEM16 revealed by cryo-EM. *eLife* **2019,** 8, e44364.

92. Das, S.; Hahn, Y.; Walker, D. A.; Nagata, S.; Willingham, M. C.; Peehl, D. M.; Bera, T. K.; Lee, B.; Pastan, I., Topology of NGEP, a Prostate-Specific Cell:Cell Junction Protein Widely Expressed in Many Cancers of Different Grade Level. *Cancer Res.* **2008,** 68, (15), 6306.

93. Milenkovic, V. M.; Brockmann, M.; Stöhr, H.; Weber, B. H. F.; Strauss, O., Evolution and functional divergence of the anoctamin family of membrane proteins. *BMC Evol. Biol.* **2010,** 10, (1), 319.

94. Jüschke , C.; Wächter , A.; Schwappach , B.; Seedorf , M., SEC18/NSF-independent, protein-sorting pathway from the yeast cortical ER to the plasma membrane. *Journal of Cell Biology* **2005,** 169, (4), 613-622.

95. Alvadia, C.; Lim, N. K.; Clerico Mosina, V.; Oostergetel, G. T.; Dutzler, R.; Paulino, C., Cryo-EM structures and functional characterization of the murine lipid scramblase TMEM16F. *eLife* **2019,** 8, e44365.

96. Paulino, C.; Kalienkova, V.; Lam, A. K. M.; Neldner, Y.; Dutzler, R., Activation mechanism of the calcium-activated chloride channel TMEM16A revealed by cryo-EM. *Nature* **2017,** 552, (7685), 421-425.

97. Dang, S.; Feng, S.; Tien, J.; Peters, C. J.; Bulkley, D.; Lolicato, M.; Zhao, J.; Zuberbühler, K.; Ye, W.; Qi, L.; Chen, T.; Craik, C. S.; Jan, Y. N.; Minor, D. L.; Cheng, Y.; Jan, L. Y., Cryo-EM structures of the TMEM16A calcium-activated chloride channel. *Nature* **2017,** 552, (7685), 426-429.

98. Ferrera, L.; Caputo, A.; Galietta, L. J., TMEM16A protein: a new identity for Ca^{2+}-dependent Cl^- channels. *Physiology (Bethesda)* **2010,** 25, (6), 357-63.

99. Ferrera, L.; Caputo, A.; Ubby, I.; Bussani, E.; Zegarra-Moran, O.; Ravazzolo, R.; Pagani, F.; Galietta, L. J. V., Regulation of TMEM16A Chloride Channel Properties by Alternative Splicing. *J. Biol. Chem.* **2009,** 284, (48), 33360-33368.

100. Lam, A. K. M.; Rheinberger, J.; Paulino, C.; Dutzler, R., Gating the pore of the calcium-activated chloride channel TMEM16A. *Nat. Commun.* **2021,** 12, (1), 785.

101. Fallah, G.; Römer, T.; Detro-Dassen, S.; Braam, U.; Markwardt, F.; Schmalzing, G., TMEM16A(a)/anoctamin-1 shares a homodimeric architecture with CLC chloride channels. *Mol. Cell. Proteom.* **2011,** 10, (2), M110.004697.

102. Sheridan, J. T.; Worthington, E. N.; Yu, K.; Gabriel, S. E.; Hartzell, H. C.; Tarran, R., Characterization of the Oligomeric Structure of the Ca^{2+}-activated Cl^- Channel Ano1/TMEM16A. *J. Biol. Chem.* **2011,** 286, (2), 1381-1388.

103. Paulino, C.; Neldner, Y.; Lam, A. K.; Kalienkova, V.; Brunner, J. D.; Schenck, S.; Dutzler, R., Structural basis for anion conduction in the calcium-activated chloride channel TMEM16A. *eLife* **2017,** 6, e26232.

104. Yu, K.; Duran, C.; Qu, Z.; Cui, Y.-Y.; Hartzell, H. C., Explaining Calcium-Dependent Gating of Anoctamin-1 Chloride Channels Requires a Revised Topology. *Circ. Res.* **2012,** 110, (7), 990-999.

105. Tien, J.; Peters, C. J.; Wong, X. M.; Cheng, T.; Jan, Y. N.; Jan, L. Y.; Yang, H., A comprehensive search for calcium binding sites critical for TMEM16A calcium-activated chloride channel activity. *eLife* **2014,** 3, e02772.

106. Lim, N. K.; Lam, A. K. M.; Dutzler, R., Independent activation of ion conduction pores in the double-barreled calcium-activated chloride channel TMEM16A. *J. Gen. Physiol.* **2016,** 148, (5), 375-392.

107. Jeng, G.; Aggarwal, M.; Yu, W.-P.; Chen, T.-Y., Independent activation of distinct pores in dimeric TMEM16A channels. *J. Gen. Physiol.* **2016,** 148, (5), 393-404.

108. Yu, K.; Whitlock, J. M.; Lee, K.; Ortlund, E. A.; Cui, Y. Y.; Hartzell, H. C., Identification of a lipid scrambling domain in ANO6/TMEM16F. *eLife* **2015,** 4, e06901.

109. Jiang, T.; Yu, K.; Hartzell, H. C.; Tajkhorshid, E., Lipids and ions traverse the membrane by the same physical pathway in the nhTMEM16 scramblase. *eLife* **2017,** 6, e28671.

110. Lee, B.-C.; Khelashvili, G.; Falzone, M.; Menon, A. K.; Weinstein, H.; Accardi, A., Gating mechanism of the extracellular entry to the lipid pathway in a TMEM16 scramblase. *Nat. Commun.* **2018,** 9, (1), 3251.

111. Le, T.; Jia, Z.; Le, S. C.; Zhang, Y.; Chen, J.; Yang, H., An inner activation gate controls TMEM16F phospholipid scrambling. *Nat. Commun.* **2019,** 10, (1), 1846.

112. Larkin, M. A.; Blackshields, G.; Brown, N. P.; Chenna, R.; McGettigan, P. A.; McWilliam, H.; Valentin, F.; Wallace, I. M.; Wilm, A.; Lopez, R.; Thompson, J. D.; Gibson, T. J.; Higgins, D. G., Clustal W and Clustal X version 2.0. *Bioinformatics* **2007,** 23, (21), 2947-2948.

113. O'Leary, N. A.; Wright, M. W.; Brister, J. R.; Ciufo, S.; Haddad, D.; McVeigh, R.; Rajput, B.; Robbertse, B.; Smith-White, B.; Ako-Adjei, D.; Astashyn, A.; Badretdin, A.; Bao, Y.; Blinkova, O.; Brover, V.; Chetvernin, V.; Choi, J.; Cox, E.; Ermolaeva, O.; Farrell, C. M.; Goldfarb, T.; Gupta, T.; Haft, D.; Hatcher, E.; Hlavina, W.; Joardar, V. S.; Kodali, V. K.; Li, W.; Maglott, D.; Masterson, P.; McGarvey, K. M.; Murphy, M. R.; O'Neill, K.; Pujar, S.; Rangwala, S. H.; Rausch, D.; Riddick, L. D.; Schoch, C.; Shkeda, A.; Storz, S. S.; Sun, H.; Thibaud-

Nissen, F.; Tolstoy, I.; Tully, R. E.; Vatsan, A. R.; Wallin, C.; Webb, D.; Wu, W.; Landrum, M. J.; Kimchi, A.; Tatusova, T.; DiCuccio, M.; Kitts, P.; Murphy, T. D.; Pruitt, K. D., Reference sequence (RefSeq) database at NCBI: current status, taxonomic expansion, and functional annotation. *Nucleic Acids Res.* **2016,** 44, (D1), D733-45.

114. Pifferi, S.; Dibattista, M.; Menini, A., TMEM16B induces chloride currents activated by calcium in mammalian cells. *Pflügers Arch.* **2009,** 458, (6), 1023-1038.

115. Ni, Y.-L.; Kuan, A.-S.; Chen, T.-Y., Activation and Inhibition of TMEM16A Calcium-Activated Chloride Channels. *PLoS ONE* **2014,** 9, (1), e86734.

116. Ye, W.; Han, T. W.; He, M.; Jan, Y. N.; Jan, L. Y., Dynamic change of electrostatic field in TMEM16F permeation pathway shifts its ion selectivity. *eLife* **2019,** 8, e45187.

117. Xiao, Q.; Yu, K.; Perez-Cornejo, P.; Cui, Y.; Arreola, J.; Hartzell, H. C., Voltage- and calcium-dependent gating of TMEM16A/Ano1 chloride channels are physically coupled by the first intracellular loop. *Proc. Natl. Acad. Sci. U.S.A.* **2011,** 108, (21), 8891-8896.

118. Yuan, H.; Gao, C.; Chen, Y.; Jia, M.; Geng, J.; Zhang, H.; Zhan, Y.; Boland, L. M.; An, H., Divalent Cations Modulate TMEM16A Calcium-Activated Chloride Channels by a Common Mechanism. *The Journal of Membrane Biology* **2013,** 246, (12), 893-902.

119. Bill, A.; Popa, M. O.; van Diepen, M. T.; Gutierrez, A.; Lilley, S.; Velkova, M.; Acheson, K.; Choudhury, H.; Renaud, N. A.; Auld, D. S.; Gosling, M.; Groot-Kormelink, P. J.; Gaither, L. A., Variomics Screen Identifies the Re-entrant Loop of the Calcium-activated Chloride Channel ANO1 That Facilitates Channel Activation *. *J. Biol. Chem.* **2015,** 290, (2), 889-903.

120. Le, S. C.; Yang, H., An Additional Ca^{2+} Binding Site Allosterically Controls TMEM16A Activation. *Cell Rep.*

2020, 33, (13), 108570.

121. Contreras-Vite, J. A.; Cruz-Rangel, S.; De Jesús-Pérez, J. J.; Figueroa, I. A. A.; Rodríguez-Menchaca, A. A.; Pérez-Cornejo, P.; Hartzell, H. C.; Arreola, J., Revealing the activation pathway for TMEM16A chloride

channels from macroscopic currents and kinetic models. *Pflügers Arch.* **2016,** 468, (7), 1241-1257.

122. Segura-Covarrubias, G.; Aréchiga-Figueroa, I. A.; De Jesús-Pérez, J. J.; Sánchez-Solano, A.; Pérez-Cornejo, P.; Arreola, J., Voltage-Dependent Protonation of the Calcium Pocket Enable Activation of the Calcium-Activated Chloride Channel Anoctamin-1 (TMEM16A). *Sci. Rep.* **2020,** 10, (1), 6644.

123. Betto, G.; Cherian, O. L.; Pifferi, S.; Cenedese, V.; Boccaccio, A.; Menini, A., Interactions between permeation and gating in the TMEM16B/anoctamin2 calcium-activated chloride channel. *J. Gen. Physiol.* **2014,** 143, (6), 703-718.

124. Cenedese, V.; Betto, G.; Celsi, F.; Cherian, O. L.; Pifferi, S.; Menini, A., The voltage dependence of the TMEM16B/anoctamin2 calcium-activated chloride channel is modified by mutations in the first putative intracellular loop. *J. Gen. Physiol.* **2012,** 139, (4), 285-294.

125. Nguyen, D. M.; Chen, L. S.; Yu, W.-P.; Chen, T.-Y., Comparison of ion transport determinants between a TMEM16 chloride channel and phospholipid scramblase. *J. Gen. Physiol.* **2019,** 151, (4), 518-531.

126. Lam, A. K. M.; Dutzler, R., Calcium-dependent electrostatic control of anion access to the pore of the calcium-activated chloride channel TMEM16A. *eLife* **2018,** 7, e39122.

127. De Jesús-Pérez, J. J.; Cruz-Rangel, S.; Espino-Saldaña, Á. E.; Martínez-Torres, A.; Qu, Z.; Hartzell, H. C.; Corral-Fernandez, N. E.; Pérez-Cornejo, P.; Arreola, J., Phosphatidylinositol 4,5-bisphosphate, cholesterol, and fatty acids modulate the calcium-activated chloride channel TMEM16A (ANO1). *Biochim. Biophys. Acta Mol. Cell Biol. Lipids* **2018,** 1863, (3), 299-312.

128. Ta, C. M.; Adomaviciene, A.; Rorsman, N. J. G.; Garnett, H.; Tammaro, P., Mechanism of allosteric activation of TMEM16A/ANO1 channels by a commonly used chloride channel blocker. *Br. J. Pharmacol.* **2016,** 173, (3), 511-528.

129. Pettersen, E. F.; Goddard, T. D.; Huang, C. C.; Meng, E. C.; Couch, G. S.; Croll, T. I.; Morris, J. H.; Ferrin, T. E., UCSF ChimeraX: Structure

visualization for researchers, educators, and developers. *Protein Sci.* **2021,** 30, (1), 70-82.

130. Pifferi, S., Permeation Mechanisms in the TMEM16B Calcium-Activated Chloride Channels. *PLoS ONE* **2017,** 12, (1), e0169572.

131. Peters, C. J.; Yu, H.; Tien, J.; Jan, Y. N.; Li, M.; Jan, L. Y., Four basic residues critical for the ion selectivity and pore blocker sensitivity of TMEM16A calcium-activated chloride channels. *Proc. Natl. Acad. Sci. U.S.A.* **2015,** 112, (11), 3547.

132. Paulino, C.; Neldner, Y.; Lam, A. K. M.; Kalienkova, V.; Brunner, J. D.; Schenck, S.; Dutzler, R., Structural basis for anion conduction in the calcium-activated chloride channel TMEM16A. *eLife* **2017,** 6, e26232.

133. Grubb, S.; Poulsen, K. A.; Juul, C. A.; Kyed, T.; Klausen, T. K.; Larsen, E. H.; Hoffmann, E. K., TMEM16F (Anoctamin 6), an anion channel of delayed Ca^{2+} activation. *J. Gen. Physiol.* **2013,** 141, (5), 585-600.

134. Scudieri, P.; Caci, E.; Venturini, A.; Sondo, E.; Pianigiani, G.; Marchetti, C.; Ravazzolo, R.; Pagani, F.; Galietta, L. J. V., Ion channel and lipid scramblase activity associated with expression of TMEM16F/ANO6 isoforms. *J. Physiol.* **2015,** 593, (17), 3829-3848.

135. Shimizu, T.; Iehara, T.; Sato, K.; Fujii, T.; Sakai, H.; Okada, Y., TMEM16F is a component of a Ca^{2+}-activated Cl^- channel but not a volume-sensitive outwardly rectifying Cl^- channel. *Am. J. Physiol. Cell Physiol.* **2013,** 304, (8), C748-C759.

136. Tian, Y.; Schreiber, R.; Kunzelmann, K., Anoctamins are a family of Ca^{2+}-activated Cl^- channels. *Journal of Cell Science* **2012,** 125, (21), 4991-4998.

137. Whitlock, J. M.; Yu, K.; Cui, Y. Y.; Hartzell, H. C., Anoctamin 5/TMEM16E facilitates muscle precursor cell fusion. *J. Gen. Physiol.* **2018,** 150, (11), 1498-1509.

138. Pettersen, E. F.; Goddard, T. D.; Huang, C. C.; Couch, G. S.; Greenblatt, D. M.; Meng, E. C.; Ferrin, T. E., UCSF Chimera--a visualization system for exploratory research and analysis. *J. Comput. Chem.* **2004,** 25, (13), 1605-12.

139. Tian, Y.; Kongsuphol, P.; Hug, M.; Ousingsawat, J.; Witzgall, R.; Schreiber, R.; Kunzelmann, K., Calmodulin-dependent activation of the epithelial calcium-dependent chloride channel TMEM16A. *FASEB J.* **2011,** 25, (3), 1058-1068.

140. Vocke, K.; Dauner, K.; Hahn, A.; Ulbrich, A.; Broecker, J.; Keller, S.; Frings, S.; Möhrlen, F., Calmodulin-dependent activation and inactivation of anoctamin calcium-gated chloride channels. *J. Gen. Physiol.* **2013,** 142, (4), 381-404.

141. Terashima, H.; Picollo, A.; Accardi, A., Purified TMEM16A is sufficient to form Ca^{2+}-activated Cl^- channels. *Proc. Natl. Acad. Sci. U.S.A.* **2013,** 110, (48), 19354-19359.

142. Yu, Y.; Kuan, A.-S.; Chen, T.-Y., Calcium-calmodulin does not alter the anion permeability of the mouse TMEM16A calcium-activated chloride channel. *J. Gen. Physiol.* **2014,** 144, (1), 115-124.

143. Jung, J.; Nam, J. H.; Park, H. W.; Oh, U.; Yoon, J.-H.; Lee, M. G., Dynamic modulation of ANO1/TMEM16A HCO_3^- permeability by Ca^{2+}/calmodulin. *Proc. Natl. Acad. Sci. U.S.A.* **2013,** 110, (1), 360-365.

144. Bethel, N. P.; Grabe, M., Atomistic insight into lipid translocation by a TMEM16 scramblase. *Proc. Natl. Acad. Sci. U.S.A.* **2016,** 113, (49), 14049-14054.

145. Ta, C. M.; Acheson, K. E.; Rorsman, N. J. G.; Jongkind, R. C.; Tammaro, P., Contrasting effects of phosphatidylinositol 4,5-bisphosphate on cloned TMEM16A and TMEM16B channels. *Br. J. Pharmacol.* **2017,** 174, (18), 2984-2999.

146. Le, S. C.; Jia, Z.; Chen, J.; Yang, H., Molecular basis of PIP2-dependent regulation of the Ca^{2+}-activated chloride channel TMEM16A. *Nat. Commun.* **2019,** 10, (1), 3769.

147. Ye, W.; Han, T. W.; Nassar, L. M.; Zubia, M.; Jan, Y. N.; Jan, L. Y., Phosphatidylinositol-(4,5)-bisphosphate regulates calcium gating of small-conductance cation channel TMEM16F. *Proc. Natl. Acad. Sci. U.S.A.* **2018,** 115, (7), E1667-E1674.

148. Yu, K.; Jiang, T.; Cui, Y.; Tajkhorshid, E.; Hartzell, H. C., A network of phosphatidylinositol 4,5-bisphosphate binding sites regulates gating of the Ca^{2+}-activated Cl^- channel ANO1 (TMEM16A). *Proc. Natl. Acad. Sci. U.S.A.* **2019,** 116, (40), 19952-19962.

149. Jia, Z.; Chen, J., Specific PIP2 binding promotes calcium activation of TMEM16A chloride channels. *Commun. Biol.* **2021,** 4, (1), 259.

150. Alevy, Y. G.; Patel, A. C.; Romero, A. G.; Patel, D. A.; Tucker, J.; Roswit, W. T.; Miller, C. A.; Heier, R. F.; Byers, D. E.; Brett, T. J.; Holtzman, M. J., IL-13–induced airway mucus production is attenuated by MAPK13 inhibition. *The Journal of Clinical Investigation* **2012,** 122, (12), 4555-4568.

151. Woodruff, P. G.; Boushey, H. A.; Dolganov, G. M.; Barker, C. S.; Yang, Y. H.; Donnelly, S.; Ellwanger, A.; Sidhu, S. S.; Dao-Pick, T. P.; Pantoja, C.; Erle, D. J.; Yamamoto, K. R.; Fahy, J. V., Genome-wide profiling identifies epithelial cell genes associated with asthma and with treatment response to corticosteroids. *Proc. Natl. Acad. Sci. U.S.A.* **2007,** 104, (40), 15858-15863.

152. Brett, T. J., CLCA1 and TMEM16A: the link towards a potential cure for airway diseases. *Expert Rev. Res. Med.* **2015,** 9, (5), 503-506.

153. Patel, A. C.; Brett, T. J.; Holtzman, M. J., The Role of CLCA Proteins in Inflammatory Airway Disease. *Annu. Rev. Physiol.* **2009,** 71, (1), 425-449.

154. Gibson, A.; Lewis, A. P.; Affleck, K.; Aitken, A. J.; Meldrum, E.; Thompson, N., hCLCA1 and mCLCA3 Are Secreted Non-integral Membrane Proteins and Therefore Are Not Ion Channels. *J. Biol. Chem.* **2005,** 280, (29), 27205-27212.

155. Sala-Rabanal, M.; Yurtsever, Z.; Nichols, C. G.; Brett, T. J., Secreted CLCA1 modulates TMEM16A to activate Ca^{2+}-dependent chloride currents in human cells. *eLife* **2015,** 4, e05875.

156. Sala-Rabanal, M.; Yurtsever, Z.; Berry, K. N.; Nichols, C. G.; Brett, T. J., Modulation of TMEM16A channel activity by the von Willebrand factor type A (VWA) domain of the calcium-activated chloride channel regulator 1 (CLCA1). *J. Biol. Chem.* **2017,** 292, (22), 9164-9174.

157. Yurtsever, Z.; Sala-Rabanal, M.; Randolph, D. T.; Scheaffer, S. M.; Roswit, W. T.; Alevy, Y. G.; Patel, A. C.; Heier, R. F.; Romero, A. G.; Nichols, C. G.; Holtzman, M. J.; Brett, T. J., Self-cleavage of Human CLCA1 Protein by a Novel Internal Metalloprotease Domain Controls Calcium-activated Chloride Channel Activation. *J. Biol. Chem.* **2012,** 287, (50), 42138-42149.

158. Berry, K. N.; Brett, T. J., Structural and Biophysical Analysis of the CLCA1 VWA Domain Suggests Mode of TMEM16A Engagement. *Cell Rep.* **2020,** 30, (4), 1141-1151.e3.

159. Chao, A. C.; Mochizuki, H., Niflumic and flufenamic acids are potent inhibitors of chloride secretion in mammalian airway. *Life Sci.* **1992,** 51, (18), 1453-1457.

160. White, M. M.; Aylwin, M., Niflumic and flufenamic acids are potent reversible blockers of Ca^{2+}-activated Cl^- channels in Xenopus oocytes. *Mol. Pharmacol.* **1990,** 37, (5), 720-724.

161. Hogg, R. C.; Wang, Q.; Large, W. A., Action of niflumic acid on evoked and spontaneous calcium-activated chloride and potassium currents in smooth muscle cells from rabbit portal vein. *Br. J. Pharmacol.* **1994,** 112, (3), 977-984.

162. Robertson, B. E., Inhibition of calcium-activated chloride channels by niflumic acid dilates rat cerebral arteries. *Acta Physiol. Scand.* **1998,** 163, (4), 417-418.

163. Sinkkonen, S. T.; Mansikkamäki, S.; Möykkynen, T.; Lüddens, H.; Uusi-Oukari, M.; Korpi, E. R., Receptor Subtype-Dependent Positive and Negative Modulation of $GABA_A$ Receptor Function by Niflumic Acid, a Nonsteroidal Anti-Inflammatory Drug. *Mol. Pharmacol.* **2003,** 64, (3), 753-763.

164. Dai, L.; Garg, V.; Sanguinetti, M. C., Activation of Slo2.1 channels by niflumic acid. *J. Gen. Physiol.* **2010,** 135, (3), 275-295.

165. Ottolia, M.; Toro, L., Potentiation of large conductance KCa channels by niflumic, flufenamic, and mefenamic acids. *Biophys. J.* **1994,** 67, (6), 2272-2279.

166. Liantonio, A.; Giannuzzi, V.; Picollo, A.; Babini, E.; Pusch, M.; Conte Camerino, D., Niflumic acid inhibits chloride conductance of rat skeletal muscle by directly inhibiting the CLC-1 channel and by increasing intracellular calcium. *Br. J. Pharmacol.* **2007,** 150, (2), 235-247.

167. Namkung, W.; Phuan, P.-W.; Verkman, A. S., TMEM16A Inhibitors Reveal TMEM16A as a Minor Component of Calcium-activated Chloride Channel Conductance in Airway and Intestinal Epithelial Cells. *J. Biol. Chem.* **2011,** 286, (3), 2365-2374.

168. Huang, F.; Zhang, H.; Wu, M.; Yang, H.; Kudo, M.; Peters, C. J.; Woodruff, P. G.; Solberg, O. D.; Donne, M. L.; Huang, X.; Sheppard, D.; Fahy, J. V.; Wolters, P. J.; Hogan, B. L. M.; Finkbeiner, W. E.; Li, M.; Jan, Y.-N.; Jan, L. Y.; Rock, J. R., Calcium-activated chloride channel TMEM16A modulates mucin secretion and airway smooth muscle contraction. *Proc. Natl. Acad. Sci. U.S.A.* **2012,** 109, (40), 16354-16359.

169. Oh, S.-J.; Hwang, S. J.; Jung, J.; Yu, K.; Kim, J.; Choi, J. Y.; Hartzell, H. C.; Roh, E. J.; Lee, C. J., MONNA, a Potent and Selective Blocker for Transmembrane Protein with Unknown Function 16/Anoctamin-1. *Mol. Pharmacol.* **2013,** 84, (5), 726-735.

170. Seo, Y.; Lee, H. K.; Park, J.; Jeon, D.-k.; Jo, S.; Jo, M.; Namkung, W., Ani9, A Novel Potent Small-Molecule ANO1 Inhibitor with Negligible Effect on ANO2. *PLoS ONE* **2016,** 11, (5), e0155771.

171. Miner, K.; Labitzke, K.; Liu, B.; Wang, P.; Henckels, K.; Gaida, K.; Elliott, R.; Chen, J. J.; Liu, L.; Leith, A.; Trueblood, E.; Hensley, K.; Xia, X.-Z.; Homann, O.; Bennett, B.; Fiorino, M.; Whoriskey, J.; Yu, G.; Escobar, S.; Wong, M.; Born, T. L.; Budelsky, A.; Comeau, M.; Smith, D.; Phillips, J.; Johnston, J. A.; McGivern, J. G.; Weikl, K.; Powers, D.; Kunzelmann, K.; Mohn, D.; Hochheimer, A.; Sullivan, J. K., Drug Repurposing: The Anthelmintics Niclosamide and Nitazoxanide Are Potent TMEM16A Antagonists That Fully Bronchodilate Airways. *Front. Pharmacol.* **2019,** 10, (51).

172. Namkung, W.; Yao, Z.; Finkbeiner, W. E.; Verkman, A. S., Small-molecule activators of TMEM16A, a calcium-activated chloride channel, stimulate epithelial chloride secretion and intestinal contraction. *FASEB J.* **2011,** 25, (11), 4048-4062.

173. Danahay, H. L.; Lilley, S.; Fox, R.; Charlton, H.; Sabater, J.; Button, B.; McCarthy, C.; Collingwood, S. P.; Gosling, M., TMEM16A Potentiation: A Novel Therapeutic Approach for the Treatment of Cystic Fibrosis. *Am. J. Respir. Crit. Care Med.* **2020,** 201, (8), 946-954.

174. Boedtkjer, D. M.; Kim, S.; Jensen, A. B.; Matchkov, V. M.; Andersson, K. E., New selective inhibitors of calcium-activated chloride channels - $T16A_{inh}$-A01, $CaCC_{inh}$-A01 and MONNA - what do they inhibit? *Br. J. Pharmacol.* **2015,** 172, (16), 4158-72.

175. Cabrita, I.; Benedetto, R.; Schreiber, R.; Kunzelmann, K., Niclosamide repurposed for the treatment of inflammatory airway disease. *JCI Insight* **2019,** 4, (15).

176. Whitlock, J. M.; Hartzell, H. C., Anoctamins/TMEM16 Proteins: Chloride Channels Flirting with Lipids and Extracellular Vesicles. *Annu. Rev. Physiol.* **2017,** 79, 119-143.

177. Falzone, M. E.; Malvezzi, M.; Lee, B. C.; Accardi, A., Known structures and unknown mechanisms of TMEM16 scramblases and channels. *J. Gen. Physiol.* **2018,** 150, (7), 933-947.

178. Stohr, H.; Heisig, J. B.; Benz, P. M.; Schoberl, S.; Milenkovic, V. M.; Strauss, O.; Aartsen, W. M.; Wijnholds, J.; Weber, B. H.; Schulz, H. L., TMEM16B, a novel protein with calcium-dependent chloride channel activity, associates with a presynaptic protein complex in photoreceptor terminals. *J. Neurosci.* **2009,** 29, (21), 6809-18.

179. Bevers, E. M.; Williamson, P. L., Getting to the Outer Leaflet: Physiology of Phosphatidylserine Exposure at the Plasma Membrane. *Physiol. Rev.* **2016,** 96, (2), 605-45.

180. Castoldi, E.; Collins, P. W.; Williamson, P. L.; Bevers, E. M., Compound heterozygosity for 2 novel TMEM16F mutations in a patient with Scott syndrome. *Blood* **2011,** 117, (16), 4399-400.

181. Malvezzi, M.; Andra, K. K.; Pandey, K.; Lee, B. C.; Falzone, M. E.; Brown, A.; Iqbal, R.; Menon, A. K.; Accardi, A., Out-of-the-groove transport of lipids by TMEM16 and GPCR scramblases. *Proc. Natl. Acad. Sci. U.S.A.* **2018,** 115, (30), E7033-E7042.

182. Bers, D. M.; Patton, C. W.; Nuccitelli, R., A practical guide to the preparation of Ca^{2+} buffers. *Methods Cell Biol.* **2010,** 99, 1-26.

183. Zhang, X. D.; Chen, T. Y., Amphiphilic blockers punch through a mutant CLC-0 pore. *J. Gen. Physiol.* **2009,** 133, (1), 59-68.

184. Tien, J.; Lee, H. Y.; Minor, D. L., Jr.; Jan, Y. N.; Jan, L. Y., Identification of a dimerization domain in the TMEM16A calcium-activated chloride channel (CaCC). *Proc. Natl. Acad. Sci. U.S.A.* **2013,** 110, (16), 6352-7.

185. Chen, M. F.; Chen, T. Y., Side-chain charge effects and conductance determinants in the pore of ClC-0 chloride channels. *J. Gen. Physiol.* **2003,** 122, (2), 133-45.

186. Middleton, R. E.; Pheasant, D. J.; Miller, C., Homodimeric architecture of a ClC-type chloride ion channel. *Nature* **1996,** 383, (6598), 337-40.

187. Kuruma, A.; Hartzell, H. C., Bimodal control of a Ca^{2+}-activated Cl^- channel by different Ca^{2+} signals. *J. Gen. Physiol.* **2000,** 115, (1), 59-80.

188. Lin, C. W.; Chen, T. Y., Probing the pore of ClC-0 by substituted cysteine accessibility method using methane thiosulfonate reagents. *J. Gen. Physiol.* **2003,** 122, (2), 147-59.

189. Stauffer, D. A.; Karlin, A., Electrostatic potential of the acetylcholine binding sites in the nicotinic receptor probed by reactions of binding-site cysteines with charged methanethiosulfonates. *Biochemistry* **1994,** 33, (22), 6840-9.

190. Yu, K.; Zhu, J.; Qu, Z.; Cui, Y. Y.; Hartzell, H. C., Activation of the Ano1 (TMEM16A) chloride channel by calcium is not mediated by calmodulin. *J. Gen. Physiol.* **2014,** 143, (2), 253-67.

191. Yu, Y.; Chen, T. Y., Purified human brain calmodulin does not alter the bicarbonate permeability of the ANO1/TMEM16A channel. *J. Gen. Physiol.* **2015,** 145, (1), 79-81.

192. Eisenman, G., Cation selective glass electrodes and their mode of operation. *Biophys. J.* **1962,** 2, (2 Pt 2), 259-323.

193. Qu, Z.; Hartzell, H. C., Anion permeation in Ca^{2+}-activated Cl^- channels. *J. Gen. Physiol.* **2000,** 116, (6), 825-44.

194. Chiamvimonvat, N.; Perez-Garcia, M. T.; Tomaselli, G. F.; Marban, E., Control of ion flux and selectivity by negatively charged residues in the outer mouth of rat sodium channels. *J. Physiol.* **1996,** 491 (Pt 1), 51-9.

195. Imoto, K.; Busch, C.; Sakmann, B.; Mishina, M.; Konno, T.; Nakai, J.; Bujo, H.; Mori, Y.; Fukuda, K.; Numa, S., Rings of negatively charged amino acids determine the acetylcholine receptor channel conductance. *Nature* **1988,** 335, (6191), 645-8.

196. Whitlock, J. M.; Hartzell, H. C., A Pore Idea: the ion conduction pathway of TMEM16/ANO proteins is composed partly of lipid. *Pflügers Arch.* **2016,** 468, (3), 455-73.

197. Pomorski, T. G.; Menon, A. K., Lipid somersaults: Uncovering the mechanisms of protein-mediated lipid flipping. *Prog. Lipid Res.* **2016,** 64, 69-84.

198. Feng, S.; Dang, S.; Han, T. W.; Ye, W.; Jin, P.; Cheng, T.; Li, J.; Jan, Y. N.; Jan, L. Y.; Cheng, Y., Cryo-EM Studies of TMEM16F Calcium-Activated Ion Channel Suggest Features Important for Lipid Scrambling. *Cell Rep.* **2019,** 28, (2), 567-579 e4.

199. Kyte, J.; Doolittle, R. F., A simple method for displaying the hydropathic character of a protein. *J. Mol. Biol.* **1982,** 157, (1), 105-32.

200. Zamyatnin, A. A., Protein volume in solution. *Prog. Biophys. Mol. Biol.* **1972,** 24, 107-23.

201. Fischer, H.; Illek, B.; Sachs, L.; Finkbeiner, W. E.; Widdicombe, J. H., CFTR and calcium-activated chloride channels in primary cultures of human airway gland cells of serous or mucous phenotype. *Am. J. Physiol. Lung Cell Mol. Physiol.* **2010,** 299, (4), L585-94.

202. Han, Y.; Shewan, A. M.; Thorn, P., HCO_3^- Transport through Anoctamin/Transmembrane Protein ANO1/TMEM16A in Pancreatic Acinar Cells Regulates Luminal pH. *J. Biol. Chem.* **2016,** 291, (39), 20345-52.

203. Hahn, A. K.; Faulhaber, J.; Srisawang, L.; Salomon, J. J.; Mall, M. M.; Mohrlen, F.; Frings, S., The Ca^{2+}-Activated Chloride Channel TMEM16A Colocalizes with CFTR Chloride Channels in Rodent Secretory Airway Epithelial Cells. *FASEB J.* **2017,** 31.

204. Hwang, S. J.; Blair, P. J.; Britton, F. C.; O'Driscoll, K. E.; Hennig, G.; Bayguinov, Y. R.; Rock, J. R.; Harfe, B. D.; Sanders, K. M.; Ward, S. M., Expression of anoctamin 1/TMEM16A by interstitial cells of Cajal is fundamental for slow wave activity in gastrointestinal muscles. *J. Physiol.* **2009,** 587, (Pt 20), 4887-904.

205. Huang, F.; Rock, J. R.; Harfe, B. D.; Cheng, T.; Huang, X.; Jan, Y. N.; Jan, L. Y., Studies on expression and function of the TMEM16A calcium-activated chloride channel. *Proc. Natl. Acad. Sci. U.S.A.* **2009,** 106, (50), 21413-8.

206. Lau, A.; McLaughlin, A.; McLaughlin, S., The adsorption of divalent cations to phosphatidylglycerol bilayer membranes. *Biochim. Biophys. Acta* **1981,** 645, (2), 279-92.

207. McLaughlin, S.; Mulrine, N.; Gresalfi, T.; Vaio, G.; McLaughlin, A., Adsorption of divalent cations to bilayer membranes containing phosphatidylserine. *J. Gen. Physiol.* **1981,** 77, (4), 445-73.

208. Ohki, S.; Kurland, R., Surface potential of phosphatidylserine monolayers. II. Divalent and monovalent ion binding. *Biochim. Biophys. Acta* **1981,** 645, (2), 170-6.

209. Zhang, X. D.; Tseng, P. Y.; Yu, W. P.; Chen, T. Y., Blocking pore-open mutants of CLC-0 by amphiphilic blockers. *J. Gen. Physiol.* **2009,** 133, (1), 43-58.

210. Hartzell, H. C., CaCl-ing channels get the last laugh. *Science* **2008,** 322, (5901), 534-5.

211. Thomas-Gatewood, C.; Neeb, Z. P.; Bulley, S.; Adebiyi, A.; Bannister, J. P.; Leo, M. D.; Jaggar, J. H., TMEM16A channels generate Ca^{2+}-activated Cl^- currents in cerebral artery smooth muscle cells. *Am. J. Physiol. Heart Circ. Physiol.* **2011,** 301, (5), H1819-27.

212. Nguyen, D. M.; Chen, L. S.; Jeng, G.; Yu, W. P.; Chen, T. Y., Cobalt ion interaction with TMEM16A calcium-activated chloride channel: Inhibition and potentiation. *PLoS ONE* **2020,** 15, (4), e0231812.

213. Hendrickson, H. S.; Fullington, J. G., Stabilities of metal complexes of phospholipids: Ca(II), Mg(II), and Ni(II) complexes of phosphatidylserine and triphosphoinositide. *Biochemistry* **1965,** 4, (8), 1599-605.

214. Latorre, R.; Labarca, P.; Naranjo, D., Surface charge effects on ion conduction in ion channels. *Methods Enzymol.* **1992,** 207, 471-501.

215. McLaughlin, S., The electrostatic properties of membranes. *Annu. Rev. Biophys. Biophys. Chem.* **1989,** 18, 113-36.

216. Frankenhaeuser, B.; Hodgkin, A. L., The action of calcium on the electrical properties of squid axons. *J. Physiol.* **1957,** 137, (2), 218-44.

217. Hille, B.; Woodhull, A. M.; Shapiro, B. I., Negative surface charge near sodium channels of nerve: divalent ions, monovalent ions, and pH. *Philos. Trans. R. Soc. Lond. B. Biol. Sci.* **1975,** 270, (908), 301-18.

218. Bell, J. E.; Miller, C., Effects of phospholipid surface charge on ion conduction in the K^+ channel of sarcoplasmic reticulum. *Biophys. J.* **1984,** 45, (1), 279-87.

219. Apell, H. J.; Bamberg, E.; Lauger, P., Effects of surface charge on the conductance of the gramicidin channel. *Biochim. Biophys. Acta* **1979,** 552, (3), 369-78.

220. Park, E.; Campbell, E. B.; MacKinnon, R., Structure of a CLC chloride ion channel by cryo-electron microscopy. *Nature* **2017,** 541, (7638), 500-505.

221. Park, E.; MacKinnon, R., Structure of the CLC-1 chloride channel from Homo sapiens. *eLife* **2018,** 7.

222. Lewis, C. A., Ion-concentration dependence of the reversal potential and the single channel conductance of ion channels at the frog neuromuscular junction. *J. Physiol.* **1979,** 286, 417-45.

223. Miedema, H., Surface potentials and the calculated selectivity of ion channels. *Biophys. J.* **2002,** 82, (1 Pt 1), 156-9.

224. Hilgemann, D. W.; Feng, S.; Nasuhoglu, C., The complex and intriguing lives of PIP2 with ion channels and transporters. *Sci. Signal.* **2001,** 2001, (111), re19.

225. Frankenhaeuser, B., Sodium permeability in toad nerve and in squid nerve. *J. Physiol.* **1960,** 152, 159-66.

226. Rostovtseva, T. K.; Aguilella, V. M.; Vodyanoy, I.; Bezrukov, S. M.; Parsegian, V. A., Membrane surface-charge titration probed by gramicidin A channel conductance. *Biophys. J.* **1998,** 75, (4), 1783-92.

227. McLaughlin, S. G.; Szabo, G.; Eisenman, G., Divalent ions and the surface potential of charged phospholipid membranes. *J. Gen. Physiol.* **1971,** 58, (6), 667-87.

228. Hille, B., Modification of gating in voltage-sensitive channels. In *Ion Channels of Excitable Membranes*, 3rd ed ed.; Hille, B., Ed. Sinauer Associates, Inc.: Sunderland, MA, 2001; pp 635-662.

229. Hille, B.; Ritchie, J. M.; Strichartz, G. R., The effect of surface charge on the nerve membrane on the action of tetrodotoxin and saxitoxin in frog myelinated nerve. *J. Physiol.* **1975,** 250, (1), 34P-35P.

230. MacKinnon, R., Potassium channels. *FEBS Lett.* **2003,** 555, (1), 62-65.

231. Corringer, P.-J.; Bertrand, S.; Galzi, J.-L.; Devillers-Thiéry, A.; Changeux, J.-P.; Bertrand, D., Mutational Analysis of the Charge Selectivity Filter of the α7 Nicotinic Acetylcholine Receptor. *Neuron* **1999,** 22, (4), 831-843.

232. Bertrand, D.; Galzi, J. L.; Devillers-Thiéry, A.; Bertrand, S.; Changeux, J. P., Mutations at two distinct sites within the channel domain M2 alter calcium permeability of neuronal alpha 7 nicotinic receptor. *Proc. Natl. Acad. Sci. U.S.A.* **1993,** 90, (15), 6971-6975.

233. Lis, L. J.; Lis, W. T.; Parsegian, V. A.; Rand, R. P., Adsorption of divalent cations to a variety of phosphatidylcholine bilayers. *Biochemistry* **1981,** 20, (7), 1771-1777.

234. Sinn, C. G.; Antonietti, M.; Dimova, R., Binding of calcium to phosphatidylcholine–phosphatidylserine membranes. *Col-loids Surf., A* **2006,** 282-283, 410-419.

235. Alsop, R. J.; Maria Schober, R.; Rheinstädter, M. C., Swelling of phospholipid membranes by divalent metal ions depends on the location of the ions in the bilayers. *Soft Matter* **2016,** 12, (32), 6737-6748.

236. Favre, I.; Moczydlowski, E.; Schild, L., On the structural basis for ionic selectivity among Na^+, K^+, and Ca^{2+} in the voltage-gated sodium channel. *Biophys. J.* **1996,** 71, (6), 3110-3125.

237. Huang, S.; Du, P.; Min, C.; Liao, Y.; Sun, H.; Jiang, Y., Poly(1-amino-5-chloroanthraquinone): Highly Selective and Ultrasensitive Fluorescent Chemosensor For Ferric Ion. *Journal of Fluorescence* **2013,** 23, (4), 621-627.

238. Lide, D. R., *CRC Handbook of Chemistry and Physics*. 85 ed.; CRC Press: Boca Raton, FL, 2005.

239. Harvey Lodish, A. B., S Lawrence Zipursky, Paul Matsudaira, David Baltimore, and James Darnell, *Molecular Cell Biology*. 4th ed.; W. H. Freeman: New York, USA, 2000.

240. Mbaye, M. N.; Hou, Q.; Basu, S.; Teheux, F.; Pucci, F.; Rooman, M., A comprehensive computational study of amino acid interactions in membrane proteins. *Sci. Rep.* **2019,** 9, (1), 12043.

241. Reithmeier, R. A. F., Characterization and modeling of membrane proteins using sequence analysis. *Curr. Opin. Struct. Biol.* **1995,** 5, (4), 491-500.

242. Adamian, L.; Nanda, V.; DeGrado, W. F.; Liang, J., Empirical lipid propensities of amino acid residues in multispan alpha helical membrane proteins. *Proteins* **2005,** 59, (3), 496-509.

243. Yau, W.-M.; Wimley, W. C.; Gawrisch, K.; White, S. H., The Preference of Tryptophan for Membrane Interfaces. *Biochemistry* **1998,** 37, (42), 14713-14718.

244. Gaede, H. C.; Yau, W.-M.; Gawrisch, K., Electrostatic Contributions to Indole−Lipid Interactions. *J. Phys. Chem. B* **2005,** 109, (26), 13014-13023.

245. Sun, H.; Greathouse, D. V.; Andersen, O. S.; Koeppe, R. E., The Preference of Tryptophan for Membrane Interfaces: INSIGHTS FROM N-METHYLATION OF TRYPTOPHANS IN GRAMICIDIN CHANNELS. *J. Biol. Chem.* **2008,** 283, (32), 22233-22243.

246. Killian, J. A.; von Heijne, G., How proteins adapt to a membrane–water interface. *Trends Biochem. Sci.* **2000,** 25, (9), 429-434.

247. de Jesus, A. J.; Allen, T. W., The role of tryptophan side chains in membrane protein anchoring and hydrophobic mismatch. *Biochim. Biophys. Acta* **2013,** 1828, (2), 864-876.

248. Melcrová, A.; Pokorna, S.; Pullanchery, S.; Kohagen, M.; Jurkiewicz, P.; Hof, M.; Jungwirth, P.; Cremer, P. S.; Cwiklik, L., The complex nature of calcium cation interactions with phospholipid bilayers. *Sci. Rep.* **2016,** 6, (1), 38035.

249. Kaya, D.; Keçeci, K., Review—Track-Etched Nanoporous Polymer Membranes as Sensors: A Review. *J. Electrochem. Soc.* **2020,** 167, (3), 037543.

250. Xiong, T.; Zhang, K.; Jiang, Y.; Yu, P.; Mao, L., Ion current rectification: from nanoscale to microscale. *Sci. China Chem.* **2019,** 62, (10), 1346-1359.

251. Pevarnik, M.; Healy, K.; Davenport, M.; Yen, J.; Siwy, Z. S., A hydrophobic entrance enhances ion current rectification and induces dewetting in asymmetric nanopores. *Analyst* **2012,** 137, (13), 2944-2950.

252. Lu, Z.; Ding, L., Blockade of a Retinal cGMP-gated Channel by Polyamines. *J. Gen. Physiol.* **1999,** 113, (1), 35-43.

253. Guo, D.; Lu, Z., Mechanism of Cgmp-Gated Channel Block by Intracellular Polyamines. *J. Gen. Physiol.* **2000,** 115, (6), 783-798.

254. Fu, L. Y.; Cummins, T. R.; Moczydlowski, E. G., Sensitivity of cloned muscle, heart and neuronal voltage-gated sodium channels to block by

polyamines: a possible basis for modulation of excitability in vivo. *Channels (Austin)* **2012,** 6, (1), 41-9.

255. Gomez, M.; Hellstrand, P., Effects of polyamines on voltage-activated calcium channels in guinea-pig intestinal smooth muscle. *Pflügers Arch.* **1995,** 430, (4), 501-7.

256. Zhang , Y.; Niu , X.; Brelidze , T. I.; Magleby , K. L., Ring of Negative Charge in BK Channels Facilitates Block by Intracellular Mg2+ and Polyamines through Electrostatics. *J. Gen. Physiol.* **2006,** 128, (2), 185-202.

257. Burnashev, N.; Monyer, H.; Seeburg, P. H.; Sakmann, B., Divalent ion permeability of AMPA receptor channels is dominated by the edited form of a single subunit. *Neuron* **1992,** 8, (1), 189-198.

258. Diering, G. H.; Huganir, R. L., The AMPA Receptor Code of Synaptic Plasticity. *Neuron* **2018,** 100, (2), 314-329.

259. Siwy, Z.; Heins, E.; Harrell, C. C.; Kohli, P.; Martin, C. R., Conical-Nanotube Ion-Current Rectifiers: The Role of Surface Charge. *J. Am. Chem. Soc.* **2004,** 126, (35), 10850-10851.

260. Lan, W.-J.; Holden, D. A.; White, H. S., Pressure-Dependent Ion Current Rectification in Conical-Shaped Glass Nanopores. *J. Am. Chem. Soc.* **2011,** 133, (34), 13300-13303.

261. Rath, D. L.; Hansen, W. N., Electrode resistance in the electrochemical cell; analysis of size effect theory with the specific adsorption of Br^- and I^- on polycrystalline gold films. *Surf. Sci.* **1984,** 136, (1), 195-216.

262. Biggs, S.; Mulvaney, P.; Zukoski, C. F.; Grieser, F., Study of Anion Adsorption at the Gold-Aqueous Solution Interface by Atomic Force Microscopy. *J. Am. Chem. Soc.* **1994,** 116, (20), 9150-9157.

263. Ramirez, P.; Manzanares, J. A.; Cervera, J.; Gomez, V.; Ali, M.; Pause, I.; Ensinger, W.; Mafe, S., Nanopore charge inversion and current-voltage curves in mixtures of asymmetric electrolytes. *Journal of Membrane Science* **2018,** 563, 633-642.

264. Frey, B.; Gaipl, U. S., The immune functions of phosphatidylserine in membranes of dying cells and microvesicles. *Semin. Immunol.* **2011,** 33, (5), 497-516.

265. Huster, D.; Arnold, K.; Gawrisch, K., Strength of Ca^{2+} Binding to Retinal Lipid Membranes: Consequences for Lipid Organization. *Biophys. J.* **2000,** 78, (6), 3011-3018.

266. Suh, B.-C.; Hille, B., PIP2 Is a Necessary Cofactor for Ion Channel Function: How and Why? *Annu. Rev. Biophys.* **2008,** 37, (1), 175-195.

267. Ibarguren, M.; López, D. J.; Escribá, P. V., The effect of natural and synthetic fatty acids on membrane structure, microdomain organization, cellular functions and human health. *Biochim. Biophys. Acta* **2014,** 1838, (6), 1518-1528.